INVESTIGATION OF THE DEEP DRAWABILITY OF STEEL AND ALUMINUM SHEETS BY FINITE ELEMENT SIMULATION

A THESIS SUBMITTED TO
THE GRADUATE SCHOOL OF NATURAL AND APPLIED SCIENCES
OF
MIDDLE EAST TECHNICAL UNIVERSITY

BY

ÇAĞLAR SÖNMEZ

IN PARTIAL FULFILLMENT OF THE REQUIREMENTS
FOR
THE DEGREE OF MASTER OF SCIENCE
IN
METALLURGICAL AND MATERIALS ENGINEERING

APRIL 2005

Approval of the Graduate School of Natural and Applied Sciences

_____

Prof. Dr. Canan Özgen
Director

I certify that this thesis satisfies all the requirements as a thesis for the degree of Master of Science.

_____

Prof. Dr. Tayfur Öztürk
Head of Department

This is to certify that we have read this thesis and that in our opinion it is fully adequate, in scope and quality, as a thesis for the degree of Master of Science.

Prof. Dr. Ing. A.Erman Tekkaya Co-Supervisor	Assoc. Prof. Dr. C.Hakan Gür Supervisor

Examining Committee Members:

Prof. Dr. Tayfur Öztürk	(METU, METE)	_____
Assoc. Prof. Dr. C.Hakan Gür	(METU, METE)	_____
Prof. Dr. -Ing. A.Erman Tekkaya	(ATILIM UNIV., MFGE)	_____
Prof. Dr. Rıza Gürbüz	(METU, METE)	_____
Assoc. Prof. Dr. Cevdek Kaynak	(METU, METE)	_____

I hereby declare that all information in this document has been obtained and presented in accordance with academic rules and ethical conduct. I also declare that, as required by these rules and conduct, I have fully cited and referenced all material and results that are not original to this work.

Name, Last name :

Signature :

ABSTRACT

INVESTIGATION OF THE DEEP DRAWABILITY
OF STEEL AND ALUMINUM SHEETS
BY FINITE ELEMENT SIMULATION

Sönmez, Çağlar
M.S., Department of Metallurgical and Materials Engineering
Supervisor : Assoc. Prof. Dr. C. Hakan Gür
Co-Supervisor: Prof. Dr. -Ing. A. Erman Tekkaya

April 2005, 221 pages

Sheet metal forming processes, especially deep drawing processes give diverse results by various materials. Extreme differences occur between steel sheets and aluminum sheets. The main causes of this variance are anisotropy, elastic modulus and microscopic material properties.

The aim of this thesis is to evaluate the deep drawing properties and also to develop suitable process parameters for aluminum and steel sheets by finite element simulation. In the simulation, the commercial dynamic-explicit code PAM-STAMP has been used. The reliability of the finite element package was verified by a comparison with the NUMISHEET 2002 benchmarks. Additionally, a commercial part is numerically simulated for experimental verification. The results of the simulations have been compared with several experiments that were performed in

Metallurgical and Materials Engineering and Mechanical Engineering Departments. Finally, the simulation results are compared with analytical expressions for verification of results.

The materials investigated for the deep drawability comparison is a deep drawing quality mild steel and an aluminum alloy designated as 6111-T4. For experimental verification St4 steel is used.

Results are in agreement with the fact that aluminum and steel materials behave differently upon deep drawing in terms of the onset of failure, wrinkling and final shape. Aluminum is found to be less formable than steel for cup drawing operations.

Keywords: Deep Drawing, Aluminum, Steel, Finite Element Analysis, Dynamic-Explicit method.

ÖZ

ÇELİK VE ALÜMİNYUM SACLARININ DERİN ÇEKİLEBİLİRLİĞİNİN SONLU ELEMAN BENZETİMİ İLE ARAŞTIRILMASI

Sönmez, Çağlar
Yüksek Lisans, Metalurji ve Malzeme Mühendisliği Bölümü
Tez Yöneticisi : Doç. Dr. C. Hakan Gür
Yardımcı Tez Yöneticisi : Prof. Dr. -Ing. A. Erman Tekkaya

Nisan 2005, 221 sayfa

Sac şekillendirme işlemleri, özellikle derin çekme prosesleri farklı malzemelerle oldukça değişik sonuçlar verir. En büyük farklılıklar çelik ve alüminyum sacları arasında oluşur. Bu farklılıkların ana kaynakları anisotropi, elastik modül ve mikroskobik malzeme özellikleridir.

Bu tez çalışması sonlu eleman benzetimi ile alüminyum ve çelik saclarının derin çekme işlemlerini değerlendirmeye ve bu işlemler için uygun parametreler geliştirmeye odaklanmaktadır. Simülasyonlar için bir ticari, dinamik-eksplisit kodu olan PAM-STAMP programı kullanılmıştır. Bu sonlu eleman paket programının güvenilirliği NUMISHEET'in 2002 bençmarkları ile karşılaştırmalar yapılarak sınanmıştır. Ayrıca, hâlihazırda üretilmekte olan ticari bir parçanın sayısal modellenmesi de deneysel sınama amacıyla yapılmıştır. Simülasyonlardan elde edilen bulgular Metalurji ve Malzeme Mühendisliği ve Makine Mühendisliği

Bölümlerinde yapılan testlerle karşılaştırılmıştır. Son olarak sayısal analiz bulguları analitik çözümlerle de karşılaştırılıp doğrulanmıştır.

Derin çekilebilirlik karşılaştırılması için derin çekme kalitesinde bir yumuşak çelik ve 6111-T4 kodlu bir alüminyum alaşımı kullanılmıştır. Deneysel doğrulama çalışmasında ise St4 kodlu bir çelik malzeme incelenmiştir.

Sonuçlar alüminyum ve çelik malzemelerin derin çekme işlemleri sonucu yetmezlik noktası, buruşma ve son şekil açılarından farklı davranışlar gösterdiklerini doğrulamıştır.

Anahtar Kelimeler: Derin Çekme, Alüminyum, Çelik, Sonlu Eleman Analizi, Dinamik-Eksplisit yöntem.

To my family and Nurhak Yorulmaz

ACKNOWLEDGMENTS

I would like to express my deepest gratitude and appreciation to my supervisor Assoc. Prof. Dr. C.Hakan Gür and my co-supervisor Prof. Dr. –Ing. A.Erman Tekkaya for their support, inspiration, criticism and patience throughout this study.

I would also like to thank to my colleague İ. Erkan Önder, whose support, suggestions and friendship made great contributions to this work.

This study was carried out as a part of an AFP research project with the project number of BAP-2002-03-02-01 at METU Metallurgical and Mechanical Engineering Departments. I would like to thank Dr. Feridun Özhan, Turhan Savaş and Atila Özbalas at company ORS for providing the sample for experimental study and allowing me to investigate the process in detail within my study.

I would like to send best wishes to my friends at the Femlab: Ömer, Özgür, Bahadır, Oya, Murat, Erge, Nagihan, Canderim, Çağrı, Muin, Alper, Koray, Hasan Ali and Şahika. I also want to thank to my friends Mehmet Nalbantoğlu, Muratcan Akçay, Levent Gaşgil and Mustafa Kaya at our band MAGICK, and the members of the METU Music Societies.

Greatest thanks to my family for their infinite support during all these years at METU.

Finally, I would like to thank to Nurhak Yorulmaz for being there all the time. You are the inspiration and joy of my life.

TABLE OF CONTENTS

LIST OF TABLES

TABLES

LIST OF FIGURES

FIGURES

CHAPTER I

INTRODUCTION

1.1 Current Trends in Automotive Metal Forming

Conventional sheet metal forming operations are among the most important operations in metal forming. Especially, in the automotive and aircraft industries, deep drawing and bending operations are widely utilized for the forming of outer panels. Some examples for such parts can be seen in Figure 1.1.

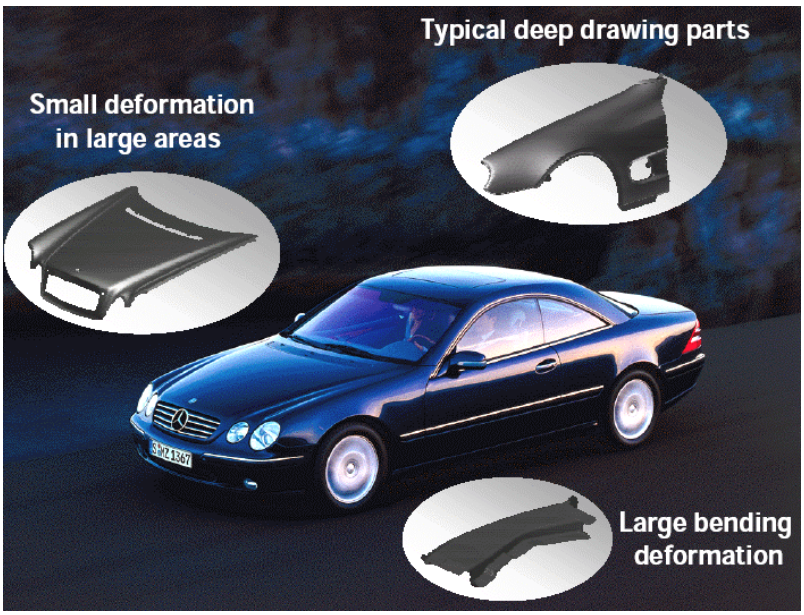

Figure 1.1: Deep drawn parts in a typical passenger car

Sheet metal forming technologies are constantly challenged by the improvements in the automotive industry in the last several decades. Due to increasing customer expectations, safety requirements and market competitions, there is a strong need for products, which can be manufactured more successfully, more economically and swiftly to satisfy ever-increasing market needs.

On the other hand, in recent years, environmental and safety concerns have forced the industry to choose lighter-yet-safer materials for automotive production, to reduce the weight of automobiles (Engl & Schneider, 1998). To improve safety, driving performance, comfort and overall quality, additional accessories, which increase weight, are being utilized in automobiles. To the contrary, to reduce fuel consumption (and therefore to preserve the environment), to improve driving dynamics, the overall weight must be minimized. Tekkaya (2000) states that the drastic reduction of development periods as well as the trend to reduce weight of the cars in order to reduce the fuel consumption leads especially in the car manufacturing industry to a rebuilding of the conventional design and manufacturing procedures. Besides this, 'alternative' materials are being studied to replace conventional steel materials to reduce weight in many parts. For this purpose, several approaches are presented:

- The usage of high strength steels
- The usage of aluminum-alloys
- The usage of magnesium-alloys
- The usage of polymers

Among all these approaches, the utilization of aluminum-alloys is becoming more popular among automotive manufacturers. Figure 1.2 reflects these expectations (N.N., 2001).

Similarly, concerning sheet metal parts, conventional steels are most widely used for outer panel production, whereas lighter materials (like aluminum-alloy sheets) are being increasingly utilized in many areas. For instance the heat treatable AA6111 aluminum alloy (which is investigated within the present study) is one of the most prominent materials employed in outer body panels of cars and light trucks

due to its unique combination of formability, paint bake strengthening and superior corrosion resistance characteristics (Quainoo & Yannacopoulos, 2004).

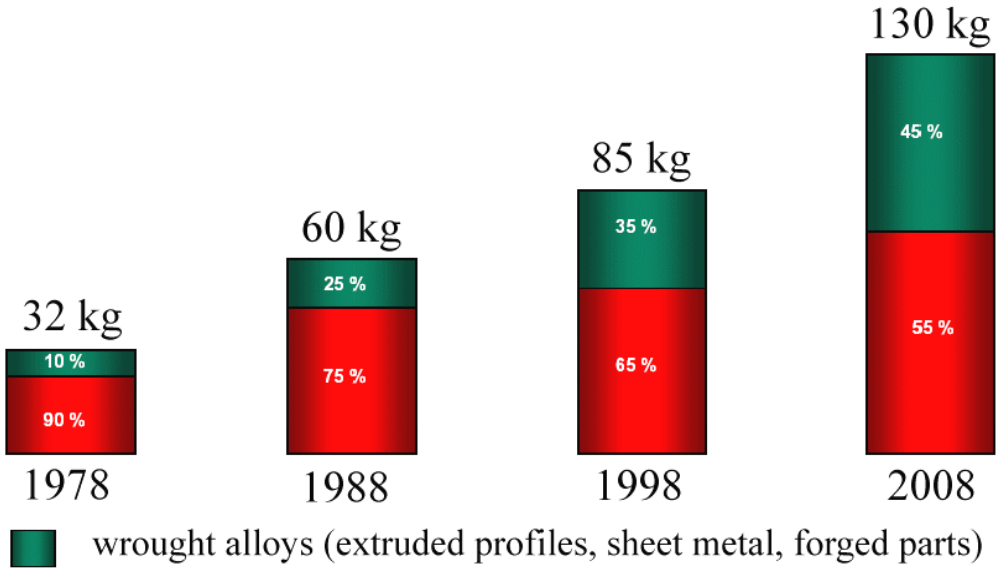

Figure 1.2: The weight of aluminum material in a typical passenger car

The manufacturing technologies are influenced from these improvements. Sheet metal forming processes', especially deep drawing processes' outcome is strongly dependent on the materials used. Therefore, the process chains and the tool designs must be re-evaluated as swiftly as possible whenever another material is proposed to produce a certain part. The most radical design difference is required when aluminum sheets are substituted for steel sheets. This occurrence is due to the differences in micro- and macroscopic material properties of both materials.

1.2 Differences of Aluminum and Steel Sheets

The normal anisotropy value (r-value) of steel is larger than unity, whereas aluminum has an r-value that is smaller than unity (Section 2.4.1). This affects the final shape variations of steel and aluminum sheets upon a forming process. Therefore, the thickness variations of these materials for the same drawing

operations may be different. Excessive thinning or thickening problems may arise, even failure may occur for these materials in uncontrolled manufacturing processes.

The elastic (Young's) modulus of aluminum is nearly one-third of that of steel, making the springback effects more dominant. Therefore, elastic recovery poses a greater problem for aluminum sheets. Additionally, the residual stress distributions become completely different compared to steel, affecting part response to successive operations and product life.

Moreover, aluminum and steel materials have different strain hardening coefficients, thus their strain hardening behaviors are different.

Furthermore, due to different grain structures, the final surface qualities of aluminum and steel sheets are different; therefore the surface properties of steel and aluminum sheets are different. Especially, the formation of large grains in aluminum due to large deformations makes aluminum sheets esthetically unusable.

1.3 Aim and Scope of the Thesis

In the light of these, the main aim of this study is to systematically investigate sheet metal forming operations using these two different materials by using numerical analysis methods. For this purpose the commercial dynamic-explicit finite element analysis (FEA) code PAM-STAMP was utilized. The deformation behavior of the materials in the numerical analyses has been described by an elasto-plastic material model.

Material-dependent forming process specifications have been determined for simple cup-drawing operations of the following materials: deep drawing quality (DDQ) mild steel and an aluminum alloy designated as 6111-T4. By varying process parameters the formation of an axisymmetric cup shape has been simulated for these materials. For a constant tool speed, the effects of the blank holding force and

lubrication conditions upon the outcome of the drawing process have been evaluated. The onsets of wrinkling and failure were determined for both materials and the thickness variations are inspected. Hence, the process windows for the axisymmetric cup drawing of the aluminum and steel materials were determined.

Additionally, the reliability of the finite element (FE) code has been investigated. For this purpose, sample analyses have been compared with a real life case (which is a commercially produced part). A ball bearing case part (which is actually in production in ORS Company) has been numerically simulated for this purpose. The actual part geometry and its mechanical properties have been compared with the findings of the FE-simulation. Additionally the metallographic analysis of the ball bearing case part has been conducted to show the grain structure of the deformed part. Moreover, the simulation results of a benchmark test proposed by NUMISHEET (2002) have been compared with NUMISHEET 2002 Benchmark's findings. Finally, the simulation results are also verified via an analytical model developed by Ramaekers (1999).

1.4 Content of this Study

The thesis is divided into nine chapters. In the first chapter, general information about the study is given. The next chapter is the literature survey, in which previous studies about the occurrences in deep drawing processes and its numerical simulations and the effects of material properties like anisotropy will be summarized. Within this chapter the concept of formability and its relation with various parameters is inspected and the occurrences in finite element analyses will be overviewed. Chapters 3 and 4 are dedicated to the theoretical backgrounds of the deep drawing process and the finite element method (FEM). The fifth chapter focuses on the determination of optimum numerical parameters for the NUMISHEET 2002 benchmark test using PAM-STAMP 2G. In this chapter the results of the numerical simulations will also be verified by comparing the results with NUMISHEET 2002 benchmark findings. In the sixth chapter, an experimental

verification is conducted, where the formation of a ball bearing case is simulated and the simulation results are compared with geometrical and mechanical properties of the actual product. The seventh chapter deals with the comparison of the deep drawability of steel and aluminum in a simple cup drawing operation. In this chapter an axisymmetric deep drawing operation is simulated for an aluminum and a steel alloy, whereas the process parameters are varied to determine the process windows for both materials. After this, the formabilities of these materials are compared. The last chapter includes the discussions, conclusions and suggestions for further studies.

CHAPTER II

LITERATURE SURVEY

2.1 Introduction

In this chapter the previous literature related to the current study will be discussed. Firstly the basics of sheet metal forming and the types of failures in deep drawing processes will be investigated. Afterwards, studies which focused on mechanical and metallurgical material properties will be overviewed. Formability issues of steel and aluminum sheets will be studied and the survey will be concluded with discussions on the application and evaluation of finite element analysis methods.

2.2 Sheet Metal Forming in Automotive Industry

For the manufacture of a typical automotive sheet metal part the following processes are conducted (Roll, 2001):

- Primary forming operations: Gravity, holding, stamping
- Secondary operations: Trimming, flanging, hemming (and springback, which is the elastic relaxation of the part upon unloading after all forming stages)

These operational steps can be visualized in the following figure (Figure 2.1):

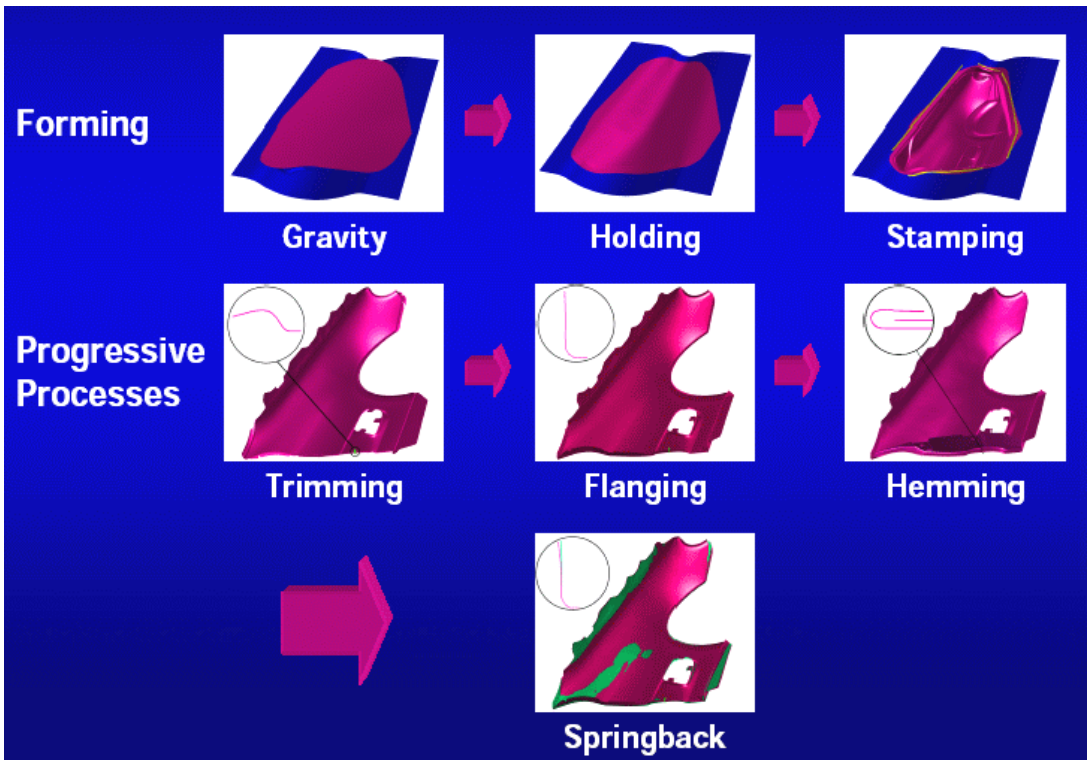

Figure 2.1: Stages of production for a typical automotive part (Roll, 2001)

2.3 Failure Modes in Deep Drawing

The most important subject in deep drawing operations is the prediction of failure in sheets. Figure 2.2 shows the typical failure types, which can be encountered in forming processes (Lange, 1985; Yano & Akashi 2001). These are:

- Bursting
- Tearing
- Wrinkling

Failure by bursting or tearing has to be avoided at all times for an acceptable product, however wrinkling problems may sometimes be removed: A wrinkled flange may be ironed at the later stages of the drawing, or the wrinkled part of the flange may be trimmed after the stamping stage, if that part of the deformed sheet is not needed at all. Actually, for some cases the presence of wrinkles is simply

avoided due to esthetical purposes. For instance, in a car hood, wrinkles will not be welcome by customers. On the other hand, wrinkled parts, which are not visible normally, can be utilized, provided that the presence of wrinkles does not affect their service life.

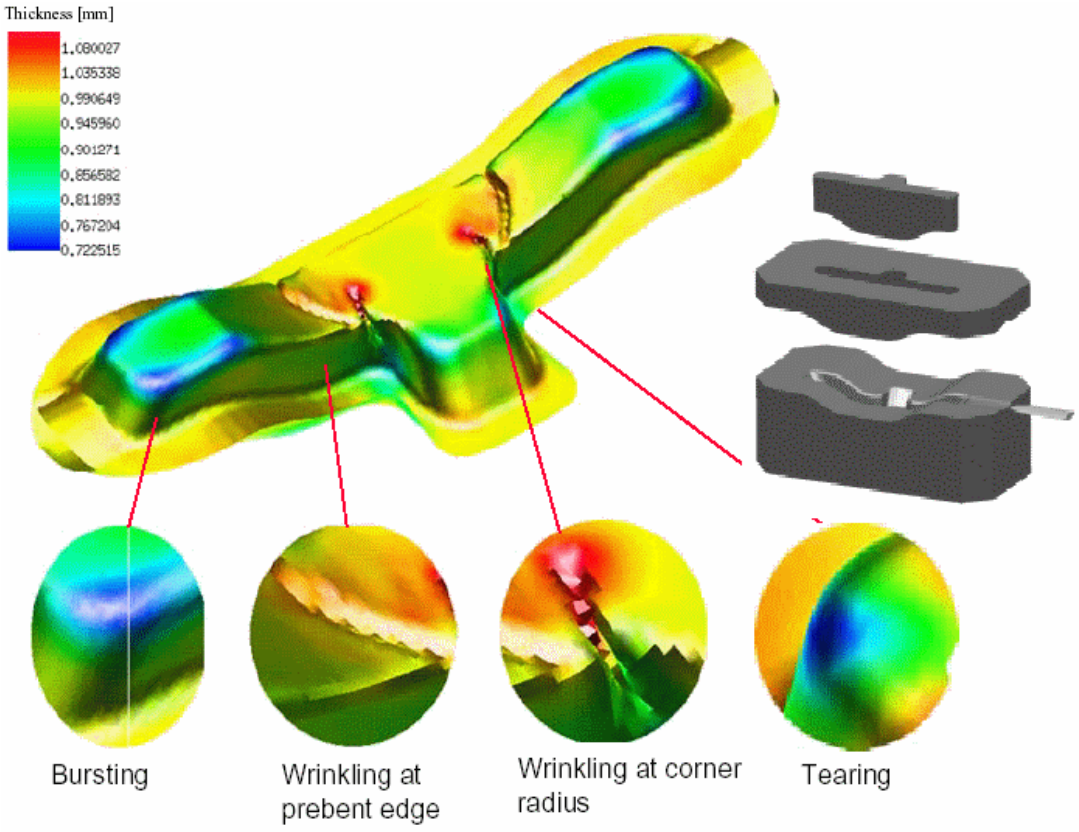

Figure 2.2: Failure modes

Additional failure types which poorly affect the appearance of the sheet metal part can be ring prints, traces, orange skin (or orange peel structure), and Lüders strips (Banabic, Bunge, Pöhlandt & Tekkaya, 2000).

2.4 Material Properties of Aluminum and Steel

The difference in material properties affects the outcome of forming processes greatly. Most of the time process designs must be re-evaluated if the used material

is to be replaced. The elastic modulus (E), strain rate coefficient (n) and the Lankford anisotropy coefficient (r) have the strongest influences on formability. Among these, the effect of anisotropy is most important.

2.4.1 Anisotropy and the Lankford Coefficient

Anisotropy is defined as the directionality of properties and it is associated with the variance of atomic or ionic spacing within crystallographic directions (Callister, 1997). For single crystals it can be the variation of properties (like the electrical conductivity, the elastic modulus, the index of refraction, etc.) in different crystallographic directions. Callister (1997) points that the extent and magnitude of anisotropic effects in crystalline materials are functions of the symmetry of the crystal structure. Since common engineering materials are polycrystalline, the crystallographic orientations of the individual grains are totally random, if complete recrystallization has taken place. Although all grains have a certain anisotropy, the overall structure will behave isotropically, since the anisotropy effect is averaged out. However if the materials are deformed for instance with no complete recovery, the crystal grains are oriented in deformation specific directions, making the material anisotropic. During deformations, the crystal lattices rotate and they affect the plastic properties (Hosford & Caddell, 1993).

The preferential crystallographic orientation of individual grains in a polycrystalline material is called texture (Callister, 1997). Texture is formed (or modified) by various physical processes as the following (Banabic, Bunge, Pöhlandt & Tekkaya, 2000):

- Plastic Deformation
- Crystallization
- Recovery
- Recrystallization
- Phase Transformation
- Particle Rotation

- Diffusion, etc.

Therefore, it can be summarized that crystallographic texture affects material properties via crystal anisotropy. In metal working point of view, texture (with other structural properties) affects crystal anisotropy and crystal anisotropy is the dependence of flow characteristics of a material with respect to direction.

In sheet metal working, anisotropy is subdivided into *normal* and *planar anisotropy*. Banabic, Bunge, Pöhlandt & Tekkaya (2000) state that normal anisotropy influences the maximum drawability of sheet (see Section 2.5), whereas planar anisotropy leads to earing (Figure 2.3).

Figure 2.3: Earing in a deep drawn cup (Tekkaya, 2003)

The anisotropy coefficient or the Lankford coefficient (Lankford, Snyder & Bausher, 1950) is a measure of anisotropy. This parameter can be called as the 'resistance to thickness change'. This coefficient is defined as

$$r = \frac{\varepsilon_2}{\varepsilon_3} \tag{2.1}$$

where ε_2 and ε_3 are the strains in the width and thickness directions (given in Figure 2.4) of uniaxial tensile tests of sheet strips.

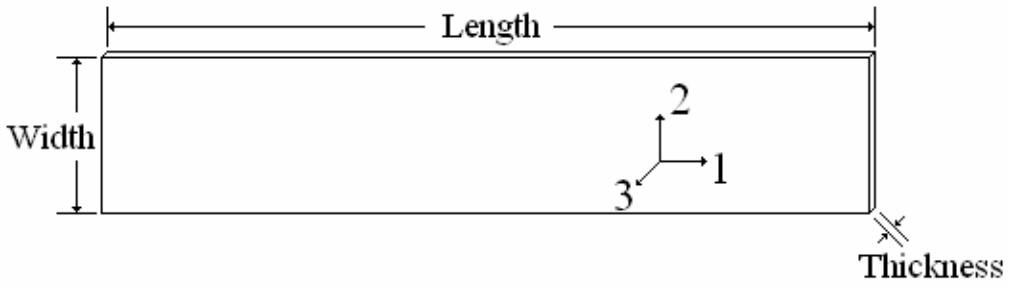

Figure 2.4: Dimensions of a sheet strip

For a successful sheet metal stamping, the normal anisotropy must be as large as possible whereas the planar anisotropy must be as small as possible. Weilong and Wang (2002) indicate when the r-value of sheet metals is greater, the thinning should be smaller and thus the formability is better. However, a greater r-value does not satisfy all sheet metal forming processes such as necking and bending, meaning that each forming process should have individual forming properties related to the anisotropy of the materials, and the different strain states would cause different forming failures (Hosford & Duncan, 1999).

The Lankford anisotropy coefficient depends on the in-plane direction. In orthogonal anisotropy three r-values are determined: Along the rolling direction (RD), along 45° to RD and perpendicular to rolling direction (transverse direction, TD). These values are denoted as r_0, r_{45}, and r_{90} respectively.

The average of these r-values in the plane of the sheet metal represents the coefficient of normal anisotropy r_n. The coefficient of normal anisotropy is obtained from Eq. 2.2 (Banabic, Bunge, Pöhlandt & Tekkaya, 2000):

$$r_n = \frac{r_0 + 2 \cdot r_{45} + r_{90}}{4} \tag{2.2}$$

A material with a high r_n value will experience less thinning during a deep drawing operation than a material having a smaller r_n value, provided that their flow characteristics are identical. For instance, aluminum usually has an r value smaller than 1 (about 0.6), whereas steel has an r_n value larger than 1 (about 1.5). In the present study, the investigated aluminum material (6111-T4) has a normal anisotropy value of 0.694, whereas the steel material (DDQ mild steel) has 2.012. Detailed information about the material properties are given in Table 5.1.

In the study of Weilong and Wang (2002) it is shown that although materials having greater r-values are more suitable for deep drawing, their deformation resistance is also increased with increasing r-values. It was stated by Marciniak, Duncan & Hu (2002) that for materials having a normal anisotropy value larger than unity, width strain is greater than the thickness strain in the tensile test; which is associated with a greater strength in the through-thickness direction, and generally a resistance to thinning. A high r_n value allows deeper parts to be drawn and in shallow, smoothly-contoured parts (like automobile panels) a high value may reduce the chance of wrinkling or ripples in the part (Marciniak, Duncan & Hu 2002). Weilong and Wang (2002) suggest that for a deep drawing operation, a suitable material must have an r-value, which is larger than unity.

A measure of the variation of normal anisotropy with the angle to the rolling direction is given by the quantity Δr,

$$\Delta r = \frac{r_0 + r_{90} - 2 \cdot r_{45}}{2} \tag{2.3}$$

known as planar anisotropy.

This value can be negative or positive. For instance, steels usually have positive Δr. In this present study, the utilized materials (6111-T4 Aluminum and DDQ grade Mild Steel) have planar anisotropy values of 0.083 and 0.401 respectively (Table 5.1).

As stated before, planar anisotropy is directly related to earing. It was stated by Marciniak, Duncan & Hu (2002) that if the magnitude of the planar anisotropy parameter is large, the orientation of the sheet with respect to the die or the part to be formed will be important. In such cases, asymmetric forming and earing will be observed. As the magnitude of the Δr value increases, the ear heights increase. Therefore for deep drawing operations, suitable materials must have smaller planar anisotropy values in magnitude. This occurrence can be seen in Figure 2.5 (Banabic, Bunge, Pöhlandt & Tekkaya, 2000)

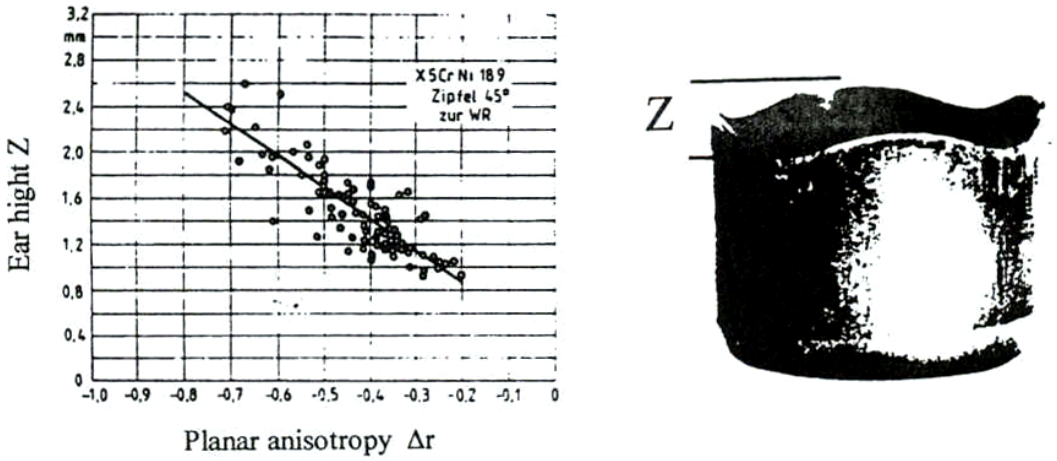

Figure 2.5: Planar anisotropy expressed by Δr (Banabic, Bunge, Pöhlandt & Tekkaya, 2000)

2.4.2 Other Material Properties

Quainoo and Yannacopoulos (2004) stated that for sheet metal parts a high dent resistance, which is proportional to the yield strength, is beneficial, but that high yield strength alloys tend to suffer detrimental springback effects and inferior formability. Considering also the elevated material costs, the usage of magnesium and titanium alloys is not significant.

Some material properties of common metals are given in the following figure (Figure 2.6).

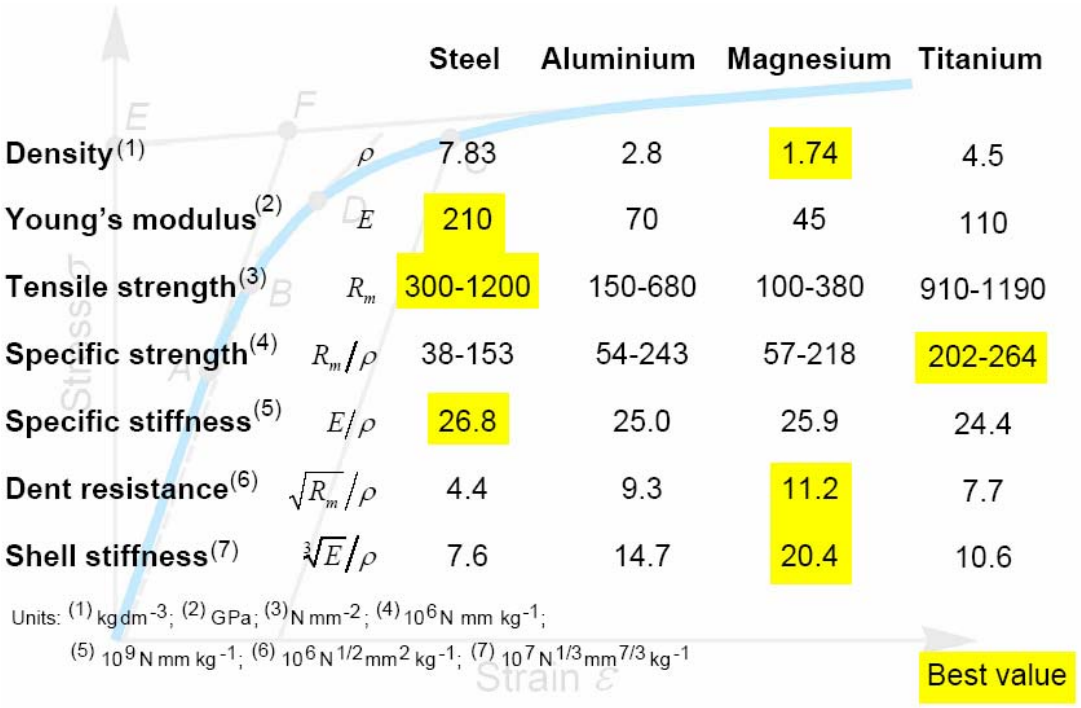

Figure 2.6: Material properties of some metals (Tekkaya, 2003)

It can be seen from Figure 2.6 that average steels have high stiffness and strength with a large density, whereas aluminum has moderate- but subjectively good values, making them more popular for deep drawing applications. On the other hand the smaller density and corrosion resistance of aluminum makes it a good candidate for a replacement material for steel.

Marciniak, Duncan and Hu (1992) stated that, the behavior of sheet metals upon deformation depends on one or more general characteristics, but which of these is more important will depend on the forming process. On the other hand, not of all these general properties can be obtained from a simple tensile test.

The general material characteristics that influence the outcome of a sheet metal forming process are the following (Marciniak, Duncan & Hu, 1992):

1. Strain hardening of the sheet:

   The greater the strain-hardening of the sheet, the better it will perform in processes where there is considerable stretching; the straining will be more

uniformly distributed, and the sheet will resist tearing when strain-hardening is high. Additionally, since necking failures are associated with the strain hardening coefficient n, materials having higher n will generally exhibit better formability (Beddoes & Bibby, 1999).

2. Initial yield strength:

   It is related to the strength of the formed part. Although for lightweight materials, higher yield strengths are preferable, such materials are harder to form and combined with low elastic moduli, it induces increased springback problems.

3. Elastic modulus:

   A higher modulus will give a stiffer component, whereas a lower modulus gives larger springback.

4. Total elongation
5. Anisotropy
6. Fracture:

   The fracture characteristic is indicated by the cross-sectional are of the fracture surface after failure, and this is difficult to measure in thin sheet. Therefore problems due to fracture may not be properly recognized.

7. Homogeneity:

   Inhomogeneities cannot be adequately identified with a single tensile test, and even with repeated test, since the actual volume of material being tested is small. Therefore these are difficult to characterize precisely.

8. Surface effects:

   The roughness of sheet and its interaction with lubricants and tooling surfaces will affect performance in a forming operation.

9. Damage
10. Rate Sensitivity:

    Although the rate sensitivity of most sheets is small at room temperature; for steel, it is normally zero or slightly positive, whereas it is zero or slightly negative for aluminum. Positive rate sensitivity usually improves forming and has an effect similar to strain-hardening.

2.5 Formability of Sheet Metals

At the end of the nineteenth century, due to the development of the sheet forming technology, sheet metal formability became a research topic. Some of the first researchers interested in this field were Bessemer and Parkers, Adamson, Considere and Erichsen. Necking, tearing, wrinkling, modification of roughness or poor qualities in appearance are the factors that generally define a limit to the deformation in sheet metal forming. Figure 2.7 summarizes the parameters affecting the formability of sheet metals.

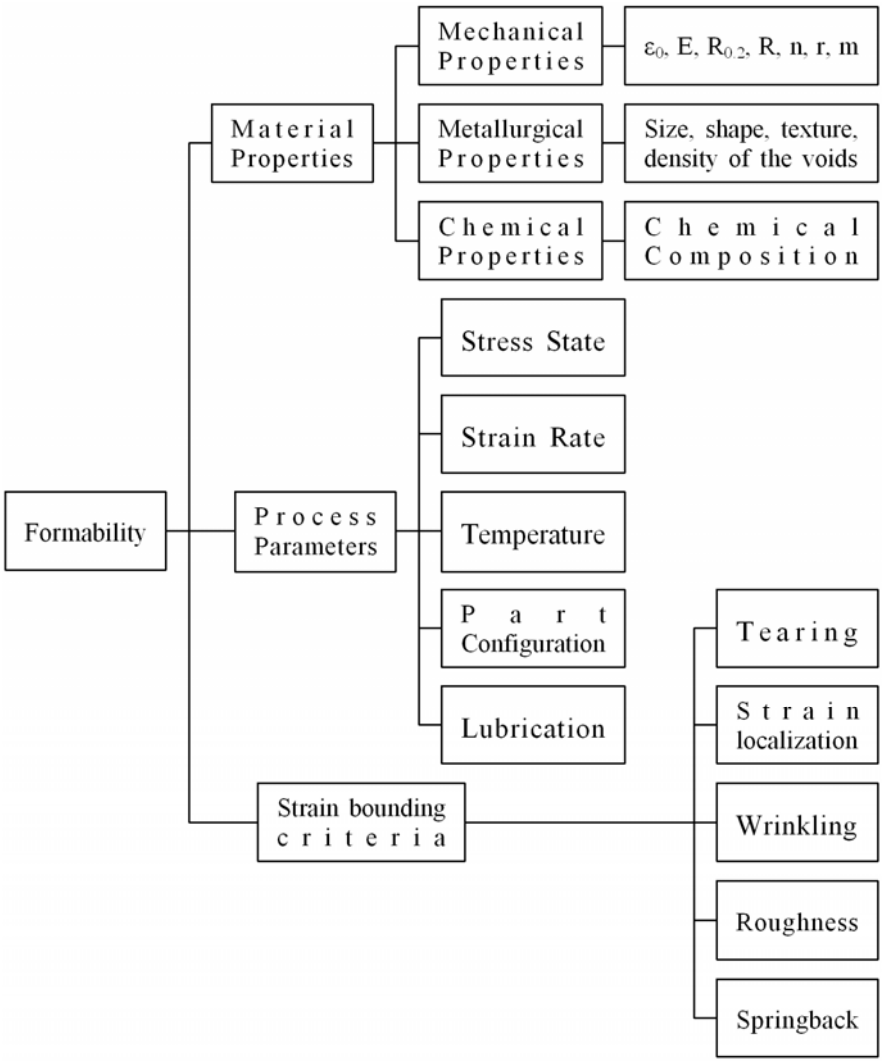

Figure 2.7: Parameters influencing sheet metal formability

2.5.1 The Limiting Drawing Ratio

In deep drawing, formability is expressed by a limiting drawing ratio (LDR), which is the largest ratio of blank-to-cup diameters (d_0 / d_1), that may be drawn fully and successfully (Hosford & Caddell, 1993). It is determined from the following equation:

$$LDR = \frac{d_{0,MAX}}{d_p} \tag{2.4}$$

Here, $d_{0,MAX}$ is the maximum blank diameter that can be fully drawn to a cup without any failure and d_p is the punch diameter.

The limiting drawing ratio is actually a function of material properties, friction conditions and blank- and tool geometry. For any material in a deep drawing operation, a higher LDR means that 'deeper' drawings are possible, whereas a lower LDR restricts the deep drawability. The LDR is strongly material dependent and for several materials the variance of LDR with normal anisotropy can be seen in Figure 2.8 (Banabic, Bunge, Pöhlandt & Tekkaya, 2000). Figure 2.8 shows that the cup depths increase (since the LDR increases) with increasing mean r-values.

Ramaekers (1999) derived a relation between LDR and the material properties, n and r, and also agreed that high r and n values are required for higher LDR values. In their study, Leu and Wu (2004) showed that LDR also strongly depends on the friction condition; a higher μ-value decreases LDR significantly. It was also stated by Leu and Wu (2004) that the effect of the strain hardening exponent n is less important and decreasing bending factor t_0/r_d (which is the division of the initial sheet thickness by the die entrance fillet radius) and the improves LDR slightly.

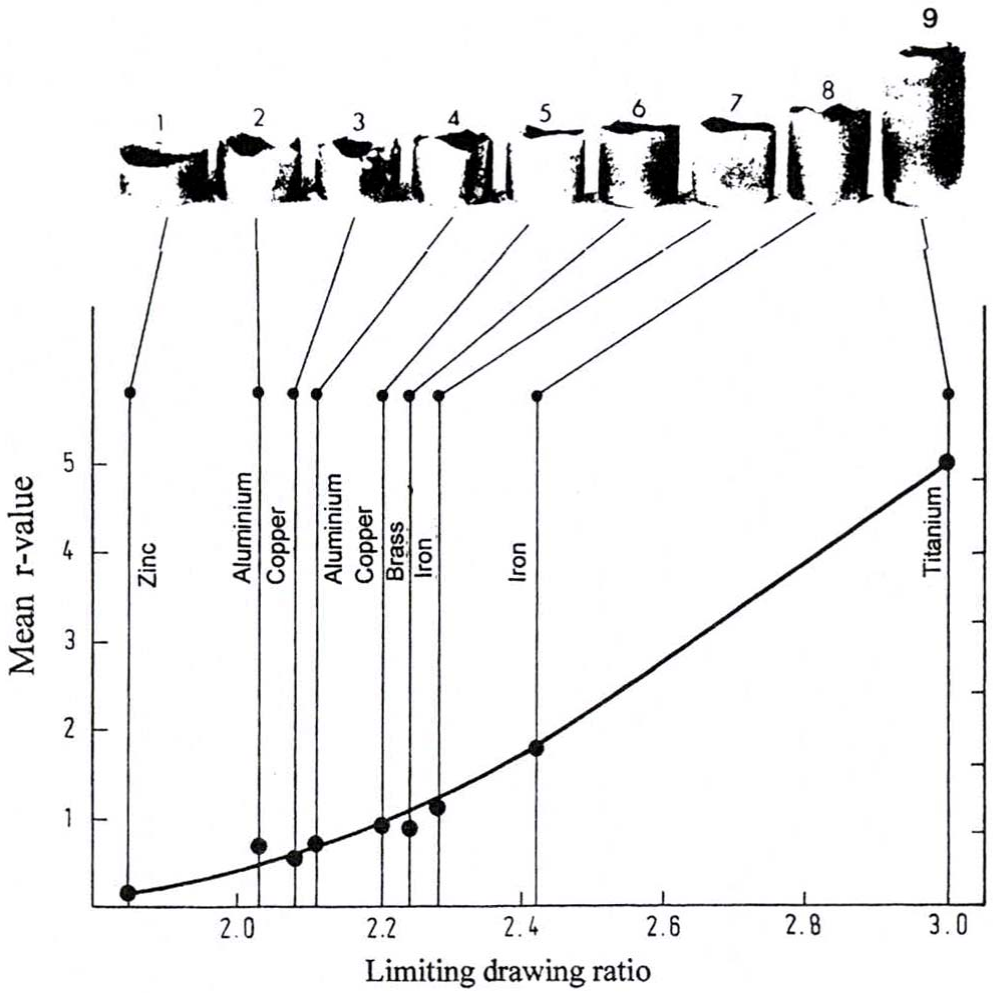

Figure 2.8: The dependence of formability on the r-value

2.5.2 The Forming Limit Diagram

The forming limit diagram (FLD) (also known as the forming limit curve, FLC) is another important concept utilized for the evaluation of the formability of sheet metals. By the use of these diagrams, the onset of failure due to local necking, or potential trouble areas on the deformed part under various loading types can be estimated and investigated (Figure 2.9).

The research in this field was pioneered by Keeler (1961), based on the observations of Gensamer (1946). Maximum values of principal strains ε_1 and ε_2 can be determined by measuring the strains at fracture on sheet components covered

with grids of circles. The most widely used technique involves printing or etching a grid of small with constant diameter on the metal sheet before forming. During forming the initial circles of the grid distort and become ellipses. From the minor and minor axes of these ellipses, the principal strains on sheet specimens can be determined. Keeler plotted the maximum principal strain against the minimum principal strain obtained from such ellipses at fracture of parts after biaxial stretching. This way, a curve limiting the tolerable range is obtained.

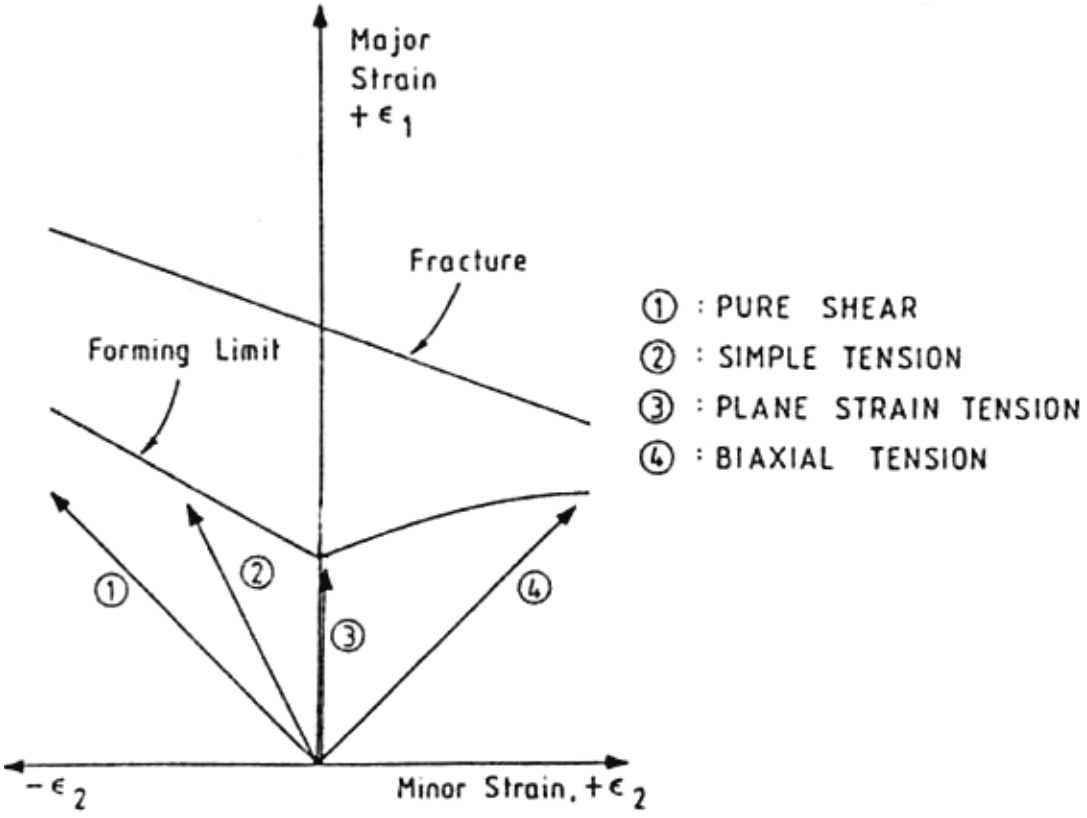

Figure 2.9: The forming limit diagram – loading types (Banabic, Bunge, Pöhlandt & Tekkaya, 2000)

Later, Goodwin (1968) plotted the curve for tension/compression domain by using different mechanical tests. In this case, transverse compression allows for obtaining high values of tensile strains like in rolling or wire drawing.

The diagrams of Keeler and Goodwin together give the values of ε_1 and ε_2 at fracture. This currently is called the forming limit diagram, sometimes also as the Keeler – Goodwin Diagram (Figure 2.9).

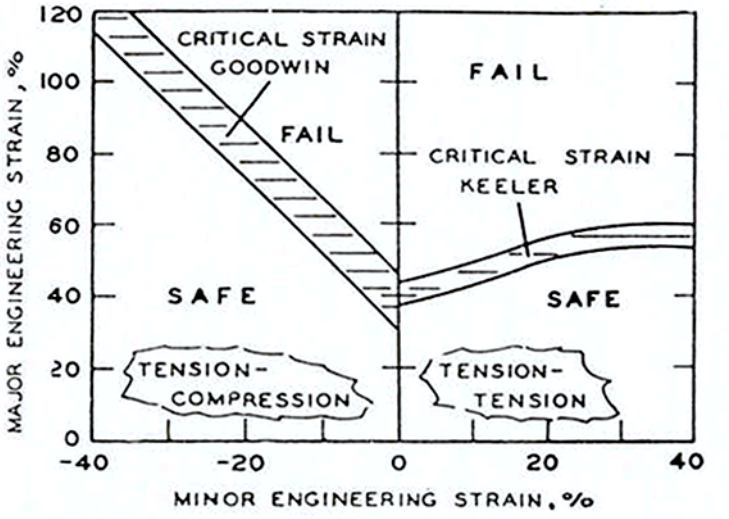

Figure 2.10: Keeler – Goodwin diagram (FLD) (Banabic, Bunge, Pöhlandt & Tekkaya, 2000)

Banabic, Bunge, Pöhlandt & Tekkaya (2000) indicated that from subsequent experimental and theoretical research, two more types of FLD's have emerged: the wrinkling limit diagram and the limit stress diagram.

There are various tests to determine the FLD experimentally (Banabic, Bunge, Pöhlandt & Tekkaya, 2000) like the uniaxial tensile test, hydraulic bulge test, punch stretching test, Keeler test, Hecker test, Marciniak test, Nakazima test and Hasek test. From these, Marciniak test or hydraulic bulge test is utilized for eliminating friction effects; uniaxial test is preferred for its simplicity and Nakazima test is suitable since it is capable of covering a great variety of strain paths.

It was stated by Banabic, Bunge, Pöhlandt & Tekkaya (2000) that there are various models present for the calculation of FLD's. The first ones were proposed by Swift and Hill utilizing the models of diffuse necking and localized necking respectively.

In the models of Swift and Hill the general formulae for limit strains (ε_1^* and ε_2^*) are determined. The forming limit curves are plotted by computing the values of these strains for various loading paths.

Swift Model gives the limit strains as follows:

$$\varepsilon_1^* = \frac{\left[1+r(1-\alpha)\right]\left(1-\frac{2r}{1+r}\alpha+\alpha^2\right)}{(1+r)(1+\alpha)\left[1-\frac{1+4r+2r^2}{(1+r)^2}\alpha+\alpha^2\right]}\cdot n \tag{2.5}$$

$$\varepsilon_2^* = \frac{\left[(1+r)\alpha-r\right]\left(1-\frac{2r}{1+r}\alpha+\alpha^2\right)}{(1+r)(1+\alpha)\left[1-\frac{1+4r+2r^2}{(1+r)^2}\alpha+\alpha^2\right]}\cdot n \tag{2.6}$$

where ε_1^* and ε_2^* are the limit strains, α is the loading ratio (σ_2/σ_1), n is the strain hardening coefficient and r is the anisotropy coefficient.

In Hill's model, the limit strains are given by Eq. 2.7 and 2.8:

$$\varepsilon_1^* = \frac{\frac{\partial f}{\partial \sigma_1}}{\frac{\partial f}{\partial \sigma_1}+\frac{\partial f}{\partial \sigma_2}}n \tag{2.7}$$

$$\varepsilon_2^* = \frac{\frac{\partial f}{\partial \sigma_2}}{\frac{\partial f}{\partial \sigma_1}+\frac{\partial f}{\partial \sigma_2}}n \tag{2.8}$$

Here ε_1^* and ε_2^* are the limit strains, n is the strain hardening coefficient, σ_1 and σ_2 are the principal stresses and f is the yield function.

Keeler and Brazier (1975) have suggested an empirical formula which was obtained from experimental trials on standard steel test specimens. Assuming that the shape of the FLD remains the same, the position of the diagram is determined by calculating the limit strain corresponding to plane strain ε_{10}:

$$\varepsilon_{10}(\%) = (23.3 + 14.13 \cdot t)\frac{n}{0.21} \tag{2.9}$$

Here, the ε_{10} is the plane strain intercept of the FLD curve, t is the initial thickness of the sheet in mm, and n is the hardening coefficient.

Therefore, this curve is only function of hardening coefficient and thickness. For common steels, this diagram yields successful results. However, it is not verified for the materials whose hardening coefficient is more than 0.21 and steel, with a thickness in excess of 5 mm. It is not suitable for aluminum and new steels, since this curve seems to be below the experimental curves. For such materials the formability may be underestimated.

Marciniak (1965) proposed a model taking into account that sheet metals are non-homogeneous from both the geometrical and structural point of view. Dudzinski and Molinari (1988) used the method of linear perturbations for analyzing the strain localization and for computing the limit strains.

In a study of Rees (2001), it is shown how the r-variation, the n-values, sheet orientation θ, prestrain history ε_0 and thickness of a sheet material may be selected to optimize its ability to stretch and draw. In sheet materials, for which $r_{90} > r_0 > r_{45}$, benefit can be derived from θ and r_n variations within the second quadrant of the FLD but not the first. Changes to n, ε_0 and t_0 serve to raise or lower this FLD in both quadrants. An optimum formability appears in thicker sheets with high n, low r_n, a 45° orientation and compressive prestrain. These influences can also be seen in a FLD employing thickness strain as a means of quality control.

2.6 Finite Element Analysis of Sheet Metal Forming

Before 1990, this technique was common for research and development purposes only, but its real industrialization did not start until around 1990 (El Khaldi, 2002). By that time, a considerable effort has been made on making the finite element analysis accessible enough for industry to use this technology in common complex industrial problems. Before the numerical simulation methods were widespread in that time, the process design (especially die design) and improvement projects were extremely costly and time consuming. However, computer-aided simulation techniques, e. g. the analysis of the forming process without any physical dies, are increasingly replacing the use of prototype and soft dies. This development is becoming more practical through rapidly growing hardware developments, which allow the processing of ever increasing amounts of computerized data in ever shorter time spans. In addition, the computer software used for process simulation has become more reliable and more user friendly.

Today, the numerical analysis of sheet metal forming operations is mainly done by finite element method (FEM). Detailed information is given by Tekkaya (2002).

There are numerous commercial FE-codes nowadays. In Table 2.1 the commonly accepted packages are summarized (Tekkaya, 2002).

The explicit finite element codes are most suitable for the simulation of 2- or 3 dimensional deep drawing operations. However, explicit codes have serious weaknesses in the calculation of stresses and residual stresses, therefore in the calculation of springback (Roll & Tekkaya, 1993). Among the explicit finite element codes, PAM-STAMP, which has a dynamic-explicit code for stamping simulations and an implicit code for springback and trimming simulations, was chosen for this study. The dynamic explicit methods have their roots in the study of Belytschko and Mullen (1977).

Table 2.1: Finite element analysis packages utilized for the simulation of forming processes (Tekkaya, 2002)

Name	Manufacturer, Country	Type	Application
ABAQUS	HKS, USA	Implicit	Generally non-linear
MARC	MARC, USA/NL, D	Implicit	Generally non-linear
NIKE3D	LTSC, USA	Implicit	Generally non-linear
LARSTRAN	LASSO D	Implicit	Generally non-linear
INDEED	INPRO D	Implicit	Sheet metal forming
ITAS3D	Prof. Nakamachi, J	Explicit, static	Sheet metal forming
DYNA3D	LSTC, USA	Explicit, dynamic	Crash, bulk, sheet metal
PAM-STAMP	ESI, F/D	Explicit, dynamic	Sheet metal forming
Optris	Dynamic Software, F	Explicit, dynamic	Sheet metal forming
MSCDYTRAN	MacNeal-Schwendler	Explicit, dynamic	Sheet metal forming
ABAQUS-explicit	HKS, USA	Explicit, dynamic	Crash, bulk, sheet metal
AUTOFORM	AUTOFORM, SW	Spec. formulation implicit	Sheet metal forming
Autoforge	MARC, USA/NL, D	Elastic-viscoplastic	Bulk, forging
DEFORM	Batelle, USA, D	Rigid-viscoplastic	Bulk, forging
FORGE 2/3	CEMEF, F	Rigid-viscoplastic	Forging
ICEM-STAMP	Control Data, D	One-step method	Sheet metal forming
ISO-PUNCH	Sollac, F	One-step method	Sheet metal forming
AUTOFORM One-step	AUTOFORM, SW	One-step method	Sheet metal forming
FASTFORM	FTI, CAN	One-step method	Sheet metal forming
SIMEX2	SimTech, F	One-step method	Sheet metal forming

One important aspect of the FE-analyses that influences the outcome of the simulation results is the mesh topology. Kawka, Olejnik, Rosochowski, Sunaga & Makinouchi (2001) and Correia & Fedron (2002) showed in their study that the wrinkling predictions of FE-analyses are dependent on mesh topology; the average wavelengths, numbers of wrinkles and the onset of wrinkling differ with different blank meshes and different FEA packages. On the other hand, Desai, Date and Narasimhan (2002) indicated that even by only varying the blank holder mesh topology the formation of wrinkles under critical conditions is affected. Therefore, as a rule of thumb, for a reliable simulation result the FE-mesh must be as fine as possible (at the cost of computation time).

CHAPTER III

DEEP DRAWING

3.1 Introduction

In this chapter, firstly the basics of the deep drawing operation will be studied. Common deep drawing systems will be overviewed and the physical aspects of deep drawing will be summarized. Finally, the theoretical background of the deep drawing operation will be studied.

3.2 Deep Drawing Technology

Schuler Metal Forming Handbook (1998) defines deep drawing as the following:

> *Deep drawing* is a method of forming under compressive and tensile conditions whereby a sheet metal blank is transformed into a hollow cup, or a hollow cup is transformed into a similar part of smaller dimensions without any intention of altering the sheet thickness.

This is done by placing a blank of appropriate size over a shaped die and pressing the metal into the die with a punch. To prevent wrinkling of the sheet metal blank, the outer portion of the blank, which is called as the flange, is held by the blank holder. The outer portion of the die, which supports the blank holder, is also named as the flange. In some deep drawing operations, draw beads are utilized in the binder area to restrain excessive material flow into the die to prevent wrinkling

problems. In Figure 3.1 a schematic representation of a single-draw deep drawing operation is given:

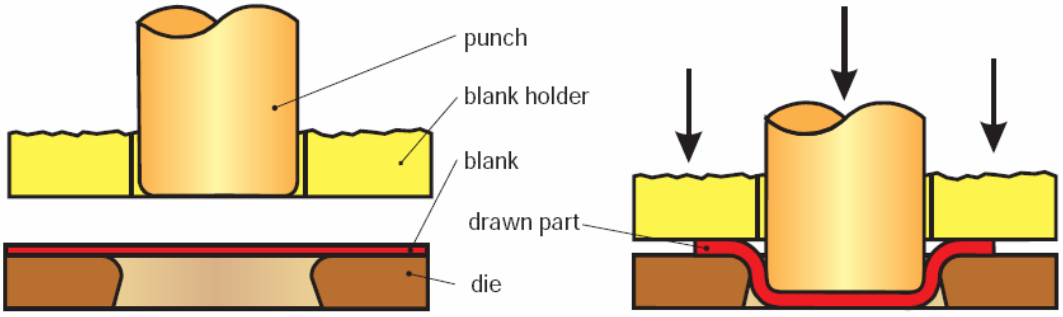

Figure 3.1: Single-draw deep drawing with blank holder (Schuler Metal Forming Handbook, 1998)

The most significant variation of deep drawing is done with a rigid tool. This basic deep drawing system comprises of a punch, a bottom die and a blank holder, which acts in a way to prevent the formation of wrinkles as the metal is drawn into the die. In special cases the punch or the die can also be from a soft material. Figure 3.2 demonstrates examples for deep drawn parts.

There are alternative deep drawing methods which make use of active media and active energy. Active media include formless solid substances such as sand or steel balls, fluids (oil, water) and gases, whereby the forming work is performed by a press using a method similar to that employed with the rigid tools. Hydroforming is the general name for this soft-tool forming technology. Soft-tool forming technologies include rubber-pad forming technology and fluid-tool forming. For instance, in Geurin and Marform processes the die is replaced with a rubber path and the punch is solid. In hydroforming, oil, water or other fluid mediums are used as the punch or the die. Hydroforming has a variety of names: hydraulic forming, hydroforming deep drawing, flexible forming, hydrobulging, high-pressure forming, low-pressure forming, and hydro-mechanical deep drawing. However

hydroforming can be used for every situation when fluid pressure is used in the process as an aid; whilst others are usually referred to as a certain specific hydraulic-forming process variation or a process aided with a fluid, respectively. Hydroforming can be classified as the following processes according to its process features:

- Tube hydroforming
- Hydro-mechanical deep drawing
- High pressure sheet metal forming

Figure 3.2: Examples of deep drawing (Tekkaya, 2002)

The greatest field of application of this technique is *hydro-mechanical deep drawing*. In hydro-mechanical deep drawing the die is replaced by a liquid medium,

so that the final shape of the part is only determined by the punch shape. Hydro-mechanical deep drawing is utilized for instance for the manufacture of components from stainless steel.

3.3 Mechanics of Deep Drawing

In the following sections, the important parameters in deep drawing systems and the physics of the deep drawing operation itself will be studied. Since the main focus of this study is occurrences in the cup drawing processes, the basic process parameters of an axisymmetric cup drawing system will be inspected.

3.3.1 Deep Drawing Parameters

Using the simplicity of the axisymmetric deep drawing, one can describe the basic parameters in deep drawing. In a simple cup drawing operation, the basic geometrical and material parameters effective for the outcome of the process can be visualized from Figure 3.3.

The parameters defining the tool geometry are the following:

- Die radius D
- Punch radius P_r
- Blank radius B_r
- Punch fillet radius R_p
- Die fillet radius R_d
- Blank thickness t

From Figure 3.3 these parameters are self explanatory.

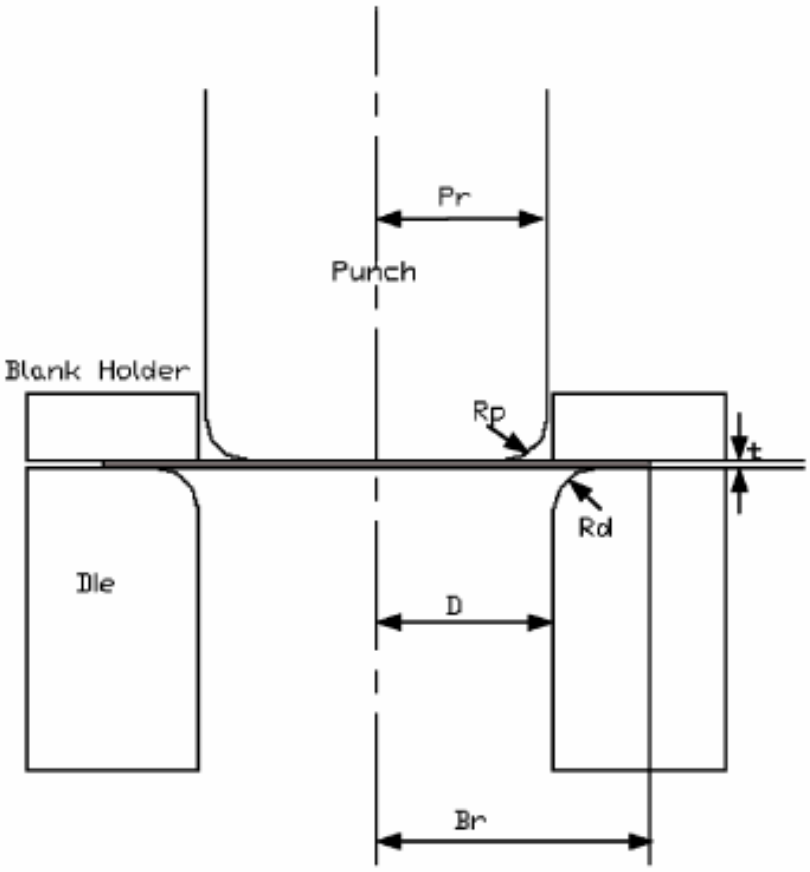

Figure 3.3: Deep drawing parameters

The clearance is another important parameter, which can be considered as a secondary parameter. It can be formulated as $D - P_r$. Its value is important since as the punch enters the die cavity, depending on the current blank thickness at the die cavity, small values may lead to *ironing*, which is simply the intentional thinning of the blank at the die cavity. Normally, to avoid ironing the clearance amount must be larger than the blank thickness, t. Usually, this amount is 25% larger than the initial blank thickness.

The physical parameters in deep drawing operations can be classified as the following:

- Blank holder force
- Punch speed

- Lubrication
- Blank material properties

3.3.2 Physical Aspects of the Deep Drawing Operation

In all deep drawing processes, the pressing force is applied over the draw punch onto the bottom surface of the drawn part. It is further transferred from there to the perimeter in the deformation zone, between the die and the blank holder.

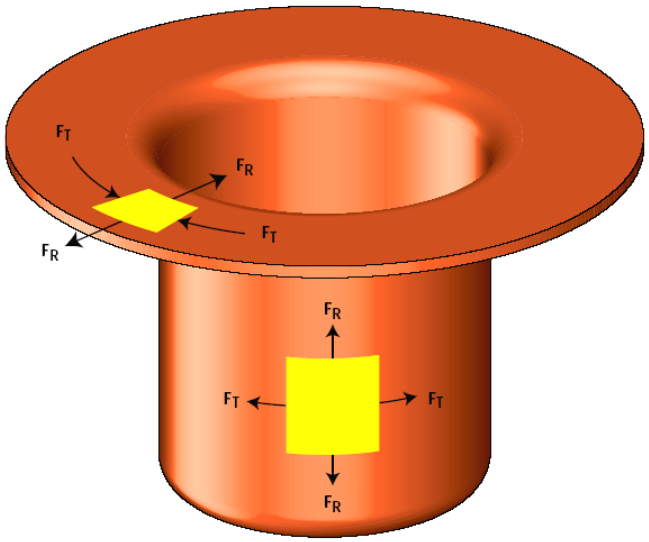

Figure 3.4: Pressing forces in deep drawing of a round cup with a blank holder (Schuler Metal Forming Handbook, 1998)

The workpiece is subjected to radial tension forces F_R and tangential compression forces F_T (Figure 3.4). The material is compressed in the tangential direction and stretched in the radial direction. As it can be seen from the figure above, there are compressive forces in the flange region and tensile forces elsewhere in the workpiece. Therefore, upon drawing, the sheet metal blank thickens at the flange region. At the bottom parts, however, there is thinning. There is a possibility of bulging in the flange region due to compressive forces. When the compressive forces at the flange region exceed a certain limit, wrinkling occurs. Therefore, the

blank holding forces, and sometimes the drawbeads, are utilized to control the flowing of the material into the die cavity to overcome compressive forces' effects.

As the draw depth is increased, the amount of deformation and the deformation resistance are also increased. The sheet metal is most severely stretched in the corner of the draw punch, corresponding to the tip of the drawn cup. Failure normally occurs at this region of the blank.

Since there is a strongly non-homogeneous deformation throughout the part, residual stresses arise. In the axial direction there is residual tension on the outside and compression on the inside, resulting from bending and unbending over the die lip. These stresses are largest near the top of the wall because of the bending that occurred near the end of the draw, where there was little net tension. These residual stresses induce a bending moment in the wall which is balanced by hoop tension near the top of the cup. In some metals, this hoop tension can lead to splitting of the walls by stress-corrosion cracking.

Owing to the presence of residual stresses, deep drawn parts are sensitive to successive operations. A workpiece may distort or fracture upon machining operations and heat treatments may cause the part to change shape.

3.4 Analytical Formulations of Cup Drawing

The draw ratio β is an important numerical value for cylindrical draw parts in determining the required number of drawing steps (Schuler Metal Forming Handbook, 1998). It is the ratio of the diameter of the initial blank form to the diameter of the drawn part and it is defined by the Eq. 3.1:

$$\beta = \frac{d_0}{d_m} \tag{3.1}$$

where d_0 is the initial blank diameter and d_m is the mean diameter of the formed cup.

The drawing ratio is dependent on many factors like the tool geometry, lubrication conditions, and the amount of blank holding forces, sheet thickness and material properties (especially the r-value). The limiting drawing ratio (LDR), on the other hand is the maximum value of the drawing ratio, which can be reached in a single drawing step. This value is theoretically calculated by membrane analysis as the following (Tekkaya, 2003):

The radial unit force at the inner radius r_m is given by:

$$T_{\phi,m} = T_f \ln\left(\frac{r_0'}{r_m}\right) \tag{3.2}$$

where $T_{\varphi,m}$ is the mean force per hoop-width in meridian direction, T_f is the material property calculated by the flow stress σ_f times the current sheet thickness to compensate the effect of work hardening, r_0' is the instantaneous blank radius.

But, since the wall can be assumed under uniaxial tension:

$$T_{\phi,m} \le T_f \qquad \text{or} \qquad \ln\left(\frac{r_0'}{r_m}\right) \le 1 \tag{3.3}$$

Hence,

$$\left(\frac{r_0}{r_m}\right)_{\max} = \beta_{\max} \le e \qquad \text{or} \qquad \beta_{\max} \le 2.72 \tag{3.4}$$

However, for practical purposes the LDR is considered to be about 2. It was indicated in Schuler Metal Forming Handbook (1998) that to achieve $\beta > 2$ several

drawings are required and it must be noted that β, because of work hardening, can only achieve a level of 1.3 in the next drawing step. If the part is annealed before the next drawing operation, a β of 1.7 can be assumed. With several drawing steps, the total draw ratio becomes a product of the individual draw ratios:

$$\beta_{tot} = \beta_1 \cdot \beta_2 \cdot \ldots \cdot \beta_n \tag{3.5}$$

For drawing round parts in a single drawing, the maximum drawing force, F_U can be calculated as follows (Schuler Metal Forming Handbook, 1998):

$$F_U = \pi \cdot (d_1 + s) \cdot s \cdot R_m \cdot 1.2 \cdot \frac{\beta - 1}{\beta_{\max} - 1} \qquad \text{[N]} \tag{3.6}$$

where

d_1 : punch diameter [mm]

s : sheet metal thickness [mm]

R_m : material tensile strength [N/mm^2]

β : actual draw ratio

β_{max} : maximum draw ratio

The calculated drawing force is equal to the drawing slide force on double-action drawing presses. With single-action presses, the drawing slide force increases by the amount of force applied to the blank holder, since the blank holder force counteracts the movement of the drawing slide during the complete drawing cycle.

Membrane analysis gives the total drawing force F_P as the follows (Tekkaya, 2003):

$$F_P = 2\pi r_m \cdot \left\{ \left[\sigma_{fm,flange} \cdot s_0 \cdot \ln\left(\frac{r_0'}{r_m}\right) + \frac{\mu \cdot F_{BH}}{\pi \cdot r_0} + \frac{\sigma_{fm,die-ring} \cdot s_0^2}{2 \cdot r_{fd} + s_0} \right] \cdot e^{\mu\phi} \right\} \cdot \sin\alpha \tag{3.7}$$

where r_m is the final cup radius, $\sigma_{fm,flange}$ and $\sigma_{fm,die\text{-}ring}$ are the flow stresses of the workpiece in the flange and in the die-ring, r_0' is the instantaneous blank radius, F_{BH} is the blank holding force, r_0 is the initial blank radius, s_0 is the initial thickness of the blank and α is the sine of the bending angle of the blank between the punch and the binder.

Beddoes and Bibby (1999) estimated the drawing force of a circular cup as the following:

$$F_d = \pi d_p t_{avg} \cdot UTS\left[\frac{d_0}{d_p} - 0.7\right] \tag{3.8}$$

where F_d is the draw force, d_p is the cup diameter, d_0 is the initial blank diameter, t_{avg} is the average wall thickness of the deformed blank and UTS is the tensile strength of the blank.

3.5 Ramaekers' Model

Ramaekers (1999) developed a computer program for the calculation of the total drawing force in an axisymmetrical cup drawing operation. This program is based on an analytical model by Ramaekers (1999), considering the relation between LDR, n and R in axisymmetrical cup drawing operations. The mathematical formulation of this program is given in Appendix A in detail. This computer program is utilized for numerical verification of simulation results in Chapters 5 and 7.

Basically, the program calculates the total drawing force (F_D) as the sum of the deformation force at the flange region (F_{Dfl}), the friction force between flange and tool (F_{Frfl}), the bending and rebending forces at the die-radius ($F_{D\rho}$) and the friction force at the die radius ($F_{Fr\rho}$) (Eq. 3.9) This total force is plotted versus the drawing ratio.

$$F_D = F_{Dfl} + F_{Frfl} + F_{D\rho} + F_{Fr\rho} \tag{3.9}$$

The program calculates this force from several input data. These are:

- Punch radius
- Die radius
- Die fillet radius
- Punch fillet radius
- Initial sheet thickness
- Initial sheet radius
- Material properties (K, ε_0, n, $r_{0°}$, $r_{45°}$,$r_{90°}$)
- Friction coefficient at the flange
- Friction coefficient at the die fillet
- Applied blank holder pressure

Besides the total drawing force, a critical force, given in Eq. 3.10, which predicts the onset of failure in the bottom corner of the cup. If the total force exceeds the critical force, according to this model a bottom tearing failure is expected.

$$F_C = \frac{\left(\frac{R+1}{\sqrt{2R+1}}\right)^{n+1} \cdot n^n}{\left(\frac{s_0}{\rho_P} + \frac{s_0}{r_P} + e^{n-\frac{\sqrt{2R-1}}{r+1}\varepsilon_0}\right)} \tag{3.10}$$

where F_C is the critical force, R is the mean anisotropy factor, n is the strain hardening factor in Swift law, s_0 is initial sheet thickness, r_P is the punch radius, ρ_P is punch fillet radius and ε_0 is the strain history of the material.

According to Ramaekers (1999), this program and its governing model are in good agreement with empirical data for steel and aluminum. However, some inaccuracies are also reported for the bending of aluminum.

CHAPTER IV

FINITE ELEMENT METHOD – DYNAMIC EXPLICIT ANALYSIS

4.1 Introduction

In this chapter, firstly the fundamental basics of the Finite Element Method, in general, will be discussed, then the dynamic-explicit FE-procedure will be studied. In the last section, the FE-code that was utilized in this thesis work PAM-STAMP will be discussed.

4.2 Basics of the Finite Element Method

The finite element method is a numerical technique by which differential equations are solved approximately up to a selected degree of accuracy (Tekkaya, 2002).

In FEM, the behavior of a continuum, which is normally impossible to determine analytically, is approximated by idealization. For this purpose, the shape and behavior of the continuum is redefined by a finite number ideal elements, for which the behavior can be estimated one by one. For this purpose, a number of finite points are defined in the continuum and the values of the function and its derivatives, when needed, are specified at these points, called nodal points. The domain of the function is represented approximately by a finite collection of sub-

domains, called finite elements. Here, the displacement (velocity) field is assumed parametrically. A mesh is composed of finite elements and nodes. Figure 4.1 illustrates the relation of the FE-mesh with finite elements and nodes (PAM-STAMP 2G User's Guide, 2002).

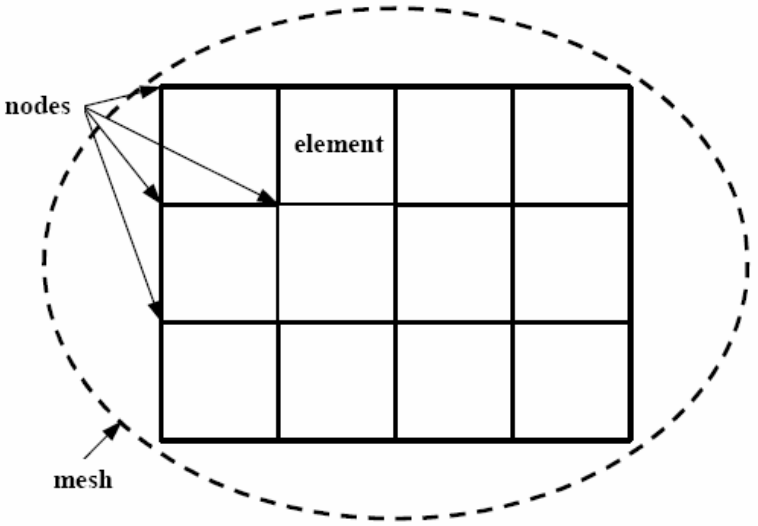

Figure 4.1: Relation of mesh, element and node

For non-deformable tools, the mesh is only a representation of the geometry, and the finite elements are only facets. On the contrary, for the blank or a deformable tool, the finite elements that form this mesh are small pieces of the material with a simplified behavior. The mechanical phenomena which occur in a blank are faithfully reproduced using a large number of these elements. The finer the mesh to be generated, the better the quality of the results, since with an increased the number of finite elements the behavior of the continuum. However, as the number of elements increases, the amount of computation required to determine the behavior of the whole system increases, thus making the calculation time longer. Note that in a simulation, a detail whose size is smaller than that of the elements cannot be represented: the size of the elements defines the precision of the simulation.

Positions, velocities, accelerations and forces are permanently calculated at the nodes, which are points linked to the material. Strains which generate stresses, hence forces on the nodes are calculated at the elements, from the position of the nodes.

To achieve this, firstly the variance of forces and displacements on the elements are governed by shape functions *N,* which relate nodal responses to total element responses.

Afterwards, the relationship between the unknown displacements and known forces at the nodes are determined with the relationship (Determination of element properties). This relationship can be either a linear relationship as in Eq. 4.1, whereas the structural stiffness is independent of displacement, or a non-linear relationship as in Eq. 4.2, whereas the structural stiffness is dependent on displacement.

$$\{F\} = [k] \cdot \{u\} \tag{4.1}$$

$$\{F\} = [k\{u\}] \cdot \{u\} \tag{4.2}$$

where F is force, k is the stiffness and u is the displacement field.

Nonlinear equations in finite element analysis are introduced by:

a) Material nonlinearity (flow of material in plastic region, large strains {not necessary})
b) Contact nonlinearity (contact of workpiece with other workpieces or tools)
c) Geometric nonlinearity (large rotation and displacement of the system with small strains {not necessary}).

The best solution corresponding to the family of assumed displacement fields is obtained by minimizing the solution error yielding the best parameters for the

displacement fields. Then the individual (local) solutions for elements are finally transformed to integrated (global) solutions by matrix algebra. Finally, the resultant forces are calculated finally from the displacements, or vice versa.

The following figure (Figure 4.2) summarizes the input parameters of a FE-simulation:

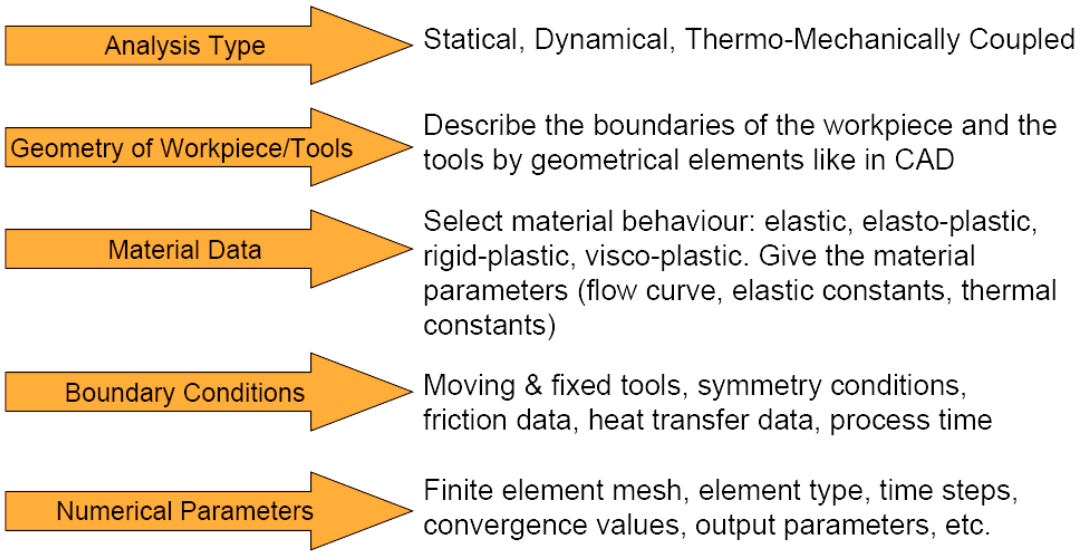

Figure 4.2: Input parameters of a finite element simulation (Tekkaya, 2002)

4.2.1 Finite Element Procedures

There are two procedures available modeling of plastic material behaviors in FEM:

a) Elastic-plastic method,

b) Rigid-plastic method.

The finite element analysis of metal forming processes using the rigid-plastic material model is very popular due to the following properties of this method:

- The material does not require the consideration of the linear kinematics of the finite deformation. Hence it is less time consuming.

- Rigid-plastic formulations are numerically rather robust and reliable.
- In three-dimensional analysis it is possible to formulate linear mixed tetrahedral elements, which allow easy automatic meshing.
- The computer implementation of rigid-plastic finite element code is simple.

Beside these advantages of rigid-plastic formulations there are some serious drawbacks.

- Any elastic based property such as residual stresses and spring-back cannot be analyzed by means of the rigid-plastic material law, which neglects elastic strains.
- A more serious drawback is the fact that rigid-plastic models utilize a pseudo-elastic description of material regions, which are assumed to be rigid. This leads to the fact that, especially in cold forming processes, friction which is always present between the tools and the workpiece in elastic regions of the workpiece is not modeled correctly.
- Another drawback is that rigid-plastic materials cannot detect stress peaks, which occur at the transition between elastic and elasto-plastic material zones.
- Finally, if net shape forming processes are analyzed, the accuracy requirements of the analysis cannot be fulfilled usually.

In the numerical analyses conducted within this thesis study, the elasto-plastic material model was used due to its advantages.

4.2.2 Obtaining the Elemental Stiffness Matrix

Consider a general element as in Figure 4.3, where U is displacement and f is the force acting.

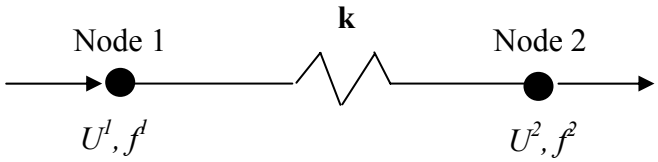

Figure 4.3: General element

From statics and the law for springs;

$$f^1 = f^2 \tag{4.3}$$

$$f^2 = -k \cdot \left(U^1 - U^2\right) \tag{4.4}$$

For a general element;

$$f^1 = k \cdot U^1 - k \cdot U^2 \tag{4.5}$$

$$f^2 = -k \cdot U^1 + k \cdot U^2 \tag{4.6}$$

Or, in matrix form;

$$\{f\} = [k] \cdot \{u\} \tag{4.7}$$

where $\{f\} = \begin{Bmatrix} f^1 \\ f^2 \end{Bmatrix}$ and $\{u\} = \begin{Bmatrix} u^1 \\ u^2 \end{Bmatrix}$ which yields to a stiffness matrix as in Eq. 4.8:

$$[k] = \begin{bmatrix} k_{11} & k_{12} \\ k_{21} & k_{22} \end{bmatrix} = \begin{bmatrix} k & -k \\ -k & k \end{bmatrix} \tag{4.8}$$

In direct approach, the components k_{ij} of the elemental stiffness can be interpreted as *influence* coefficients. For example, k_{ij} is the force (response) of the element at the i^{th} node.

4.2.3 Formation of the Shape Functions

Consider the element in Figure 4.4 with the local coordinate system,

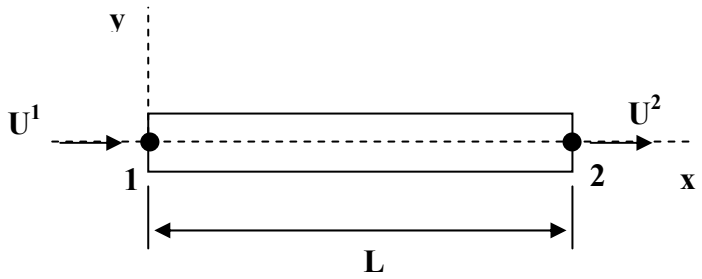

Figure 4.4: A simple element with local coordinate system

the variation of U(x) is assumed to be as

$$U(x) = \alpha \cdot x + \beta \tag{4.9}$$

The unknown coefficients, which are called as *general coordinates*, can be found by the boundary conditions.

$$U(0) = U^1 \qquad \text{and} \qquad U(L) = U^2 \tag{4.10}$$

So, combined with Eq's. 4.10, Eq. 4.9 yields to be:

$$U(x) = \left(1 - \frac{x}{L}\right) \cdot U^1 + \left(\frac{x}{L}\right) \cdot U^2 \tag{4.11}$$

which can be written as

$$U(x) = N^1 \cdot U^1 + N^2 \cdot U^2 \tag{4.12}$$

In matrix form Eq. 4.12 can be rewritten as

$$U(x) = [N] \cdot \{U\} \tag{4.13}$$

N matrix is defined as the local shape function. Shape functions are used define the weight of the nodal deformations on the element.

4.2.4 Transformation to the Global System

The local coordinate system is converted to the global system by means of a transformation matrix (Figure 4.5).

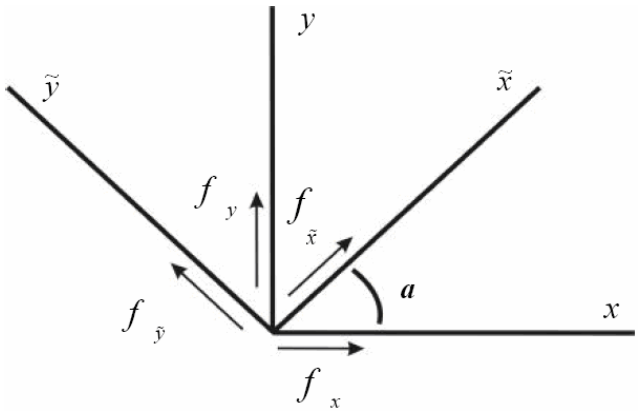

Figure 4.5: Transformation of local coordinate system

Having the relations between the local and global system as rotation, one can write down the relations as follows:

$$f_x^1 = f_{\tilde{x}}^1 \cdot \cos\alpha \tag{4.14}$$

$$f_y^1 = f_{\tilde{y}}^1 \cdot \cos\alpha \tag{4.15}$$

In matrix form all the variables can be expressed as

$$\begin{Bmatrix} f_x^1 \\ f_y^1 \\ f_x^2 \\ f_y^2 \end{Bmatrix} = \begin{vmatrix} \cos\alpha & 0 \\ \sin\alpha & 0 \\ 0 & \cos\alpha \\ 0 & \sin\alpha \end{vmatrix} \cdot \begin{Bmatrix} f_{\tilde{x}}^1 \\ f_{\tilde{y}}^1 \end{Bmatrix} \tag{4.16}$$

In a more general form, the equations will include the A matrix which is named as the transformation matrix.

$$\{f\} = [A]^T \cdot \{\tilde{f}\} \tag{4.17}$$

Substituting Eq. (4.1)

$$\{f\} = [A]^T \cdot [\tilde{K}] \cdot \{\tilde{U}\} \tag{4.18}$$

Similar to force components, displacement components can also be related as

$$\tilde{U}^1 = U^1 \cdot \cos\alpha + V^1 \cdot \sin\alpha \tag{4.19}$$

$$\tilde{U}^2 = U^2 \cdot \cos\alpha + V^2 \cdot \sin\alpha \tag{4.20}$$

In matrix form

$$\begin{Bmatrix} \tilde{U}^1 \\ \tilde{U}^2 \end{Bmatrix} = [A] \cdot \begin{Bmatrix} U^1 \\ V^1 \\ U^2 \\ V \end{Bmatrix} \tag{4.21}$$

$$\{\tilde{U}\} = [A] \cdot \{U\} \tag{4.22}$$

Combining Eq. 4.22 with 4.17 yields to

$$\{f\} = [A]^T \cdot [\widetilde{K}] \cdot [A]\{U\} \tag{4.23}$$

With the help of Eq. 4.23, global stiffness matrix can be expressed as

$$[K] = [A]^T \cdot [\widetilde{K}] \cdot [A] \tag{4.24}$$

4.3 Algorithms of Numerical Simulation Solvers

Algorithms used by the solver of numerical simulation, work step-by-step in order to find equilibrium at each step. Two different types of algorithms can be used: explicit and implicit. The main differences are briefly mentioned in the next this section and the mathematical foundations of the dynamic-explicit solver are studied in the next section.

4.3.1 Differences between Implicit and Explicit Approaches

In the static implicit methods, which were the very first methods used in simulation of metal forming processes, static equilibrium is satisfied in the unknown final configuration of a time increment (Tekkaya, 2000). This method enables a full static solution of the deformation problem with convergence control. Theoretically the increment sizes can be very large; practically, however, it is limited by the contact conditions. Computational times increase almost quadratically with increasing element number. Because of the matrix inversion step and accurate integration schemes, memory requirements are also high. Another disadvantage of the implicit methods is said to be the problem of divergence of the solution. This is basically initiated due to the large number of contact nodes which can overload many implicit contact algorithms. Of course, it is questionable, whether to receive the feedback that the solution is wrong is a real drawback or not. Another disadvantage of the

implicit methods is the singularity of the stiffness matrix at bifurcation points, such as instabilities at wrinkling initiation.

On the other hand, it is stated by Tekkaya (2000) that the most important advantage of the dynamic explicit method is its robustness. There is no check of unbalanced forces and hence no convergence control. The computational speed is higher and the memory requirement is less than the static implicit methods. Tekkaya (2000) indicates that the explicit solution scheme is capable of determination of the wrinkles. Numerical inaccuracies initiate the formation of wrinkles; the region of the wrinkles is quite accurately determined, however the number of wrinkles and the amplitude of the wrinkles may be inaccurate due to the numerically driven initiation process. A final advantage is the simplicity of programming. On the other hand, Tekkaya (2000) states that there are several disadvantages: The explicit character of the numerical scheme is fulfilled if and only if the mass matrix is lumped, i.e. is diagonal. Furthermore, the speed advantages can be hold only if the element computations are as few as possible. This is maintained by using single-quadrature elements, which deliver rather poor stress and strain accuracy. It is claimed that the error introduced by a lumped mass matrix is compensated by the reduced integration schemes of the elements. However, this leads to the disadvantages that local stresses and springback is not reliably computed. Besides, the absence of convergence control is a critical issue. Finally, remeshing leads to a reduction of the time step.

Table 4.1 summarizes the differences of static-implicit and dynamic-explicit approaches (PAM-STAMP 2G User's Guide, 2002).

Table 4.1: Comparison table showing the basic differences between the algorithms

	Explicit	Implicit
Increment	Very small time step	Large
Inversion of matrix	Easy diagonal matrix	Inversion of full stiffness matrix at each increment
Robustness	Result is guaranteed while using small time step	Sometimes instability in case of: - large deformations - large contact surface - non linear material properties
Needed Memory	Small	Large
CPU time	May be large	Generally small
Application	Processes with highly non-linear behavior: stamping	Static and quasi-static processes, easy non-linear behavior: springback

4.3.2 Dynamic-Explicit Solution Algorithm

The principle of virtual work after neglecting body forces can be written as (Tekkaya, 2000):

$$\int_V T_{ij}\delta u_{i,j}dV = \int_A t_i \delta u_i dA \tag{4.25}$$

Where T_{ij} is the Cauchy stress tensor, u_{ij} the gradient of the displacements, t_i the traction vector and δ the variational operator. The Euler equations of this statement are simply the static equilibrium equations. Tekkaya (2000) indicates that in classical sheet metal forming processes the work done by body (dynamic) forces is roughly four orders of magnitude less than the plastic deformation energy. However, the virtual work equation Eq. 4.25 can be modified by an inertia term to

$$\int_V T_{ij}\delta u_{i,j}dV = \int_A t_i \delta u_i dA - \int_V \rho \ddot{u}_i \delta u_i dV \tag{4.26}$$

where ρ is the density and $\ddot{u}_i$ the acceleration of material particles. Discretization of this equation yields

$$[M]\ddot{u}^t = \{F^t\} - \{I^t\} \tag{4.27}$$

In this equation, [M] is the lumped mass matrix, {F} the external force and {I} the internal force vector at a given time t. Now, an explicit central difference scheme for the time marching (Rebelo, Nagtegaal, Taylor, 1992) is utilized in form of

$$u^{t+\Delta t} = u^t + \Delta t^{t+\Delta t} \cdot \dot{u}^{t+\Delta t/2} \tag{4.28}$$

with

$$\dot{u}^{t+\Delta t/2} = \dot{u}^{t-\Delta t/2} + \frac{\Delta t^{t+\Delta t} + \Delta t^t}{2} \ddot{u}^t \tag{4.29}$$

Eq. 4.27 must be modified by an artificial damping term in order to compensate for possible density manipulations in the structure to (Schweizerhof, Hallquist, 1991) Eq. 4.30:

$$[M]\ddot{u}^t + [C]\dot{u}^t = \{F^t\} - \{I^t\} \tag{4.30}$$

The central difference algorithm is conditionally stable Therefore, the time step has to be less than

$$\Delta t \leq \frac{L}{C_d} \approx \frac{2}{\omega} \approx \frac{L}{\sqrt{E/\rho}} \tag{4.31}$$

where L is a characteristic length of the element, C_d the speed of sound in the workpiece material, ω the largest eigenvalue of the system, E the Young's modulus and ρ is the density of the material.

Consider a typical deep-drawing operation for which C_d is 5000 m/s for steel, L is in the order of mm's, say 1 mm (this corresponds to the smallest element in the mesh!), the punch speed is about 0.5 m/s and the punch traveling distance is roughly

300 mm. The time for deep drawing can found as 0.6 s. The minimum time step is given by Eq. 4.31 as 2×10^{-7} s. Dividing the total process time by the minimum time step yields the number of time increments as 3×10^{6}. This is an unacceptable high number of increments, which would make the dynamic explicit methods unfeasible. For this reason, two different numerical tricks are applied (Tekkaya, 2000):

1. The punch speed is increased as compared to the real process speed. In order to reduce the undesired effects of the artificial mass forces numerical damping is introduced. The damping matrix is taken proportional to the mass matrix usually. This precaution, however, does not work if the material is strain rate sensitive. Also, if thermomechanical phenomena are involved, increasing the process speed is not allowed. In such cases the second treatment is used.
2. Increasing the density of the material leads to a reduction of the speed of sound in the material and hence an increase in the allowable time increment. Increasing the density by a factor of 100 reduces the speed of sound by a factor of 10 and so increasing the time increment by a factor of 10. In this case, however, introducing numerical artificial damping is not possible.

Most of the commercial FE - codes uses some stability protections in time step calculations. If large bendings exist in the process, Eq. 4.32 must be used for element time step calculation, especially if the mesh contains small and thick shell elements (PAM-STAMP 2G User's Guide, 2002). Besides, there are two criteria to define the characteristic length of a shell element, the *large* and *small* criteria. The large criterion is the standard criterion whereas, the small criterion is more stringent and it can assure solution stability in severe cases (availability of highly distorted mesh), however the use of the small criterion may considerably reduce the time step, and therefore increase the CPU time.

$$\Delta T_{el} = \min\left(\frac{L}{\sqrt{E/\rho}}, \frac{L}{\sqrt{E/\rho}} \times \frac{L}{t} \times \sqrt{\frac{3(1-\nu)}{2}} \right) \tag{4.32}$$

where ΔT_{el} is the element time step, L is the characteristic length of the element, E is the elastic modulus, ρ is the density of the material, t is the sheet thickness and ν is the Poisson's ratio.

Furthermore, stability of the explicit method is ensured if global time step is lower than the smallest element time step. The global time step ΔT_{Gl} is obtained according to the following equation (PAM-STAMP 2G User's Guide, 2002).

$$\Delta T_{Gl} = \eta \times \left(\sqrt{1+\xi^2} - \xi\right) \times \min\left(\Delta T_{el}\right) \tag{4.33}$$

where

η is the time step scaling factor

ΔT_{el} is element time step

ξ is a damping ratio calculated by the solver.

4.3.3 Friction Modeling

Friction is a complex physical phenomenon that involves the characteristics of the surface such as roughness, temperature, normal stress and relative velocity. Since the modeling of friction can be complex with the variables defined above, it is simplified to two idealistic models.

The most popular friction model for cold forming is the adhesive friction or Coulomb friction model (Eq. 4.34).

$$\sigma_{fr} \leq -\mu\sigma_n \tag{4.34}$$

where σ_n is the normal stress, σ_{fr} is the tangential (friction) stress and μ is the friction coefficient. The minus sign denotes that the friction stress, caused by the compressive normal stress, is tensile.

In contact problems, often neutral lines develop which means that along a contact surface, the material flows in one direction in a part of the surface, and in the other direction in another part. This discontinuity in the value of σ_{fr} can result in numerical difficulties. During the simulations the solver can overcome these difficulties by smoothing the friction line (Figure 4.6).

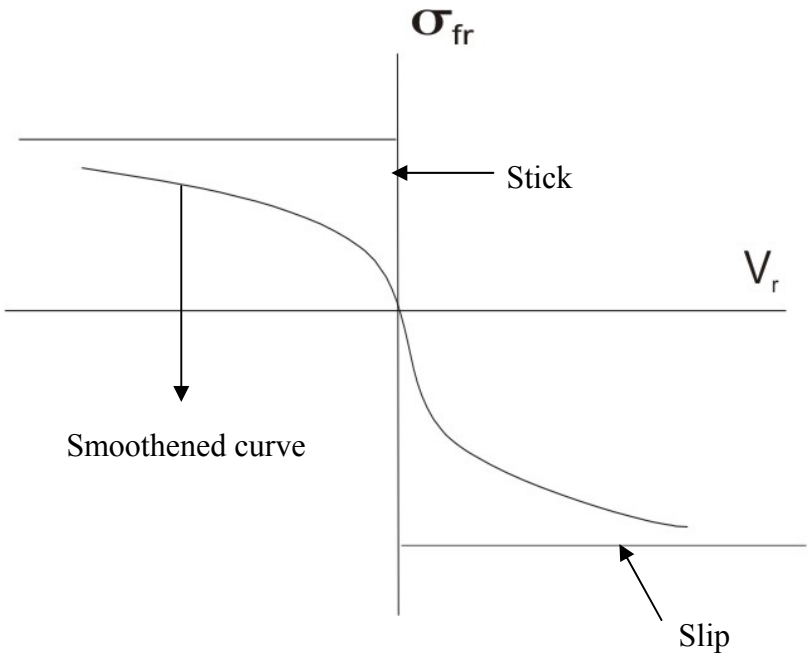

Figure 4.6: Smoothening of the curve

The second friction model is the shear model as shown in Eq. (4.35).

$$\sigma_{fr} \leq -m\frac{\sigma_f}{\sqrt{3}} \tag{4.35}$$

The shear model is not applicable to sheet metal forming and it is normally used in bulk metal forming applications, whereas for sheet metal forming the Coulomb friction model is applied. Therefore, the Coulomb friction model is utilized within this study, and friction coefficients given in following chapters will be Coulomb friction coefficients.

4.4 Features of PAM-STAMP 2G

As stated before, PAM-STAMP 2G is the FEA-package that is utilized for the numerical simulations within this thesis study. In this section the properties of the package (modules, specifications, and the user environment) will be overviewed.

PAM-STAMP 2G is specifically designed for sheet metal forming operations. The main solver of the package is has dynamic-explicit algorithm. However for springback calculations an iterative implicit solver is also present. The program is manipulated via a graphical user interface. Subjectively, the graphical representations of the package is colorful and of good quality.

The package is composed of several modules (PAM-STAMP 2G User's Guide, 2002):

- **DeltaMESH®** is an automatic meshing tool suited to stamping simulations. It is used to generate meshes from CAD models of the stamping tools, adapted to the needs of numerical stamping simulations. For instance, CAD data in .igs format is imported by DeltaMESH, and meshed according to the user's needs automatically.
- **PAM-DIEMAKER** is an easy-to-use geometry modeler for the design of deep-drawing tools. PAM-DIEMAKER module focuses on the quick developing of tools.
- The **Morphing** technology enables rapid and direct manipulation of the part geometry, with instantaneous mesh updating, without resorting to operations such as modifying the geometry in the CAD application and the ensuing re-meshing. The CAD definition of the part is only updated after the run-off is optimized and validated.
- **PAM-QUIKSTAMP** has a simplified approach where some components of the press tool are deduced from the initial part and where the real kinematics is not completely defined. PAM-QUIKSTAMP allows the die designer to quickly check and evaluate different die geometry parameters issued from

PAM-DIEMAKER. Simplified, first time analyses (which lack precision) can be conducted with this module.

- **PAM-AUTOSTAMP** is the actual simulation module, in which actual industrial conditions such as gravity, binder development, multiple stage forming, trimming, springback, flanging, etc. can be analyzed.

The several modules of PAM-STAMP 2G are summarized in the following figure (Figure 4.7) (PAM-STAMP 2G User's Guide, 2002):

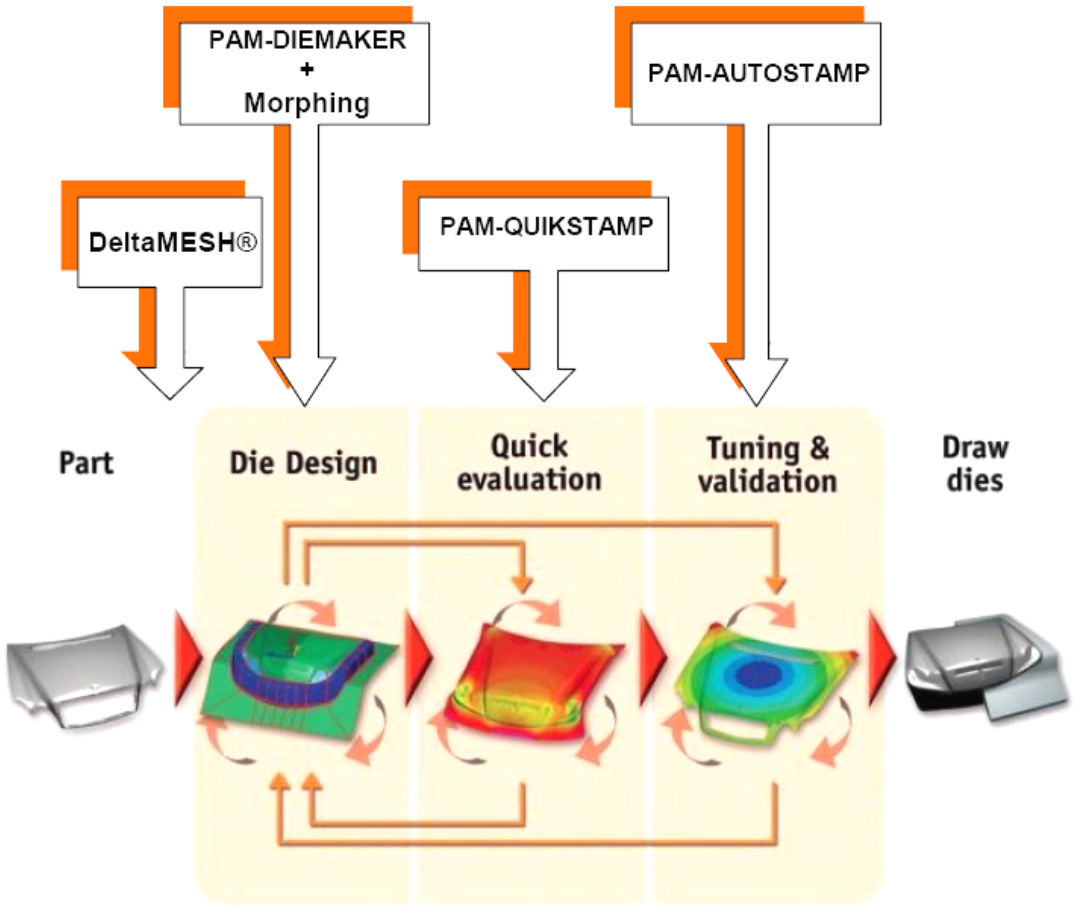

Figure 4.7: PAM-STAMP 2G modules

CHAPTER V

VERIFICATION OF NUMERICAL ANALYSIS

5.1 Overview

On the NUMISHEET 2002 meeting, a series of benchmark tests for finite element analysis packages have been presented. One of the tests was deep drawing of cylindrical cups. A simple cup shape was to be drawn using two blank materials (**6111-T4** aluminum and **DDQ** grade mild steel). This test aimed to investigate the anisotropic behavior of sheets under high blank holding forces and the wrinkling behaviors of sheets under low blank holding forces. The test specifications will be given in the next section.

Within this benchmark test, results of several FE-analyses from numerous participants using various FEA packages were compared to some experimental results. Since participants utilized various packages, the benchmark is useful for determining the reliability and accuracy of any FEA package and to evaluate the efficiency of participants in conducting numerical simulations with FEA-packages.

In this chapter, the results of conducted cup drawing analyses (using PAM-STAMP version 2000 and PAM-STAMP version 2G) will be compared with NUMISHEET's results. Additionally the simulation results of both PAM-STAMP

versions will be compared with the findings of NUMISHEET, and the reliability of these two versions will be inspected.

5.1.1 Process Geometry

The tooling geometry and initial set-up are sketched as follows (Figure 5.1). The deep drawing system is axisymmetric with a simple geometry to produce a cup shape. It should be noted that there is a die clearance of 1.25 mm. The initial blank thickness is given as 1 mm, so that the die clearance removes the possibility of ironing.

Blank thickness t = 1 mm
R_1 = 50.0 mm
R_2 = 51.25 mm
R_3 = 9.5 mm
R_4 = 7.0 mm
R_0 : Radius of initial blank 90 or 105 mm
Clearance : (R_2 – R_1) 1.25 mm

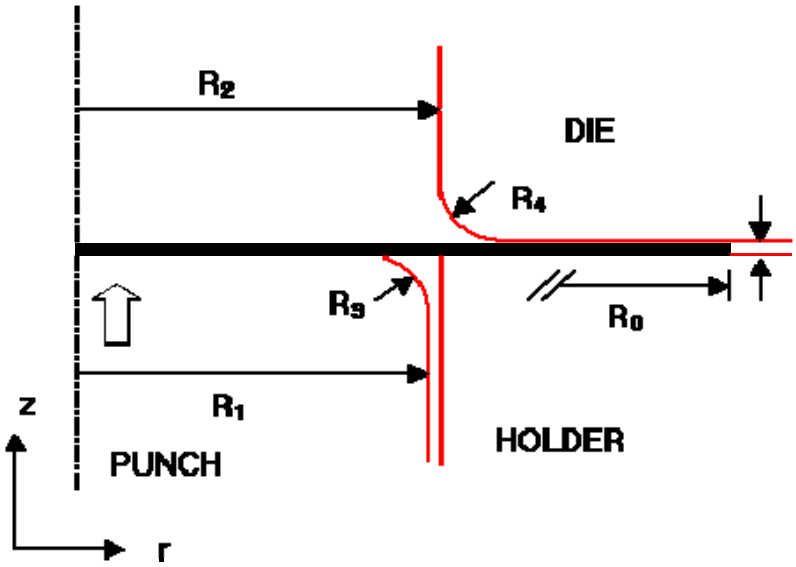

Figure 5.1: Tool for cylindrical cup drawing

The radii of the blanks are given as 90 mm for aluminum and 105 mm for steel.

5.1.2 Material Properties, Machine and Tooling Specifications

The blank materials are manufactured by two companies: ALCOA (U.S.A.) supplied the aluminum material (with the SAE designation AA 6111-T4), and the steel material provided by POSCO (Korea) is mild steel with deep drawing quality

(DDQ). The material characterizations were carried out at the respective companies (Table 5.1). Detailed information about the materials is given in Appendix C.

Table 5.1: Material properties of 6111-T4 aluminum and DDQ mild steel

Material	K [MPa]	n	R_0	R_{45}	R_{90}	Δr	r_n
6111-T4	538.225	0.2255	0.894	0.611	0.660	0.083	0.694
DDQ mild Steel	547.763	0.2692	2.160	1.611	2.665	0.401	2.012

Material	ρ [g/mm³]	ν	ε_0	E [GPa]	σ_Y [MPa]	% Elongation Total
6111-T4	2.6	0.3395	0.00256	70.725	180.825	27.350
DDQ mild Steel	7.8	0.3	0.00088	221.368	193.918	48.069

These materials are chosen because of their similarities in some aspects. In fact, the main aim of this benchmark study in NUMISHEET 2002 is to demonstrate the great differences of behavior of such materials on same deformation processes. As it can be observed from Table 5.1 above, the K and n values, the parameters of the Swift Law (which is given in Eq. 5.1) of the materials are close to each other; meaning that their plastic flow curves (so their plastic flow behaviors) more or less resemble each other.

$$\sigma = K \cdot (\varepsilon + \varepsilon_0)^n \tag{5.1}$$

This similarity is seen in the flow curves of these materials in Figure 5.2. The plastic flow behaviors of these two materials are nearly identical as far as the flow curve is concerned; the difference in product properties arises therefore from the differences in anisotropy and elastic properties.

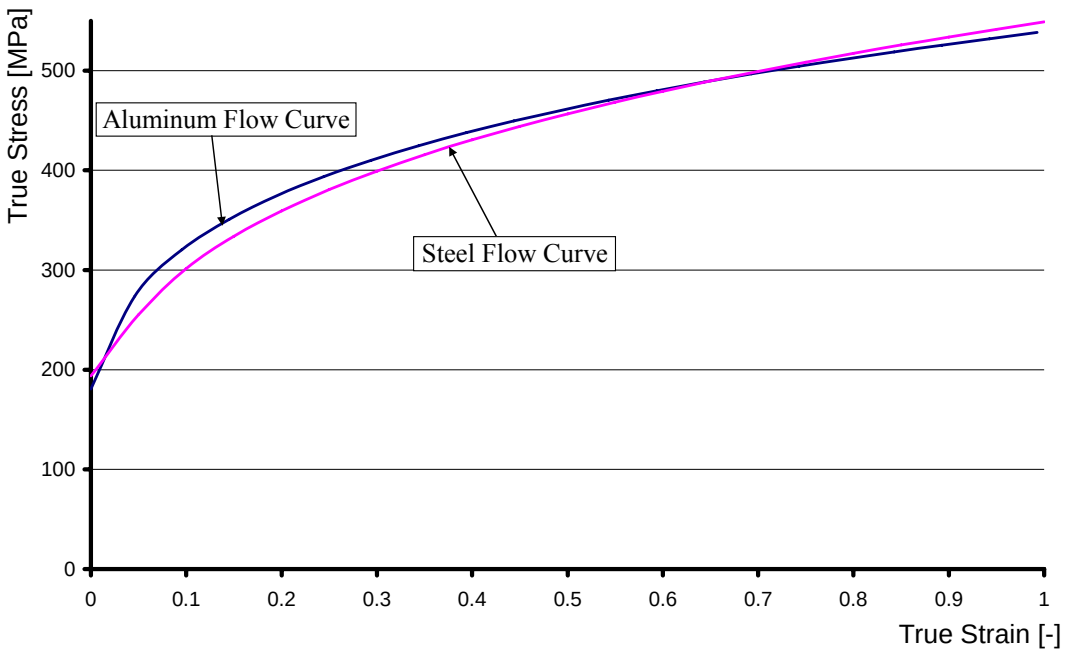

Figure 5.2: Flow curves of 6111-T4 aluminum and DDQ mild steel

On the other hand, the elastic behaviors of these materials are completely different, due to the differences in their elastic moduli. This can also be observed from Table 5.1. Therefore, for many processes, aluminum and steel materials will surely result in different product shapes simply due to the presence of springback alone. However, springback occurrences are not inspected within this NUMISHEET benchmark, since FE-analysis of springback is a tedious and problematic task, which requires different solution algorithms (and different FEA programs possibly).

Additionally, the anisotropy constants (strain ratios at three different angles to rolling direction) of the two materials show (Figure 5.3) that their anisotropic behaviors are entirely different. This difference in anisotropy is also an important reason for differences in product shapes and qualities. The effect of anisotropy is inspected within this benchmark and it will be commented on this subject in the following pages.

The similarity in flow curves and the difference in anisotropy and elasticity make these two materials suitable candidates for the deep drawability comparison, which is reported in detail in Chapter 7.

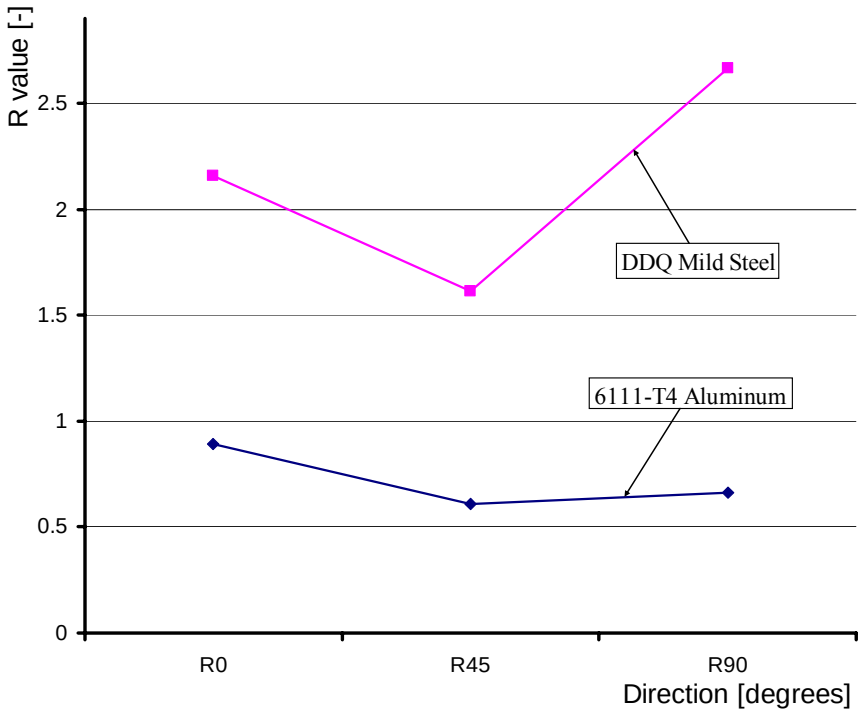

Figure 5.3: R-values of 6111-T4 Aluminum and DDQ mild steel

The process specifications and assumptions as given by NUMISHEET are as follows:

Punch stroke: **40mm**

Blank holder forces:

- Aluminum:

  High blank holder force = **50 kN**

  Low blank holder force = **10 kN**

- Steel:

  High blank holder force = **70 kN**

  Low blank holder force = **10 kN**

From now on, the abbreviations HBHF *and* LBHF *will refer to* high blank holder force *and* low blank holder force *respectively.*

Coulomb Friction Coefficient (average for the whole system):

Aluminum: **0.0096**

Steel: **0.0426**

Heat effects are neglected, in other words the processes are assumed to occur at constant, room temperature. Additionally, strain rate effects are also neglected.

The punch speed is advised by NUMISHEET to be kept constant between **1 mm/s** and **50 mm/s**, but to save computational time faster punch speeds (**500 – 1000 mm/s**) are preferred since the results at these moderate speeds do not differ significantly from the given upper speed limit's results. Additionally it is observed in initial (trial) simulations that the results remain acceptable even up to punch speeds of 10000 mm/s. On the other hand, to be on the safe side, such high speeds are not chosen since the computational times are small enough at 500 to 1000 mm/s range with a precise simulation result. It will be commented on the effects of the punch speed on the outcome of the simulations in the following sections.

As it can be deduced from the data above, for the NUMISHEET benchmark, two sets of analyses must be conducted for both materials; one with a high blank holder force, the other with low blank holder force. Doing this, wrinkling phenomena can be inspected. However, to gain information about the reliability of the PAM-STAMP FEA package, and to learn the effects of many internal (affecting the FEA solver) and external (regarding to the actual process) parameters upon the simulation results several, additional analyses were conducted. These separate simulations were conducted prior to the actual benchmark tests.

In this benchmark of NUMISHEET, the system to be inspected is axisymmetric. If the effects of anisotropy are neglected, it would be possible to analyze smaller parts (even a thin slice) of the whole system due to axial symmetry. It is also clear that

the analysis of smaller parts is favorable, since this allows the participant to use a smaller number of elements, thus reducing computational time. Therefore many participants conducted one-quarter analyses of the system. The presence of orthogonal anisotropy is limiting the symmetry advantage to one-quarter of the whole system. Also for this study, for the sake of simplicity, and to save computation time, one quarter of the whole system was analyzed most of the time. As symmetry conditions are applied more and more, the reality of the simulation model deviates from the actual case, therefore when accuracy is of greater importance, full analyses have to be conducted, but during the initial tests where the process characteristics and the effects of numerical parameters were familiarized, one quarter of the whole system has been modeled. However, symmetry conditions caused unexplainable deviations in the simulation results of PAM-STAMP version 2G, whereas version 2000 was successful in utilizing symmetry. This occurrence may be due to an implementation problem of the revised FE-code of the newer version, therefore the usage of symmetry conditions was avoided when utilizing the newer version of the FE-package in Chapters 6&7. This problem will be thoroughly investigated in Section 5.3.

The following pictures (Figure 5.4) taken from PAM-STAMP 2G, show mesh structures of quarter and full analyses:

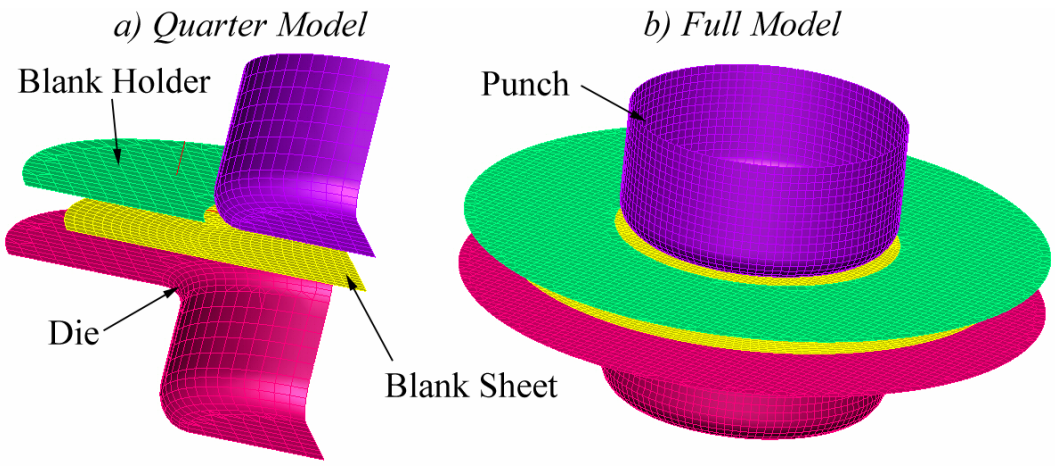

Figure 5.4: Mesh structures of quarter (a) and full (b) analyses

5.2 Initial Simulations

In the following sections, results of several analyses (with varying process parameters and material properties) are reported and discussed. The effects of process parameters like punch speed, blank holder force, friction coefficient and numerical parameters like blank element size, mesh structure, time step scale factor, adaptive meshing, and mass scaling on the simulation will be evaluated and their results will be compared with the experimental and simulation results of NUMISHEET benchmark participants later.

5.2.1 Varying Punch Speeds

In this section, the effect of punch speed on the analysis accuracy and computation time will be inspected. For this purpose, the following punch speeds are used for both materials:

20 mm/s(*), 50 mm/s, 100 mm/s, 500 mm/s, 1000 mm/s,
2 m/s, 5 m/s, 10 m/s, 15 m/s, 20 m/s, 50 m/s, 100 m/s, 200 m/s, 500 m/s,
1 km/s.

At 20 mm/s punch speed, the analysis program could not give any result even after 7 days of computation. Therefore much smaller punch speeds are not tried in further analyses, since at slower rates the simulation cannot be finalized at a reasonable time. However punch speeds larger or equal than 50 mm/s gave satisfactory results up to 200 m/s, where the analysis became erratic since an acceptable time step cannot be used for a stable solution in the iterative process of PAM-STAMP.

The following figures (Figure 5.5 and 5.6) are taken from ‘trial’ analyses (conducted with PAM-STAMP 2000) to inspect the effect of punch speed upon the final blank thickness. These figures give the thickness contours of a HBHF aluminum drawing simulation and a HBHF steel drawing simulation using PAM-

STAMP 2000. For both cases the results are similar, if the thickness contours (and minimum and maximum thickness values) are investigated for punch speeds of 50mm/s and 500mm/s, as expected. However as the punch speed is increased on and on the FE-analyses become problematic, since dynamic effects arise and since the required time steps cannot be reached.

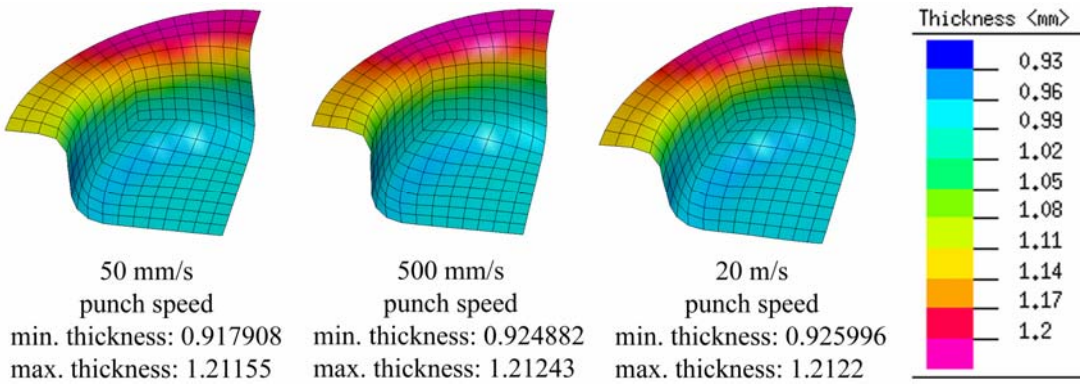

Figure 5.5: Final thickness contours of aluminum HBHF analyses with varying punch speeds

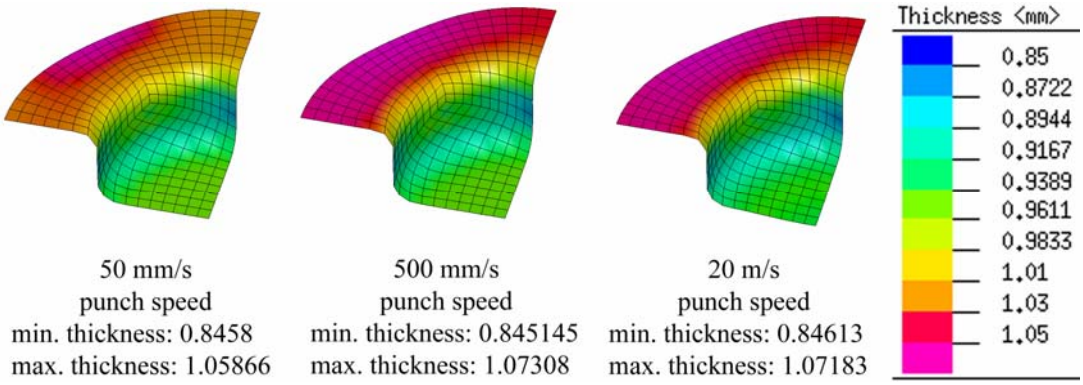

Figure 5.6: Final thickness contours of steel HBHF analyses with varying punch speeds

From the minimum and maximum thickness values, it can be deduced that it is possible to use a faster punch without losing accuracy greatly. As stated before, one can utilize a punch with 500 mm/s speed instead of the upper limit (suggested by

NUMISHEET) of 50 mm/s safely. This way a great deal of computational time can be saved. In this section further comments on this subject will be made, for instance the effect of punch speed on the force requirement of the process is also investigated (Figure 5.11 and 5.12), but at this point it must be stressed that there is a limit of *safe* punch speeds. One cannot speed up the analysis arbitrarily and infinitely; after a certain point all simulation accuracy is lost and the results become unusable. After punch speeds of ca. 50 m/s extreme dynamic effects make the results unacceptable due to the presence of very large vibrations. As it is explained in Chapter 4, PAM-STAMP uses a dynamic-explicit finite element analysis solver. Therefore, dynamic effects are always present in its simulations, where the deformable bodies easily accept and amplify any vibration like a jelly.

Additionally, it is possible to assign velocities in several ways (Figure 5.7). One can assume a constant speed for the moving tool (which will be the punch in this case) or the velocity may be function of a variable like the stroke or time. Although it seems easier to assign a constant speed at first (the solid line in Figure 5.7), undesired dynamic effects arise in the simulation due to the rapid *strike* of the punch to the deformable body (the blank sheet in this case). After the collision, the blank starts to vibrate forcefully and the precision of the simulation is diminished due to these unrealistic vibrations. However, in reality the tools firstly accelerate from a stationary position to a maximum speed, and then decelerate until stopping again (the dashed line in Figure 5.7). This stroke controlled velocity function decreases the vibration of the blank at the first contact, making the simulation more successful, realistic and accurate. The presence and intensity of vibrations can be observed in the force – displacement curves of the punch and in the kinetic energy – stroke curves of the blank sheet. This effect will be observed in Figures 5.7, 5.8, 5.9 and 5.10.

It should be noted that in Figure 5.7, the areas under the curves must give the same punch stroke of 40 mm. To achieve this, the operation time for the stroke controlled velocity case is increased slightly, increasing the overall simulation CPU-time.

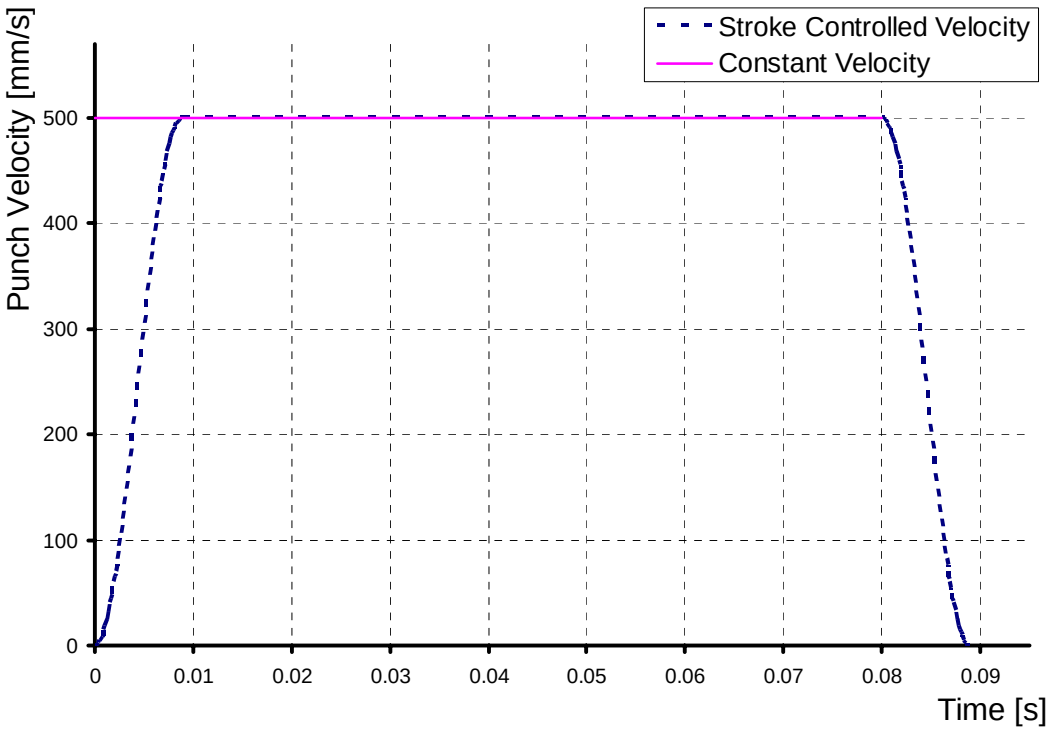

Figure 5.7: Punch velocity control

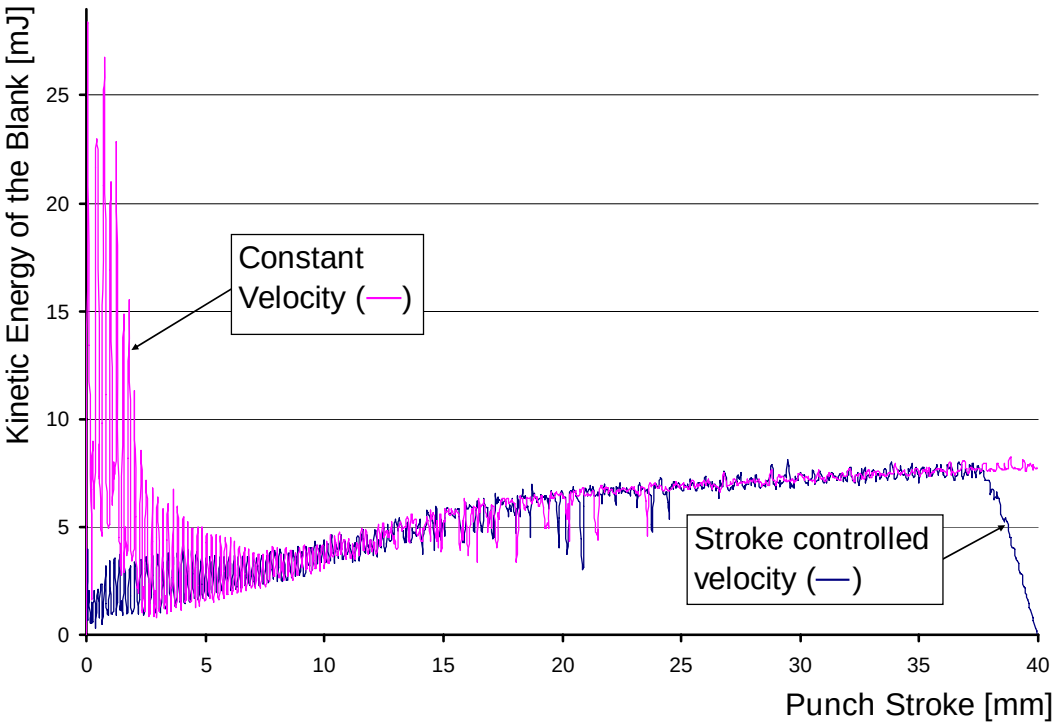

Figure 5.8: Vibrations on blank sheet

These two figures (Figures 5.7 and 5.8) refer to the HBHF aluminum analysis using a maximum tool speed of 500 mm/s.

The kinetic energy of a blank sheet can be estimated by using the basic kinetic energy formula as given in Eq. 5.2:

$$E_{kin} = \frac{1}{2} m v^2 \tag{5.2}$$

Here, E_{kin} denotes the kinetic energy, m is the mass and v is velocity. It can simply be found that for an aluminum blank with 90 mm radius and 1 mm thickness; if a maximum deformation speed of 500mm/s is applied the kinetic energy will be about 8 mJ. The final values of Figure 5.8 tend to 8 mJ, so the estimate is acceptable. Figure 5.8 shows that the vibrational energy (at the start of the punch – blank contact) makes a peak for the constant speed case, and as the simulation progresses, the vibrations damp until the estimated kinetic energy maximum (at the end of the simulated process) is obtained. In Figure 5.8, the peak kinetic energy value of the constant velocity simulation (the pink line) at the start of the process is an indication of larger blank vibrations than the stroke controlled velocity case (the blue line).

The undesired dynamic effects can also be observed at very high speeds on the graphical interface of the program as deformations on the blank, and/or as contact and penetration problems. The following two figures (Figure 5.9 and 5.10) show this phenomenon in aluminum and steel analyses with constant tool speeds of 200 m/s and 500 m/s respectively. In Figure 5.9, the blank seems to be bulged under the punch, as if there is a pressure between the punch and the blank. Actually, the bottom side of the blank is accelerating away from the punch, and the sides of the punch are penetrating into the blank. On the other hand, in Figure 5.10 the punch passes through the deformable blank, as if the blank is a liquid. In this figure, the excessive vibration of the blank is observable. Although they take couples of seconds, the results of both simulations are unrealistic and unacceptable because of the erratic behavior of the deformable material due to excessive punch speeds.

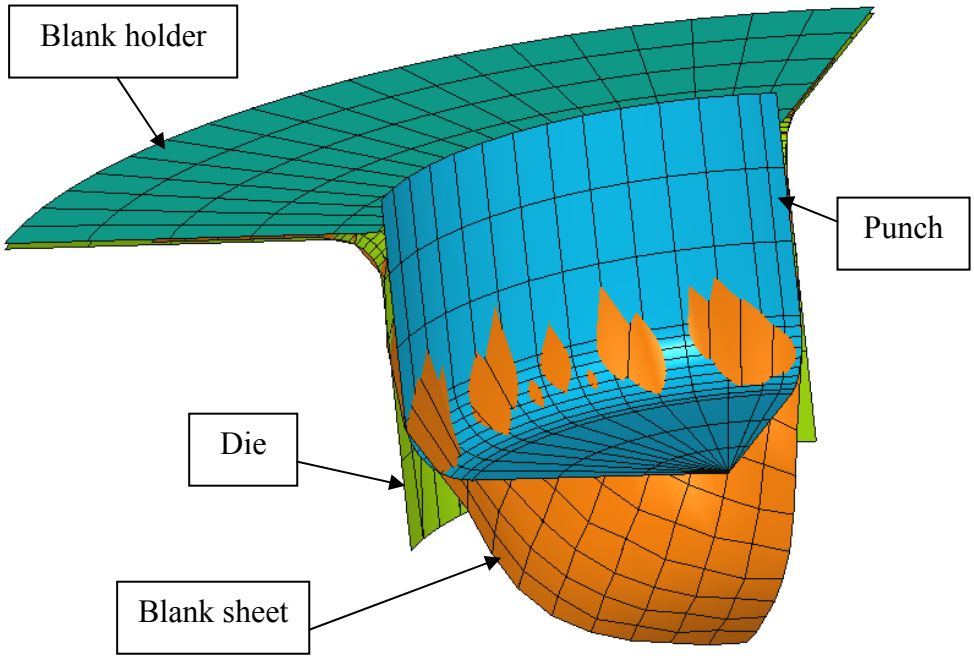

Figure 5.9: Penetration of the blank due to high punch speed (200 m/s)

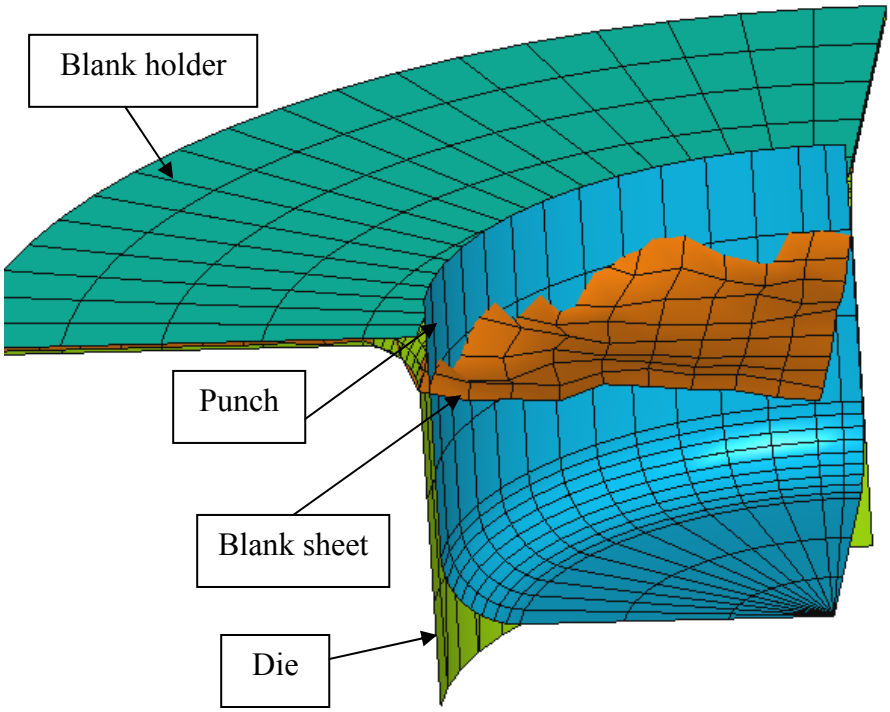

Figure 5.10: Penetration of the blank due to high punch speed (500 m/s)

As expected, the blank still vibrates even when the velocity is appropriately applied, but the extent of these vibrations are not too large to affect the precision of the analysis greatly. On the other hand, as the velocity is increased on and on, besides the visible dynamic effects, the punch force – punch displacement behavior, the strain contours and the thickness contours deteriorate. As time steps for the FE-iterations increase due to increasing operation velocity, accuracy is lost, and after a certain point, it becomes impossible to obtain a stable solution.

Figures 5.11 and 5.12 give the effect of velocity magnitude on the force requirement of the processes for aluminum and steel in PAM-STAMP 2000. Additionally, CPU times for the simulations of the processes are given in Figure 5.13. For these analyses the maximum velocities are assigned as stroke-dependent functions.

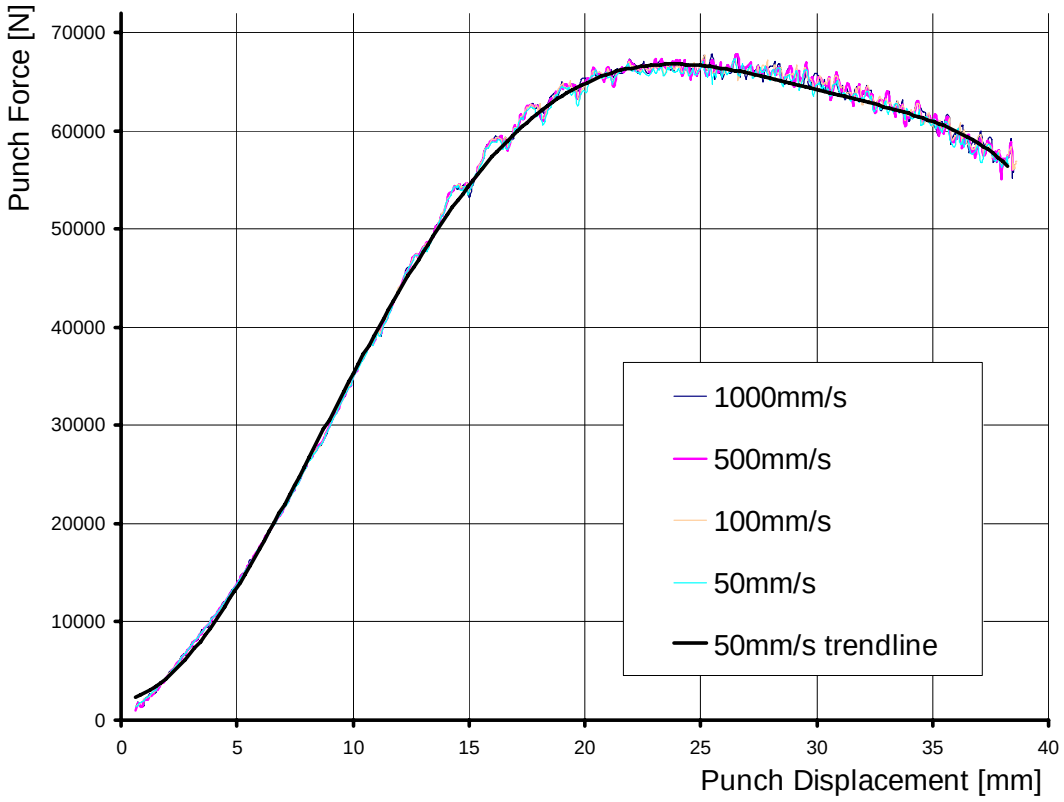

Figure 5.11: Force – displacement curves for aluminum material (HBHF analysis)

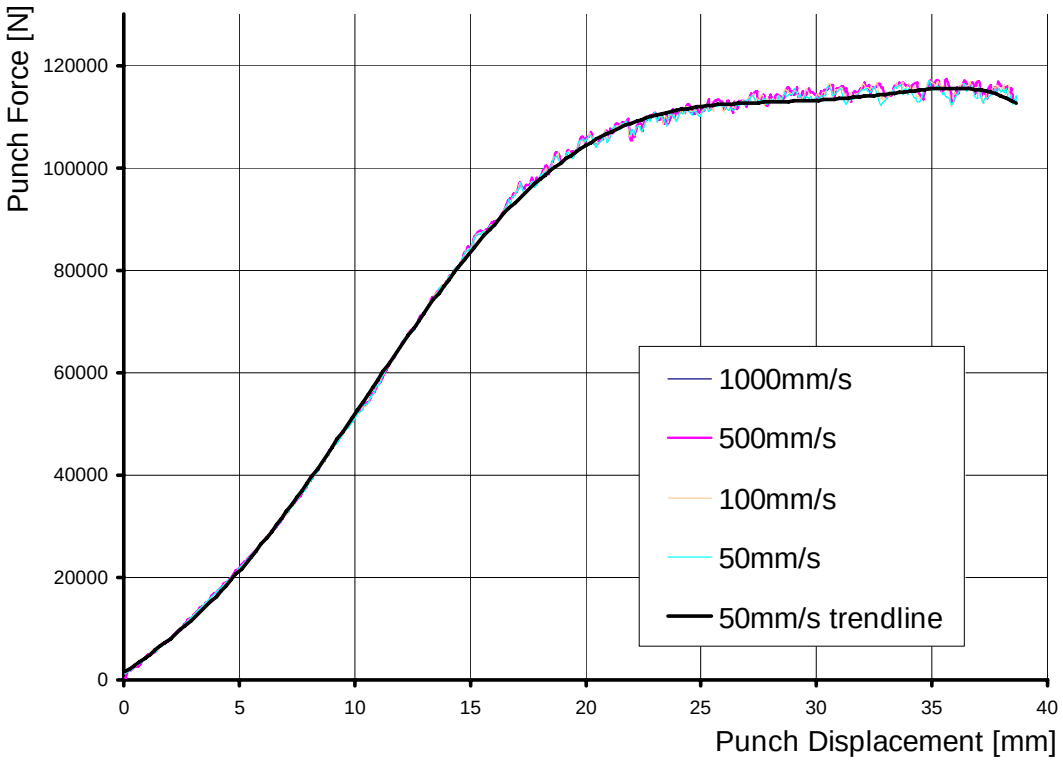

Figure 5.12: Force – displacement curves for steel material (HBHF analysis)

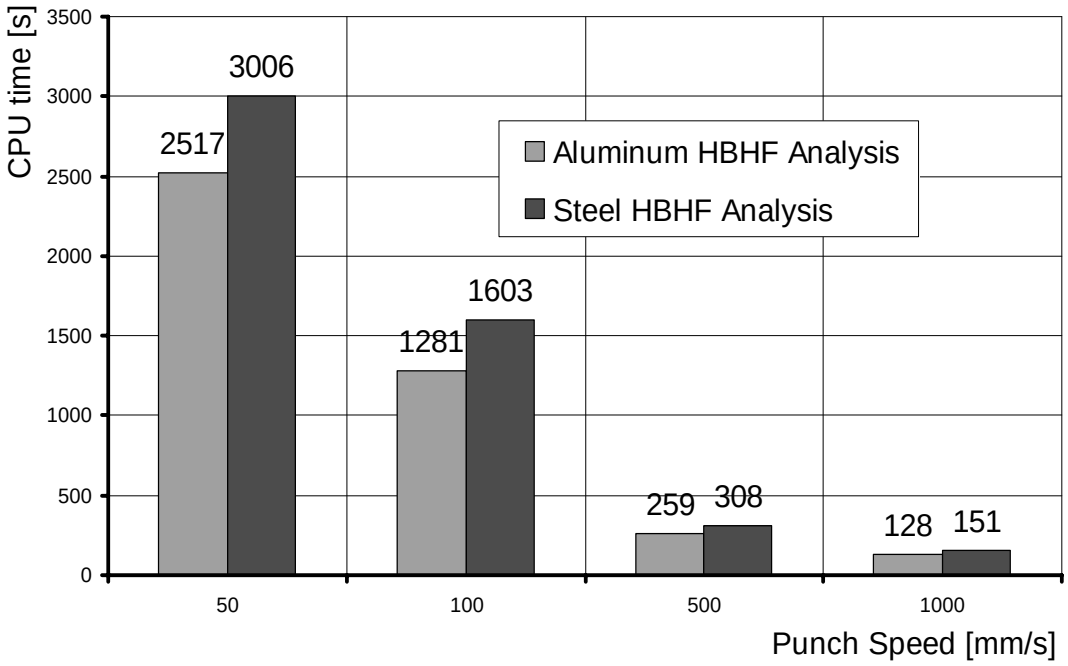

Figure 5.13: CPU times for various punch speeds

The CPU times in Figure 5.13 are obtained using PAM-STAMP 2000 on an AMD Athlon 2000+ computer with 243 elements for the 90 mm blank and 300 elements for the 105 mm blank. With increasing punch speed, the overall execution time of the analysis decreases rapidly. The fastest possible punch speed was given by NUMISHEET as 50 mm/s, but as it can be seen from the Figures 5.11 and 5.12, the force requirements of the processes do not vary significantly for punch speeds of 50 mm/s to 1000 mm/s like the thickness contours on Figures 5.5 and 5.6. On the other hand, the required process time drops to nearly one twentieth of the 50 mm/s analyses if a punch speed of 1000 mm/s is used. Now, the effect of faster punch speeds on the force requirements will be inspected:

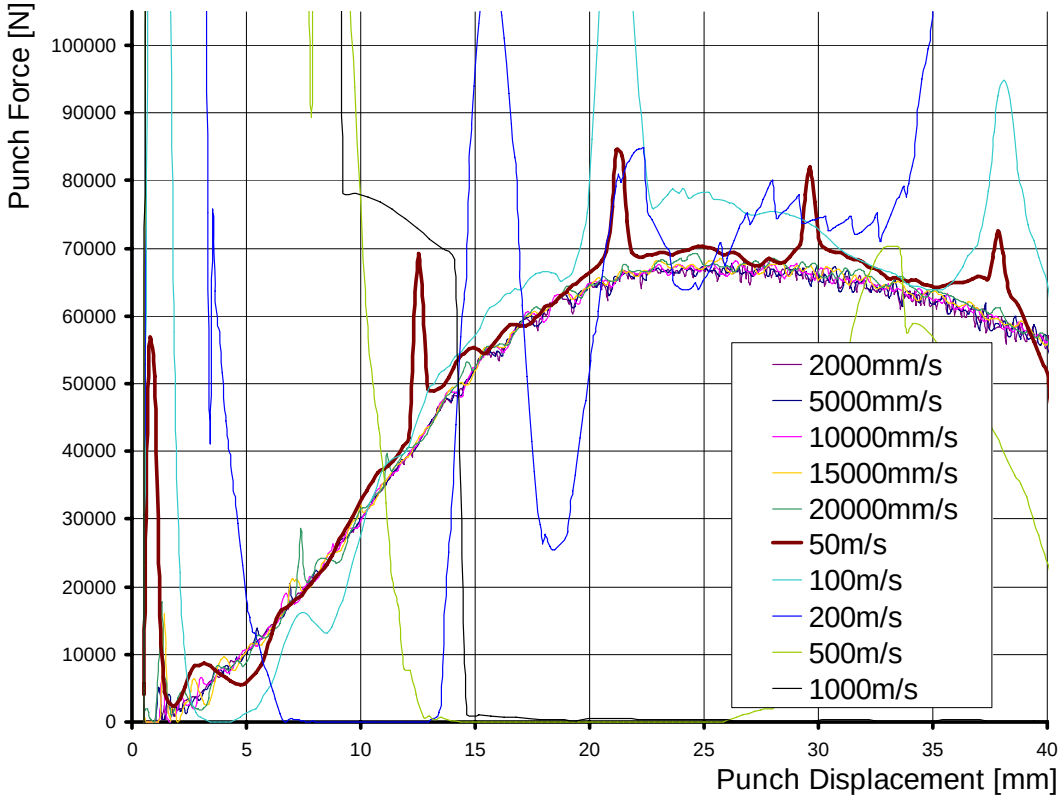

Figure 5.14: Upper limit for punch speeds – aluminum HBHF

From Figure 5.14 it is deduced that after ca. 50 m/s dynamic effects dominate and accuracy of the analysis is lost. The force-displacement relation shows (as well as

the visualization of the resulted simulation) that the analysis does not give an acceptable solution after 50000 mm/s. On the other hand, after punch speeds like 20000 mm/s the analysis times drop to several seconds, meaning that further increasing the punch speed does not result in significantly faster computations.

Hence, to be on the safe side one can use 10000 mm/s for such an analysis, if only the force – displacement (f-d) relationships are considered. At that level, the solution has acceptable precision in terms of the f-d relation, and is it not extremely long to obtain. However, to diminish the dynamic effects mentioned before and therefore to improve the overall quality of the solution (like in the thickness contours in Figure 5.6 and 5.7), one should choose slower and safer tool speeds like 500 mm/s or 1000 mm/s. The similar results are also obtained for the steel sample (Figure 5.15). Here, exceeding 20000 mm/s will give certainly false (in other words, unacceptable) results:

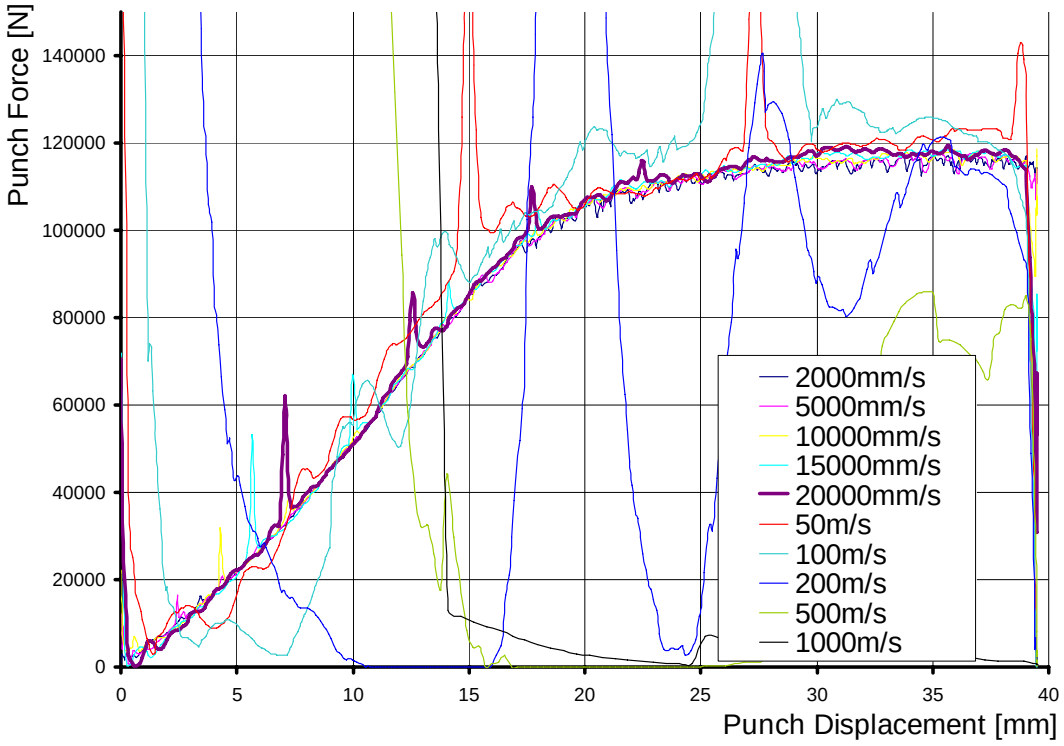

Figure 5.15: Upper limit for punch speeds – steel (HBHF)

5.2.2 Varying Blank Holder Forces

NUMISHEET requires two analyses to be conducted with two different blank holder forces (BHF's). However, some more analyses were conducted by varying the blank holder forces to inspect and demonstrate the wrinkling phenomenon. The blank holder forces are varied as the following (Table 5.2):

Table 5.2: Variation of the blank holder forces

	Aluminum	Steel
Blank Holding Force [kN]	50 (HBHF)	70 (HBHF)
	10 (LBHF), 5, 4, 3.5, 3, 2.5, 2, 1.5, 1, 0.5	

The range 1 – 5 kN is inspected thoroughly, because severe wrinkling was expected to be observed at blank holder forces lower than 5 kN. At the LBHF level (10 kN), no wrinkling was observed for both cases. For instance, the effect of wrinkling (due to insufficient blank holding) on the final shape can be visualized in Figure 5.16.

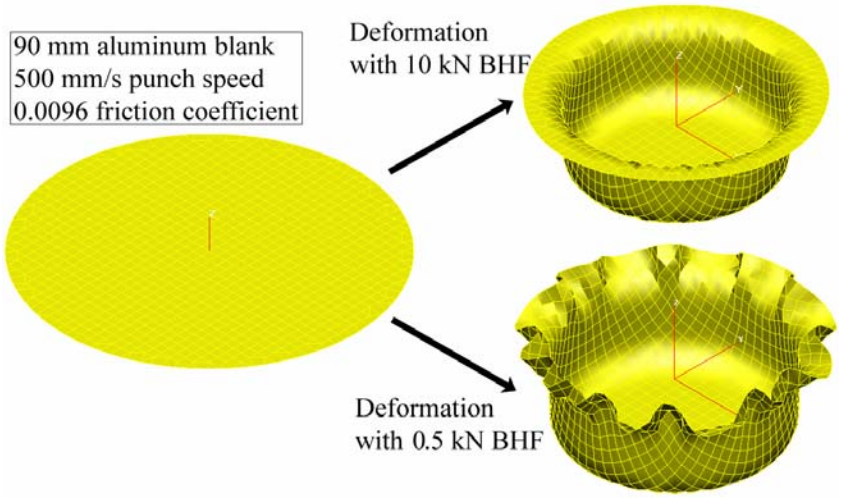

Figure 5.16: Effect of blank holder force on wrinkling

Fig 5.16 depicts the resulting blank shapes of two separate analyses with 10 kN (LBHF) and 0.5 kN blank holder forces on the aluminum blank. All other process and simulation parameters with the material properties are identical for both analyses.

In the 10 kN case, no wrinkling is observable, whereas the 0.5 kN case wrinkles as expected. In this figure, the wrinkling waves of the low-force case are visually observable without argument. However, scientifically one has to *determine* wrinkling by measuring the height oscillations in the flange region. This is done in the FE-analysis by tabulating the height of the outermost nodes in the flange region of the blank with respect to the angular displacement from the rolling direction (which is set as the x-axis for all simulations). This way, smaller wrinkling waves, which cannot be observed visually, can be detected. For instance, for an intermediate case (Figure 5.17) where the wrinkling waves cannot be clearly identified visually, if the height profile of the outermost nodes is inspected, the presence of wrinkling is detected (Figure 5.18). This way, interpretation mistakes during visual inspection are prevented.

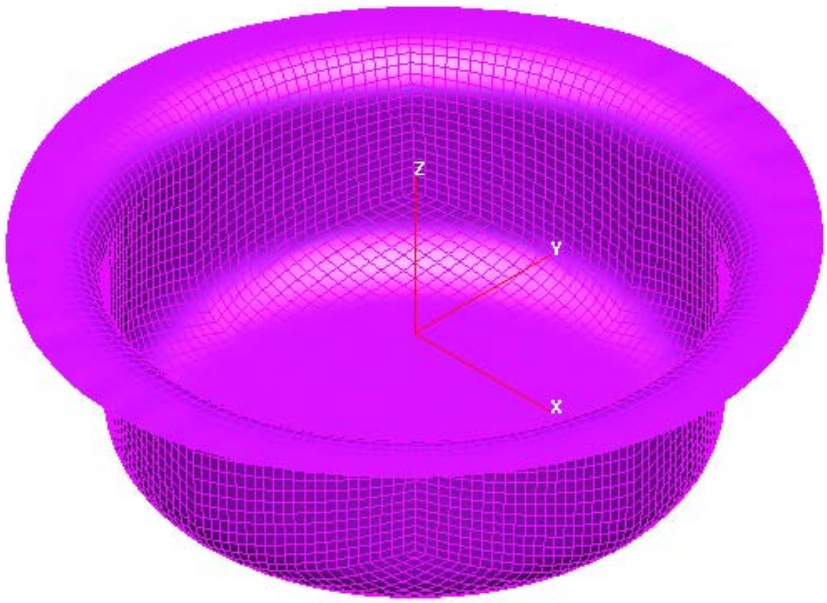

Figure 5.17: Slight wrinkles on a sheet

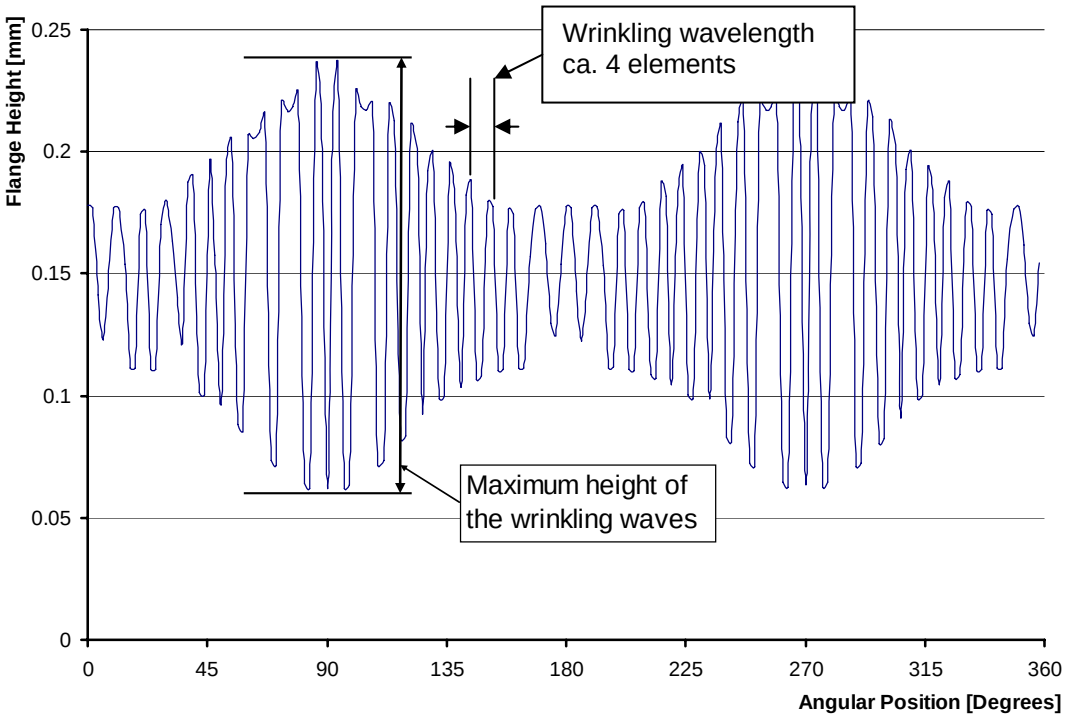

Figure 5.18: Height profile of a slightly wrinkled sheet

It should be noted that for this case, the variation in the flange height is ca. 180 microns at max (Figure 5.18). The wrinkling waves are is approximately 4 elements long. Any user must decide, whether the magnitude fluctuations in the flange height profile depict wrinkling or not. The reason of these fluctuations in the amplitude of the wrinkling waves will be explained in Section 5.2.2.2.

However, these fluctuations are not solely due to wrinkling as the shape of them imply; in Figure 5.18, it is seen that the amplitude of the wrinkling waves increase in 90 and 270 degrees w.r.t. rolling direction. Here, the amplitude of the wrinkling wave also varies with angular direction. This arises due to numerical problems - namely contact problems between the deformable blank and the rigid tools due to element size incompatibilities- and the utilization of anisotropic material under rigid tools. These occurrences are investigated in detail in the following Sections 5.2.2.1 and 5.2.2.2 respectively.

5.2.2.1 Loading Types in PAM-STAMP

In PAM-STAMP loads can be applied either as forces or pressures, which can be defined with a constant value or as a function of time. When loads are applied to a surface tool object, the object must be defined as a rigid body. PAM-STAMP 2G reference manual defines the rigid body as a set of elements to which *no strain* is applied and the movement of which can be *described by the six degrees of freedom of its center of gravity*: three translations and three rotations. A blank object is a deformable body.

For a rigid body, the value of the force is assigned to the nodes of the object. On the other hand, pressure is applied by converting the given pressure to nodal forces by considering the total area of the object and by using the normals of the elements. Therefore, the effective value of a pressure is dependent on the object size. Additionally the orientation of the normals should be consistent. A positive value of pressure is applied in the opposite direction of the normals. For instance, if a blank holding load is to be applied to a blank holder as a force, one must define the blank holder (BH) as a rigid body. For instance, the HBHF load (50 kN) in the aluminum analysis is distributed evenly among all nodes of the blank holder and applied to all nodes of the blank holder, which come in contact with the deformable body. On the other hand, if the same load is to be applied as a pressure, the area of the blank holder must be calculated (Eq. 5.3), and the corresponding pressure is determined by dividing the force by the blank holder area (Eq. 5.4).

$$A_{BH} = \pi \cdot \left(R^2 - r^2\right) \tag{5.3}$$

A_{BH} is the blank holder area and R and r are the outer and inner radii of the blank holder respectively. The inner radius r is specified by Numisheet as 51.25 mm.

$$P_{BH} = \frac{F_{BH}}{A_{BH}} \tag{5.4}$$

Here, P_{BH} is the blank holding pressure and F_{BH} is the blank holding load.

If R is taken as 90 mm (which is the blank radius for aluminum analyses), the blank holding area is calculated from Eq. 5.3 as:

$$A_{BH} = \pi \cdot \left(90^2 - 51.25^2\right) \approx 17195.311 \text{ mm}^2$$

Hence, the blank holding pressure for aluminum HBHF analysis using a 90 mm blank holder is calculated from Eq. 5.4 as:

$$P_{BH} = \frac{50000}{17195.311} \cdot \frac{kN}{mm^2} \approx 2.908 \text{ MPa}$$

The blank holding pressure (BHP) for steel analysis can also be calculated similarly. However, it must be noted that the steel blank has a radius of 105 mm, therefore the blank holder must also be enlarged to support the larger blank appropriately. The following table (Table 5.3) gives the blank holder forces and their corresponding blank holder pressure values for several blank holder radii:

Table 5.3: Conversion of the blank holding loads:

	For 90 mm BH	For 105 mm BH
Blank Holder Area [mm^2]	17195.311	26384.470
	Blank Holding Pressure [MPa]	
70 kN BHF (Steel HBHF)	*4.071 (not used)*	2.653
50 kN BHF (Aluminum HBHF)	2.908	*1.895 (not used)*
10 kN BHF (LBHF for both)	0.582	0.379

There is one important point when determining the blank holding loads: forces are insensitive to the object (here, the blank holder) size, whereas pressures are dependent on the object size. Applying the same pressure on two different-sized blank holders will give different simulation results. For instance the effect of BHP and BHF with varying blank area can be inspected from Figures 5.19 and 5.20. A 6111-T4 aluminum blank with a radius of 90 mm is drawn with a punch speed of 500 mm/s and an overall Coulomb friction coefficient of 0.15 throughout the system. For this purpose a 90 mm BH and a 105 mm BH are utilized. The blank holding load is given as 2.5 MPa and 43000 kN (which is the corresponding force for a 90 mm BH).

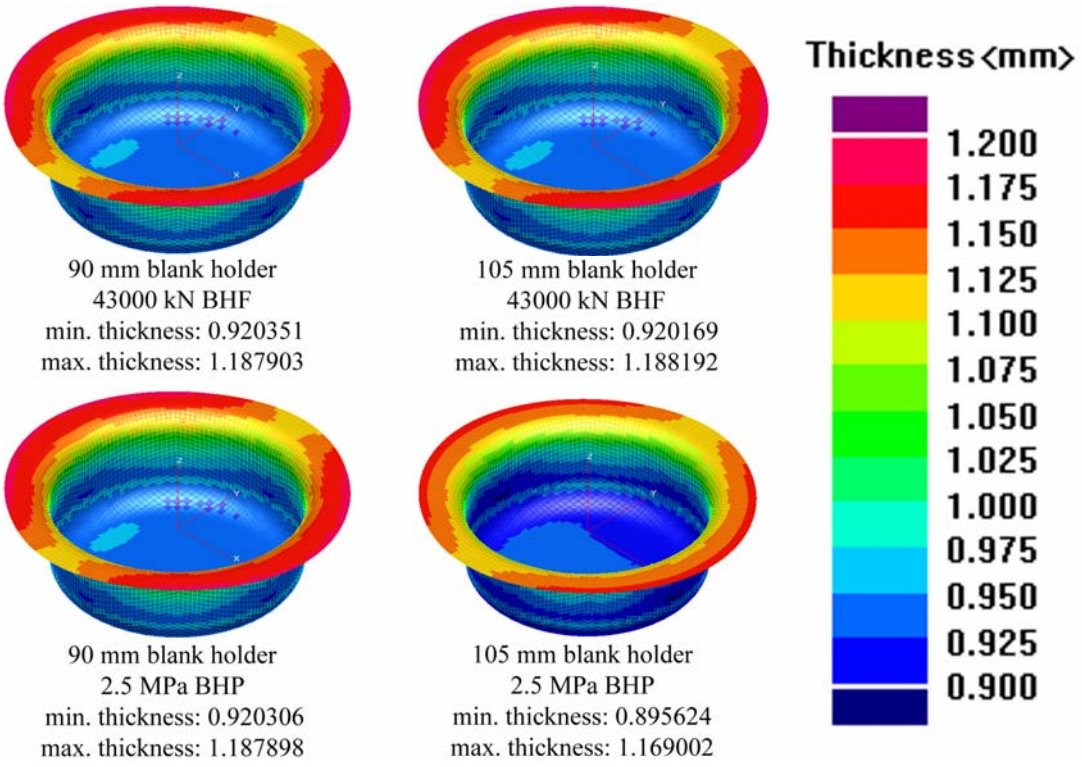

Figure 5.19: Thickness contours for varying blank holding loads of aluminum analyses

The thickness contours and the maximum and minimum thickness values in Figure 5.19 prove that the results are nearly identical for the different-sized blank holders

when the blank holding load is applied as a force. On the other hand, the smaller BH (having 90 mm outer radius, identical to blank radius) gave the same results again for pressure, whereas the larger BH gave entirely different results for pressure, since that pressure corresponds to a larger force due to a larger blank holding area. Naturally, a larger blank holding load imposes a larger restraining force on the flange, causing the blank to become thinner at the end of the operation. Similarly, with an increasing restraining force for the drawing operation, the overall force requirement of the process must increase as well. This occurrence is observed in Figure 5.20:

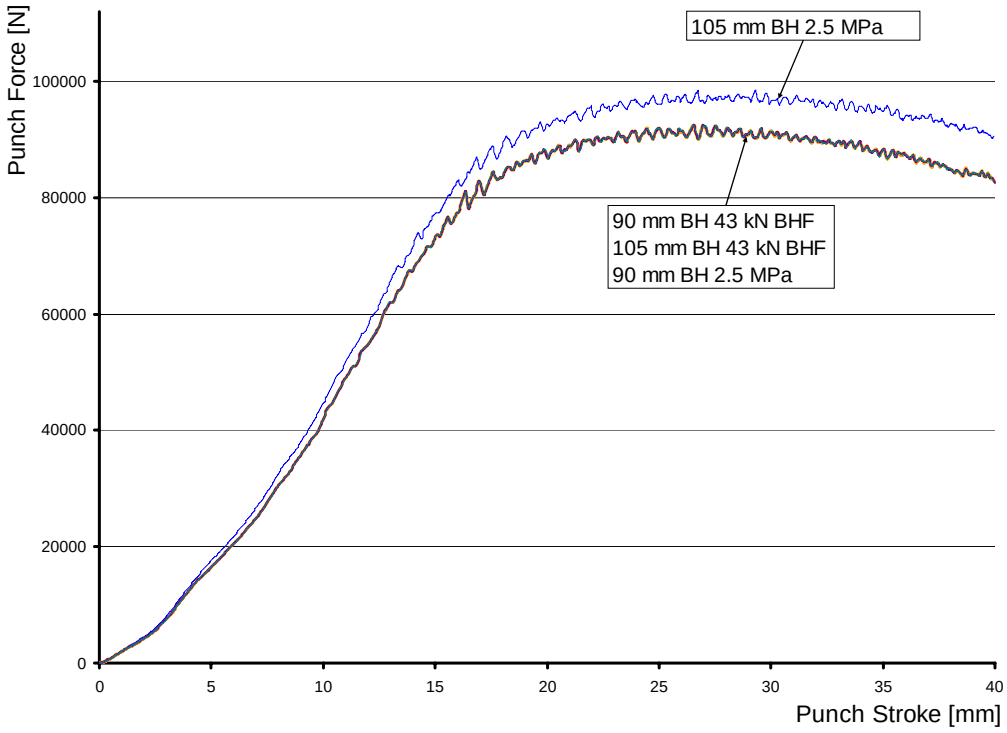

Figure 5.20: Force – displacement curves for varying blank holding loads

Figure 5.20 shows that the force requirement of the three cases (90 mm and 105 mm BH with 43 kN BHF and 90 mm BH with 2.5 MPa BHP) fall on top of each other, whereas the 105 mm case with the blank holding pressure of 2.5 MPa has a larger force requirement for the process. This is in agreement with the previous findings.

For any process, the dependence of the effectiveness of the load on the size of the object that applies the load is a weakness of PAM-STAMP. In actual processes, the forces or pressures of the tool are concentrated on the deformable body; therefore the value of the pressure (if the loads are defined in terms of pressures) will depend on the area of the tool – blank contact interface, not the whole area of the loading tool. Additionally in force loaded tools, the effectiveness of the blank holder loads increase as the drawing progresses, since the flange area (which is the active area for the blank holding) decreases continuously. PAM-STAMP computes blank holding pressures by converting the given values by considering the blank holding area. For an actual process, the blank holding area will be unimportant. Therefore, any user must define the blank holder size and loads carefully for successful and realistic deep drawing simulations, if the loads are to be given as pressures for simplicity, or the loads must be applied always as forces to prevent problems.

Additionally, the mesh structures also affect the outcome of the simulation. Normally, the mesh structures of the rigid tools are considered to be used only to represent the geometrical properties of the bodies. However, the mesh density affects the contact algorithm and the loading. If a coarse mesh is used for a tool body having a simple geometry (like the blank holder), contact problems arise (Figure 5.21), introducing unrealistic effects. This occurrence is due to the nature of FE-modeling. The infinite continuum is discretized as a finite number of nodes and the loads are applied to that finite number of nodes on the blank holder object, for instance. The loading is as accurate and as uniform as the number of nodes of the blank holder object and the blank object in contact for the deep drawing simulation. As seen in Figure 5.21, if the blank holder object is coarsely meshed, the loading may be unrealistic, due to a mesh mismatch between the two objects. In the ideal case, the FE-simulation can be conducted identically to the real case by utilizing an infinitely fine mesh, but since such a simulation will take infinite time to complete, a trade-off is done between modeling precision and computation time. For best results, it is advised that the tool and blank meshes are equally fine when using PAM-STAMP for FE-simulations.

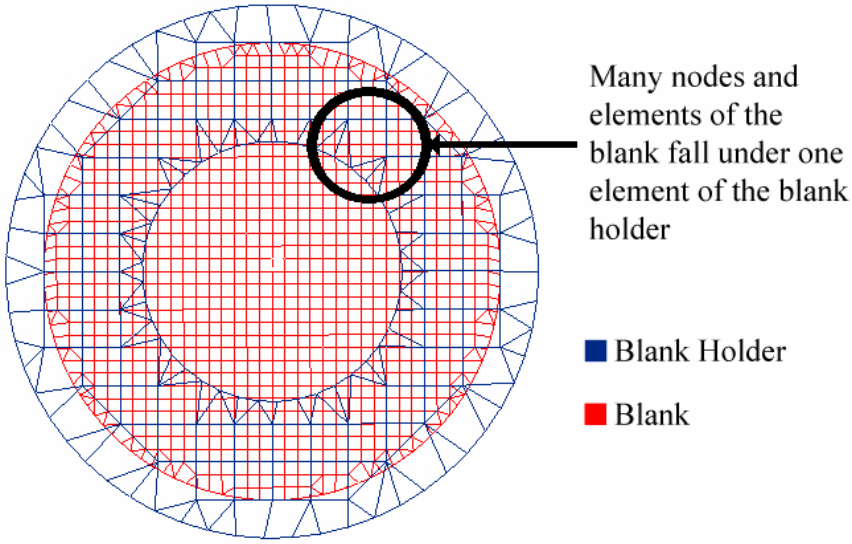

Figure 5.21: Mesh mismatch between the blank and the blank holder

5.2.2.2 The Secondary Wrinkling Phenomenon

There is another interesting phenomenon in deep drawing simulations when using PAM-STAMP. It is explained in Section 5.2.2.1 that the tools must be modeled as rigid bodies in PAM-STAMP, meaning that they will not experience any deformations during drawing operation. On the other hand (rigid) tool – (deformable) blank contact is determined by the blank thickness. For this purpose, half of the total thickness of the blank is applied to the upper and lower surfaces of the blank as represented in Figure 5.22. The geometrical position of the blank mesh is called the mid-plane, and the extended ½ sheet thickness from the mid-plane is called the contact thickness.

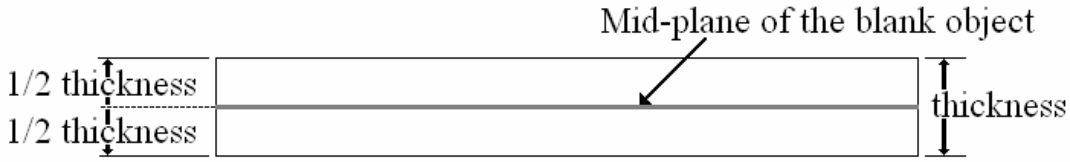

Figure 5.22: Thickness of the blank object

The contact thickness is updated as the sheet thickness varies; this way, tools are always *touching* the sheet surface. However, since the blank thickness is not constant at the flange region due to the presence of anisotropy, contact problems arise. At the regions where the flange is thicker, there is satisfactory contact of the blank with the blank holder (Figure 5.23). However, since the blank holder object is rigid, there is insufficient contact at the regions where the flange has experienced less thickening. Therefore at these regions, namely the Y and –Y directions of the flange, the loading cannot be applied fully, causing some partial wrinkling. These kinds of wrinkles are called as *secondary wrinkles* throughout this thesis study, and this wrinkling phenomenon is called as *secondary wrinkling*.

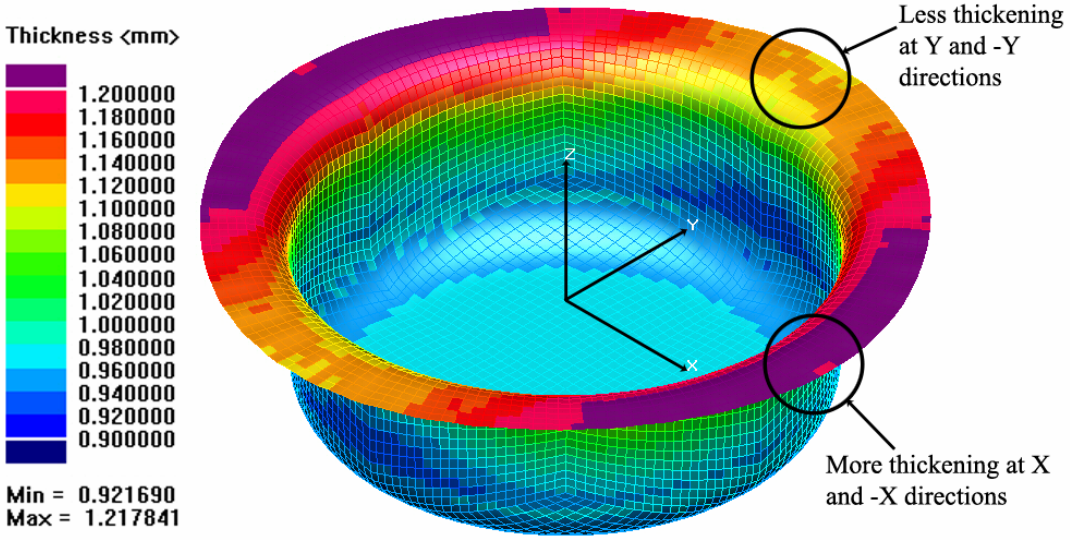

Figure 5.23: Thickness variation at the flange in an anisotropic blank

The presence of secondary wrinkles can be inspected from Figure 5.24. In this figure, the height profiles of two drawing simulations (one with an anisotropic material, the other with an isotropic material) are tabulated with respect to angular displacement to the rolling direction. It should be noted that the rolling direction is defined as the X-direction on Figure 5.23. It is observed (from Figure 5.24) that secondary wrinkling is present for the anisotropic analysis at 90 and 270 degrees, where the thickening is less than that at 0 and 180 degrees (Figure 5.23).

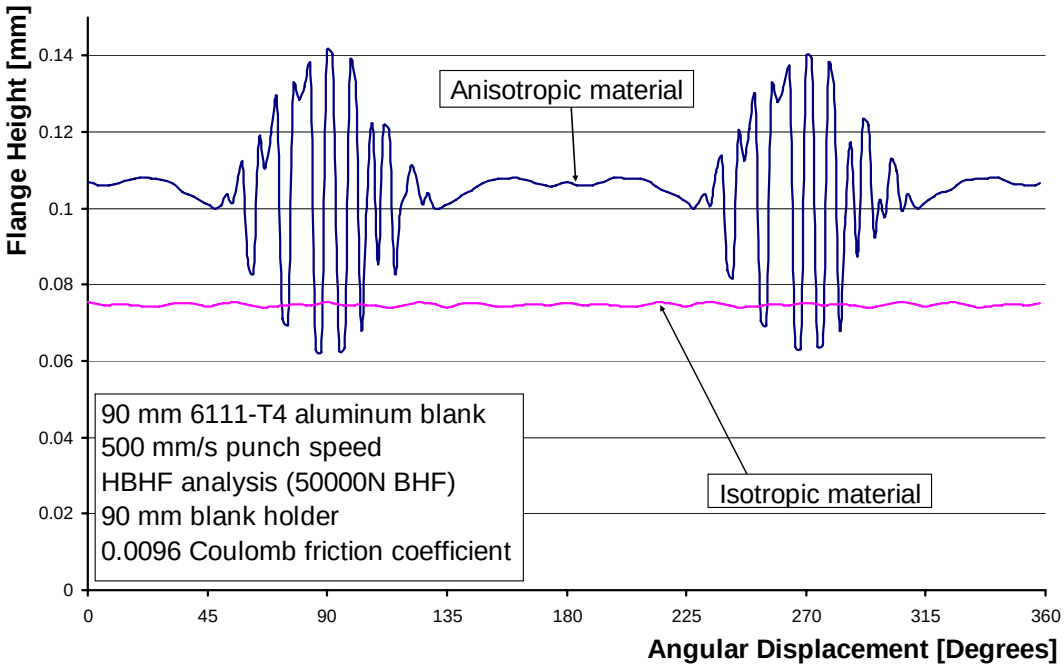

Figure 5.24: Height profiles of anisotropic and isotropic materials

Additionally, the secondary wrinkling is not present for the isotropic analysis, since the thickening of the flange is uniform throughout.

It should be noted that this phenomenon is artificial; in real processes the tools are not completely rigid. Although they are significantly stronger and harder than the deformed bodies, they still deform elastically during the deformation operations. This way, the tools deform slightly over the softer material, 'covering' the material perfectly. To the contrary, the perfectly rigid tools in PAM-STAMP come in poor contact with the deformable body due to its thickness variances. Therefore the determination of wrinkling in FE-analyses of PAM-STAMP is a problematic task. Except for extreme cases, the secondary wrinkles are present for all deep drawing simulations to some extent. For instance in Figure 5.24, the anisotropic case shows secondary wrinkles, whereas the analysis may be considered as successful, since the wrinkling waves are only present in 90° and 270° regions. On the other hand, in Figure 5.18, although the wave amplitudes vary due to secondary wrinkles, the

wrinkling trend is continuous throughout the flange. That part may be considered as failed due to wrinkling.

5.2.2.3 Effect of Blank Holder Forces

Having defined the mechanics of the application of loads in PAM-STAMP, and investigated the weak points of the wrinkling analysis using this software, one can investigate the effects of varying blank holder forces on the outcome of the simulations.

When the blank holder force is decreased beyond 5 kN, wrinkling is observed. The effect of wrinkling to the force requirement is also observable from Figures 5.25 and 5.26. As the *restricting* force of the blank holder diminishes, the punch draws the blank into the die easier, thus the force requirement of the punch decreases with decreasing blank holder force. As the Figures 5.25 and 5.26 imply, with increasing blank holder force, the force requirement of the process increases slightly. Actually the reason of this increase being small is that the friction forces in the systems being very low. If there were larger friction forces between the flange and the blank and/or the blank holder and the blank, the force requirement would increase rapidly. Even it could result in tearing failure.

On the other hand, the form of the force displacement curves for the lowest blank holder force cases (0.5 kN) are interesting. The force requirements of these lowest blank holder load cases are unexpectedly large, owing to two occurrences: Firstly, the decreased slope of the f-d curve between 10 and 20 mm punch stroke is due to severe wrinkling. Since the blank holding loads are insufficient to *hold* the flange, the flange wrinkles up, and friction forces (restricting flow of material and thus increasing the punch force) decrease due to decreased area of the flange in contact with the binder and blank holder. After 20 mm punch stroke, the wrinkled region of the flange starts to be drawn into the die cavity, restricting material flow due to folding of the wrinkles between the punch and the die. After this point on, the punch force increases swiftly.

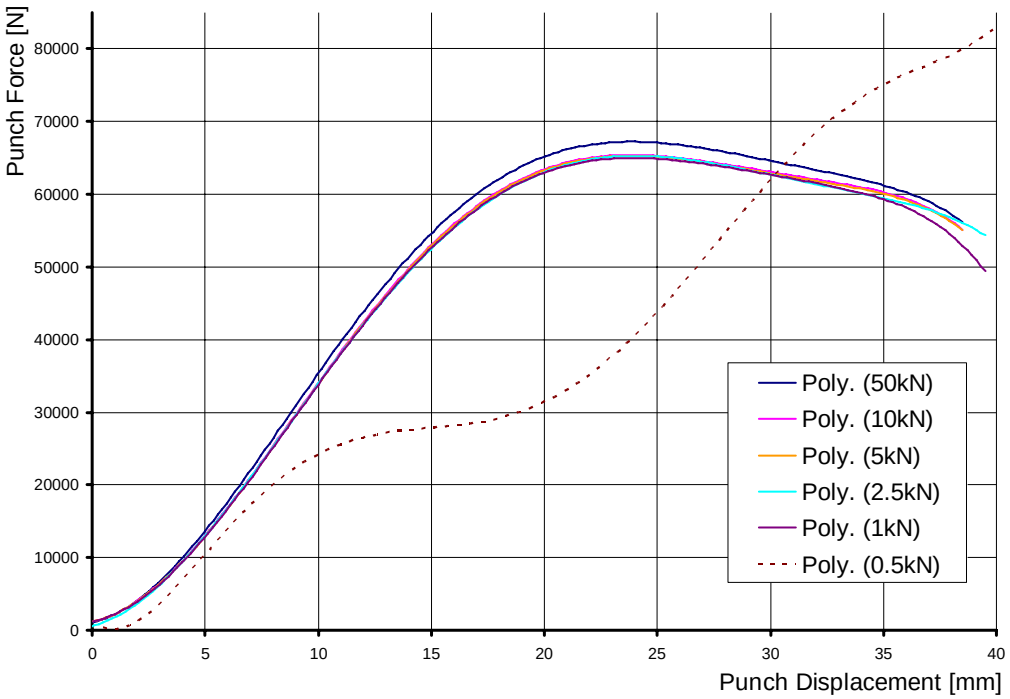

Figure 5.25: Effects of blank holder force on force requirement of the process – aluminum

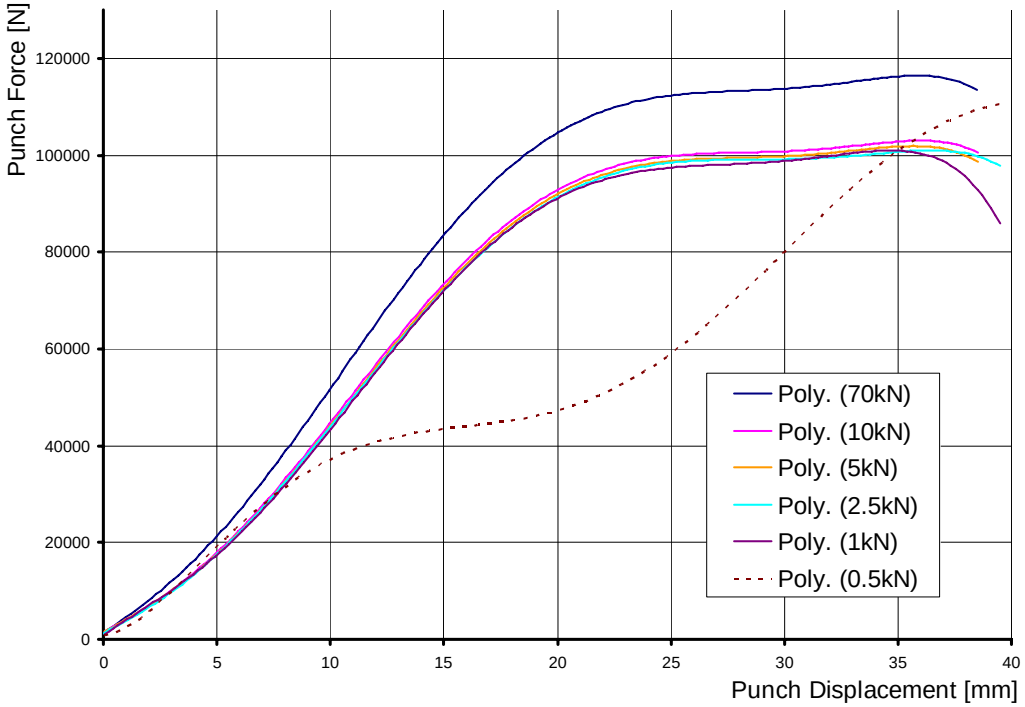

Figure 5.26: Effects of blank holder force on force requirement of the process – steel

As expected, the variation of blank holder forces does not affect computational time (Figure 5.27): The computation times are nearly identical for all aluminum analyses, and the same is true for steel analyses. The difference in the computational times of steel and aluminum arise from the fact that the steel blank has a larger diameter, making the number of elements in steel simulations larger.

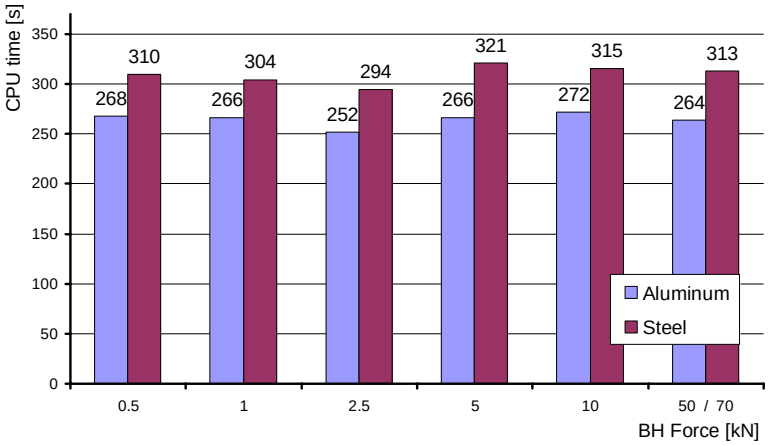

Figure 5.27: CPU times for various blank holder forces

5.2.3 Varying Friction Coefficient

In this section, the effects of Coulomb friction factors upon the result of the analyses are inspected. These friction coefficients are measured by NUMISHEET 2002 Benchmark's material suppliers for the processes. The measured values are in three sets for the two analyses and for the actual benchmark the average of these friction coefficients are suggested. Friction coefficients for lubricated and non-lubricated cases are measured within the material characterizations by friction tests with flat dies. The same lubricant is used in the tests. In this section, three cases where a lubricant is present and one case without lubrication is examined for both materials. Since the non-lubricated case resulted in excessive stretching of the blank, the blank mesh is made finer for that case so that accuracy is not lost due to excessive deformation of blank elements. Therefore there are totally five cases of lubrication conditions to study for both materials (Table 5.4):

Table 5.4: Lubrication conditions for aluminum and steel analyses

Aluminum		Steel	
Friction coefficient (μ)	**Element size**	**Friction coefficient (μ)**	**Element size**
0.0087	5	0.0420	5
0.0096	5	0.0426	5
0.0105	5	0.0439	5
0.1348 (no lubricant)	5	0.1459 (no lubricant)	5
0.1348 (no lubricant)	3	0.1459 (no lubricant)	3
0.1348 (no lubricant)	2	0.1459 (no lubricant)	2

The first three values for both materials are very close to each other; therefore it was expected to have very close results for these cases. On the other hand, the non-lubricated cases gave significantly different results. Therefore, more emphasis is given on them.

It is observed (from Figures 5.28 and 5.29) that the non-lubricated cases result in peaks in the force displacement curve (at nearly 20mm punch stroke) for both aluminum and steel analyses. As stated above, this is due to stretching of the blank under the blank holder – flange region due to high friction. With coarse meshes, excessively deformed elements cause a loss in simulation accuracy. Applying finer meshes before simulation or utilizing remeshing (adaptive mesh) during simulation are usually solutions to reduce distorted elements in the simulations. Remeshing will be considered later. Therefore, to effectively inspect the stretched region finer meshes are utilized. In reality, this stretching must be carefully controlled; else there will be failures due to excessive thinning. To correctly determine whether the workpiece will fail under the non-lubricated case (or in any other case) the mesh has to be as fine as possible. However, the mesh quality affects computation time directly. The user shall make a trade-off between accuracy and speed. The default mesh size (which is 5 mm), is sufficient for the prediction of failure here; much coarser meshes will not give as accurate predictions as finer meshes, since they fail to represent the details of the geometry after deformations.

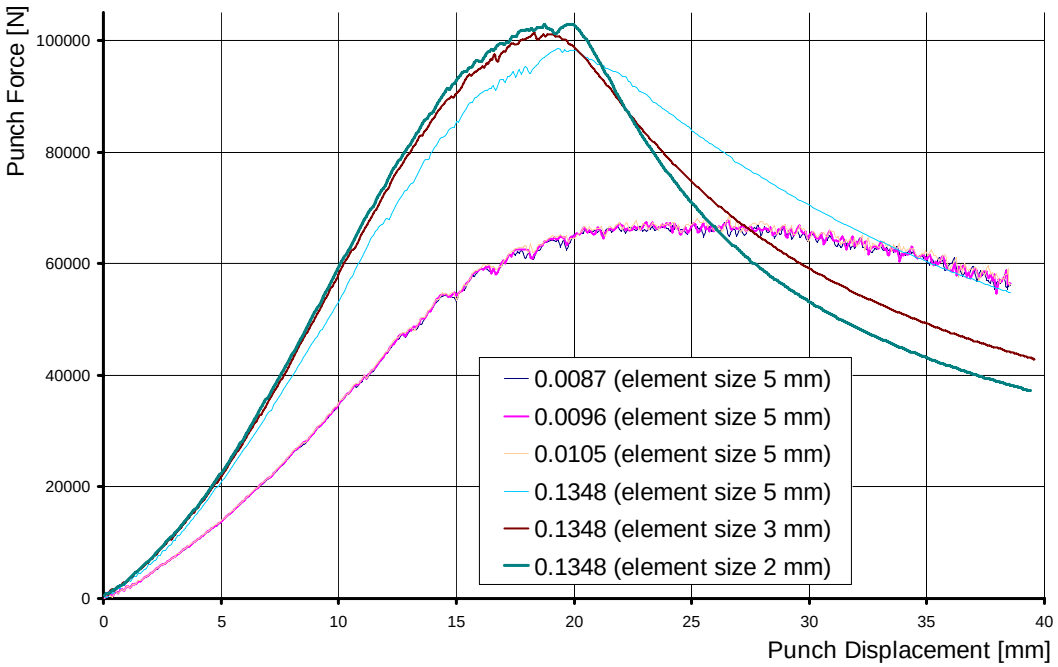

Figure 5.28: Effect of friction coefficient upon force requirement of the process – aluminum

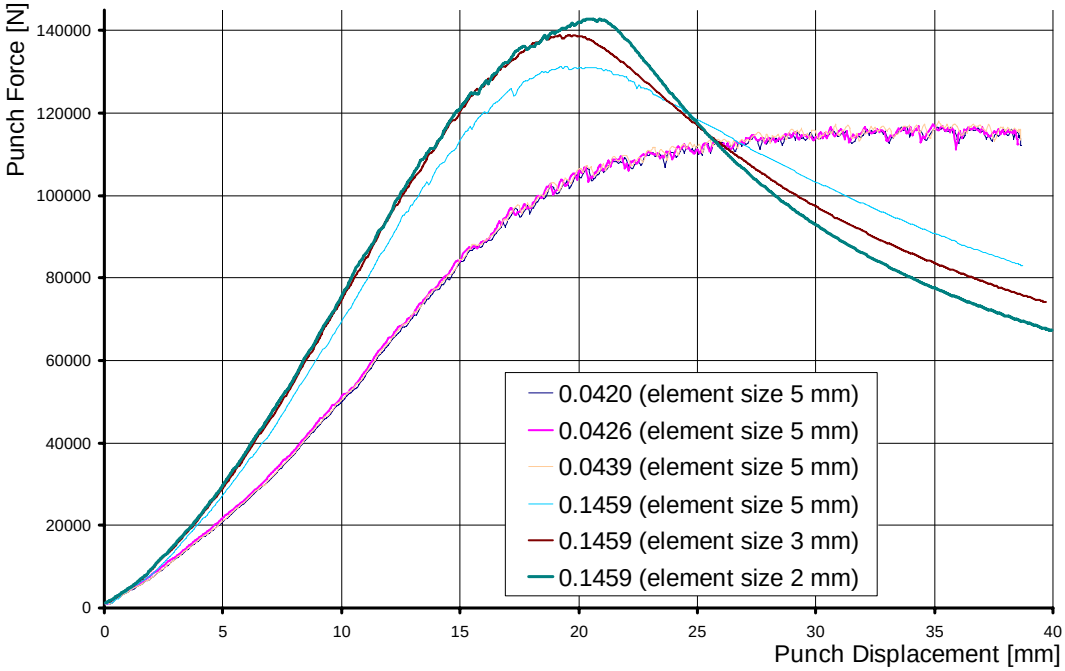

Figure 5.29: Effect of friction coefficient upon force requirement of the process – steel

Disregarding the effect of increased number of elements (due to the finer meshes in the last two non-lubricated cases), it is clear that the variation of friction has no direct effect on computation time (Figure 5.30). On the other hand, it is logical that increased number of elements increases the critical time step for the finite element analysis, thus making the computations longer. The variations in results obtained from the simulations using maximum element sizes of 5 mm and 3 mm is obvious from Figures 5.28 and 5.29. However, the ones for element sizes of 3 mm and 2 mm are very similar to each other, whereas the computation time (Figure 5.30) increases drastically for the finer meshed analyses. This can be concluded as maximum element size of 3 mm is sufficient for reliable results even there is excessive deformation in the process due to the non-lubricated tools.

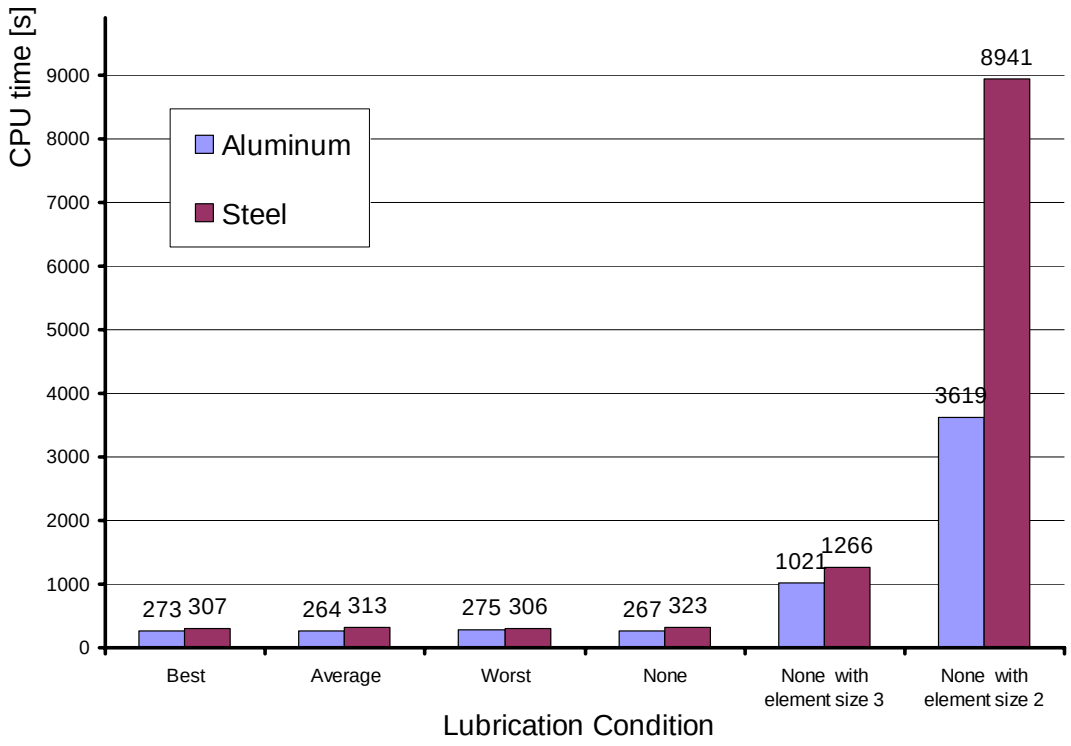

Figure 5.30: Effects of lubrication on CPU time

5.2.4 Varying Blank Element Size

As explained above, the increasing number of elements will result in increasing computation time. On the other hand there are certain advantages of finer meshes:

- Finer meshes will allow the user to obtain more precise results from any analysis.
- Not only the mesh structures of deformable bodies are important; as it is discussed briefly in Section 5.2.2.1, the mesh structure of the rigid tools must also be carefully determined.
- Inconsistent mesh structures will result in poor results due to contact problems.
- Moreover, when the meshes are of poor quality, unacceptable penetrations between the tool and the deformable bodies may occur. Therefore, the trade-off of time and accuracy must be carefully determined for any FE-simulation. An example is given in the following figure (Figure 5.31):

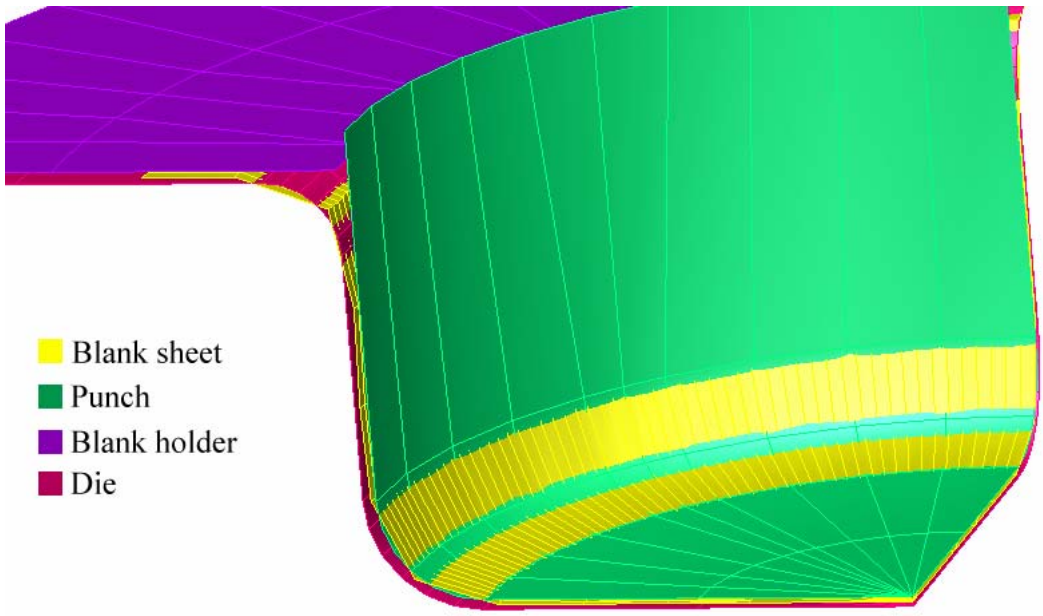

Figure 5.31: Penetration due to coarse blank mesh

Since the blank mesh is not fine enough to 'cover' the punch fillet, the blank penetrated the punch at the punch corners (Figure 5.31). This occurrence is unrealistic and must be avoided. Either the initial mesh must be made finer, or refinement must be applied to the blank during the simulation.

In this section, the effects of blank element size and blank mesh shape on the accuracy of the analysis will be inspected. Blank element size gives the average element size in mm. It is the average edge length of square elements.

In this section, four identical simulations with quadratic elements having four different edge lengths (7, 5, 3 and 2 mm) were performed to determine the trade-off of the accuracy and time (the tool element sizes are kept constant at 5mm, which seemed accurate enough without causing any penetration).

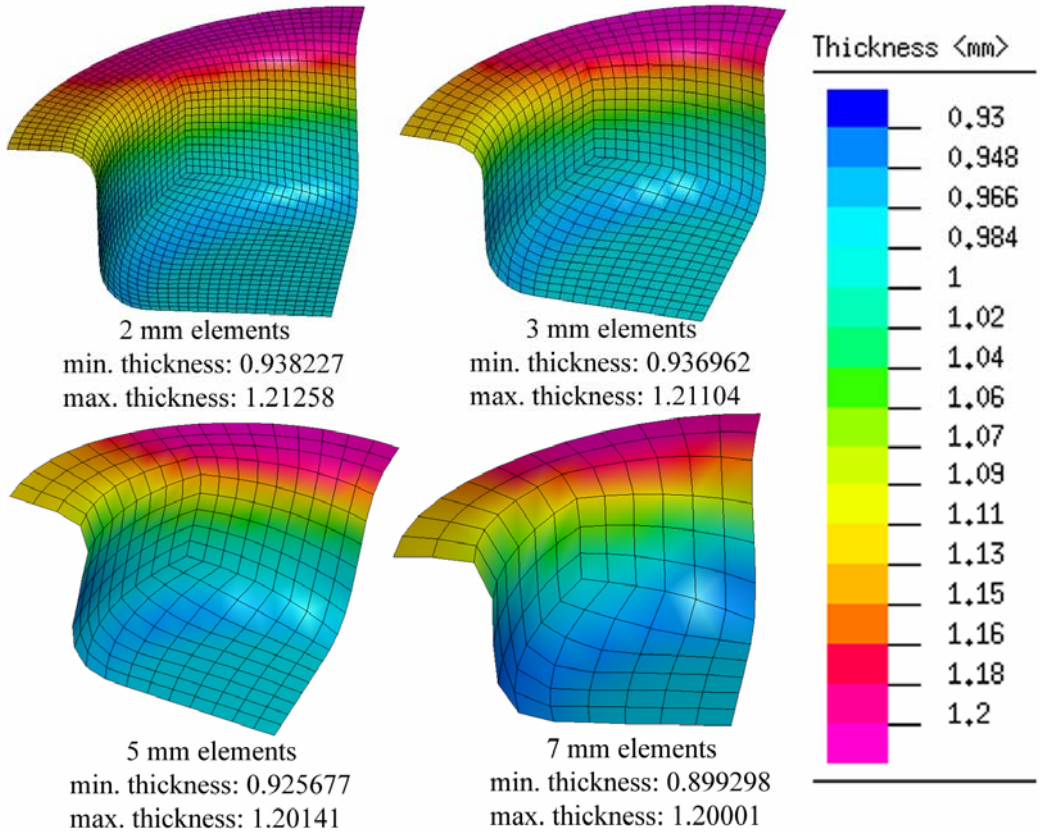

Figure 5.32: Thickness contours for various element sizes

Figure 5.32 shows the thickness contours of HBHF aluminum simulations with varying element sizes. It is known that the finer mesh will result in more accurate solutions. The results of simulations with 2 mm and 3 mm element sizes do not differ greatly, whereas as the element size is increased further (as in simulations with 5 and 7 mm elements), the result accuracy decreases. Although the simulation with element size 5 mm can represent the part geometry successfully, as far as the accuracy is concerned, the finer meshes are more preferable. The coarsest meshed-simulation has results in poor quality in all aspects. The same findings are observed for steel analyses also, and the force requirements of the processes give the same trend (Figures 5.33 and 5.34).

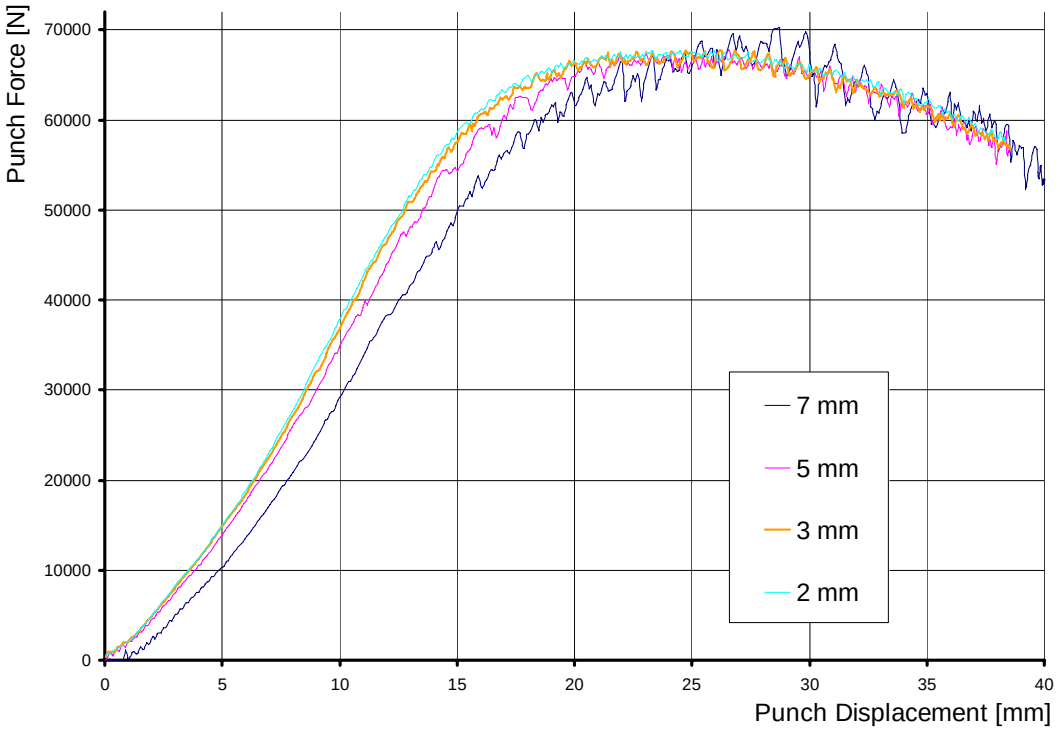

Figure 5.33: Effect of element size – aluminum

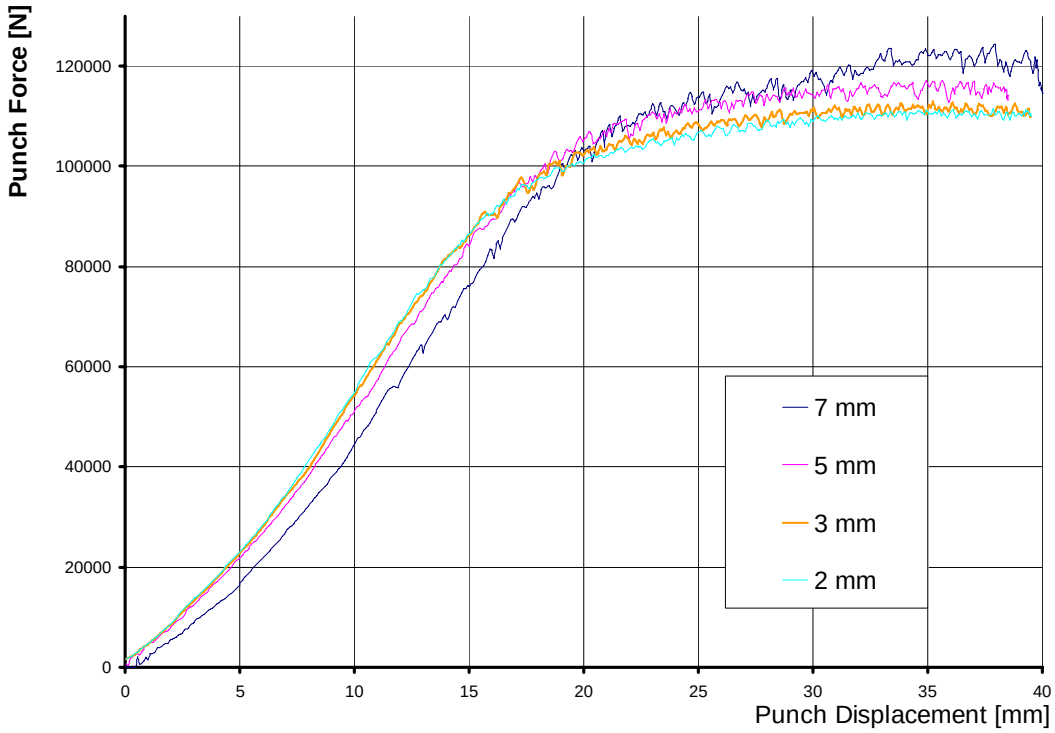

Figure 5.34: Effect of element size – steel

Figures 5.33 and 5.34 show that the force – displacement curves belonging to simulations with element size of 2 mm and 3 mm are almost identical. The usage of 2 mm elements has improved the result, yet numerical simulations are feasible if and only if they are accurate enough and cost efficient. The question about the optimum element size is revealed in Figure 5.35 that the cost paid is significantly high for that amount of improvement in the results.

Similar to the punch speed case, increasing the accuracy of the analysis by decreasing the element size costs a lot of computation time, whereas the increase in accuracy is not significant. Therefore too small element sizes are not a must for this simulation. On the other hand too large element sizes (extremely coarse meshes) will result in poor accuracy, or the FE-package may fail to give a solution since the required time step cannot be achieved (Eq. 4.31). Having much smaller CPU-time with an acceptable accuracy, the element size of 3 mm is most suitable for the present simulation. However, different processes with different part sizes and shapes will require different average element sizes of course.

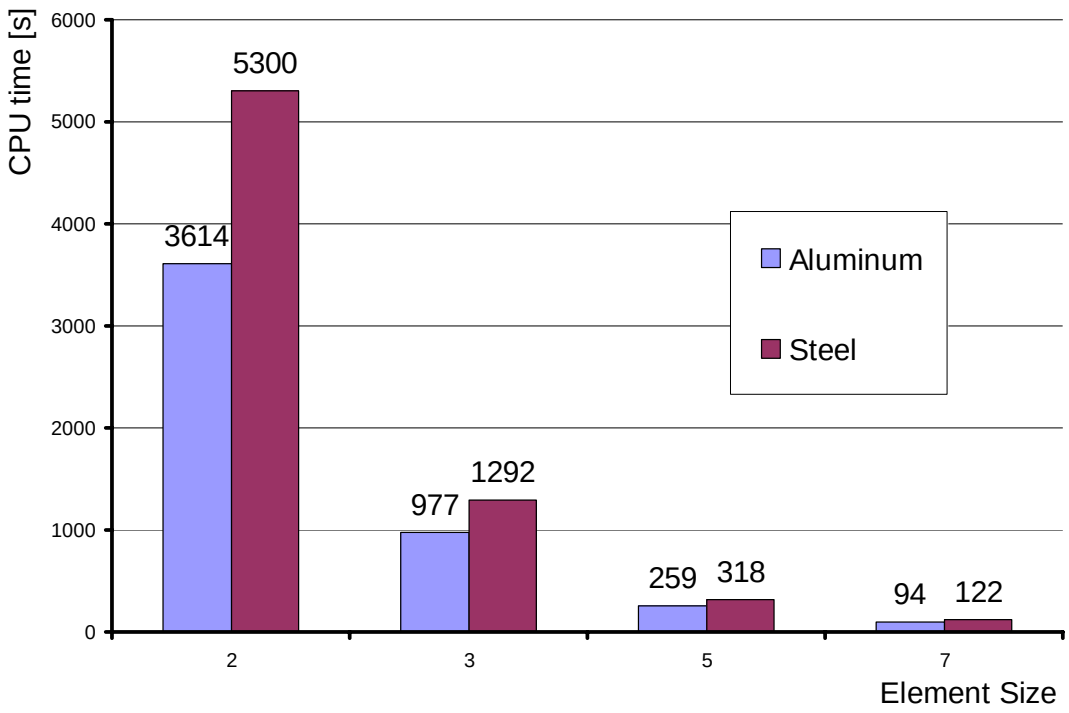

Figure 5.35: Effect of element size on CPU time

5.2.5 Varying Mesh Topology

Beside the element size, the mesh topology is also important in FE-analyses. Mesh structures of each body in the simulations should be a good representation of their actual geometry and they should be compatible to each other. Seemingly good meshes may result in poor accuracy after heavy deformation. It is known that the quality of the analyses depends on the quality of the elements; therefore, it is always suggested to conduct trial analyses to observe the deformed mesh shape to see whether the initial mesh structure is acceptable or not. Of course, adaptive meshing can also be utilized to overcome such problems, but sometimes it is avoided to save computational time.

In the following pages the simulation results of two different FE-meshes will be compared. The aluminum material with the standard NUMISHEET 2002 benchmark process parameters (HBHF and LBHF, 500 mm/s punch speed, 0.0096 friction coefficient) will be simulated. Figure 5.36 gives two blank mesh topologies

for a blank with 90 mm radius and an average element size of 2 mm. Mesh A has a homogeneous distribution of elements at the outer rim of the blank, whereas mesh B has uniform elements throughout the surface but the outer rim. Mesh B has triangular elements at the rim. It is clear that any other mesh topology can also be utilized, but within this study, the reliability of these two topologies are investigated, since Mesh A is obtained from PAM-STAMP 2000 and Mesh B is obtained from PAM-STAMP 2G.

Mesh A can cause a numerical anisotropy at the four regions within its surface, where the elements are smaller, whereas mesh B may show strange behavior like unexpected, unrealistic thickness and/or strain peaks or drops at the outer rim, where triangular elements are present.

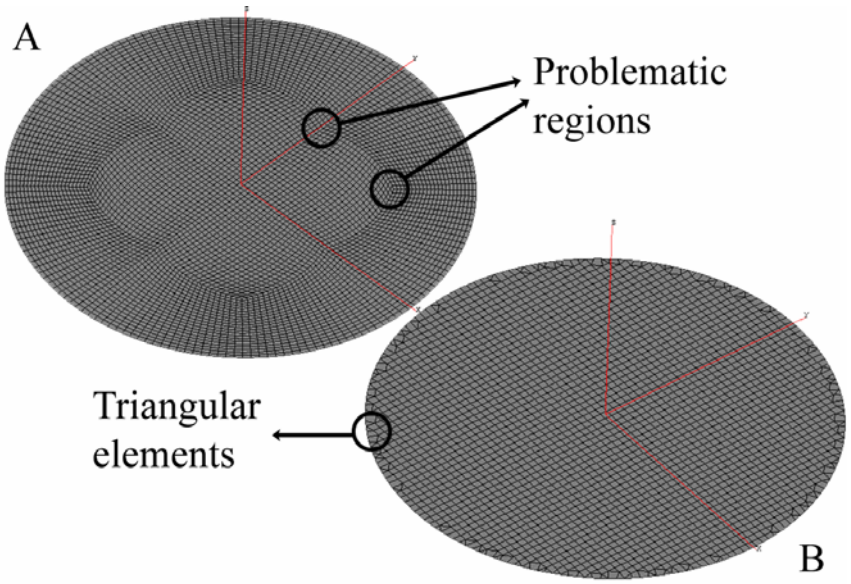

Figure 5.36: Two different mesh topologies (Top left: structure A, bottom right: structure B)

In PAM-STAMP the equivalent plastic strain is denoted as the membrane plastic strain. The following figures (Figure 5.37 and 5.38) give the plastic strain contours for mesh structures A and B, calculated at the mid-plane of the deformable body for HBHF an LBHF aluminum analyses respectively.

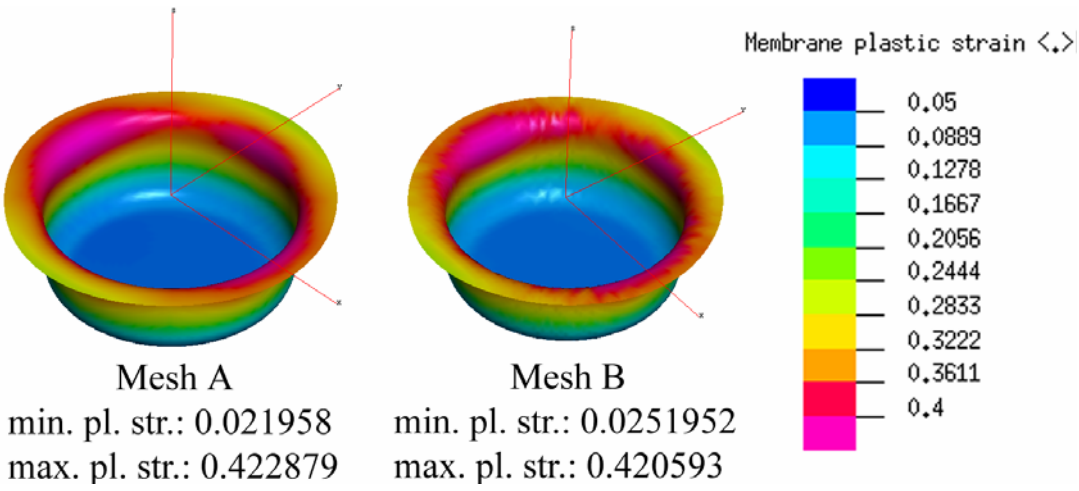

Figure 5.37: HBHF aluminum analysis

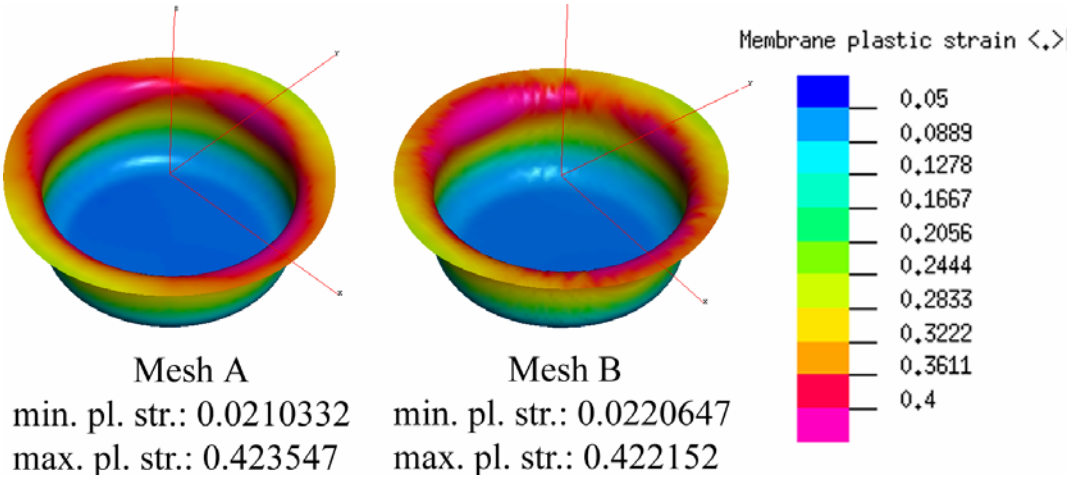

Figure 5.38: LBHF aluminum analysis

From Figures 5.37 and 5.38 it seen that for shape B, the minimum strains are higher and the maximum strains are lower for both HBHF and LBHF cases, compared to structure A. This same result will be obtained for the steel case as well, but before that let us observe the force displacement relationships for the aluminum analyses. Figures 5.39 and 5.40 show that the force requirement of the processes are slightly higher for shape B, compared to shape A. Therefore, from these findings it can be concluded that shape B behaves stiffer.

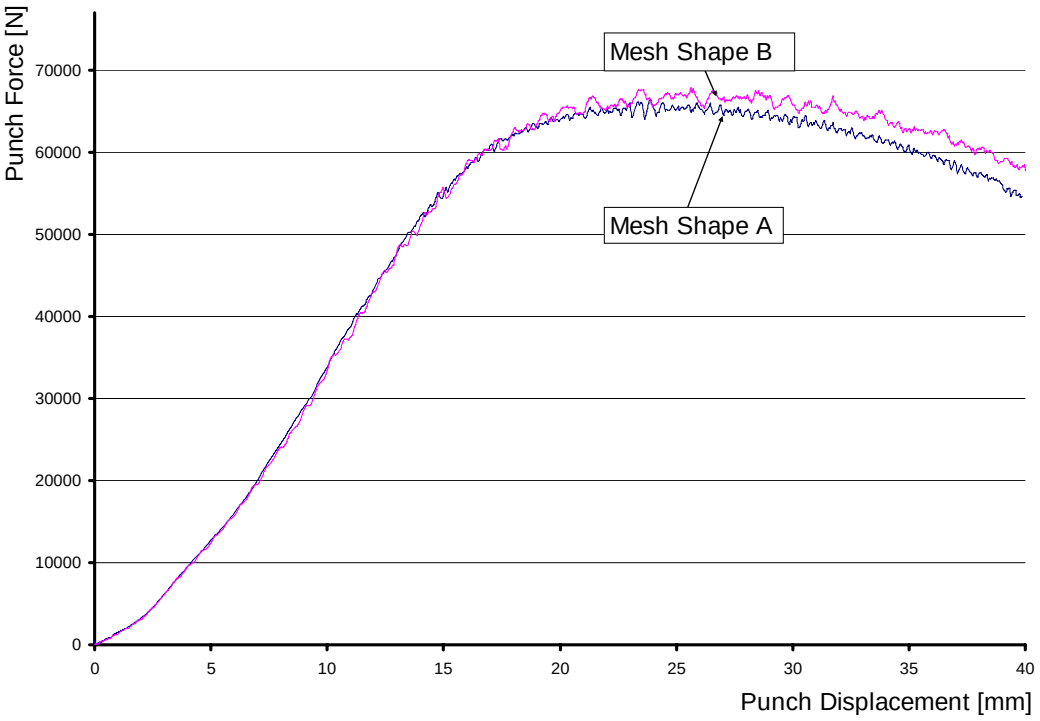

Figure 5.39: Effect of mesh blank structure on the force – displacement relationships for HBHF aluminum analysis

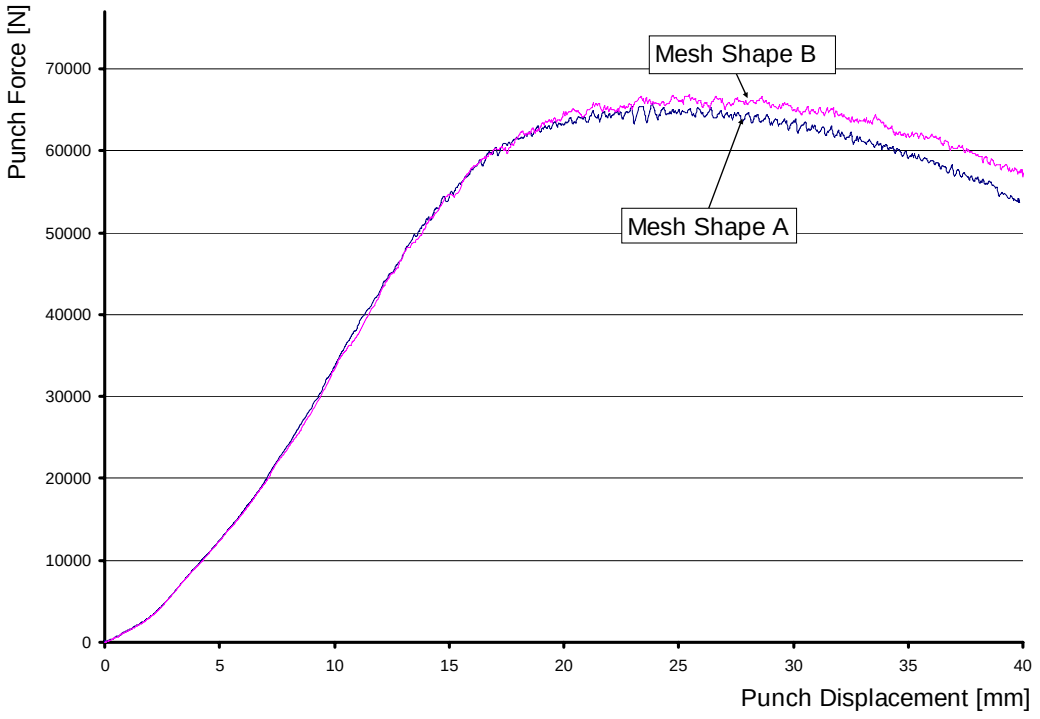

Figure 5.40: Effect of mesh blank structure on the force – displacement relationships for LBHF aluminum analysis

This conclusion is reached by inspecting the maximum and minimum strains and the force-displacement relationships from Figures 5.37 to 5.40. However, these observations do not point out a better mesh clearly. Further analyses (and with finer meshes) shall be conducted to obtain more reliable information about this subject. Although mesh shape B seemingly has a good mesh quality in the middle, the outermost elements of the mesh are not preferable since they can cause problems when (for example) inspecting wrinkling phenomena or the outer profile of the deformed shape. On the other hand, if the shapes of the force-displacement graphs are closely inspected, one can say that the results of shape A is more preferable since its curves look smoother, but this judgement is based on pure intuition, and it has no physical backup.

Again, the similar occurrences are present in steel's analyses also:

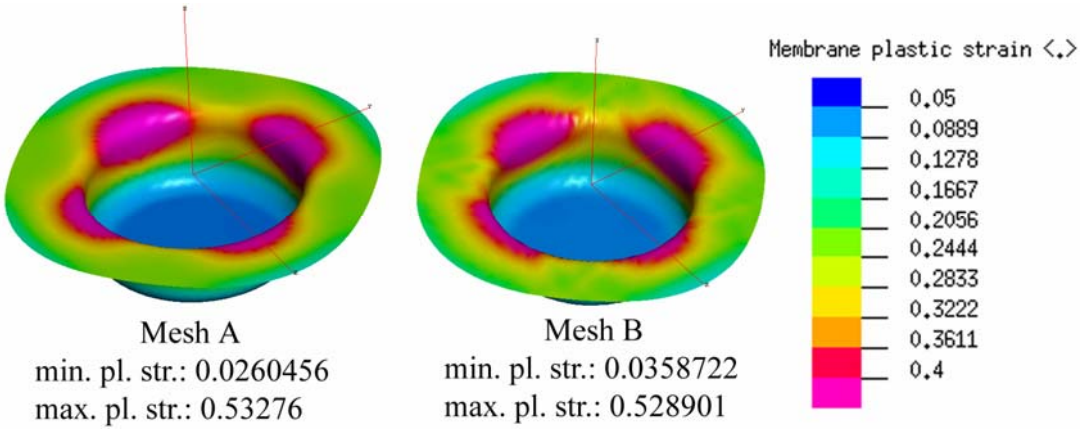

Figure 5.41: HBHF steel analysis

Again, the shape B results in a *tighter* strain distribution (Figure 5.41 and 5.42) with a *rougher* strain contour, and the force requirements for the both mesh structures as expected: the f-d curves for the mesh structure B lie above that of mesh structure A (Figure 5.43 and 5.44). These findings are in agreement with the previous ones: Mesh structure B behaves stiffer, independent of the material used.

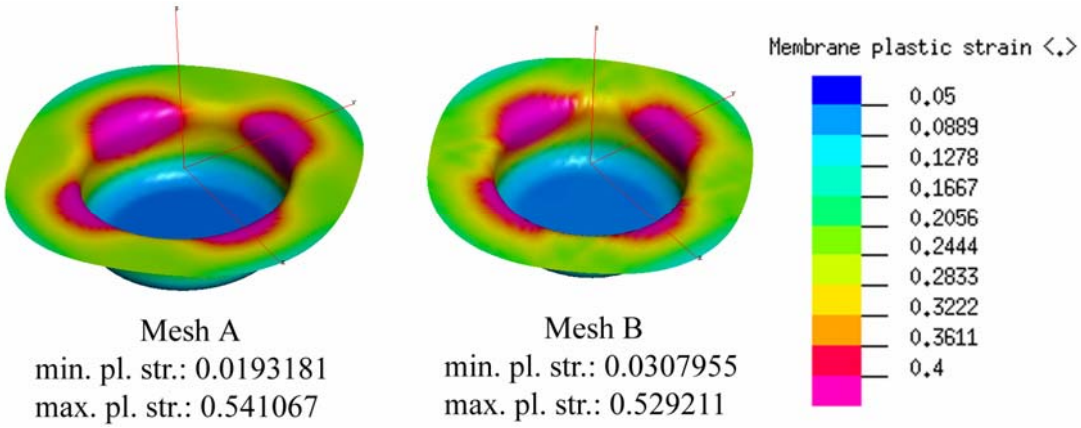

Figure 5.42: LBHF steel analysis

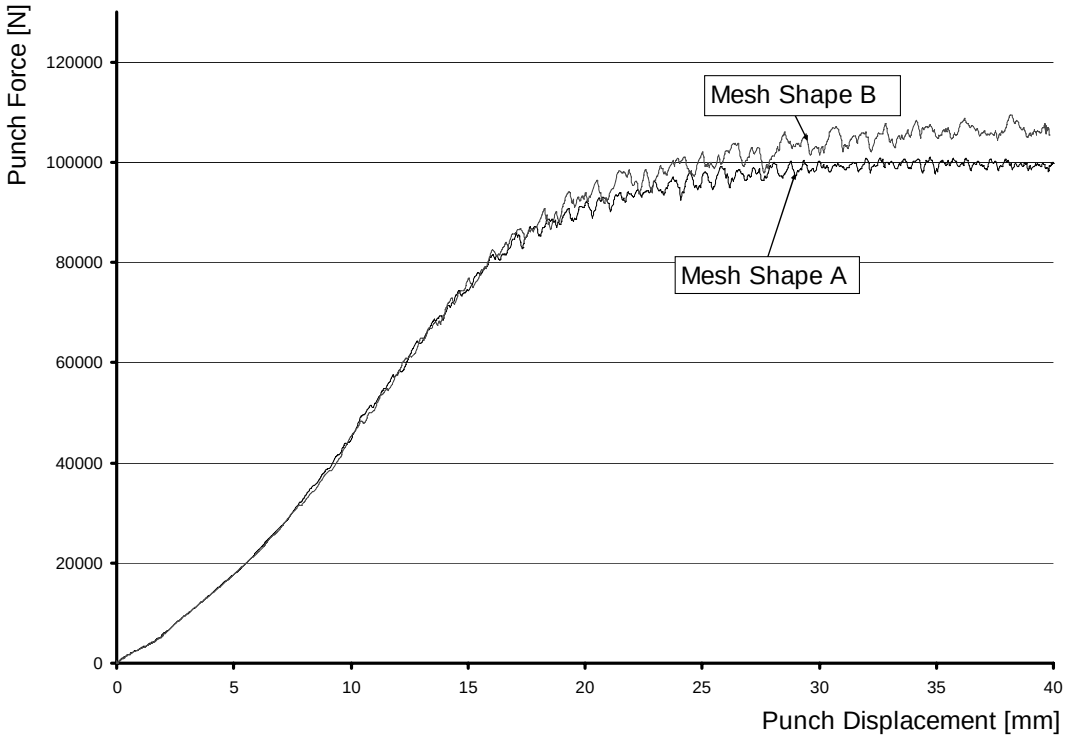

Figure 5.43: Effect of blank mesh structure on the force – displacement relationships for HBHF steel analysis

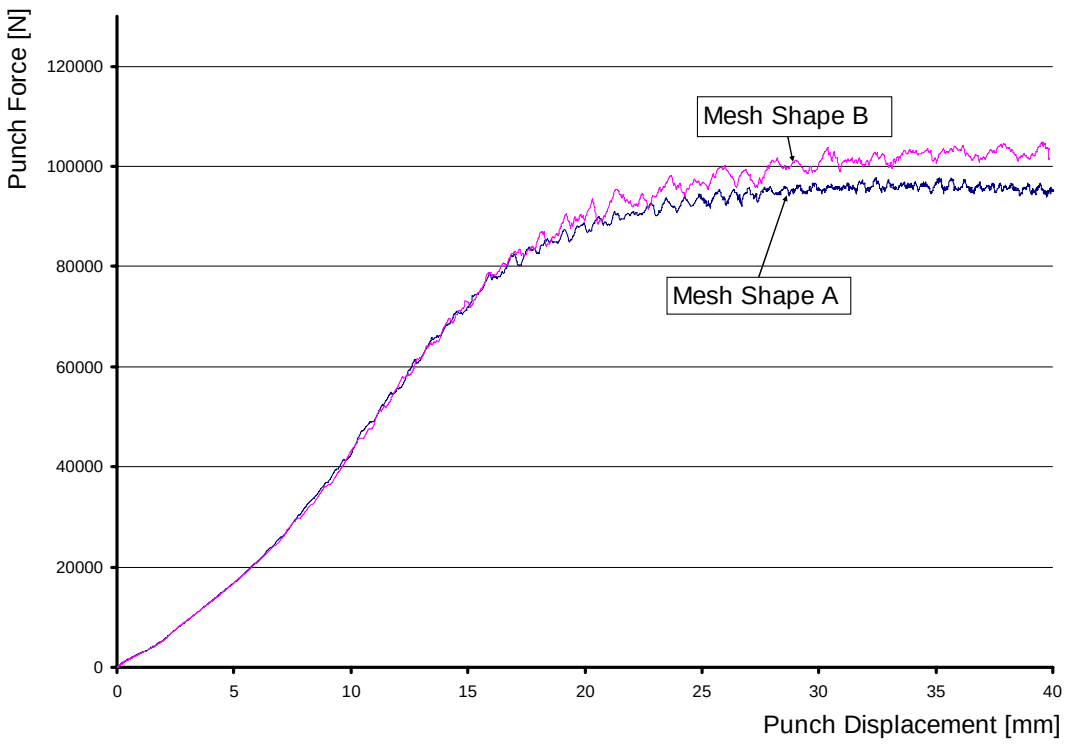

Figure 5.44: Effect of blank mesh structure on the force – displacement relationships for LBHF steel analysis

These observations point out the fact that, besides the numerical parameters and process parameters, the quality of the analyzed mesh structures is also important for a successful simulation.

5.2.6 Varying Time Step Scale Factor

In explicit FEM, the nonlinear equations governing the state of the system are solved incrementally. To obtain a stable solution, the increments must have a limit maximum time step value. If a larger time step value is forced to the program, the algorithm fails. This limit value depends on the element sizes and the material properties associated to these elements. It can be estimated for any analysis by a simple relationship (Eq. 4.31). The smallest of all element time steps is the global time step value. This value will vary during the numerical analysis due to element distortions, remeshing and changes in material properties.

To ensure the stability of the solution, PAM-STAMP reduces the global time step by a scale factor. This scale factor acts like a safety factor to guarantee a solution. The global time step is the smallest of all element time steps. It is used in the overall analysis. By default, PAM-STAMP takes the time step scale factor as 0.9. It is clear that the limiting time step would have the respective time step scale factor of 1. One can play with this value "swiften up" the analysis by making the time steps larger (thus decreasing the analysis time with the risk of obtaining a problematic solution) or "slow down" the analysis by making the time steps smaller (thus increasing accuracy). However, choosing large time step scale factors will make the program fail in many ways.

In this section six different time step scale factors are used for simulation to inspect the effects of time steps on the well-being of the analysis. 0.5, 0.7, 0.9, 1, 1.1 and 1.2. For aluminum and steel only one set of analyses are conducted, where the high blank holding forces are utilized.

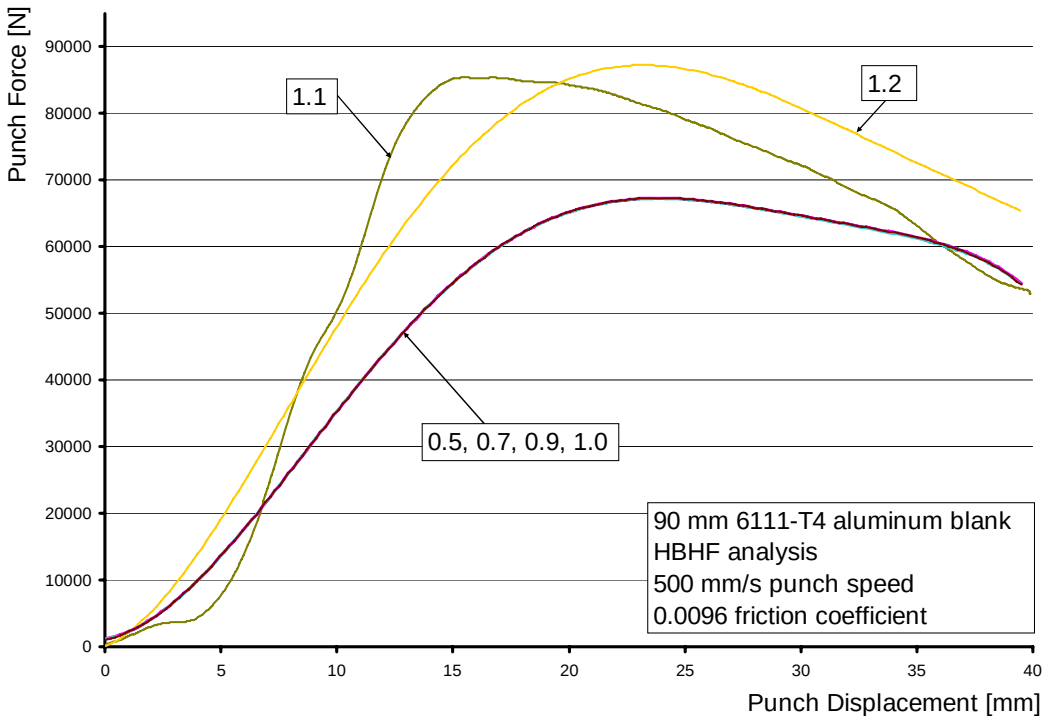

Figure 5.45: Effect of time step scale factor – aluminum

The results for time step scale factors 0.5, 0.7, 0.9 and 1.0 are exactly equal in terms of the force displacement curves of the punch, since they fall on top of each other for both the aluminum and steel material's analyses (Figure 5.45 and 5.47). This means that the lower (and default) time steps give exactly the same results. However the CPU times are be different for these simulations. It can be expected that the results' accuracy will increase as the time step scale factor is decreased. This is because that the time step itself is lowered with smaller time step scale factors, thus increasing the number of FE-iterations.

On the other hand larger scale factors will result in strange behaviors of the program. For instance at 1.2 the solver gives erratic results, proving that stable solutions cannot be achieved at this high time step value (Figure 5.46).

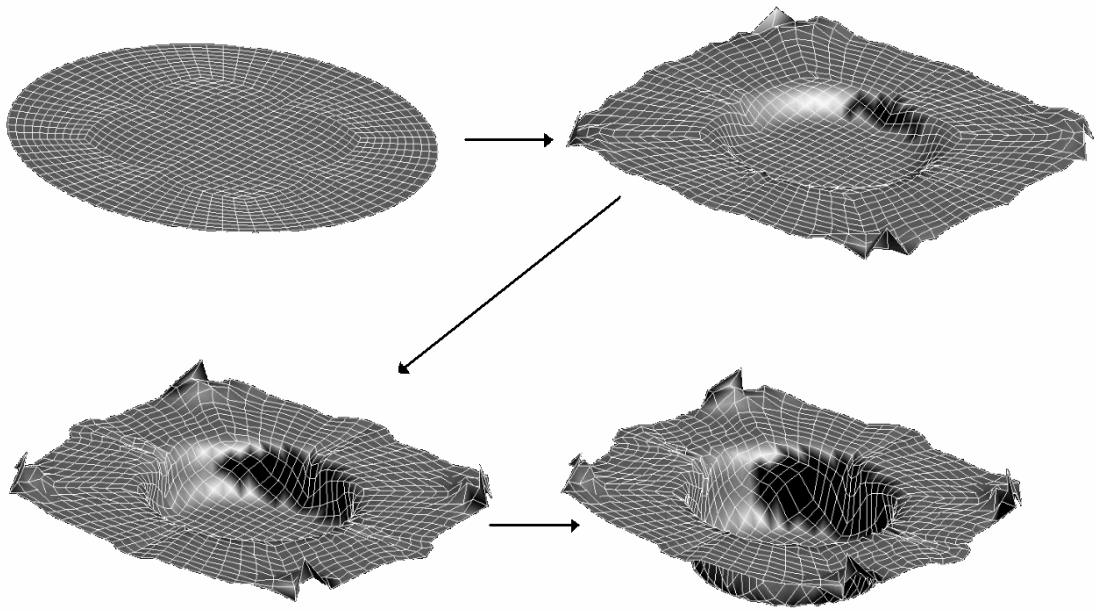

Figure 5.46: Strange distortion of the blank

The similar occurrences are also encountered for steel. One can say that the time step scale factor must be kept well under 1.0 to obtain an acceptable result. Here the default value of 0.9 is satisfactory. If extra precision is required this value can be

reduced, but their effect is not significant in the force requirement of the processes. This occurrence was expected, since the punch speed also did not affect the force requirement of the process significantly under a certain level. It is known that the time step is dependent on punch speed (Eq. 4.31). Since the time step scale factor directly controls the time step, increasing the time step scale factor affects the simulation in a similar way like reducing the tool speed.

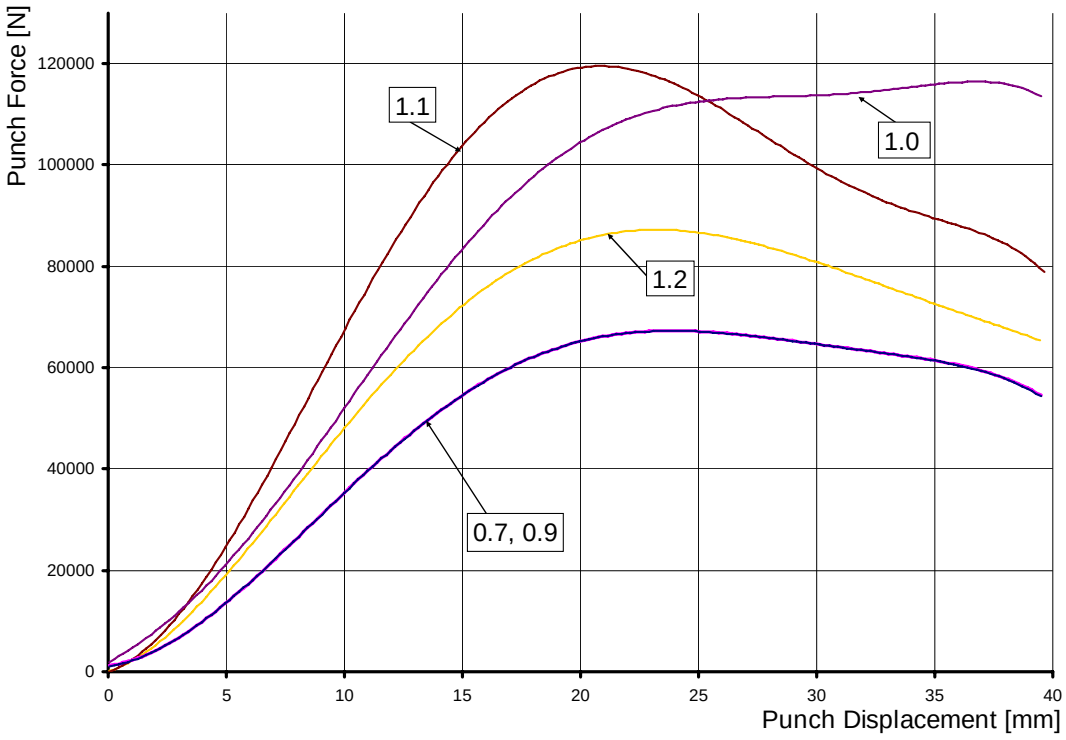

Figure 5.47: Effect of time step scale factor – steel

On the other hand, although it is expected that high time step scale factors will "boost" the analysis, where a stable solution cannot be achieved the analysis will take longer at very high time step scale factors. At these cases there will be either no output from the program or a strange result indicating that the analysis did not converge to an acceptable result. This can be seen in the next figure. At 1.1 level, for aluminum the analysis takes unusually long whereas for steel the analysis gives an error when run (Figure 5.48).

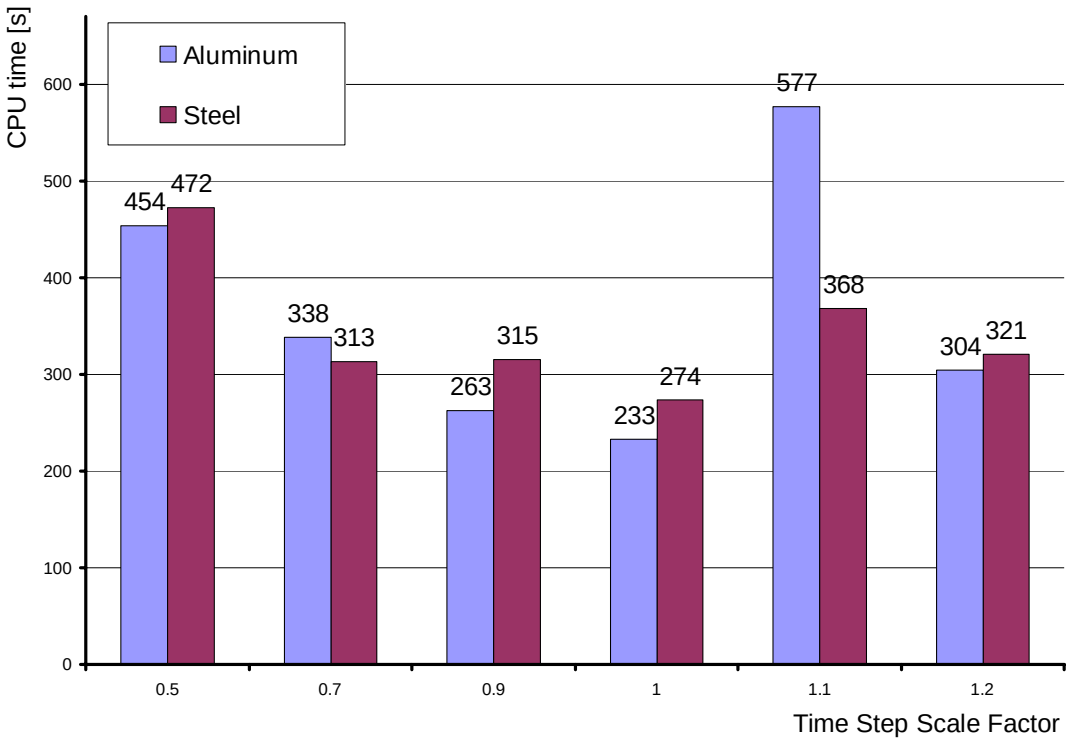

Figure 5.48: Effect of time step scale factor on CPU time

5.2.7 Adaptive Meshing

The adaptive meshing automatically refines the mesh of a deformable body, where and when certain conditions exist. Usually, FE-codes use two criteria to determine whether there should be refinement or not: angle criterion and geometrical criterion.

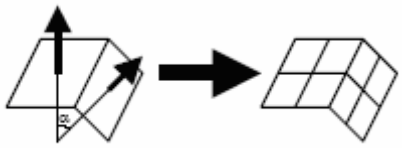

Figure 5.49: The angle criterion (PAM-STAMP 2G user manual)

In the angle criterion (Figure 5.49), solver refines an element when the variation of the angle between its normal and that of one of its neighbor elements exceeds a certain limit angle (generally 10°). This criterion is also useful for the detection of wrinkling. On the other hand, the geometrical criterion (Figure 5.50) adapts the density of the mesh according to the curvature of the tool segments close to the deformable body.

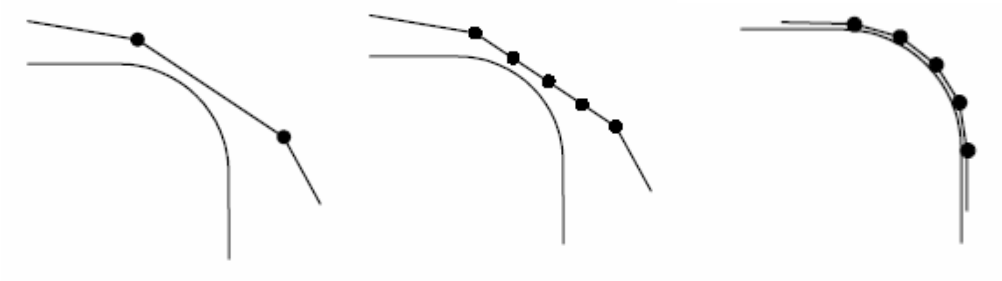

Figure 5.50: The geometrical criterion

This criterion usually enables a more accurate calculation of the stress field. It should be activated especially when springback results are required.

The assessment of adaptive meshing is done by performing six identical simulations by varying initial element sizes and refinement levels (Table 5.5). The simulations having adaptive meshing option activated, use both angle and geometrical criteria. According to these criteria, elements refined and level of refinement in the mesh are shown in Figure 5.51. Refinement is done by splitting the element into four new elements that have approximately half of the initial element size.

Table 5.5: Six successive simulations for the assessment of adaptive meshing

	Element Size (Initial) [mm]	Refinement Level	Element Size (Final) [mm]
Simulation 1	5	2	2.5
Simulation 2	10	2	5
Simulation 3	5	*no refinement*	5
Simulation 4	10	*no refinement*	10
Simulation 5	10	3	2.5
Simulation 6	2.5	*no refinement*	2.5

Table 5.5 shows that in three simulations refinement is applied (simulations 1, 2 and 5), and three simulations are without refinement (simulations 3, 4 and 6). Refinement is required where element distortions during deformation are greatest. Figure 5.51 shows the regions of refinement. As expected, the refinement focuses on the cup walls as seen in Figure 5.51, since the heaviest element distortions are present at that region.

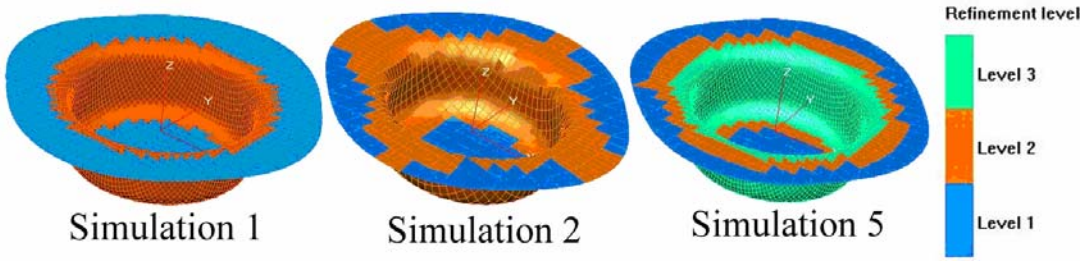

Figure 5.51: Refinement levels

Adaptive meshing changes the element size and thus, reduces the time step. The effects of element size and time step on simulation results were considered in Sections 5.2.4 and 5.2.6 respectively. It is stated before that although finer meshes result in more accurate solutions, the CPU time increases drastically as the element size decreases. In adaptive meshing, instead of doing the whole simulation with a fine mesh, the simulation is initiated with coarse elements, where the computations

are less critical and then they are split into finer element to compensate the accuracy requirements whenever it is needed (checked by the two criteria). For that reason, adaptive meshing is an elegant way to balance the accuracy with the cost of computation. However, the success of adaptive meshing depends on the intelligence of the refinement algorithm used by the solver.

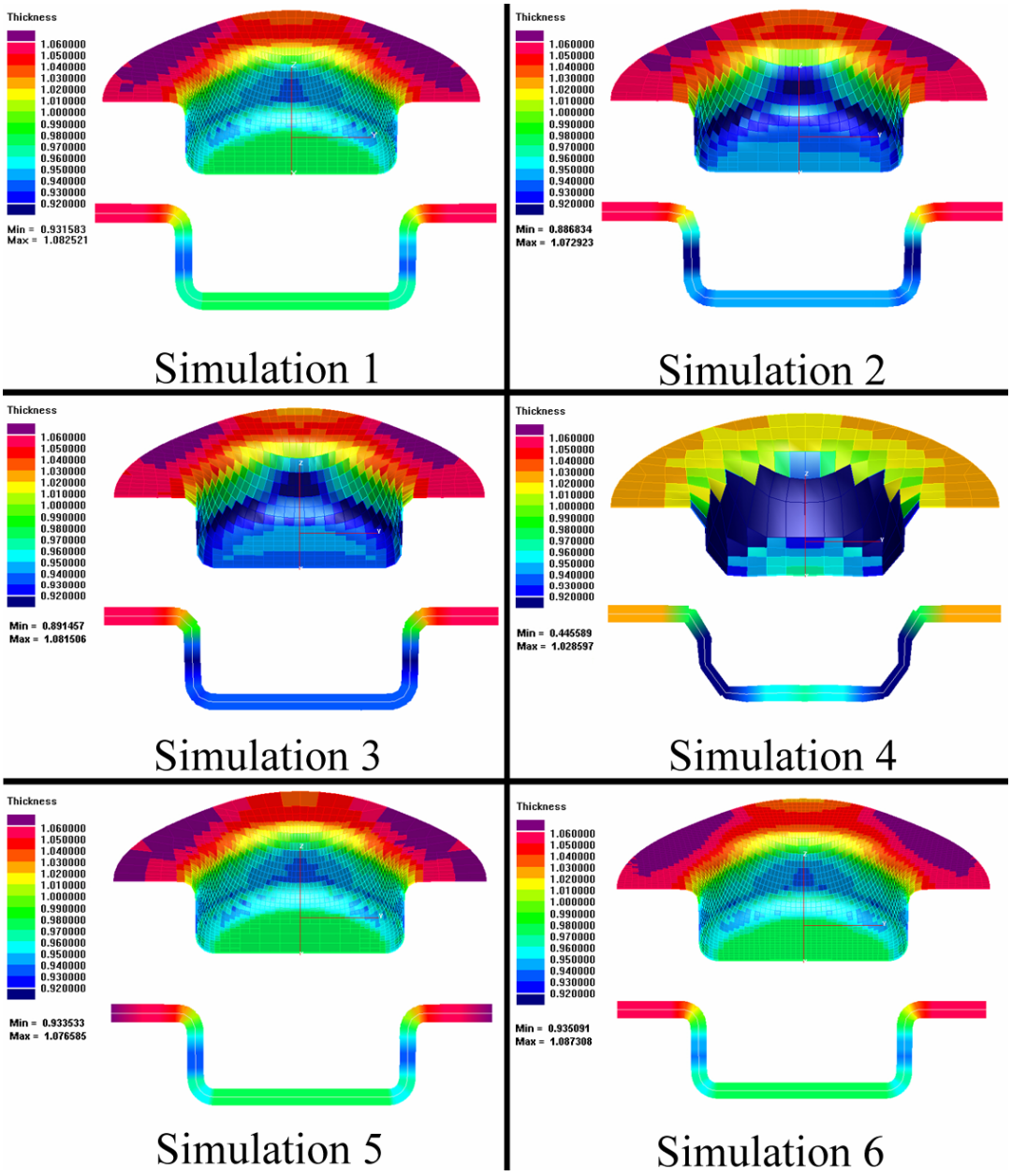

Figure 5.52: Thickness contours for refinement simulations

Figure 5.52 shows the thickness contours and minimum and maximum thicknesses of each simulation whose meshing properties are given in Table 5.5. At the final stage, simulations 1, 5 and 6 have approximately same minimum element size (2.5 mm).

Inspection of the thickness contours in Figure 5.52 shows that although six simulations with different initial element sizes and refinement levels are concerned throughout the assessment, the results can be classified into three groups. Independent from the initial element sizes, the results of analyses having the same final element sizes are compatible to each other form groups.

Simulation 4 belongs to the first group with final element size of 10 mm (Table 5.5). Its initial element size is also 10 mm and no refinement is used through the simulation. Figure 5.52 shows that 10 mm as an initial element size is unacceptable for this analysis and the results obtained are invalid. For that reason, other results of simulation 4 will not be considered further and they are excluded from assessment.

Simulation 2 and 3 form the second group having final element size of 5 mm (table 5.5). Although simulation 2 has initial element size of 10 mm like the simulation 4 does, the results are acceptable since after adaptive meshing, smaller elements (which preserve simulation accuracy upon deformation) are created. Compared with the simulation 2, whose initial and final element sizes are approximately 5 mm, the result of simulation 3 are satisfying. The thickness contour curves (Figure 5.53) and the punch force – displacement curves (Figure 5.54) of both simulations are compatible to each other. The only difference between two simulations is the CPU time spent. Simulation 3 predicts the same result in a slightly longer time than the simulation 2, where adaptive meshing was utilized (Figure 5.55).

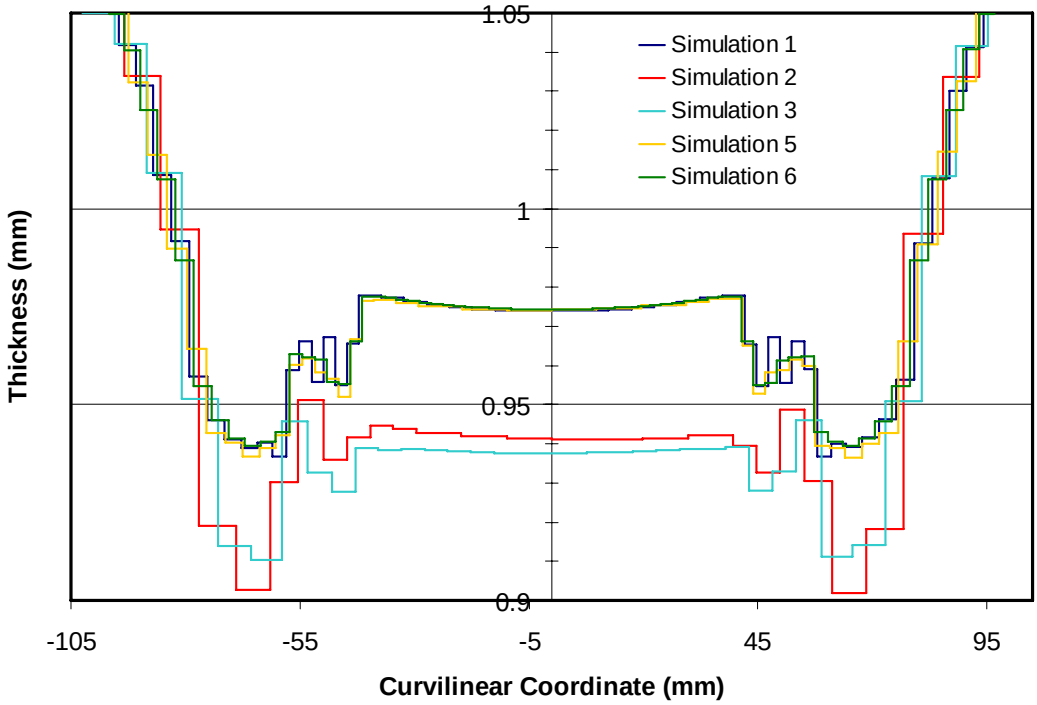

Figure 5.53: Thickness distribution of each simulation along the curvilinear coordinate on YZ-plane

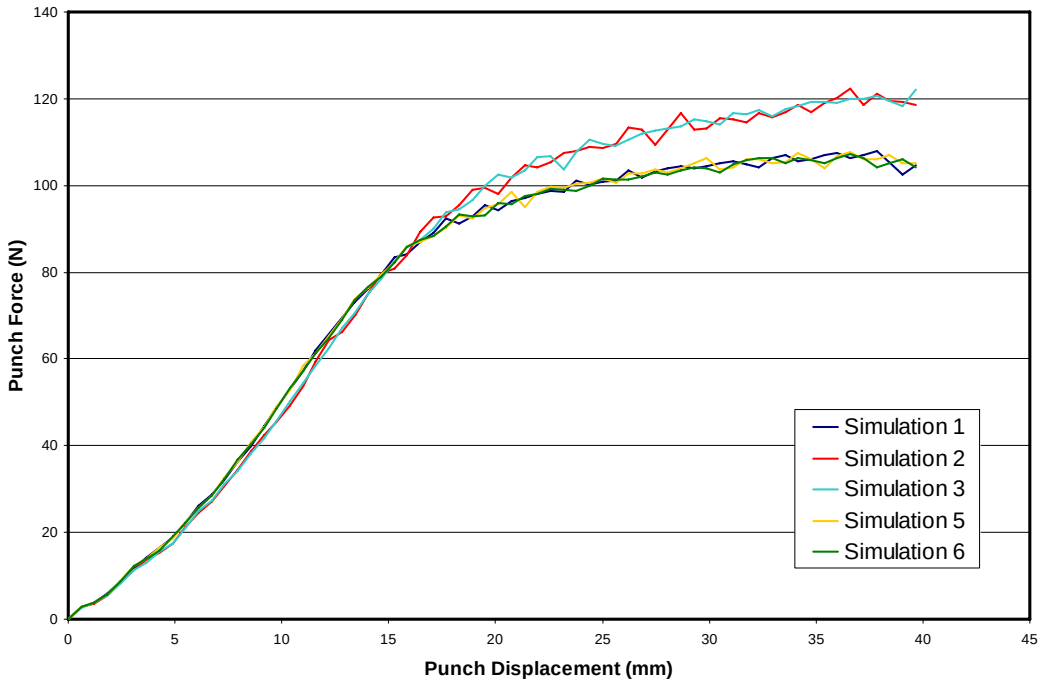

Figure 5.54: Punch force – punch displacement curves of simulations

Although simulations 1, 5 and 6 have different initial element sizes of 5 mm, 10 mm and 2.5 mm respectively (Table 5.5), having the same final element size (2.5 mm) makes them belonging to the last group. As the thickness contour curves (Figure 5.52 and 5.53) and punch force – displacement curves (Figure 5.54) are inspected, another similarity is observed that the results are almost the same even though the mesh sizes and mesh density is completely different in all three simulations. Simulation 6 consists of a uniform mesh, having an average element size of 2.5 mm. No refinement is used and only 9 % percent of change occurred in the time step and as well as in the element size, according to the Eq. 4.31 through the simulation (Table 5.6).

Table 5.6: Computational times and time step changes of simulations

	Initial Time Step [s]	Final Time Step [s]	Decrease in Time Step [%]	CPU Time [s]
Simulation 1	5.15E–04	2.33E–04	55%	2384
Simulation 2	1.24E–03	4.78E–04	61%	633
Simulation 3	5.15E–04	4.68E–04	9%	837
Simulation 5	1.24E–03	2.34E–04	81%	1993
Simulation 6	2.47E–04	2.25E–04	9%	3761

There are 20649 elements at the end of the simulation 6 and the CPU time is very high compared to the other simulations (Figure 5.55). On the other hand, in simulation 1, two dominant element sizes exist in the mesh at the end of the analysis. A level 2 refinement is used in the simulation, meaning that some region of the initial mesh consisting of 5 mm elements are split into four child elements whose sizes are approximately 2.5 mm (Figure 5.51). Total element size at the end of the simulation is less than that of simulation 6, and the decrease in time step during the simulation is about 55 % throughout the simulation because of the refinement of some elements (Table 5.6). Simulation 5, which is the last analysis of group 3, consists of elements with 10 mm length at the beginning of the simulation. It is shown before in Figure 5.52 that results obtained with this element size are

obviously unacceptable and invalid. However, Figure 5.52 shows that the results of simulation 5 are nearly identical with the results of simulation 6, which uses 2.5 mm long elements during the whole simulation. This improvement is the consequence of using 3 levels of refinement in the simulation. 10 mm long elements are first divided into four elements with 5 mm length and then again subdivided into 2.5 mm long elements where and when certain conditions exist to satisfy the accuracy requirement and exhibit geometry details properly in the analysis (Figure 5.52). There is an 81 % decrease of time step during the simulation. This huge amount of reduction can be explained with high level of refinement (level 3). The simulation starts with relatively large time steps and then as the analysis proceeds and size of the elements decrease so that time step is reduced to avoid instability. However, when the overall performance is concerned, it is seen that the most time efficient analysis is done by simulation 5 within the third group (Figure 5.53).

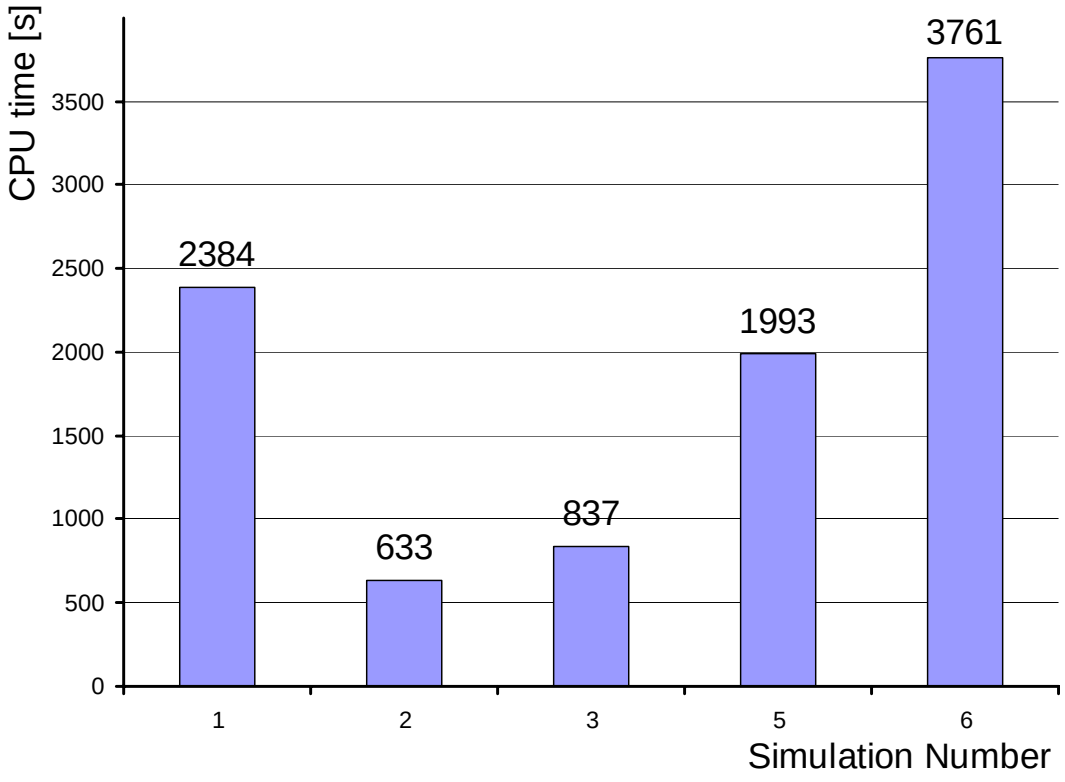

Figure 5.55: Comparison of CPU times of simulations

5.2.8 Mass Scaling

The purpose of mass scaling is to reduce CPU time by increasing the time step. To do this, the mass of some elements is artificially increased, and thus according to Eq. 4.32, the corresponding element time steps also increase. However, the increase in the mass of the elements increases the inertia of deformable body, and this can lead to erroneous results, therefore the mass scaling should be used cautiously.

The mass scaling option is used in PAM-STAMP 2G by defining a reference element size. This allows the program to increase the mass of elements having smaller elements sizes than the reference size. The masses of the smaller elements are automatically scaled by the solver, so that their corresponding time steps do not decrease the global time step. Since the scaling is done automatically, the extent of the mass scaling is determined by the reference element size. Inspection of the effect of mass scaling on the accuracy of analysis results is done by using a series of mass scaling factors respectively in the simulations (Table 5.7):

Table 5.7: Series of simulations with various element sizes, refinement levels and mass scaling conditions

	Element Size [mm]	**Refinement Level**	**Mass Scaling Criteria**	
			Reference Size [mm]	**Corresponding Time Step [s]**
Simulation 1	5	2	*no mass scaling*	
Simulation 2	5	2	1.70	2.84E–04
Simulation 3	5	2	5	8.34E–04
Simulation 4	10	2	*no mass scaling*	
Simulation 5	10	2	10	1.67E–03
Simulation 6	10	3	*no mass scaling*	
Simulation 7	10	3	2.06	3.43E–04
Simulation 8	10	3	5	8.34E–04
Simulation 9	10	3	10	1.67E–03

Within this assessment, there are three simulations having the mass scaling option disabled (Simulations 1, 4 and 6). In the other six simulations (2, 3, 5, 7, 8 and 9), various mass scaling factors are used on elements having different lengths (Table 5.7). These nine simulations can be divided into three groups according to the meshing properties. The first three simulations have the same element size and refinement level. Three different reference element sizes for the application of mass scaling are imposed to the simulations respectively within the group. All remaining simulations have 10 mm long elements at the initial step. Simulations 4 and 5 use refinement level 2 and from the second group, whereas simulations 6, 7, 8, and 9 have a level 3 refinement and belong to group three.

The assessment of the simulations will be done within the subgroups according to the results showing the thickness distribution, forming force – displacement relation, and equivalent plastic stress variation. For instance, Figure 5.56 shows the 2D thickness sections cut from each simulation taken on YZ-plane.

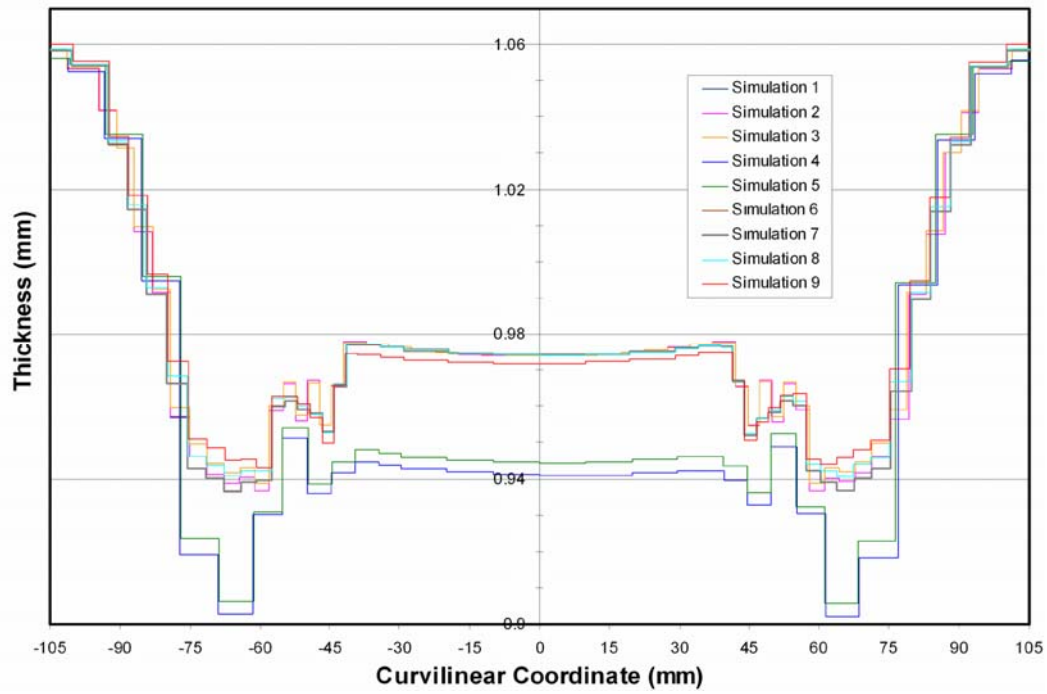

Figure 5.56: Thickness distributions of all simulations along the curvilinear coordinate on YZ-plane

From Figure 5.56, it is observed that the results are grouped in two. Simulations 4 and 5 show some variation, since their element sizes are larger than that of other simulations, although refinement is present (Table 5.7). If a more precise observation is done on the thickness contours, it is found that the results of simulations 1, 2, 3 (Figure 5.57) and 6, 7, 8, 9 (Figure 5.58) are compatible to each other.

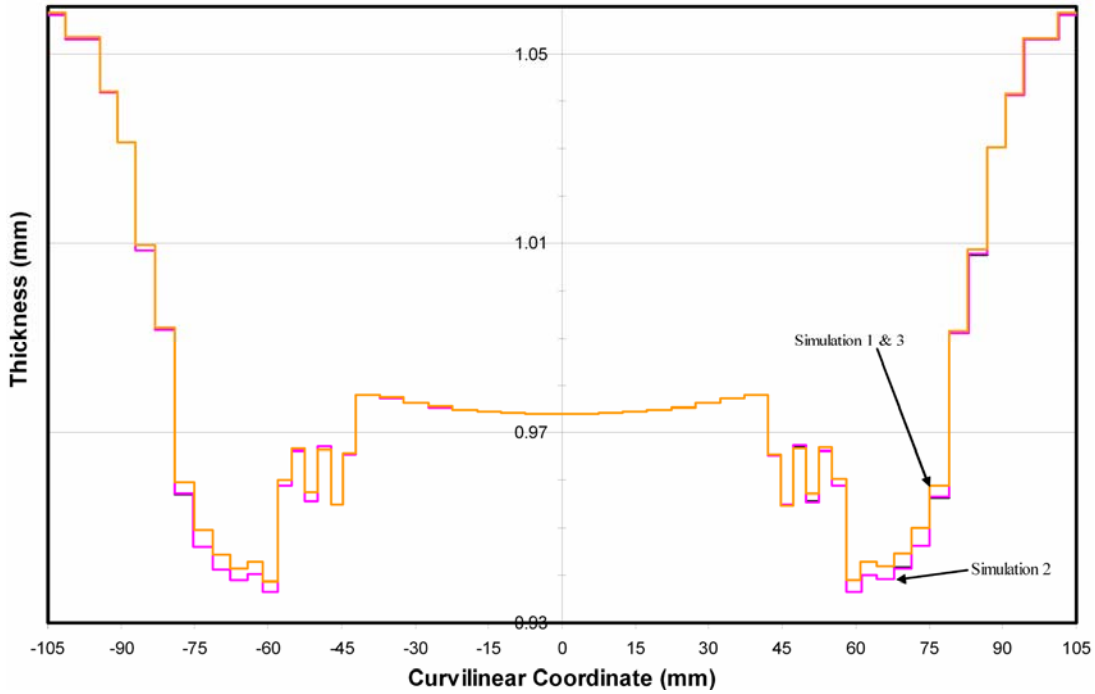

Figure 5.57 Thickness distributions of simulations 1, 2 and 3 along the curvilinear coordinate on YZ-plane

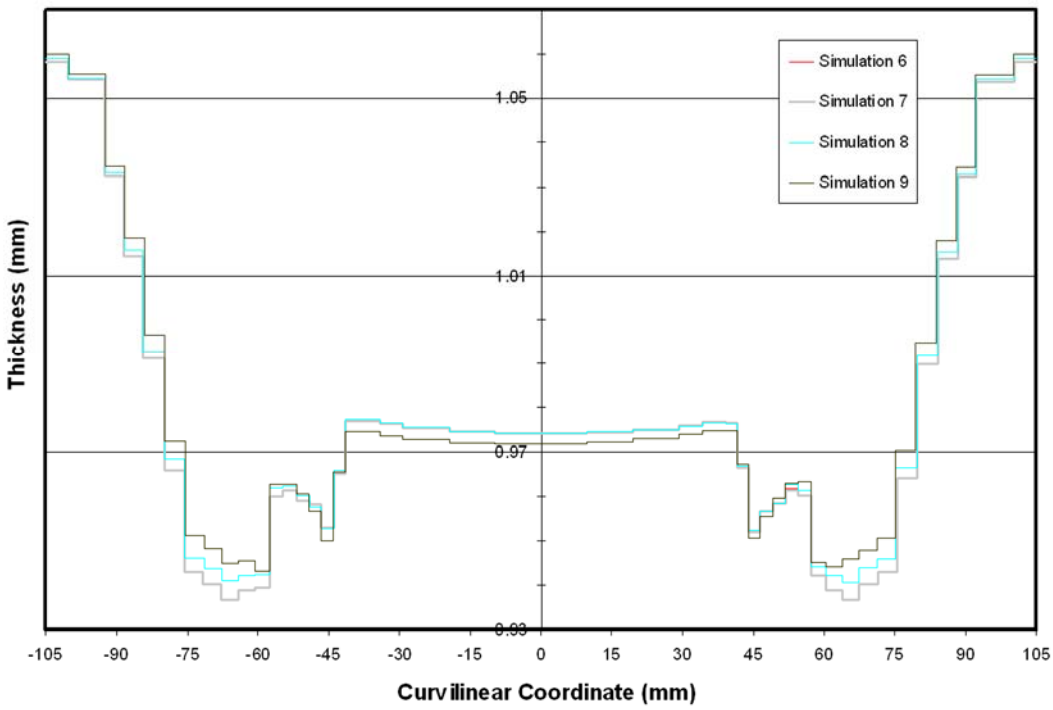

Figure 5.58: Thickness distributions of simulations 6, 7, 8 and 9 along the curvilinear coordinate on YZ-plane

When the forming force - displacement curves of all simulations observed, two sets of curves are detected (Figure 5.59). Simulations 4 and 5, whose element sizes are approximately 5 mm at the final stage, form the upper set of curves, whereas the remaining six simulations' force - displacement curves belong to the lower set of curves. In addition, it is seen that simulations 5 and 9 exhibit a sudden fall at the end of the force - displacement curves. The reason of this unexpected behavior is the large mass scaling factor used in both simulations. Such high mass scale factors, as stated before have the risk of causing undesired and unrealistic dynamic effects.

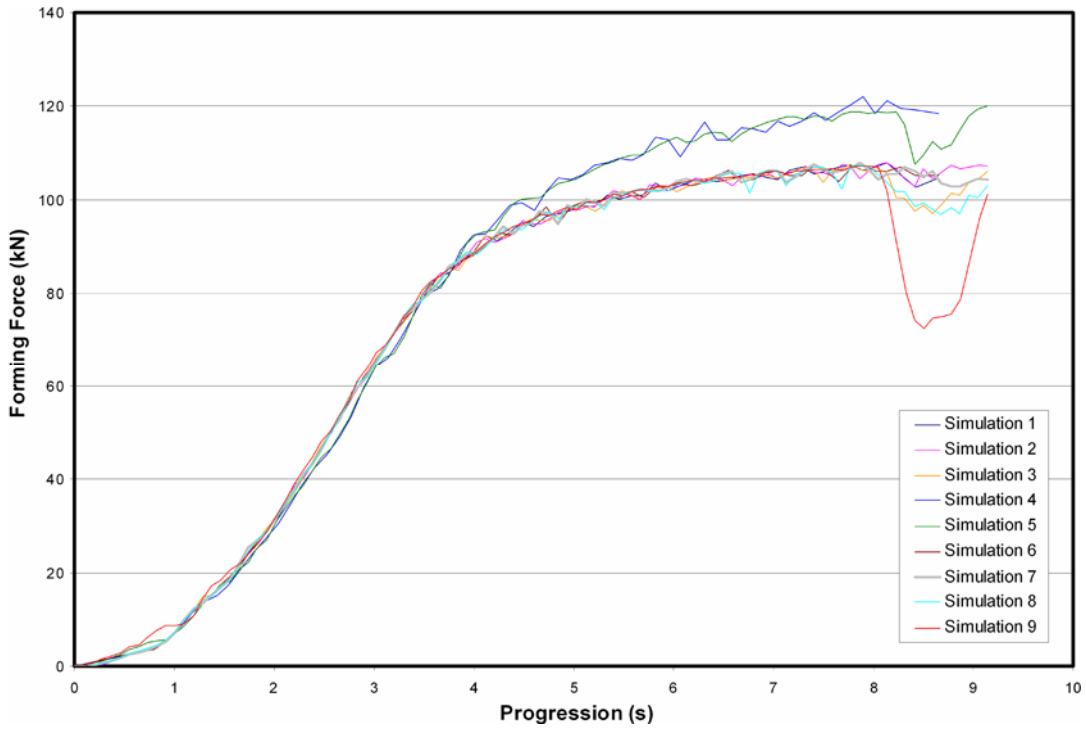

Figure 5.59: Punch force – displacement curves of all simulations

When the equivalent stress variations on 2D and 3D sections are observed (Figure 5.60), it is seen that the effects of mass scaling are more obvious in the stress calculations than the thickness (or the strain) estimations. The results show a 10 % variation between the upper and lower bound of set of curves. Moreover, it is known that simulations 4 and 5 estimate the thickness distribution lower than the others (Figure 5.56). On the contrary, in case of stress calculation they predict higher minimum stress values (Figure 5.60), and the curvilinear stress plot along X=0 shows that they predict higher equivalent stress values overall (Figure 5.61). On the other hand, the results for simulations 1, 2, 3, 6, 7, 8 and 9 are more or less close to each other.

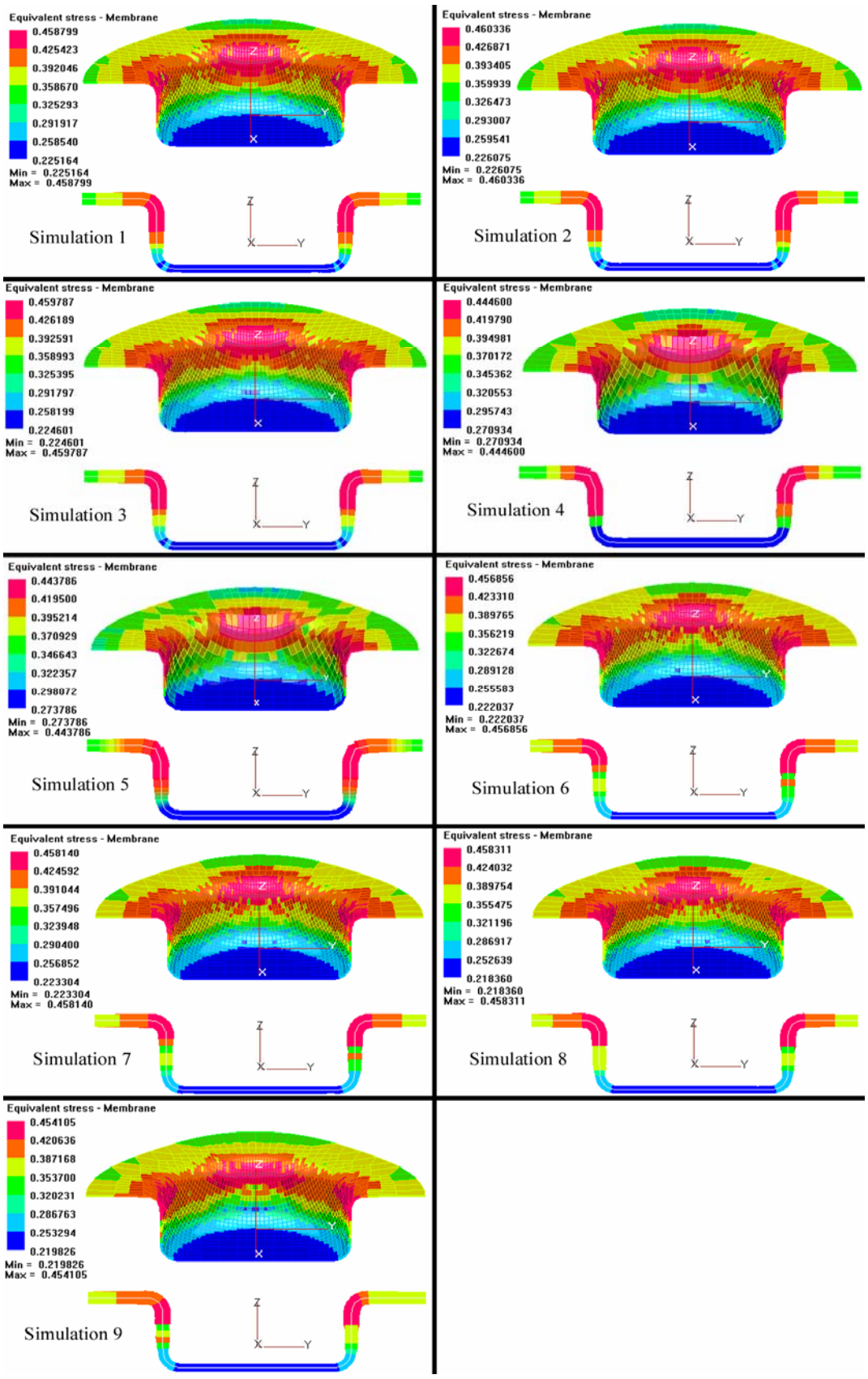

Figure 5.60: 2D and 3D stress contours of the mass scaling assessment simulations

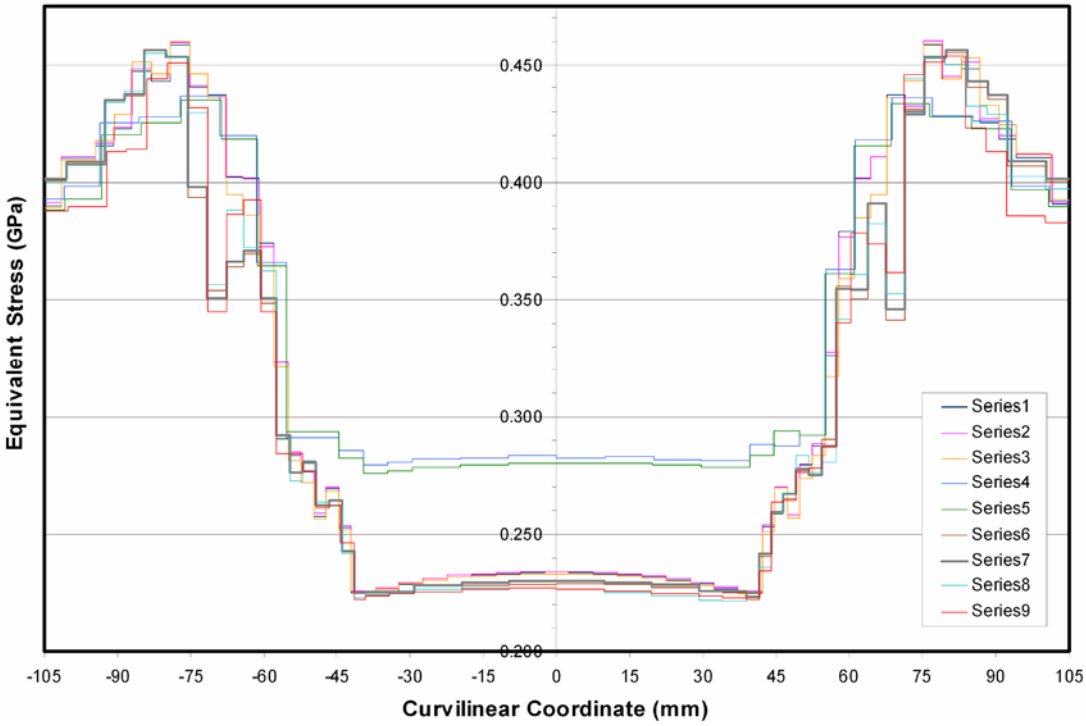

Figure 5.61: Variation of equivalent stress along the curvilinear coordinate on YZ-plane for all simulations

If a thorough observation is done on the equivalent stress variations along the bottom part of the 2D section of Figure 5.61, three more set of curves is noticed (Figure 5.62). The results of simulations 1, 2, and 3 are similar to each other and they form the upper bound of those six curves. Furthermore, the stress curve of simulation 8 is resembles to that of simulation 9 and together they form the lower bound of simulation results. Equivalent stress variation curves of simulations 6 and 7 show another correlative behavior, and these simulations are in the middle of upper and lower bounds (Figure 5.62). The tendency toward forming groups in the simulation result is not by chance instead, they group together according to the similarities between the element size, refinement level and magnitude of the mass scaling used (Table 5.7).

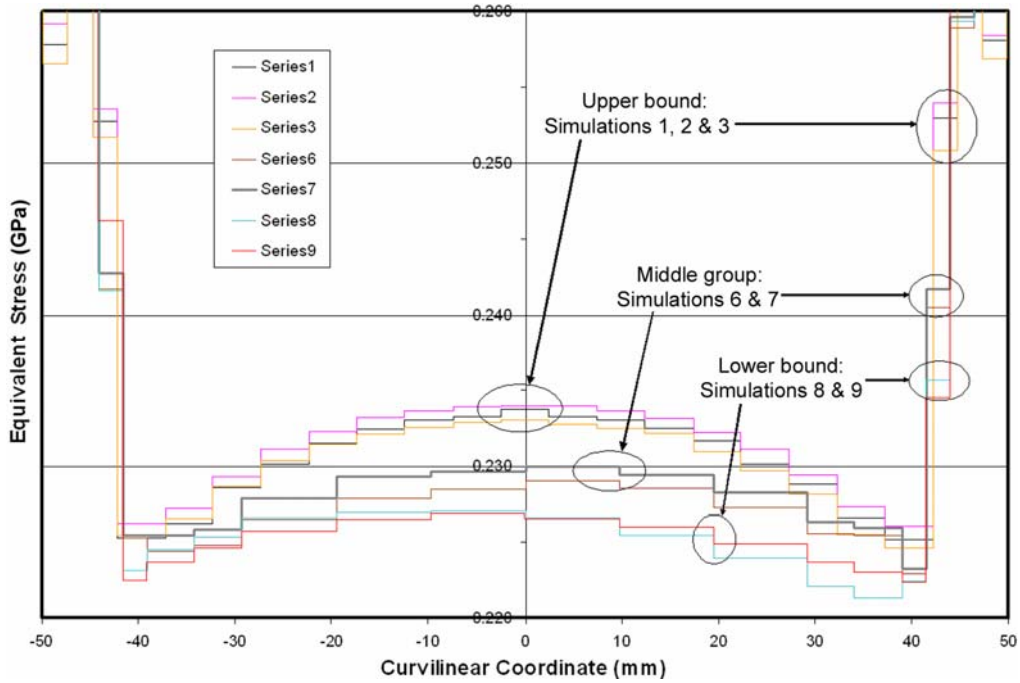

Figure 5.62: Variation of equivalent stress along the curvilinear coordinate on YZ-plane (bottom of the cup)

In simulations 3, 5 and 9 large mass scaling factors are used. The reference element size given for the mass scaling is equal to the initial element size. Therefore, the solver increases the mass of some elements even at the beginning of the simulation to achieve an increase in the time step of these elements. Table 5.8 shows the number of scaled elements and the increase in the mass of the deformable body. The numbers of mass scaled elements and their scaling extent cannot be effectively traced for simulations 2, 7 and 8, since the total number of elements change due to refinement in the intermediate stages of the simulations.

Table 5.8: Amount of mass increase at the start of the simulations

	Number of Elements Scaled	**Total Mass Before Scaling [kg]**	**Total Mass After Scaling [kg]**	**Increase in Mass [%]**
Simulation 3	1389	0.263	0.341	29.50
Simulation 5	352	0.263	0.357	35.85
Simulation 9	352	0.263	0.357	35.85

Initial and final time steps, decrease in time steps during the analysis and CPU time of each simulation are listed in Table 5.9. It is seen that simulation 5 has the smallest CPU time, while simulation 1 has the largest. However, the assessment of simulations should be done within each subgroup according to the accuracy requirement of the process since subgroups have different accuracy level in the prediction of stress variation or thickness distribution. Comparison of the CPU times of each subgroup is given in Figure 5.63.

Table 5.9: Time step changes and computational times of each simulation

	Initial Time Step [s]	**Final Time Step [s]**	**Decrease in Time Step [%]**	**CPU Time [s]**
Simulation 1	5.15E–04	2.33E–04	55	2.38E+03
Simulation 2	5.15E–04	2.84E–04	45	1.90E+03
Simulation 3	8.34E–04	8.31E–04	< 1	1.35E+03
Simulation 4	1.24E–03	4.78E–04	61	6.33E+02
Simulation 5	1.67E–03	1.66E–03	< 1	5.56E+02
Simulation 6	1.24E–03	2.34E–04	81	1.99E+03
Simulation 7	1.24E–03	3.40E–04	73	1.85E+03
Simulation 8	1.24E–03	8.29E–04	33	9.46E+02
Simulation 9	1.67E–03	1.66E–03	< 1	5.10E+02

Firstly, considering the sudden fall that has no physical meaning, in the forming force – displacement curves of simulations 5 and 9, it can be suggested that large mass scaling parameters (e.g. 10 mm reference element size) that cause an increase larger than 20% in the weight of deformable body should not be used although they are the two fastest simulations in the assessment. It is clear that the computational speed is not more important than the computational accuracy. The mass scaling option is disabled in the simulation 4, but since the final element size is larger than the other simulation, it is still accepted as a fast computation. However, accuracy in

determination of thickness distribution and forming force calculation is poor because of the insufficient mesh size.

When the first group formed by simulations 1, 2 and 3 is observed, it is seen that simulation 3 is the most favorable one. These three simulations predict nearly identical thickness distributions; however, simulation 3 performs this prediction 40 % faster than simulation 1 (no mass scaling). If residual stresses are concerned, parameters used in simulation 2 are suggested, which has a moderate CPU time. The CPU time reduction in simulation 2 is more than 20 percent (Table 5.9).

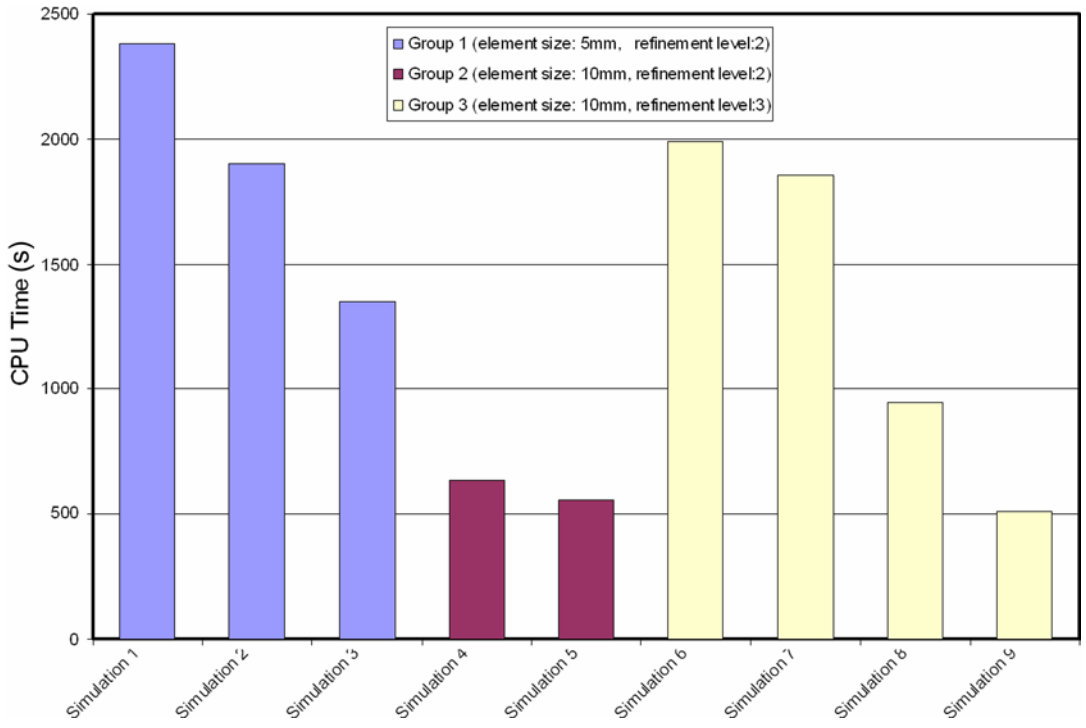

Figure 5.63: CPU time of each simulation within 3 groups

5.3 PAM-STAMP 2000 AND 2G COMPARISON

Up to this point, the effects of various numerical and process parameters upon the analysis results are inspected. By doing this, a solid understanding of the PAM-STAMP family FEA packages are gained, and the strong and weak points of FEM

is demonstrated in general. From now on the results will be discussed and they will be compared with NUMISHEET 2002 Benchmark's findings in the next section thoroughly.

Actually, two versions of PAM-STAMP are used for the analyses: version 2000 and version 2G. The latter is a newer version of PAM-STAMP, and it is said to be more effective and accurate than the previous versions. In this section, some results of these two versions will be compared, and in general, their reliability will be inspected.

The main difference of PAM-STAMP 2000 and PAM-STAMP 2G is their contact algorithms. In version 2000 penalty and Lagrangian contact algorithms are available, whereas in version 2G only a contact algorithm called as the non-linear penalty contact is available. PAM-STAMP 2G User's Guide (2002), defines this algorithm as the following:

> This contact permanently prohibits the nodes of the blank sheet from penetrating the volume of the element of the tool during a calculation.
> The nodes are kept exactly at the surface of the element owing to the contact forces being precisely calculated.
> The volumes of the impenetrable elements are defined as follows:
> - Shell Elements: the solver adds half the thickness of the element above and below the neutral fiber. The thickness used is the evolutive current thickness, thus enabling the contact to take into account any thickening during the process.
> - Volume Elements: they are considered as the assembly of six shells that correspond to the facets of the elements with nil thickness.
>
> A node is considered as a ball with a diameter equal to the mean of the elements to which it belongs. There is penetration when the node ball penetrates the volume of an element declared impenetrable for the node.
> When the diameter of the ball is nil (slave is defined by solid elements or shell elements with a nil thickness) and the master element is a shell element with a nil thickness or a solid element, penetration is no longer possible. In order for the algorithm to operate, a contact thickness is added to the element (contact advanced parameter). This contact thickness is automatically calculated and can also be given by the user.

As a result of these, this algorithm is said to give better stress calculations, but it is also stressed that the tool mesh must be of high quality, since the algorithm respects tool geometry greatly. On the other hand, penalty contact is defined as a contact type allowing small penetrations between the slave and master objects. In this algorithm, the tool geometry is less important and therefore stress calculations are less accurate.

Actually, PAM-STAMP 2G manuals state that the penalty algorithm is available, but analyses using penalty algorithms do not proceed at all. Possibly this algorithm is not implemented to PAM-STAMP 2G release 2003. In newer versions this problem may be overcame, but since PAM-STAMP 2G release 2003 was utilized during this thesis study, no further comment will be made on the (unusable) penalty and Lagrangian contact algorithms of PAM-STAMP 2G.

Anyway, it is expected that the PAM-STAMP 2G version using the non-linear penalty algorithm will give more precise results in terms of contact forces and stresses, as far as the manuals are considered. The following analyses agree with this expectance. For the comparison of the results, the HBHF and LBHF aluminum analyses of NUMISHEET 2002 Benchmark are conducted with both versions of PAM-STAMP.

First of all, it must be stated that PAM-STAMP 2G has two types of solvers in terms of computational precision: Single precision and double precision. The single precision solver is normally utilized for simple analyses, however if a springback analysis is to be conducted afterwards, utilization of the double precision solver is advised. It is stated that the results of the double precision solver are more accurate, thus improving the simulation accuracy of springback calculations. Firstly, the performance of these two solvers will be investigated.

Figure 5.64 shows the force – displacement curves for the single precision (SP) and the double precision (DP) solvers for aluminum HBHF and LBHF analyses. It is

seen that the results in terms of forces do not vary significantly for both solvers in both analysis cases:

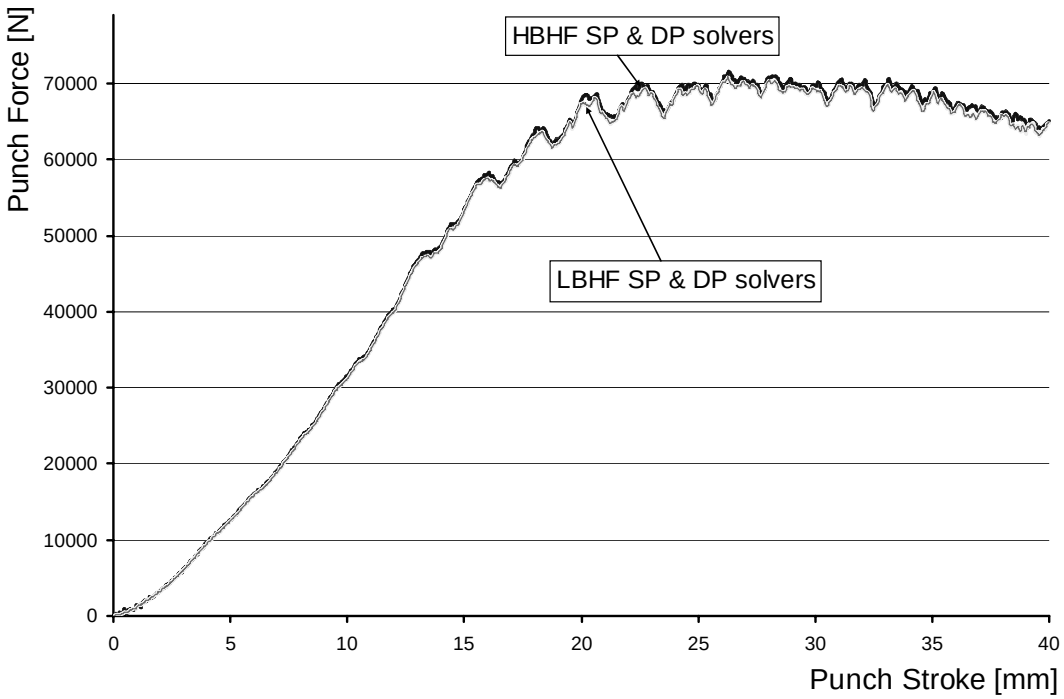

Figure 5.64: Comparison of PAM-STAMP 2G's solvers

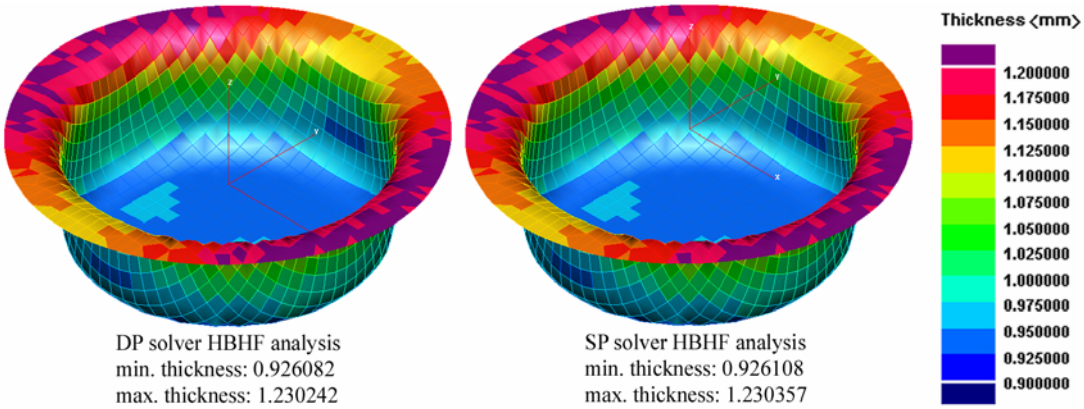

Figure 5.65: Thickness contours computed by DP and SP solvers

The inspection of thickness contours gives also a similar result (Figure 5.65). If the minimum and maximum thickness values in Figure 5.65 are inspected, one can say that the results are practically identical. However, the computation times differ considerably (Figure 5.66). As the name implies, the double precision solver does more computational work to obtain more precise results, having a larger computation time for the analyses. Therefore, the usage of the double precision solver is normally avoided. Only in the next chapter, where springback and trimming operations are also simulated, the double precision solver will be utilized.

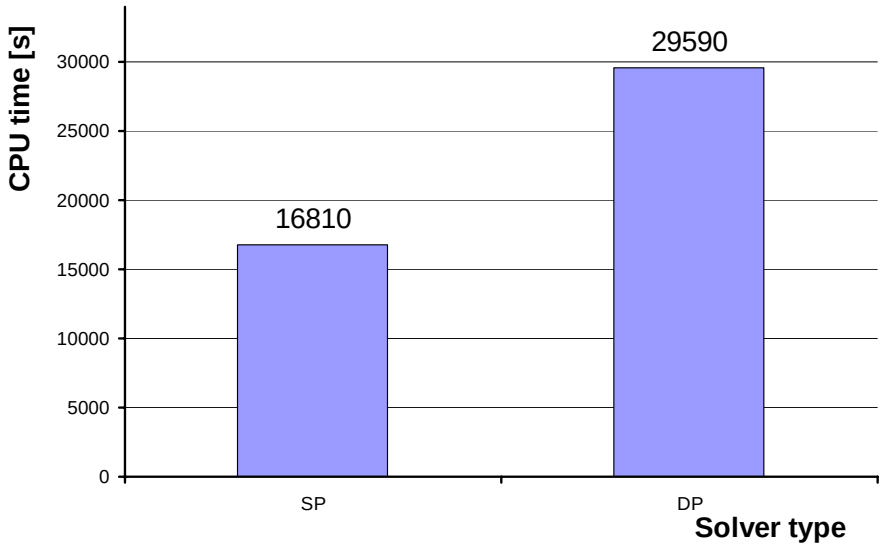

Figure 5.66: Comparison of CPU times for both solvers

Now, the simulation results of PAM-STAMP versions 2000 and 2G are compared. To form a basis of verification, some of the experimental findings of NUMISHEET 2002 benchmarks will also be utilized. This way, it will be possible to determine which package has a better reliability.

Figure 5.67 shows the force – displacement behaviors of identical simulations conducted under both PAM-STAMP versions. For the sake of simplicity, trend lines are utilized in the graph.

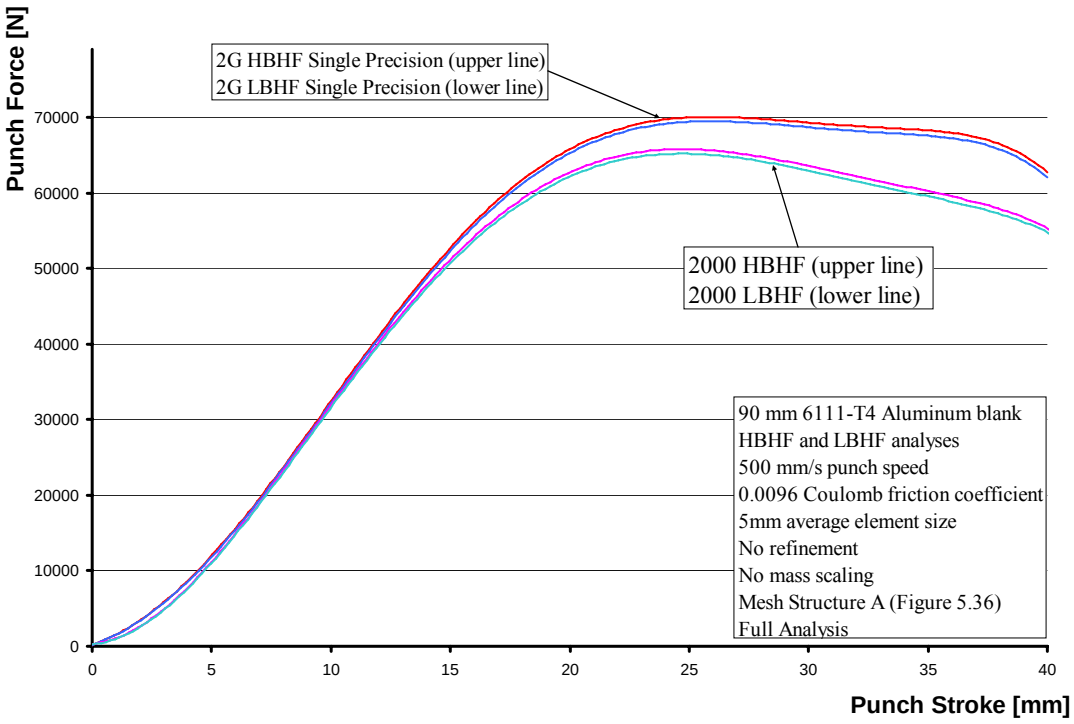

Figure 5.67: Comparison of force – displacement behaviors of PAM-STAMP 2G and 2000 analyses

Figure 5.67 shows that the force – displacement relationships for the simulations under the two versions have a small difference. The results of version 2G act somehow stiffer after a punch stroke of ca. 15 mm. Since all process and numerical parameters are identical for the simulations in the two versions, the main reason of this discrepancy is the difference of the utilized contact algorithms in the FE-packages. If the simulation results of these two versions are compared with the experimental findings of NUMISHEET 2002 Benchmark, it is observed that the newer version is more successful in estimating the punch force – punch stroke behavior of the deep drawing processes (5.68). This occurrence was also predicted by the user's manual of PAM-STAMP 2G, that the force (and stress) calculations in the newer version will be more accurate due to the nonlinear penalty contact algorithm utilized. The experimental results of the participants of NUMISHEET 2002 Benchmarks are tabulated as AE-XX, where XX is the participant number. Detailed info on the participants of NUMISHEET 2002 is given in Appendix B.

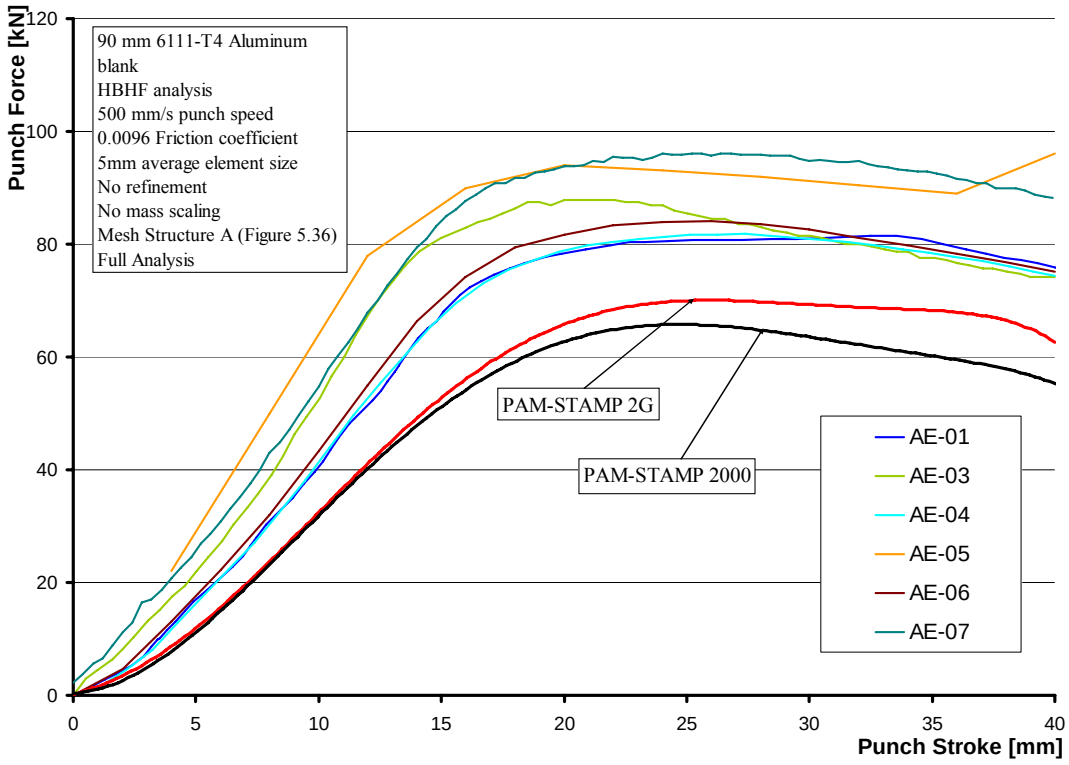

Figure 5.68: Comparison of the force – displacement graphs of PAM-STAMP 2000 and 2G's analyses with experimental findings

It was stated that the utilization of symmetry conditions posed unexplainable problems in PAM-STAMP 2G, whereas in the older version the symmetry conditions were safely utilized to save computational time. Figure 5.69 demonstrates the effects of symmetry conditions on the simulation results of PAM-STAMP 2000, compared to a full analysis of PAM-STAMP 2G. It is observed from Figure 5.69 that the results do not vary excessively with imposed symmetry conditions. However, the results of PAM-STAMP 2G (in terms of the force requirements of the deep drawing simulation) show a tendency to increase with increasing number of symmetry conditions (Figure 5.70).

Consequently, for further analyses the newer version of PAM-STAMP will be utilized, since it gives better simulation results with a higher accuracy. However the symmetry conditions will not be utilized at all in numerical simulations conducted with this version, since the symmetry conditions cause unexplainable problems

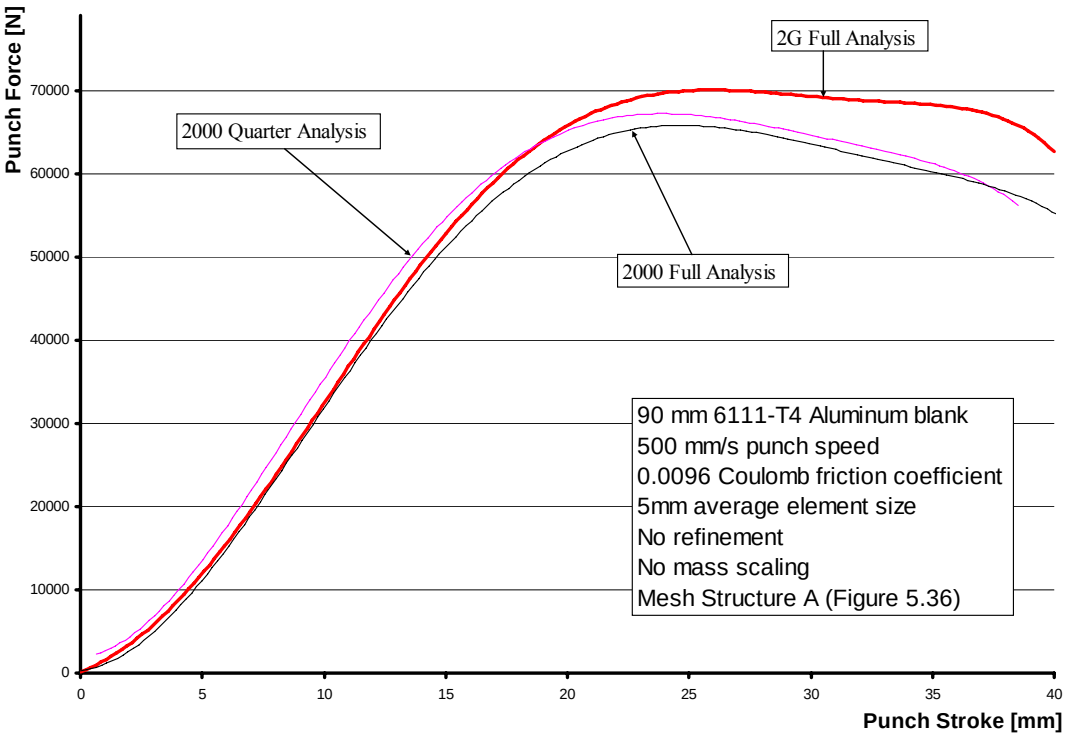

Figure 5.69: Effect of symmetry conditions on PAM-STAMP 2000 results

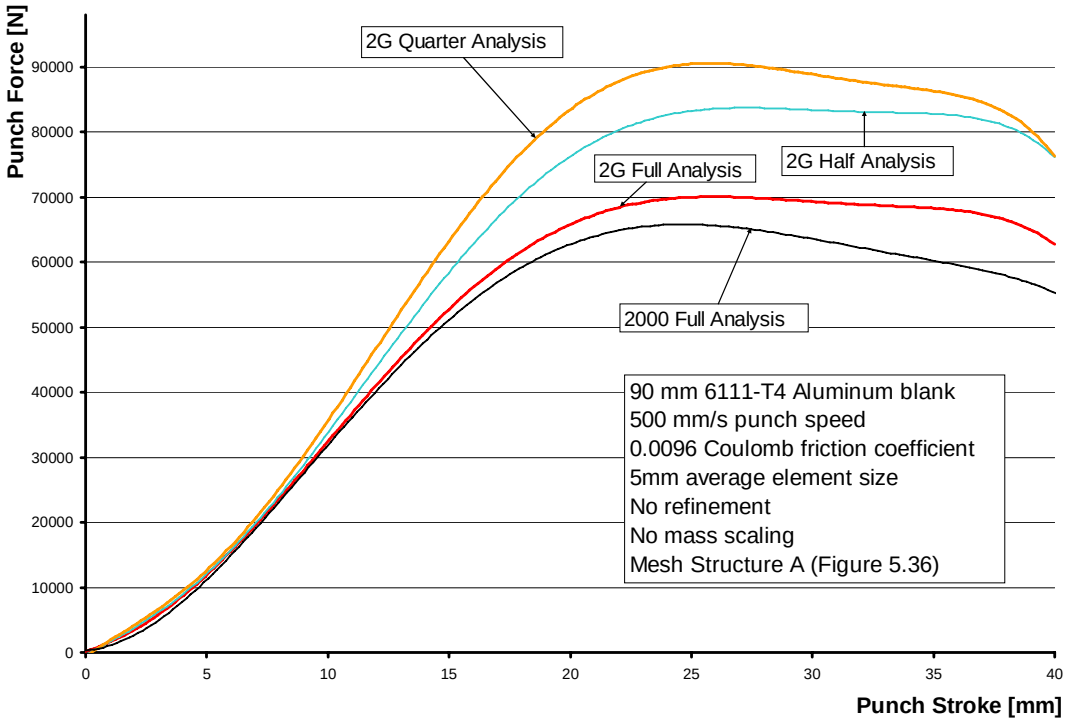

Figure 5.70: Effect of symmetry conditions on PAM-STAMP 2G results

5.4 Comparison with NUMISHEET 2002 Benchmarks

According to the investigations and observations in Sections 5.2 and 5.3, a set of reliable process and numerical parameters are defined for the 2002 benchmark simulation of NUMISHEET. In this section, the results numerical simulations of the cup drawing benchmark will be compared with the participant's findings.

The process setup and geometry of tools used in the benchmark are already given in Figure 5.1. In the same setup, two different anisotropic materials with 1 mm thickness were used as workpieces. The material data for these workpieces were tabulated in Table 5.1 previously. The radii of workpieces are 90 mm for aluminum blank and 105 mm for steel blank. Same geometrical data is used to build the meshes in the simulation. The following table summarizes all parameters defined for the benchmark simulation:

Table 5.10: All simulation parameters for the benchmark comparison

	6111-T4 Aluminum	**DDQ Mild Steel**
Blank Radius [mm]	90	105
Blank holder radius [mm]	90	105
Punch Speed [mm/s]	500	
Punch Speed Type	Stroke Controlled	
Punch Stroke [mm]	40	
Blank Holder Load [N]	HBHF: 50000 LBHF: 10000	HBHF: 70000 LBHF: 10000
Friction Coefficient	0.0096	0.0426
Blank Element Size [mm]	3	
Mesh Topology	Structure A	
Time Step Scale Factor	Default (0.9)	
Adaptive Meshing	Not applied	
Mass Scaling	None	

Twenty-three participants have supplied results to the benchmark. Seven of them have conducted experiments, whereas the rest of them participated with simulation results obtained from different finite element packages. Detailed information about the participants can be found in Appendix B.

The comparison between simulation and benchmark is done by inspecting the forming force - displacement curves, thickness variations along 0°, 45°, and 90° directions, outer radii of flange and numbers of wrinkles occurred on the flange. Those results are compared for both aluminum and steel blanks. Firstly, the results of steel blank are investigated.

Figure 5.71 shows the comparison of simulation (Steel-HBHF) with the experiments done by different participants, for high blank holder forces respectively.

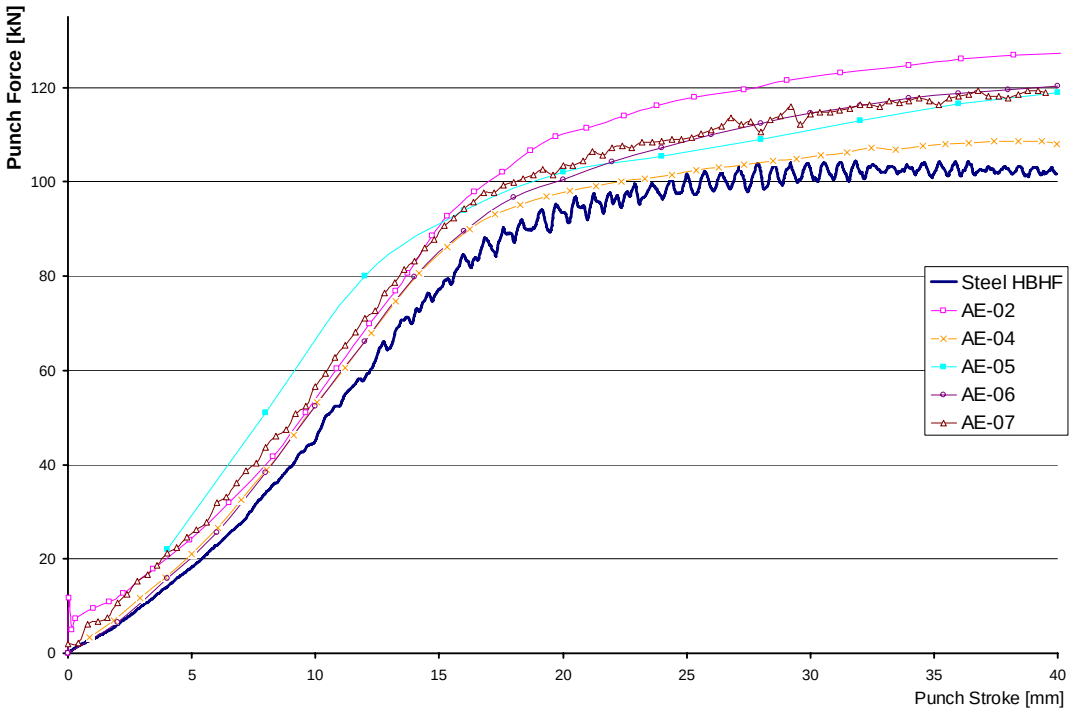

Figure 5.71: Comparison of forming force – displacement curve of steel HBHF simulation with five benchmark experiments

In Figure 5.71, it can be noticed that the best compliance exists between the simulation result and AE-04. The results supplied by other participants are slightly higher that this agreement, however these differences may exist because of the external influences. For instance, E.H. Atzema (Appendix B) from Corus Research, Development and Technology has stated that the grid applied to the steel blank influenced the friction condition, thus it increased the values in the force – displacement graphs by 5 percent. Anyway, it is surprising that the experimental findings of the participants show a considerable variance. There is a difference of ca. 20 kN in the measured maximum punch forces between the highest and lowest experimental findings in Figure 5.71.

Outer profiles of flange are compared in Figure 5.72 and 5.73 for steel blank with high blank holder force (HBHF). In Figure 5.72, the outer circumference of flange is plotted with respect to the r and θ in cylindrical coordinates and in Figure 5.73 it is plotted in Cartesian coordinates.

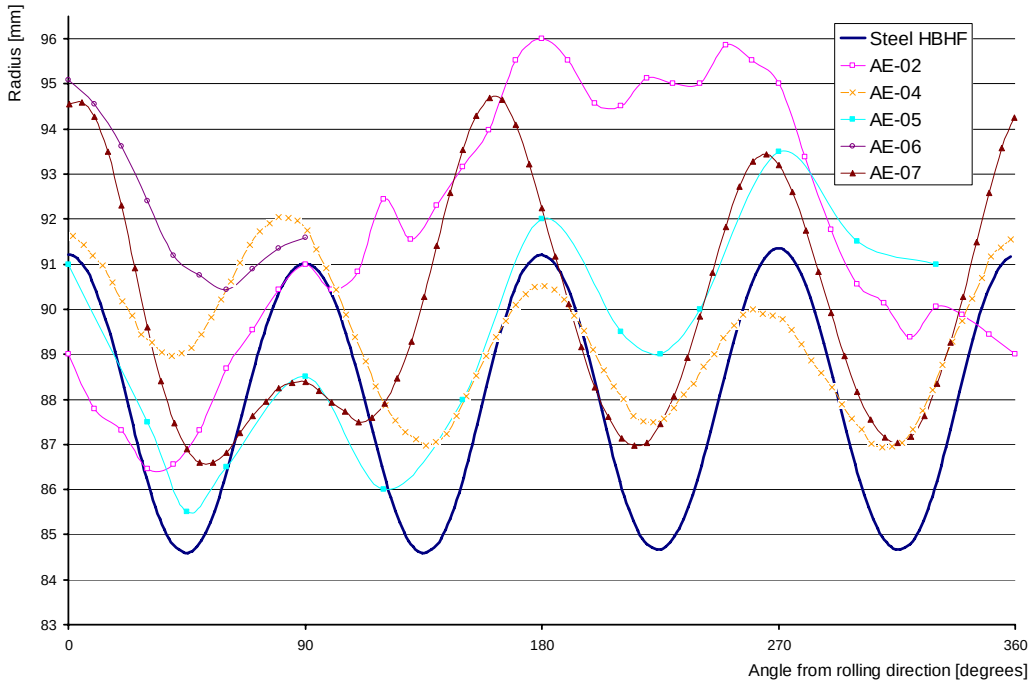

Figure 5.72: Comparison of outer profiles as a function of angle, starting from RD (Steel HBHF analysis)

It is shown that the simulation result only shows some variations with benchmark experiments AE-02 and AE-07 and is compatible with other three experiments (Figure 5.72). The reason of the variation can be the misalignment of the blank according to the rolling direction and eccentric placement of blank on the die. In the steel HBHF simulation such incorrect orientations cannot be happened since the recent finite element codes have features like “auto-positioning”.

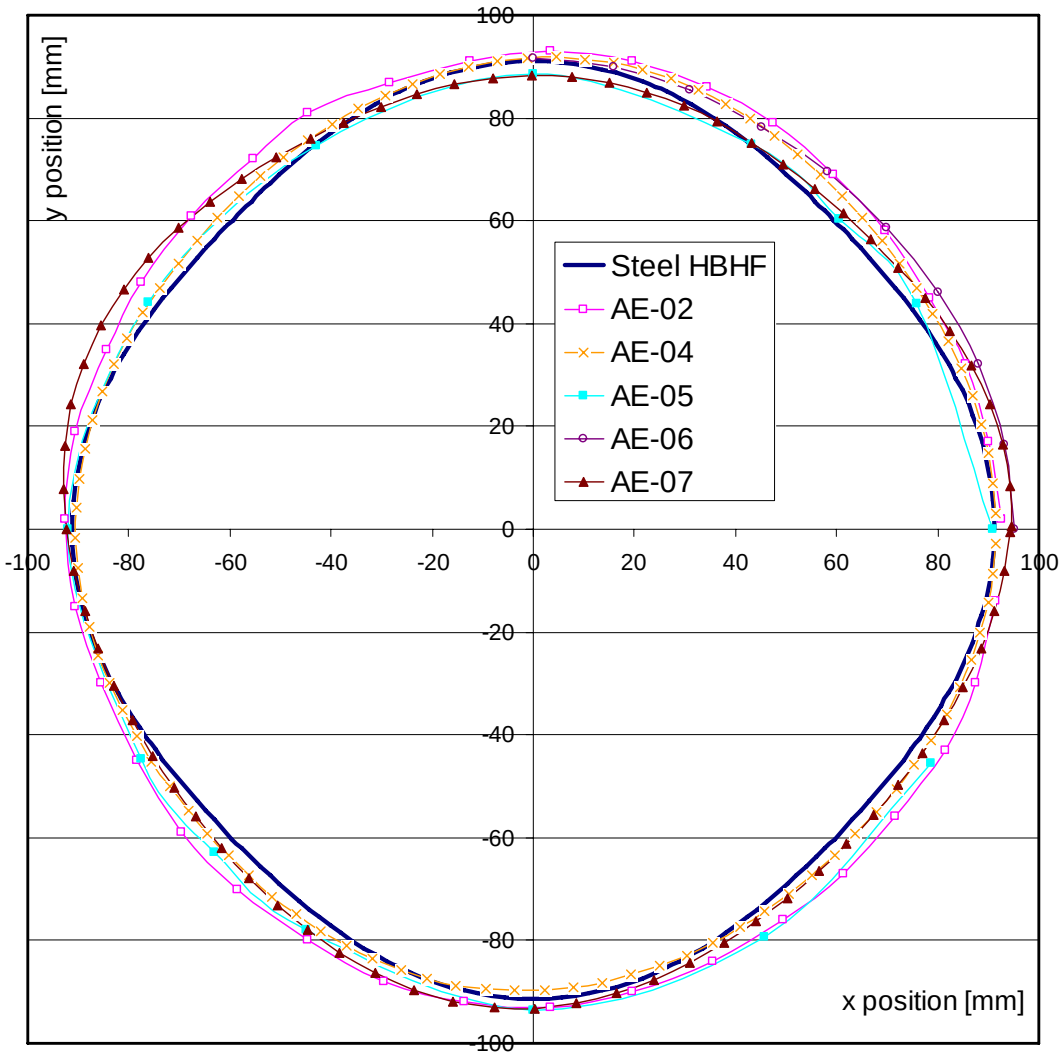

Figure 5.73: Comparison of flange profiles of steel HBHF simulation and benchmark experiments (plotted in Cartesian coordinates)

Thickness variations along 0°, 45°, and 90° directions with respect to rolling direction of steel LBHF simulation are respectively given and compared in Figures 5.74 to 5.76 with the result of three benchmark experiments.

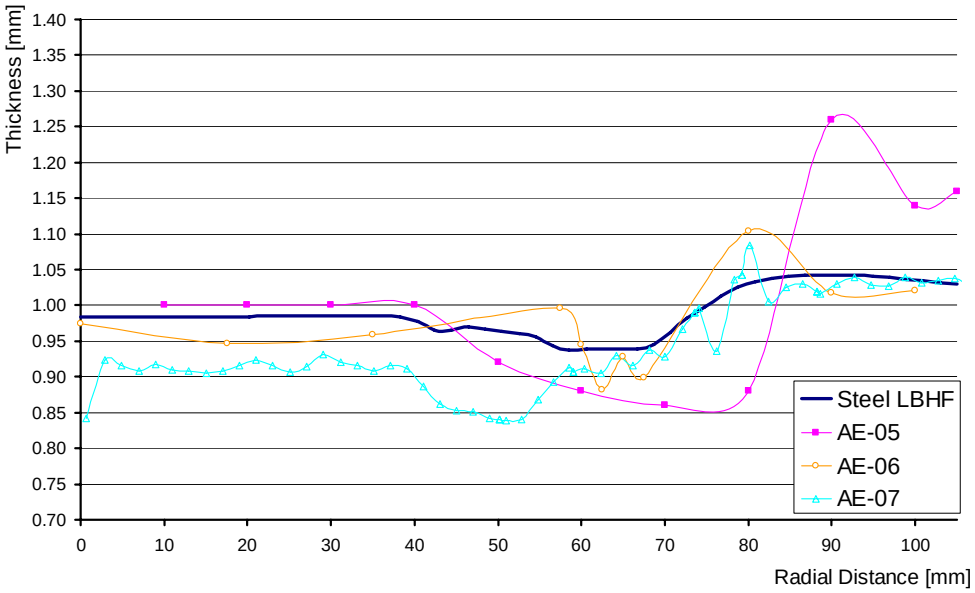

Figure 5.74: Comparison of thickness profiles of steel LBHF analysis and experiments along RD

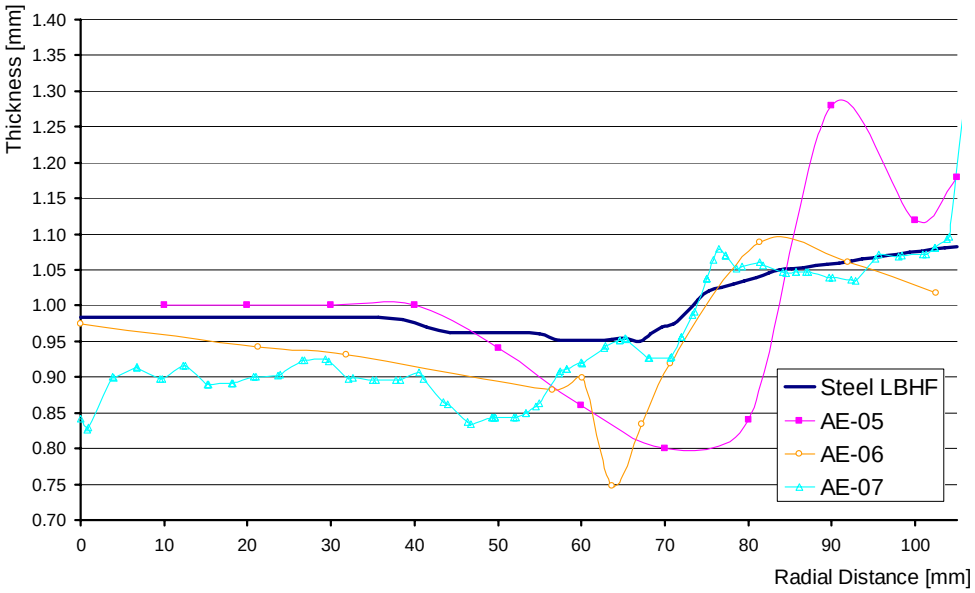

Figure 5.75: Comparison of thickness profiles of steel LBHF analysis and experiments along 45 degrees to RD

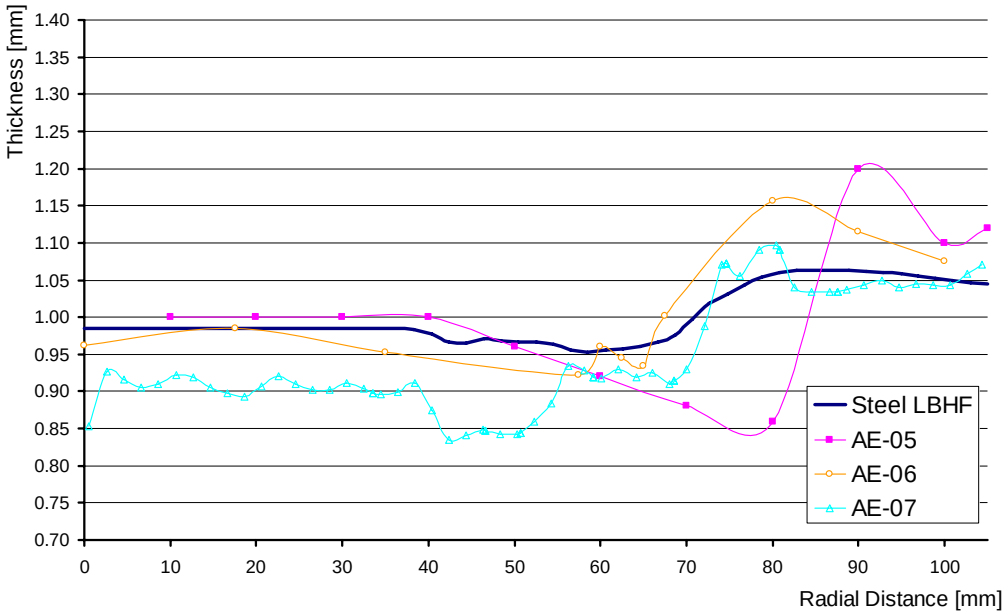

Figure 5.76: Comparison of thickness profiles of steel LBHF analysis and experiments along 90 degrees to RD

The thickness variation figures (Figures 5.74 to 5.76) show that even the result of experiments are not analogous to each other, it is hard to validate the simulation result by considering the thickness variation. A possible reasons for the variety in the experiment results can be the quality of the tools, the precision of the experiment and the measurement. If the thickness distributions along the first 40 mm of the radial distance in all directions are observed, the results of experiment AE-05 seems reasonable. The blank has deformed plastically slightly at that region since the bottom of punch is a smooth horizontal plane. Thus, the thickness distribution should be almost constant between 0 and 40 mm. Result of experiment AE-07 shows some deviations in thickness along the bottom part. The cause of this behavior can be the poor quality of the punch – die surface, and as well as the bad condition of tool setup including improper lubrication. If the thickness distribution of experiment AE-06 is inspected in all directions, it is seen that the same problem is experienced again, yet in a larger extent. Since there is no plastic deformation at the bottom of the workpiece, the thickness variation is expected to be almost same in all directions. However, it is not the case and great deviation is observed in the results for that set of experimental findings. The possible cause of this unexpected

deviation can be explained with non-planar geometry of the punch bottom surface and the stroke of punch being not eccentric with the other tool parts. The punch may be slightly inclined in experiment AE-06. Not the values but the trend of the LBHF steel simulation result is compatible with the expected behavior. The simulation results show that the blank has a constant thickness close to the initial value (1 mm) along the bottom, it decreases along the bottom fillet, and the lateral surface, and it increases and becomes more than the initial thickness (1 mm) along the flange.

In addition, when blank holder force is decreased from 70 kN to 10 kN in the deep drawing process, wrinkles are expected to occur at the flange. Dynamic explicit finite element codes using shell elements are capable of showing the wrinkling. The estimation of wrinkling zone and number of wrinkles in LBHF steel analysis are compared in Figure 5.77 with the benchmark experiments.

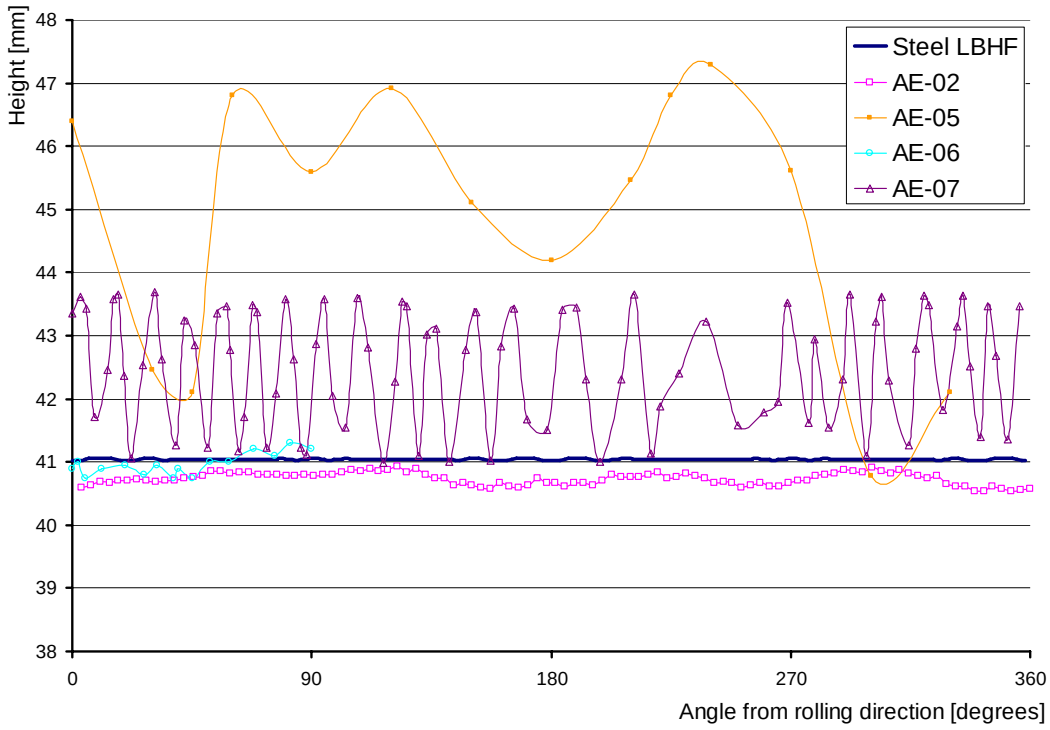

Figure 5.77: Comparison of the height profile of the upper surface along the flange at R = 75 mm for steel LBHF simulation and experiments

Height of the outer profile of the flange at the final step is measured by taking the lower surface of the bottom of the workpiece as reference (z = 0). Punch stoke is given as 40 mm, so that the height distribution (z-coordinate) of the flange circumference is expected to show deviation around 41 mm (Punch stroke + initial sheet thickness). The results of experiments AE-02, AE-06, AE-07 and LBHF steel simulation satisfy this condition (Figure 5.77).

On the other hand, results of experiment AE-05 are not reliable since a very low number of data points are used in the measurement. In addition, in Figure 5.77, no wrinkles are observed for the experiment AE-05, whereas, in Figure 5.79, it is stated that there are 22 wrinkles counted on the flange.

When the rest of the results are observed from Figure 5.77 wrinkles are visible, but the range and amplitude of the wrinkles show variations. The reason of difference in the range can be explained with the incorrect referencing in the measurement and excessive or inadequate stroke of punch. For instance, the experiment AE-07 gives a homogeneous distribution of wrinkling waves with an average amplitude of ca. 1.5 mm (from Figure 5.77), the wave amplitudes of experiment AE-02 are about a quarter of a millimeter. Furthermore, the LBHF steel simulation showed considerably slight wrinkling, compared to the experiments (Figure 5.78).

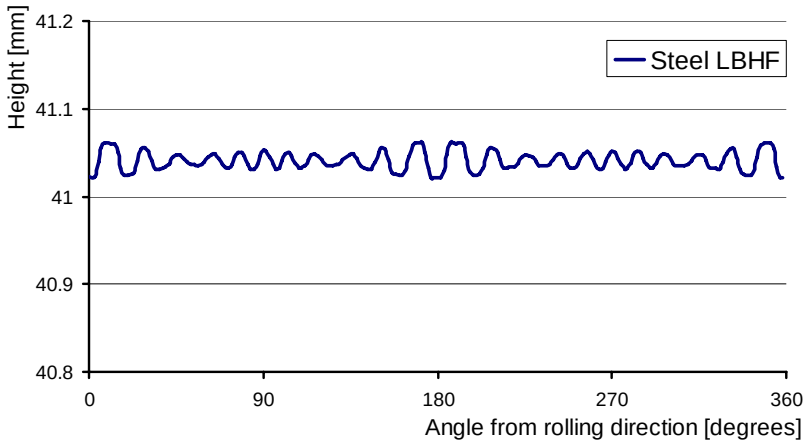

Figure 5.78: Wrinkling waves of the LBHF steel simulation

The reason of changes in amplitude of wrinkles can be related with the possible differences in the applied blank holder force and the uncontrollable variation of friction forces throughout the experimental setup. Experiment setup may be insufficient to transfer desired force (10 kN) exactly onto the flange.

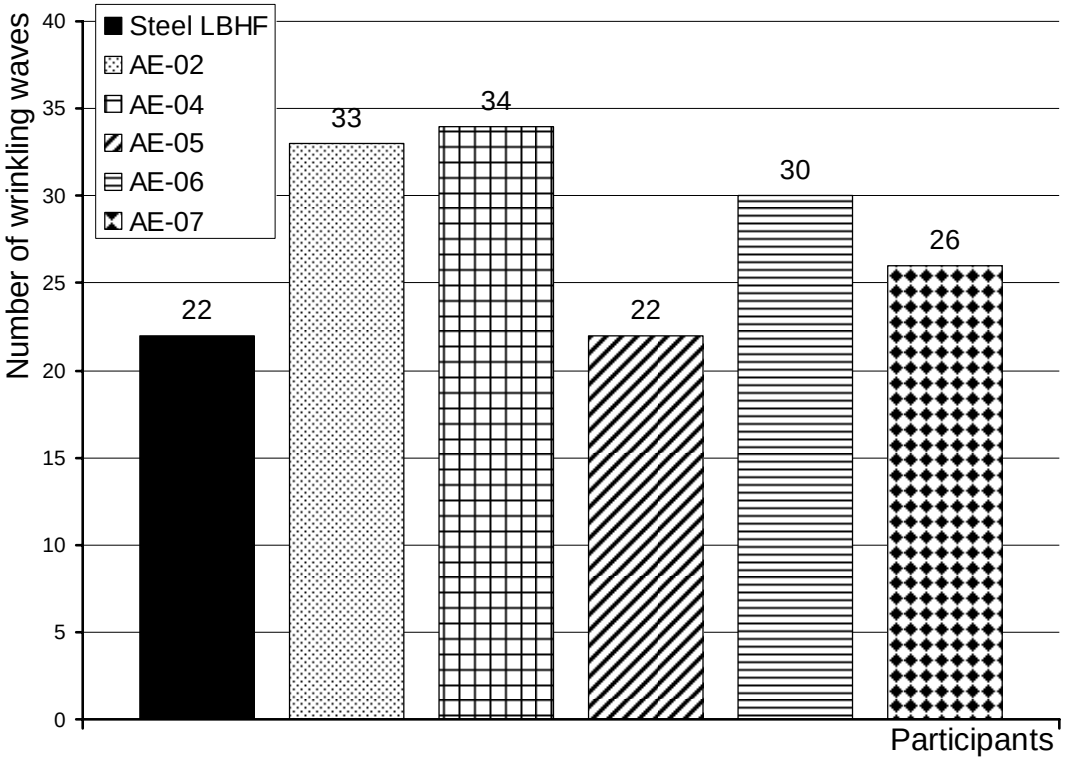

Figure 5.79: Number of wrinkles occurred on the flange of Steel LBHF simulation and experiments

Almost all simulation results of steel material are verified perfectly with benchmark experiments. The compliance between the results is not only determined by the general behavior but also satisfied numerically. Besides the cylindrical cup drawing of steel blank, aluminum material is also concerned,

Figure 5.80 shows the force – displacement curves and compares the HBHF aluminum simulation with experiments. As the curves are inspected, it is seen that there is 25 percent to 45 percent variation between the results. Yet the experiments

themselves differentiate from each other about 20 percent. To reveal the reason of poor estimation and large variation between the results, further studies are performed.

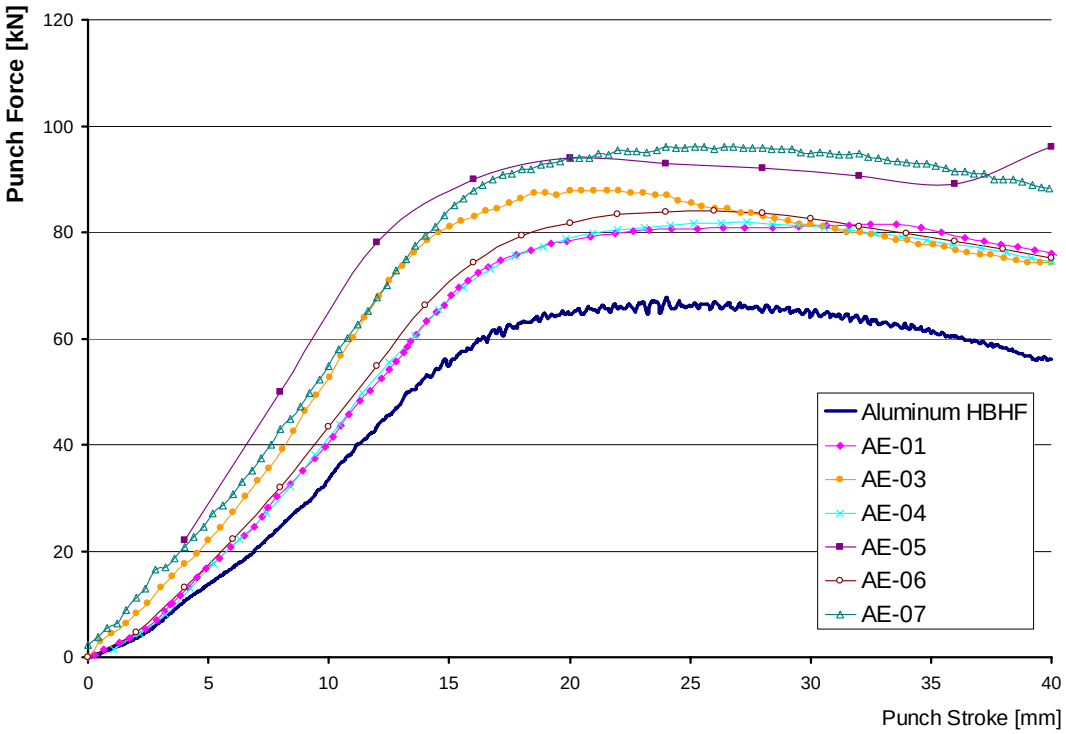

Figure 5.80: Comparison of forming force – displacement curve of aluminum HBHF simulation with six benchmark experiments

Firstly, the HBHF aluminum simulation results are compared with 14 benchmark simulations. Figures 5.81, 5.82 and 5.83 show the comparison between the forming force - displacement curves of aluminum HBHF simulation and the benchmark simulations. Dynamic-Explicit, Static-Explicit and Implicit finite element codes are utilized by the participants in the benchmark. AS-02, AS-03, AS-07, AS-13, AS-14, and AS-16 estimated lower than the HBHF aluminum simulation result, whereas results of AS-01, AS-08, and AS-15 are higher estimations. AS-05, AS-06, AS-10, and AS-12 have the nearly same results in terms of the f-d relationships with the HBHF aluminum simulation. It should be noted that AS-06 and AS-12 also used the PAM-STAMP package, therefore it is not surprising to have identical

results with these participants. However, the compatibility of the results of A-06 and AS-12 with the HBHF aluminum analysis must also be investigated by inspecting the thickness contours and flange profiles.

Another important observation is that the result of AS-11 meets with lower bound of benchmark experiment results (Figure 5.83). When the information about AS-11 is inspected (Appendix B), it is noticed that this participant utilized an implicit finite element code. It is known that the performance of implicit codes in the computation of stresses and forces are better than that of the explicit codes. However, AS-08, AS-09, AS-15, and AS-16 also employed implicit codes, which underestimated the experiment result. The other differentiating property of AS-11 is the material law utilized in the analysis.

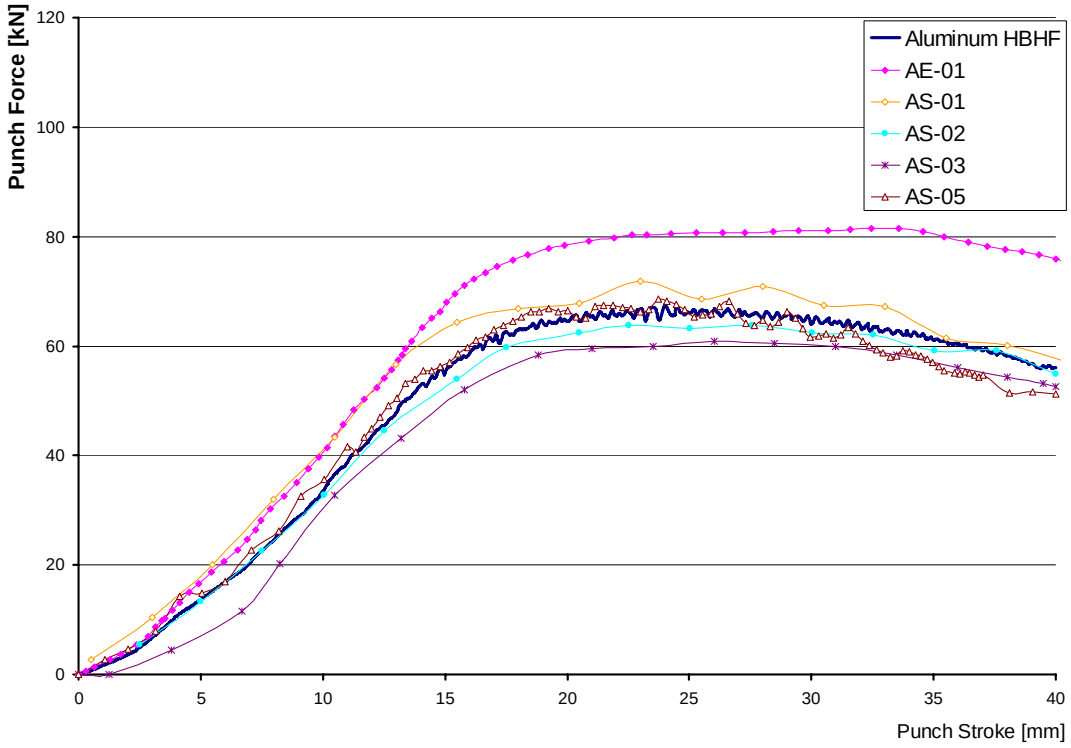

Figure 5.81: Comparison of forming force – displacement curve of HBHF aluminum simulation with benchmark simulations (1)

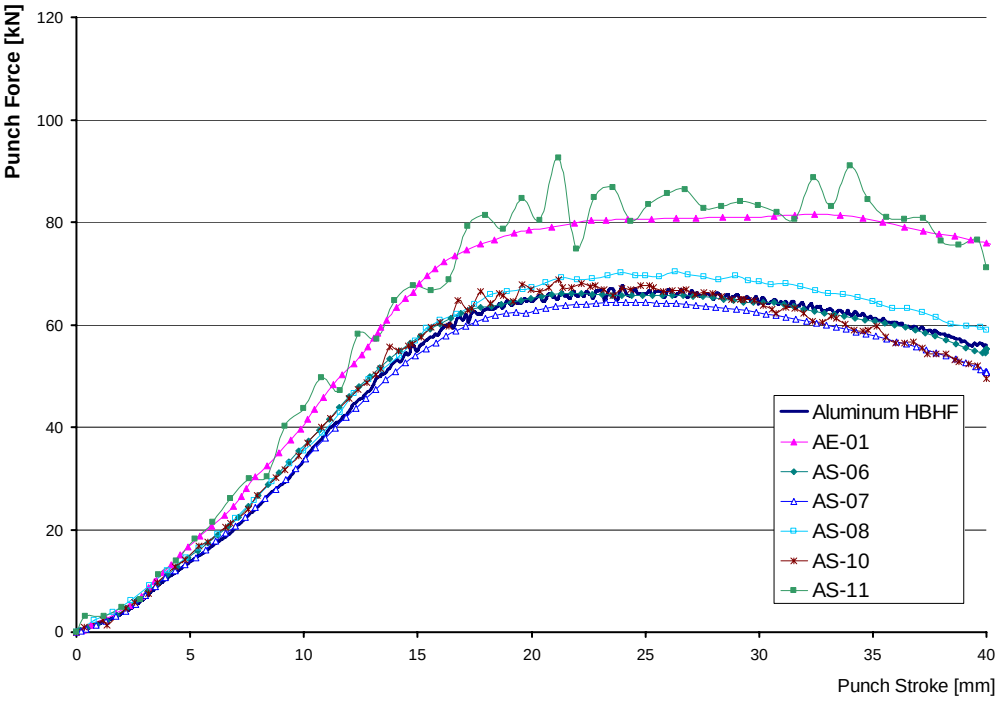

Figure 5.82: Comparison of forming force – displacement curve of HBHF aluminum simulation with benchmark simulations (2)

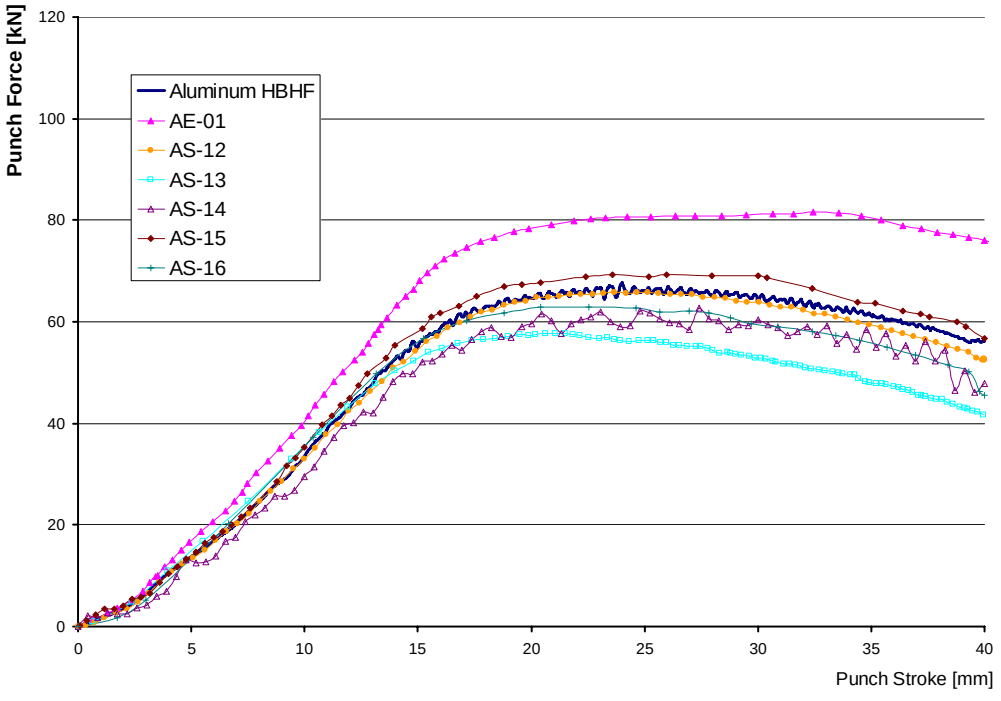

Figure 5.83: Comparison of forming force – displacement curve of HBHF aluminum simulation with benchmark simulations (3)

According to the planar anisotropy data supplied by the NUMISHEET for the aluminum workpiece, orthotropic Hill 1948 isotropic hardening material law is used in the simulations within this thesis study, as well as in all benchmark experiments except AS-11. However, Banabic, Bunge, Pöhlandt and Tekkaya (2000) state that the Hill 1948 yield criterion should be only used in order to obtained simple approximations of the anisotropic behavior of sheet metals and it would be better to avoid its use especially for aluminum alloys. Hill 1990, Barlat and Karafillis – Boyce yield criteria can be used to obtain more accurate models for the plastic behavior of anisotropic sheet metals, including the aluminum alloys. Nevertheless, those criteria need excessive experiments and material data that are not provided by the NUMISHEET, thus Hill 48 yield criterion inevitably is used as the basic material law in the simulations. This reveals why deep drawing simulations of the aluminum material give poor results compared to the experiments. Therefore, no more results are compared with the benchmark; instead, additional study about the yield criteria is done.

For anisotropic materials the present state-of-art of numerical analysis is somewhat confusing, since various yield criteria are proposed up to now and they are still being used. In practice, the choice of a yield criterion depends on the experimental constraints. Table 5.11 lists the experimental data required for the formulation of various yield criteria.

Table 5.11: Required experimental data for the formulation of yield criteria (Banabic, Bunge, Pöhlandt and Tekkaya, 2000)

Author, Year	σ_0	σ_{45}	σ_{90}	σ_b	τ	r_0	r_{45}	r_{90}
Hill 1948	x					x		x
Hill 1990	x	x	x	x	x		x	
Chu 1995	x			x		x	x	x
Barlat et al. 1996	x	x	x	x		x	x	x
Lin, Ding 1996	x		x	x		x	x	x

Except of Hill 1948, these yield criteria in Table 5.11 necessitate the experimental determination of the equibiaxial yield stress σ_b, which requires additional work and special testing devices. Therefore, commercial finite element codes frequently use the Hill 1948 yield criterion, since it is easiest to implement. Banabic, Bunge, Pöhlandt and Tekkaya (2000) state that Hill 1948 yield criteria can represent neither the "anomalous" behavior observed by Woodthrope & Pearce (1970), where $r < 1$ *and* $\sigma_b > \sigma_u$ nor the "second order anomalous" behavior where

$$\frac{r_0}{r_{90}} > 1 \ \textit{and} \ \frac{\sigma_0}{\sigma_{90}} < 1 .$$

5.5 Comparison with Analytical Formulations

Simulations compared with NUMISHEET 2002 Benchmarks are also verified with the analytical formulation proposed by Ramaekers (1999). The computer program is run for the calculation of the forming force of cylindrical cup drawing process of DDQ steel sheet. The material and process data required by the program are summarized in Table 5.12:

Table 5.12: Material properties and process parameters used in the analytical formulation for steel workpiece

Material Properties		**Process Data**			
K [MPa]	547.763	Punch radius [mm]	50	Friction coefficient at the flange	0.0426
ε_0	0.00088	Die radius [mm]	51.25		
n	0.26921	Punch fillet [mm]	7		
R_0	2.16	Die fillet [mm]	9.5	Blank holding pressure [MPa]	2.653
R_{45}	1.611	Blank radius [mm]	105		
R_{90}	2.665	Blank thickness [mm]	1		

The results of the program is given in Figure 5.84 including critical forming force, four force component curves, forming force curve with respect to instantaneous drawing ratio β(i), which is

$$\beta(i) = \frac{r_u(i)}{r_i} \tag{5.6}$$

where $r_u(i)$ is the radius of the rim of the sheet at increment i, r_i is the mean radius of punch (r_p) and die (r_d)

All forces are made dimensionless, by dividing them by the following (Eq. 5.7):

$$F^* = \frac{F}{2\pi r_i s_0 C} \tag{5.7}$$

where F^* is the dimensionless force, F is the true force value, r_i are the mean radii of punch and die, s_0 is the initial sheet thickness, C is the hardening coefficient.

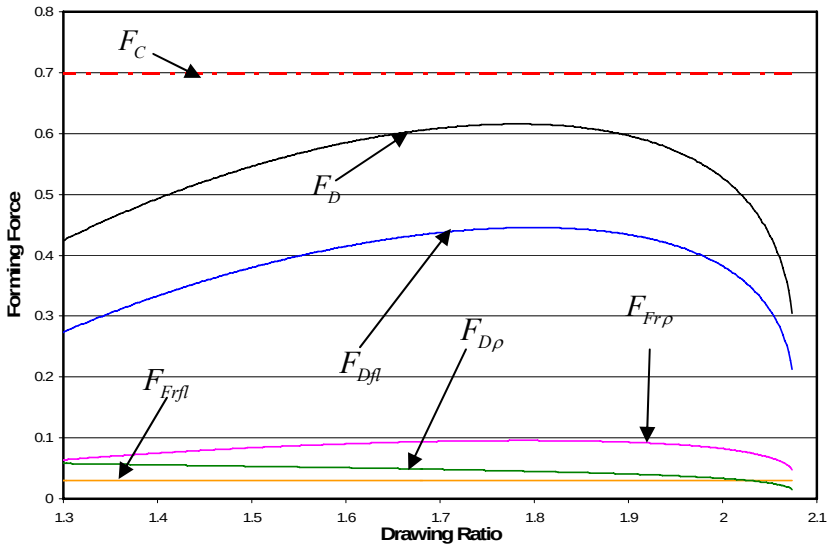

Figure 5.84: Friction force on the flange (F_{Frfl}), friction force at the die fillet ($F_{Fr\rho}$), bending-rebending force at the die fillet ($F_{D\rho}$), flange deformation force (F_{Dfl}), critical force (F_C) and total forming force (F_D)

Same material properties and process data is also used in the simulation and punch force – displacement curve is obtained at the end of the analysis. Figure 5.85 shows initial, final, and intermediate stages of simulation and its thickness distribution. In the axisymmetrical deep drawing simulation, punch force can be taken as equal to the forming force it is drawn with respect to the instantaneous drawing ratio β(i) that is defined with Eq. (5.6).

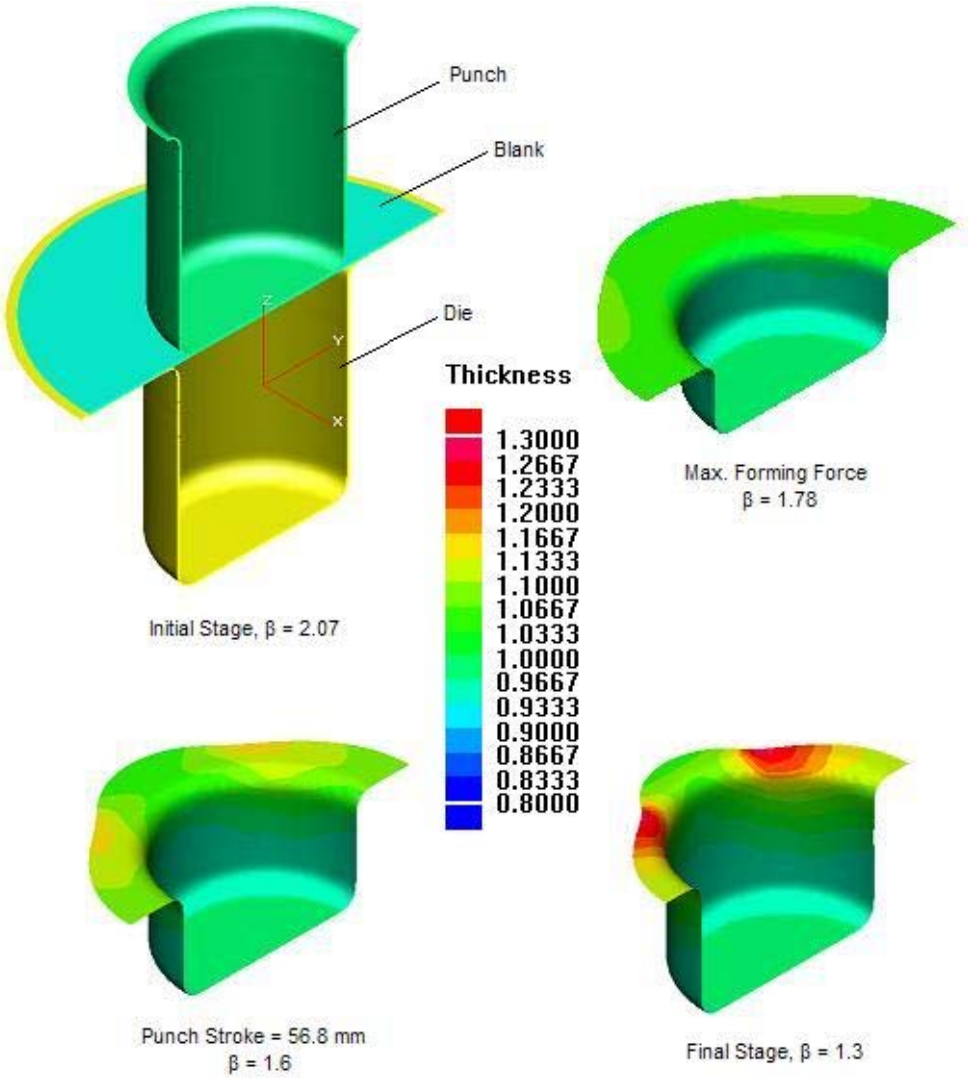

Figure 5.85: Initial, intermediate and final stages of axisymmetrical HBHF deep drawing simulation of DDQ steel and the thickness distribution

Figure 5.86 shows that forming force curves of analytical formulation and numerical experiment are very similar to each other almost at all regions except the initial and final stages of the drawing process. The source of the dissimilarity at the beginning of the process is related with the formulation of the analytical approach. It assumes that forming force has a non-zero value at the very first increment of the process whereas in the simulation the calculation starts when the punch is stationary and has no contact with the blank, thus the forming force is zero. Besides, the simulation result is higher than the analytical formulation at the late increments of the process, where the thickened flange is drawn into the die cavity. When the flange is drawn in, ironing may occur. Simulation can calculate the ironing force and increase the total force requirement of the forming process, but the analytical formulation suggested by Ramaekers (1999) neglects the additional forces created by ironing; therefore it estimates a lower forming force.

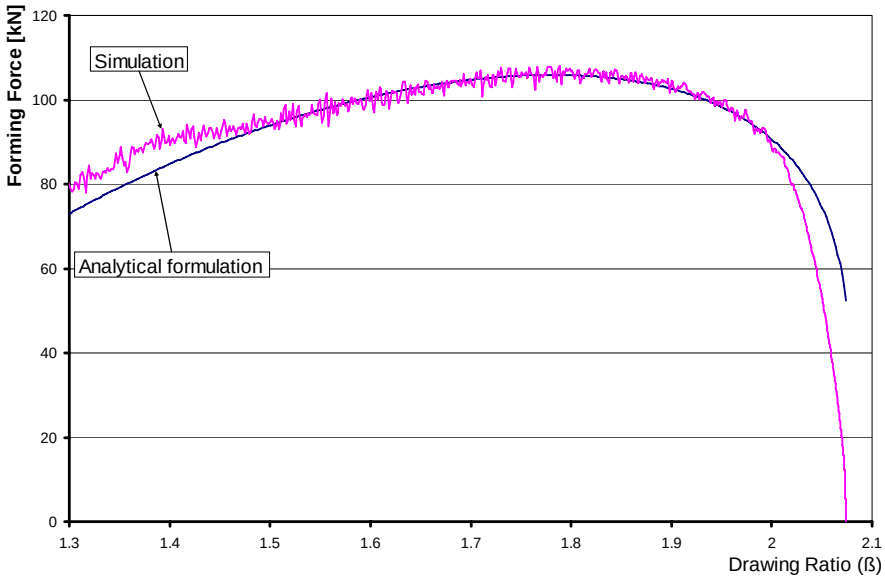

Figure 5.86: Comparison of forming force vs. instantaneous drawing ratio of HBHF steel drawing simulation and analytical formulation

The same comparison is also done for the aluminum workpiece whose radius is 90 mm. All the other material properties and process parameters used in the calculation program and simulation are given in Table 5.13:

Table 5.13: Material properties and process parameters used in the analytical formulation for aluminum workpiece

Material Properties		**Process Data**			
K [MPa]	538.225	Punch radius [mm]	50	Friction coefficient at the flange	0.0096
ε_0	0.00256	Die radius [mm]	51.25		
n	0.2255	Punch fillet [mm]	7		
R_0	0.894	Die fillet [mm]	9.5	Blank holding pressure [MPa]	2.908
R_{45}	0.611	Blank radius [mm]	90		
R_{90}	0.660	Blank thickness [mm]	1		

Simulation of the axisymmetrical HBHF aluminum deep drawing is performed by using the identical data provided for the benchmark. The forming force variation in the domain of drawing ratio between β_{max}=1.78 and β_{final}=1.3 is obtained and plotted with respect to the instantenous drawing ratio in Figure 5.87.

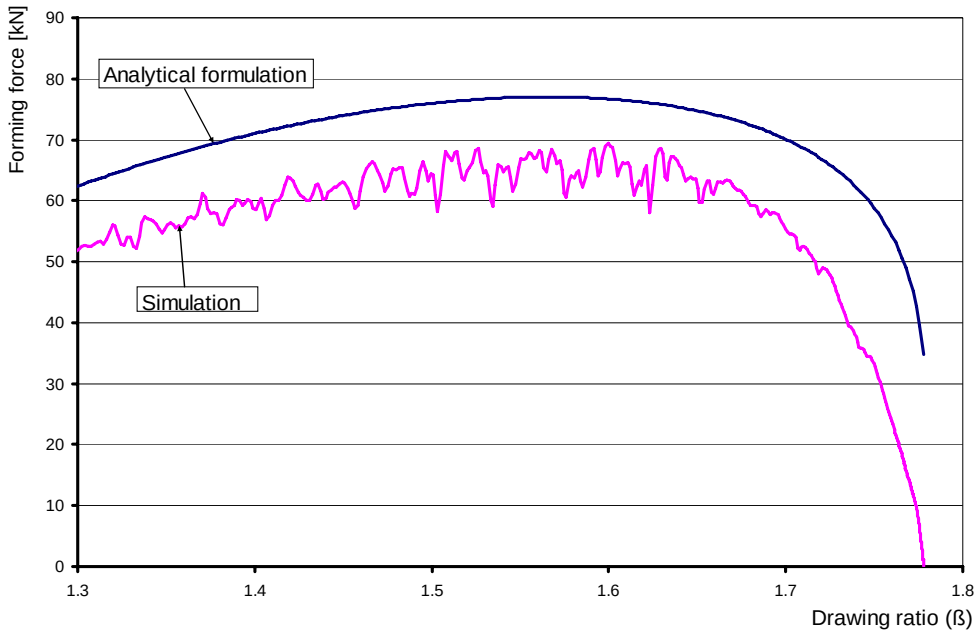

Figure 5.87: Comparison of forming force vs. instantaneous drawing ratio of HBHF aluminum simulation and analytical formulation

Simulation presents the general behavior of the forming force curve but underestimates the value of it. This phenomenon is mentioned in Section 5.4, where the simulation is compared with experiments. The simulation using Hill 1948 yield criterion to define the plastic behavior of aluminum workpiece underestimates the contact forces and principal stresses. Comparison with analytical result also verifies the reason of poor estimations and the consequence of the usage of improper yield criteria that is explained in section 5.4.

Furthermore, if the blank holder force is increased from 50 kN to 70 kN for the same aluminum workpiece, and if the part diameter is increased to 105 mm, with keeping the other variables and parameters unchanged, the analytical program will predict a failure since the critical force is exceeded (Figure 5.88).

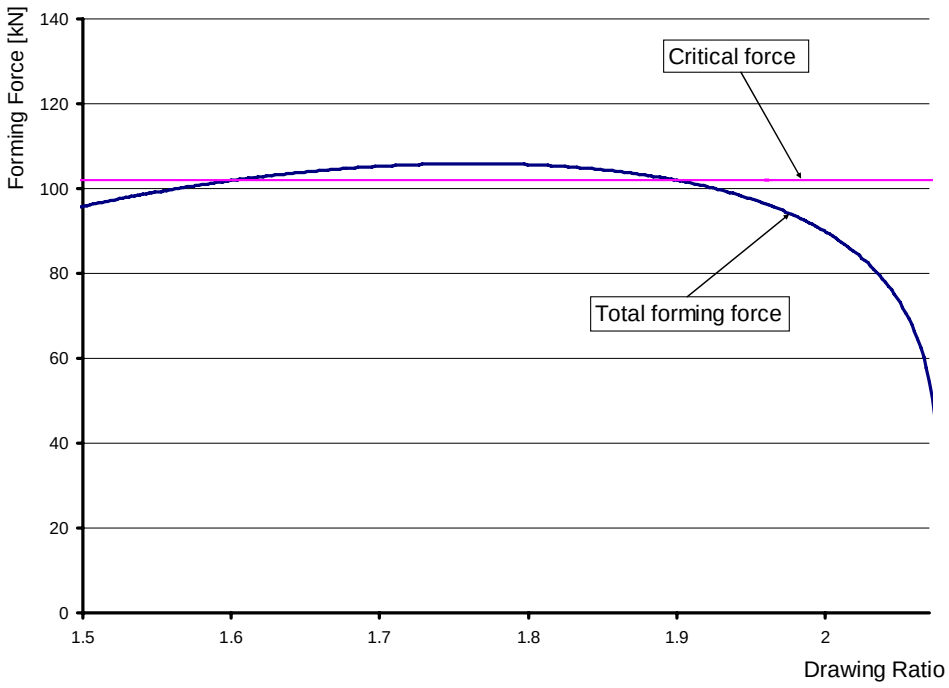

Figure 5.88: Analytical calculation of total forming force and critical force for the deep drawing of aluminum blank

In Figure 5.88, it is seen that total forming force exceeds the critical force when the drawing ratio is equal to 1.89. This can be interpreted as an excessive thinning

occurring at the bottom fillet of the workpiece. According to the analytical calculation, the blank will fail when the corresponding drawing ratio is achieved.

On the other hand, the simulation with the parameters mentioned above will not predict this failure. If the thickness distribution at the time when the instantaneous drawing ratio is equal to 1.89 at Figure 5.89 is inspected, it is seen that the part shows about 17 %. According to the material properties (Table 5.1) the process is successful, since the material can undergo thinning up to 27 %. This reveals another consequence of using improper yield criterion that while the force and stresses are underestimated in the simulation, thickness distribution is overestimated and results are insensitive to possible failure modes. Therefore, for further analyses it must be noted that the forming limit of aluminum is overestimated by the current Hill 48 material model.

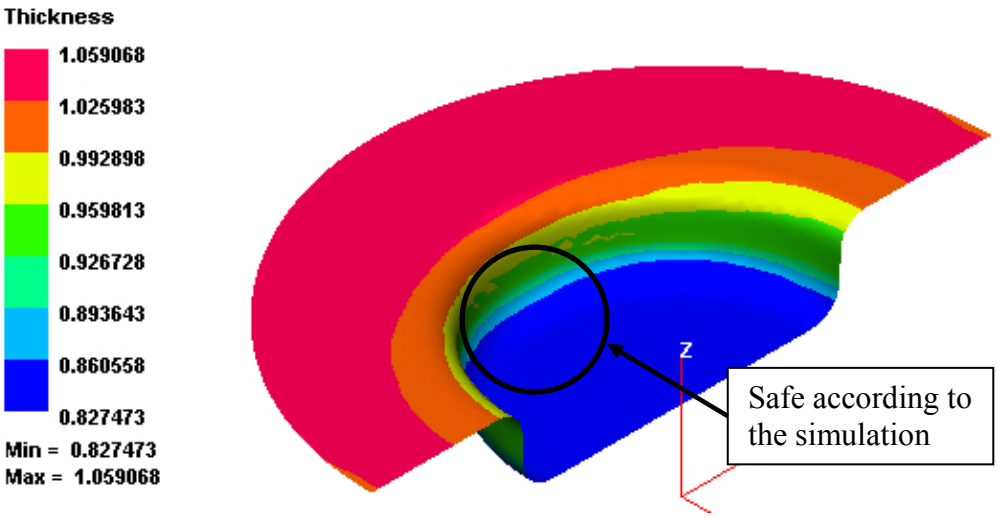

Figure 5.89: Thickness distribution of aluminum blank at the instantaneous drawing ratio of 1.89

CHAPTER VI

EXPERIMENTAL VERIFICATION

6.1 Introduction

In this chapter, the numerical simulation of a ball bearing case (provided by ORS Company) will be conducted. Firstly, the part geometry and the material properties of the workpiece and the process parameters for formation of the workpiece will be discussed. Then, the simulation results will be compared with the actual part. Finally, the metallographic investigation of the workpiece will be conducted.

6.1.1 Geometry of the Ball Bearing Case

The ball bearing case is a circular part having a cup-like shape. Figure 6.1 is a picture of the sample and Figure 6.2 is a sketch of the sample, showing the dimensions. The part has an outer diameter of 66.75 mm, a cup height of 12.95 mm, the hole of the part has a diameter of 52.8 mm and the inner ring of the part has a diameter of 61.3 mm.

The bearing case is formed from a DIN St4 sheet metal, with an initial thickness of 0.5 mm. The workpiece is coated with manganese phosphate after formation.

Figure 6.1: Picture of the ORS ball bearing case

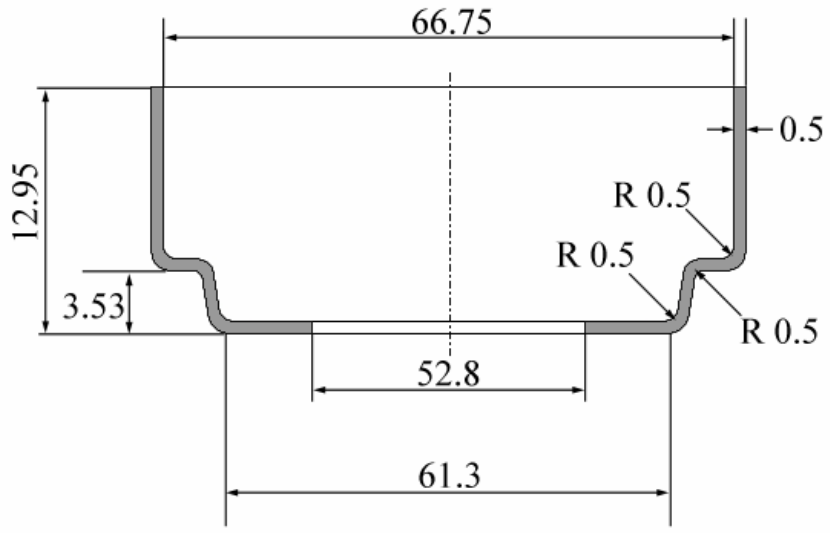

Figure 6.2: Dimensions of the ball bearing case

6.1.2 Process Geometry and Process Parameters

The part is formed in a mechanical press. The snapshot of the tool model is given in Figure 6.3. The upper part of the tool is mobile, whereas the lower part is stationary, except for the lower blank holder part. The part coded with color pink acts as the punch. In this system the punch is stationary, whereas the female die (yellow) moves onto the punch. Initially a circular part with a diameter of 84.25 mm is cut from the sheet. Afterwards, the blank is held between the binder and the lower blank holder. The blank holding pressure is supplied with 10 springs under the lower blank holder part and 8 springs over the upper blank holder part. Maximum stroke of the tool is 14.25 mm, and the tool velocity is about 100 mm/s.

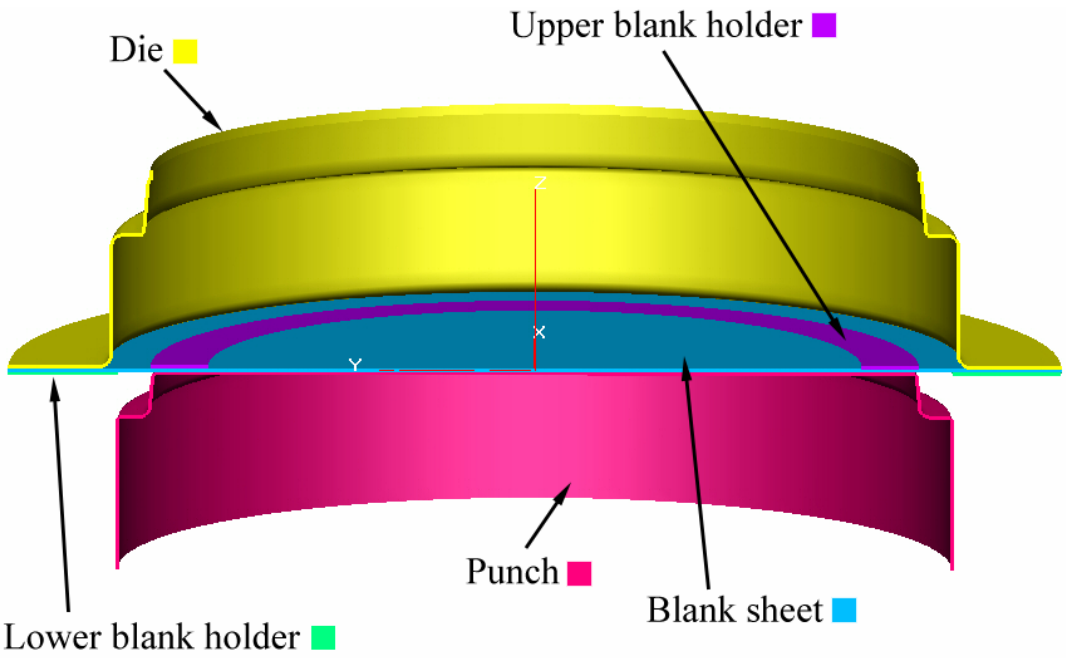

Figure 6.3: The tool setup

Upper springs supply a force of 2 kg/mm, whereas lower springs supply 2.3 kg/mm. Considering the maximum stroke of 14.25 mm, the blank holding forces of the upper and lower blank holder parts as a function of stroke are as tabulated as follows (Figure 6.4):

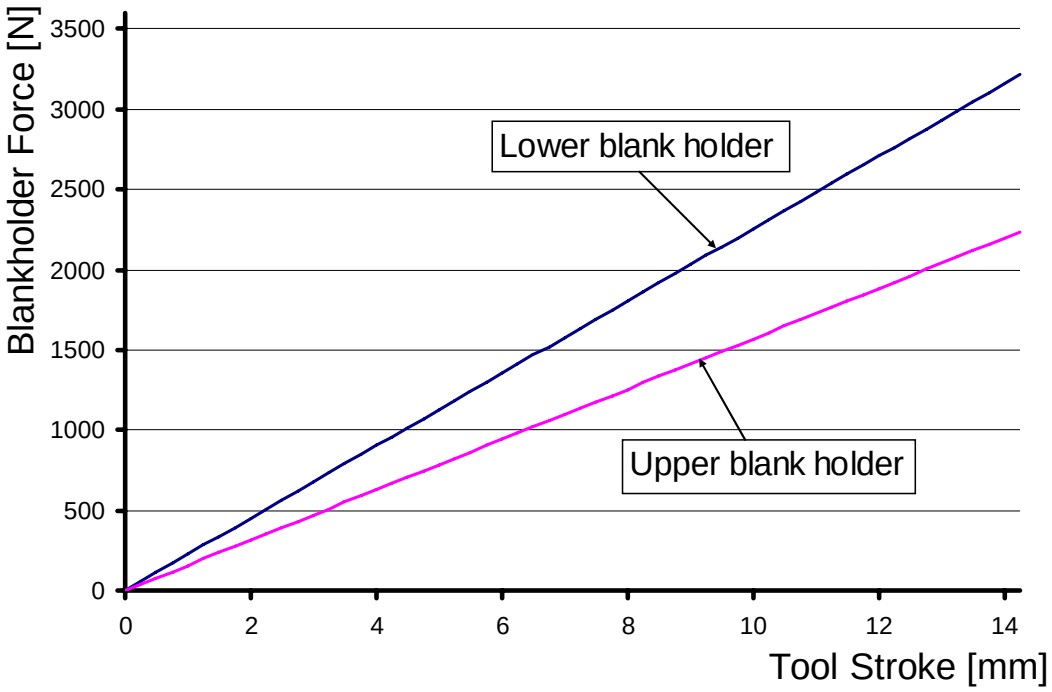

Figure 6.4: Blank holder forces as a function of tool stroke

One important aspect of the tool geometry is that there is a die clearance of 0.49 mm. Therefore ironing present in this part. The pictures of the deformed workpiece also show this occurrence (Figure 6.5)

Figure 6.5: Ironing marks at the side of the workpiece

6.1.3 Material Properties

Material of the bearing case is St4. Its chemical composition and some mechanical properties are tabulated in Table 6.1:

Table 6.1: Material properties of the bearing case

Hardness [HV]	σ_Y [N/mm^2]	Tensile Strength [N/mm^2]	Elongation [%] L_0=80
94	168	302	40

% C	% Mn	% Si	% P	% S	% Al
0.030	0.210	0.020	0.012	0.018	0.035

R_0	R_{45}	R_{90}
1.77	1.16	1.94

Since there were no data available about the anisotropic behavior of the material of the ball bearing case, the anisotropy parameters for the material in concern (St4 steel) are taken from the material database of PAM-STAMP 2G.

6.2 Numerical Simulations of the Bearing Case

The following sections give the comparison of numerical simulations with the part's behavior. The part is modeled exactly from the technical drawings. Blank holding forces are taken as in Figure 6.4 for the upper and lower parts. The lubrication condition is assumed to be uniform and constant throughout the tool, since no information about the lubrication conditions of the tool setup were provided by ORS company due to confidentiality, Coulomb friction coefficient is assumed to be 0.10 throughout the whole system. To speed up the computations, the tool speed is scaled to 5000 mm/s at maximum. The tool is assumed to accelerate from still position to the maximum speed and decelerate to a halt at the end of the stroke. Since the part is considerably smaller than the NUMISHEET 2002 Benchmark's

workpieces, a much smaller element size of 0.8 is used with one level of adaptive meshing. The springback of the part and its behavior upon cutting are also taken into consideration. Trimming and springback stages are also simulated after the drawing (stamping) operation. For this purpose, the implicit solver algorithm of PAM-STAMP 2G is utilized. Table 6.2 summarizes the process and numerical parameters for this operation

Table 6.2: Process and numerical parameters for the simulation of the part

Parameter	Value
Material	St4 steel
Thickness of the sheet [mm]	0.5
Punch stroke [mm]	14.25
Maximum punch speed [mm/s]	5000
Punch speed type	Stroke controlled
Blank holding	Spring loaded, according to Figure 6.4
Friction coefficient	0.10 throughout the system
Initial element size [mm]	0.8
Mesh topology	Structure B from Figure 5.36
Refinement	One level
Mass scaling reference size [mm]	0.203015
Time step scale factor	Default (0.9)
Simulation algorithm for drawing	Explicit, Double Precision
Simulation algorithm for springback	Implicit, Double Precision

6.2.1 Sample Figures Comparing the Experiments and Simulations

The following figures (Figures 6.6 to 6.9) compare the actual pictures and simulation snapshots of several key steps in the formation of the bearing case part.

As seen in Figure 6.6, in stage 1 of deformation, the punch draws the part into the die. As the die walls are reached stage 2 starts, where ironing starts. At stage 3, the bottom part of the die is contacted. The process is finalized with the trimming of the inner part of the part off.

Stage 1 of deformation

Stage 2 of deformation

Stage 3 of deformation

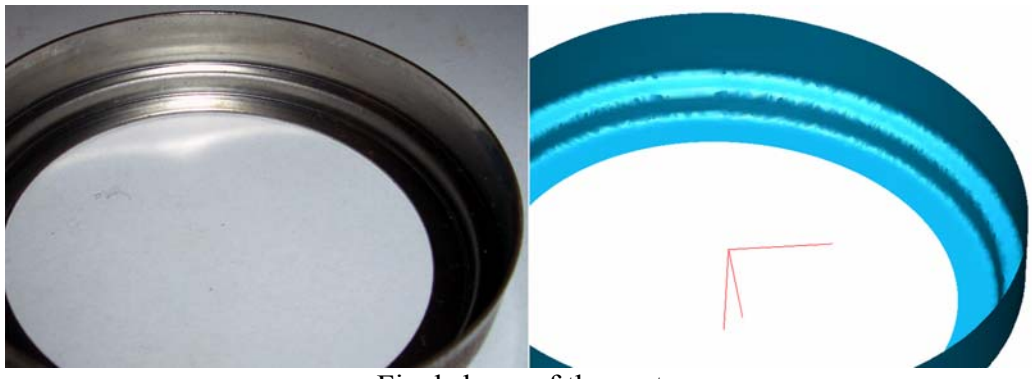

Final shape of the part

Figure 6.6: Stages of deformation

6.2.2 Comparison of the Simulation Results with Part Specifications

In this section the simulation results will be compared with the dimensional measurements and geometrical properties of the actual part, and the effectiveness and the accuracy of the numerical simulation will be inspected.

First of all, as given in Figure 6.7, the actual part wrinkles in the initial stages of deformation, since there is not enough blank holding force at the initial stages, due to the fact that the spring loaded blank holders cannot apply the maximum pressure instantly. As depicted in Figure 6.4, the blank holding forces are assumed to increase linearly with increasing tool stroke. However, the wrinkles in flange region of the actual part in Figure 6.7 are not visible in the simulation case. The punch stroke, at which the picture was taken, is 6.5 mm.

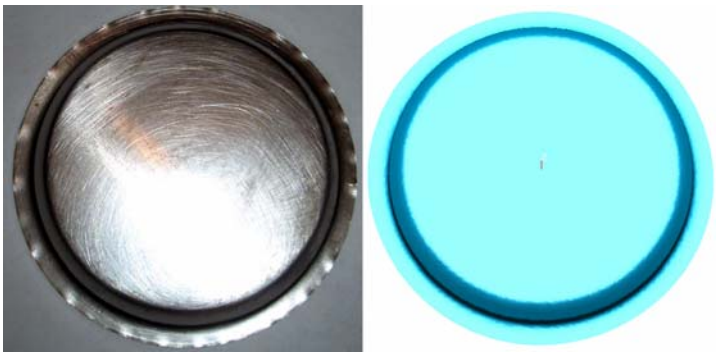

Figure 6.7: Wrinkles in the flange of the actual part

A more thorough examination of a possible wrinkling pattern is conducted by plotting the height profile of the simulated part with respect to the angular direction to rolling direction (which is the X-direction) (Figure 6.8). Some wave-like trend in the flange is observed, which seems dependent on material anisotropy in the simulations. However, no significant wrinkling is present in the figure, the height of estimated wrinkles are too small to be considered physically significant; it may be stated that the simulation failed in determining the wrinkling behavior of the actual part during formation. This may be due to the presence of triangular elements,

which exhibit poor accuracy at the edges of the blank object. However, this may also be due to the fact that the lubrication conditions in the actual system are unknown. Additionally, the blank holding conditions of the system may be assumed wrong for the simulation; the loads provided by the springs may be smaller than expected, or there may be excessive friction between the moving tool parts (especially the upper blank holding part and the die), restricting the free movement of the lower blank holding part, altering the effectiveness of the blank holding loads.

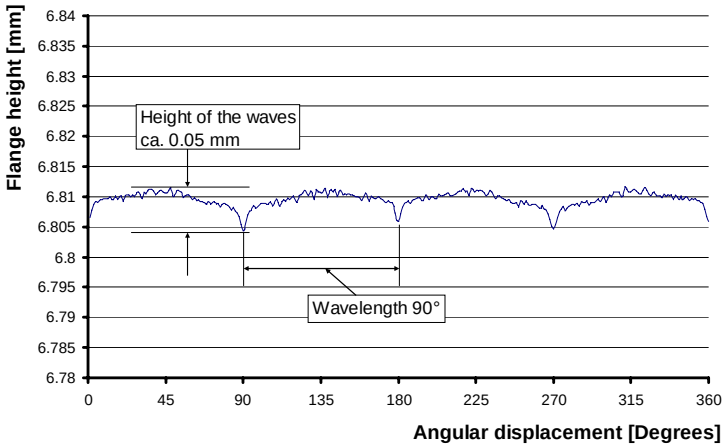

Figure 6.8: Height profile of the simulation in the early stage

On the other hand, in the further stages of the forming process, the effects (and also the presence) of this wrinkling are removed due to ironing.

It is stated before that the part is trimmed in the center after the deformation process. The effects of this trimming (as well as the springback associated with it) are simulated as well. The following figure (Figure 6.9) shows the thickness distributions in the part before and after trimming. The greatest amount of thinning is observed at the middle fillet of the part, where the heaviest deformation is expected to be present. However, the thinning (which has a maximum value of ca. 35 %) at this region is within the safe limit of 40 % allowable elongation. It should also be noted that the part walls have some thinning due to ironing as expected.

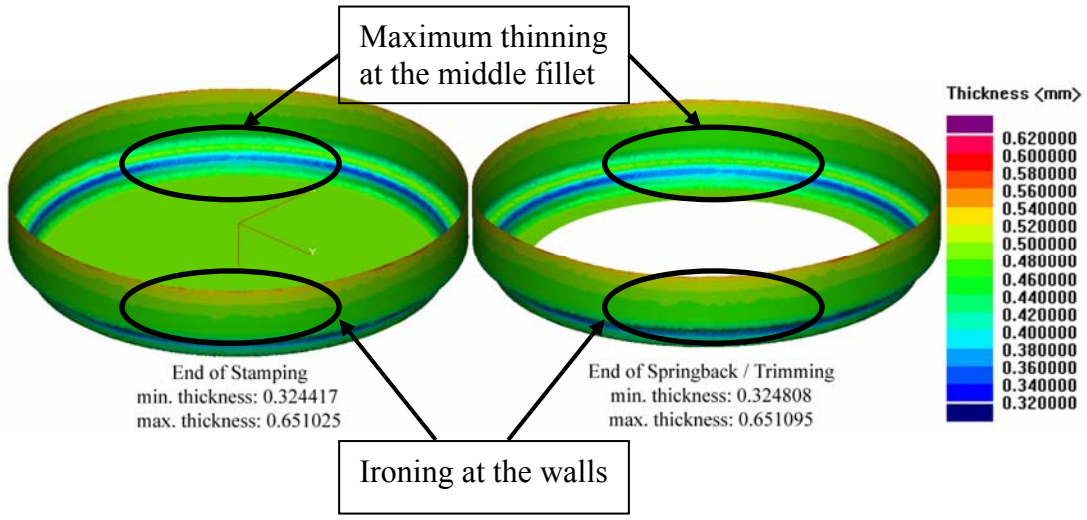

Figure 6.9: Thickness contours of the part at the end of forming stages

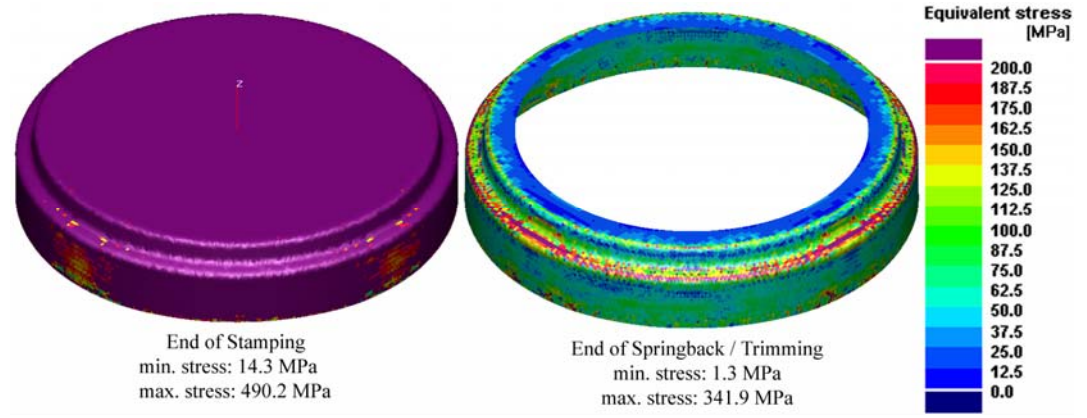

Figure 6.10: Stress contours of the part at the end of forming stages

It is not surprising that the equivalent stress distributions in the part after the two stages are completely different. As it is seen in Figure 6.10, there is a remarkable amount of plastic stress on the part after the stamping stage, whereas the part is still under deformation loads. However, after springback, the part is relaxed, resulting in smaller stresses throughout the part. It is noted that the region near the inner ring of the part is completely unloaded, whereas there are large residual stresses in the middle fillet region of the part. If the overall contour is inspected, it is found that the part is under the influence of residual stresses, which are significantly higher than the stresses present on the material in the loaded case.

Figure 6.11 gives the outer radius variation versus the angular displacement to the rolling direction of the part after stamping and springback respectively. The product specifications of the part (provided by the ORS company) define the outer radius of the part to be 66.75 mm with a tolerance range of ±0.03 mm (Figure 6.2). Since this radius value is measured from the inner surface, the radial positions obtained from the numerical simulation are modified by subtracting half of the final thickness of the region in concern. The purpose of this modification is that the numerical simulation gives the positions of the nodes at the middle surface of part walls (Figure 5.22). By subtracting half the thickness, the radial position of the inner surface (which is not actually demonstrated in PAM-STAMP, since the FE-solution procedure uses 2D shell elements), is correctly calculated.

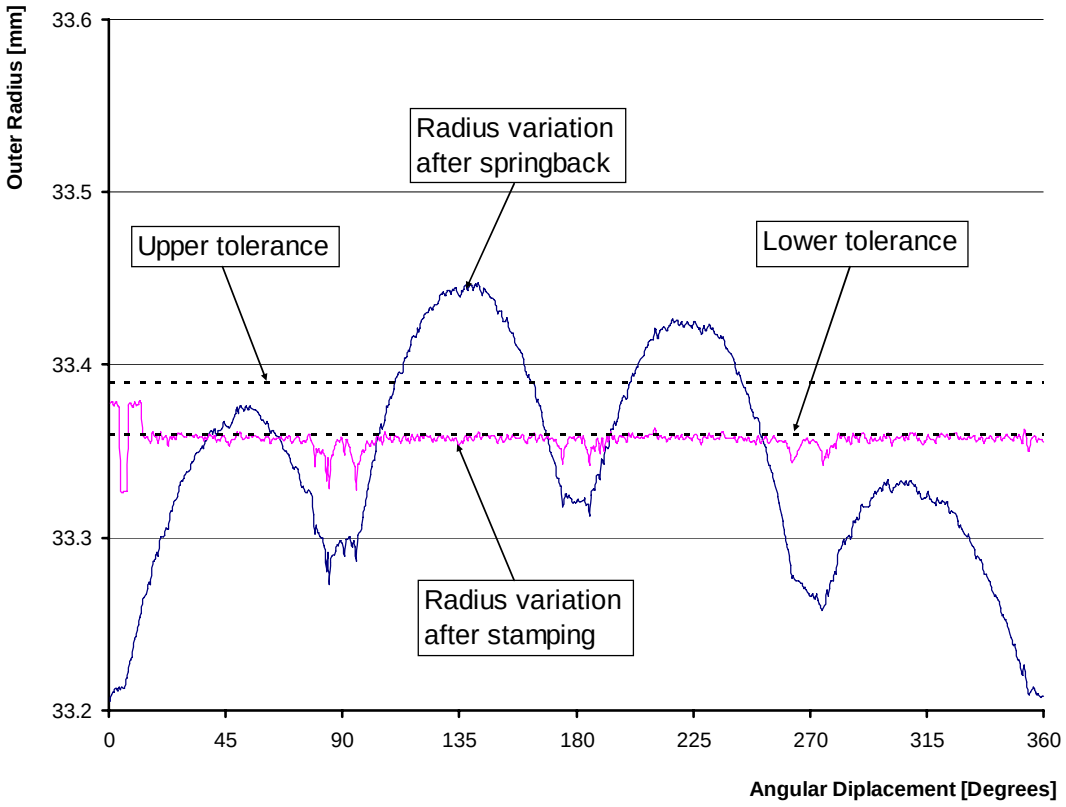

Figure 6.11: Variance of the outer radius of the ball bearing case with respect to angular displacement

It is seen from Figure 6.11 that the results of the numerical simulation does not fall into the defined tolerance range. However, the result is acceptable if the stamping simulation is concerned. This occurrence shows the weakness of the implicit springback algorithm of PAM-STAMP. Additionally the data given in the springback algorithm is obtained from the explicit analysis, and its precision strongly affects the outcome of the springback analysis naturally. Displacement tolerances are lost upon the springback analysis. This may be due to the incompatibilities of the material properties utilized in the simulation with the real material's behaviors. On the other hand, the variance of outer radii is just under the lower limit, with no excessive fluctuations for the stamping simulation. The small fluctuations of the radius may be related to the presence of triangular elements in the sides of the blank mesh. It is known that the triangular elements have a reduced accuracy compared to the quadrilateral elements. However, after trimming and springback, the results deteriorate significantly, showing a wave-like variation trend. It is also observed that the maxima and the minima of the waves correspond to the angular displacements of 45, 90, 135, 180, 225, 270, 315 and 360 degrees. Therefore, it is supposed that the cause of these variations is the orthotropic anisotropy of the material model.

The effect of anisotropy is more clearly observed from Figure 6.12. The height profile of the simulations show earing formation; the magnitude of the height constantly increases up to 45°, than it tends to a minimum at 90° and then it rises again up to the maximum value at 135°, and so on. As expected, after springback, the height decreases throughout the whole part, since the *stretching* effect of the tool loads are removed from the system. The part contracts slightly upon springback.

Although the inner radius of the falls into the tolerance range, there is still a fluctuation on the estimated value (Figure 6.13). An isotropic material will not show such behavior. On the other hand, the tolerance range for the inner radius is larger than the previous dimensions. Therefore, the results being within the tolerance range for the inner radius do not guarantee the success of the simulation.

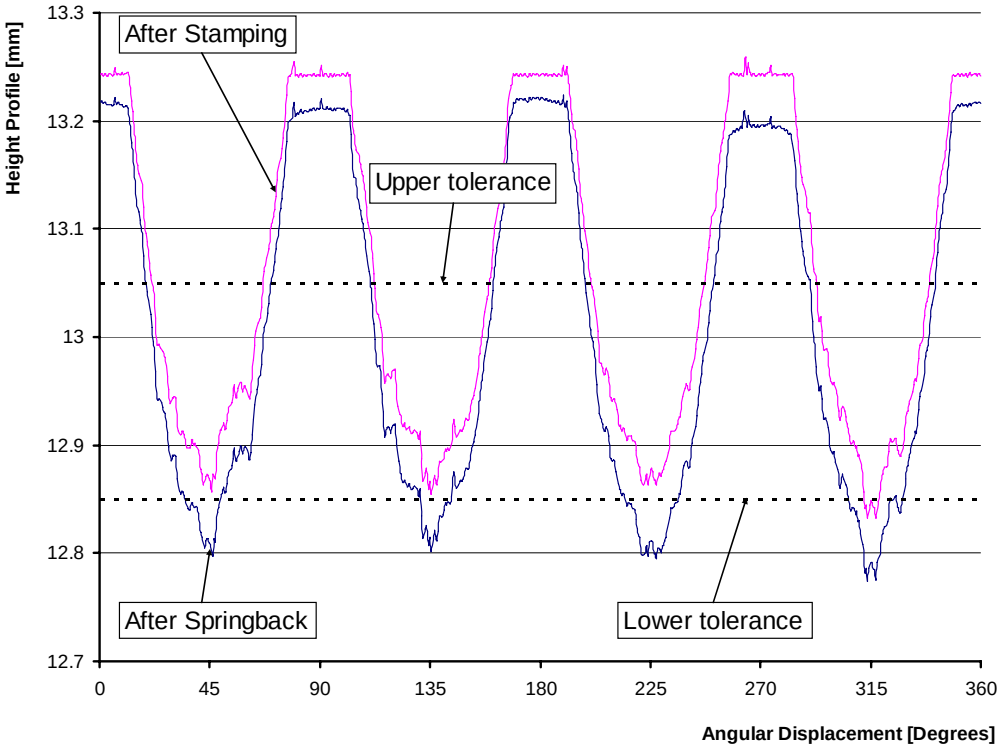

Figure 6.12: Height profile of the ball bearing part

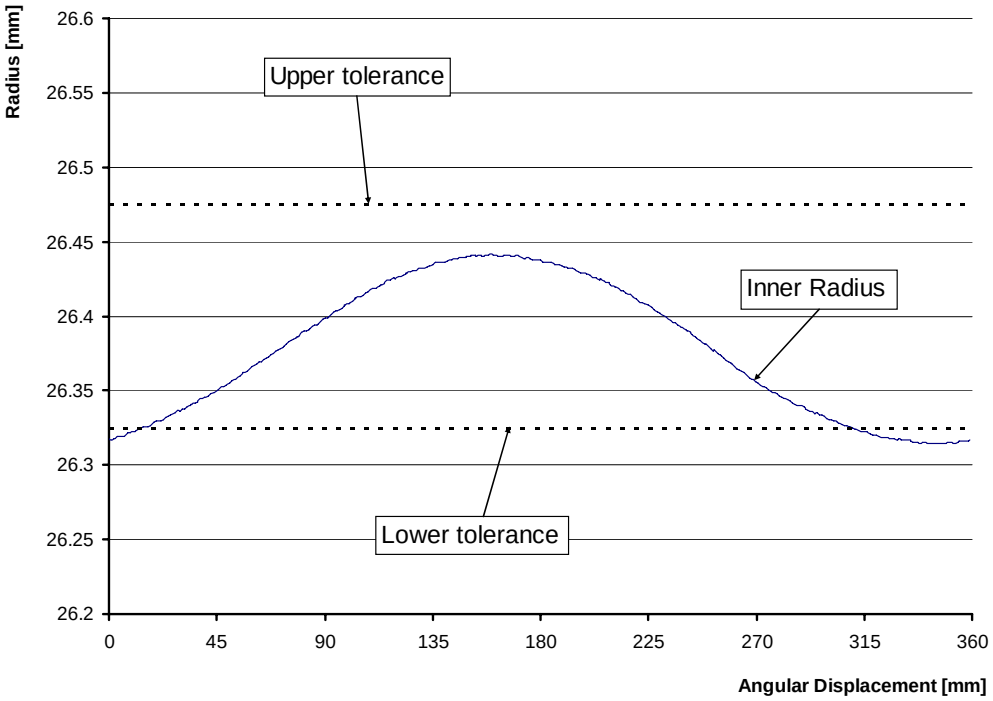

Figure 6.13: Inner radius of the ball bearing part

6.3 Metallographic Analyses

For metallographic analysis, undeformed sheet samples and samples of the ball bearing case part have been obtained from ORS company. The specimens have been cut into small slices, and grounded into bakelite. Three sheet specimens were prepared to inspect the property variations of the material along three directions of the sheet as given in Figure 6.14a. Direction 1 is the sheet surface, direction 2 is the thickness, and direction 3 is the width along the rolling direction.

The specimens have been ground, polished and etched with 5% Nital acid solution. Afterwards, microstructure photos of the samples have been taken. Grain alignments at the deformed piece were inspected, average grain sizes of the samples were measured and microhardness tests were conducted on the samples.

6.3.1 Material

The material (DIN St4 steel) is supplied to ORS company in the form of cold rolled sheet strips. The supplier company is confidential; therefore no further information about the deformation and heat treatment history of the material is available. However, it is noticed that the sheet is covered with a protective oil layer to enhance its corrosion resistance.

The carbon content of 0.03% denotes that the steel is almost a single phase alloy, consisting of a ferrite matrix and a very low amount of pearlite. The percentages of the ferrite and pearlite phases are calculated from a simple lever rule as the following:

$$\%\alpha = \frac{0.76 - \%C}{0.76 - 0.022} \cdot 100 = \frac{0.76 - 0.03}{0.76 - 0.022} \cdot 100 \approx 98.9\% \tag{6.1}$$

$$\%P = 100 - \%\alpha = 1.1\% \tag{6.2}$$

where %α is the mass fraction of the ferrite phase, 0.76 is the eutectoid composition in the Fe-Fe_3C diagram, %C is the weight percentage of carbon, 0.022 is the maximum solubility of ferrite and %P is the mass fraction of the pearlite phase.

Since the percentage of the ferrite phase is considerably high than the pearlite phase, only the ferrite phase is expected to be observed in the microstructure pictures. The microstructure pictures (actually taken with a 400X magnification) in Figure 6.14 do not reveal a pearlite phase at all, as if the material is purely ferritic. To fit the pictures into the page margins, they were resized; therefore the magnification levels changed into 150X.

Micrographs in Figure 6.14 show that no inclusions are present in the specimen and the grains are uniformly distributed. No preferred alignment of the grains is visible is on the sheet surface in micrograph 1 (6.14b). On the other hand, horizontally elongated grains due to rolling are visible in the micrograph 2 of Figure 6.14. At the sheet thickness, the grains are compressed due to rolling. The nearly-vertical marks on the surface are due to poor metallographic preparation.

It is also observed (from Figures 6.14c and 6.14d) that the grains are smaller compared to these on Figure 6.14b. Since the micrographs 2 and 3 represent the sheet thickness and width, elongation of the grains on these micrographs (Figures 6.14c and 6.14d) during rolling of the material into sheet is usual.

Figure 6.14d shows the microstructure of the sheet at the width direction (position 3). Although there are some small grains elongated in the vertical direction (which is the RD), unlike to Figure 6.14c, the alignments of the grains are less, meaning that the effect of rolling are partially removed, possibly due to recrystallization of the sample, pointing the fact that the sheet has undergone some kind of heat treatment. On the other hand it is also possible that the actual microstructure of the part is affected during the preparation of metallographic samples.

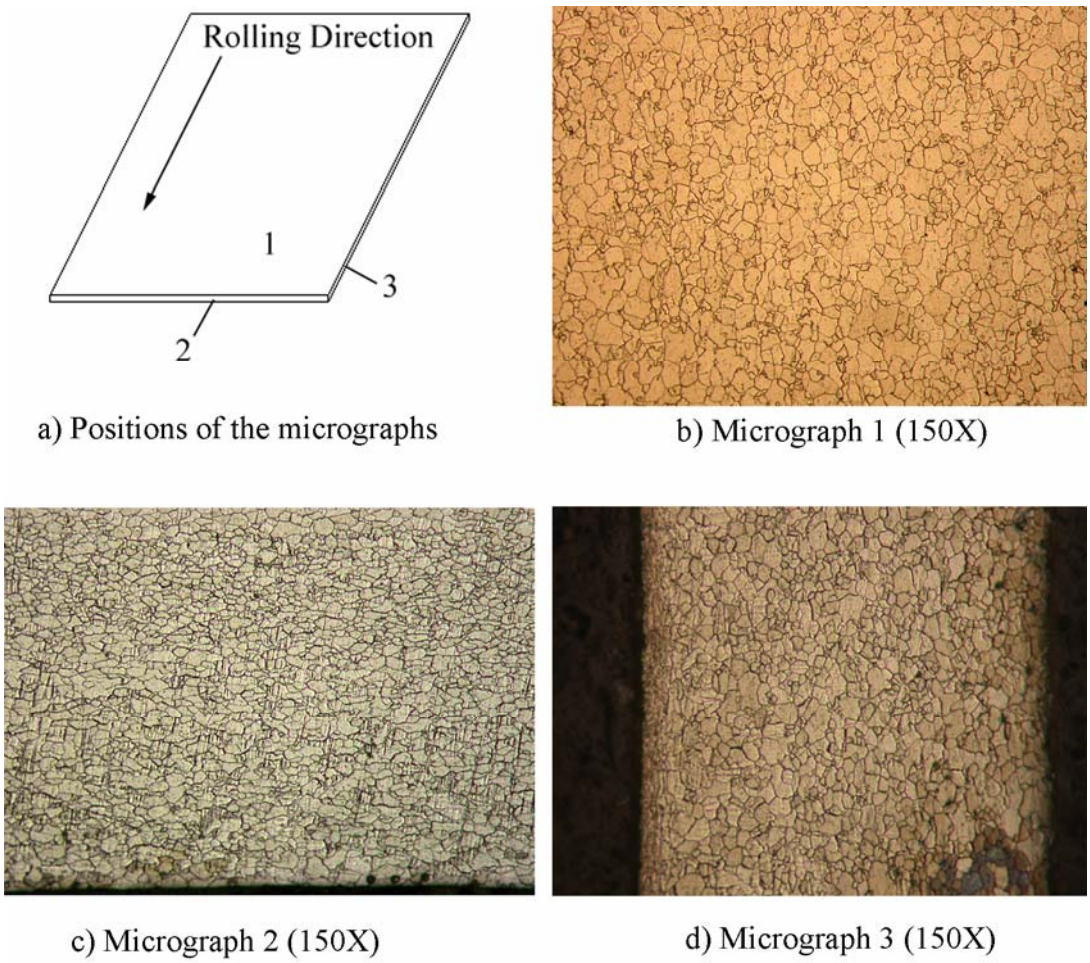

a) Positions of the micrographs

b) Micrograph 1 (150X)

c) Micrograph 2 (150X)

d) Micrograph 3 (150X)

Figure 6.14: Positions of the specimens (a) and the micrographs of the sheet at three positions at 150X (b,c,d)

Knoop microhardness tests were conducted on all metallographic specimens. For this purpose a diamond indenter with a 500 g indentation load was utilized. The indentation lengths were measured in microns under 100X magnification. Then, the corresponding Knoop microhardness (HK) numbers are obtained. Table 6.3 summarizes the findings for the sheet specimen.

Due to the nature of the rolling deformation, the aligned grains at positions 2 and 3 result in larger hardness values (Table 6.3). As expected, the highest microhardness values are encountered at direction 3. The lowest microhardness values are measured at the surface, where the strain hardening effects of the deformation are minimum.

Table 6.3: Knoop microhardness test data of the sheet specimen

Specimen Direction	Indentation Depth [µm]	Average Indentation Depth [µm]	Standard Deviation [µm]	HK
1	274, 256, 263, 264, 257, 264, 265, 259, 262, 262	262.6	5.038	102.85
2	213, 221, 235, 218, 210, 229, 220, 220, 225, 217	220.8	7.361	145.65
3	201, 215, 224, 213, 190, 208, 210, 206, 210, 206	208.3	8.932	164.45

Finally, the grain size of the sheet surface was measured. For this purpose a good quality digital picture of the specimen was processed with an image analysis program. The grains boundaries were marked, and with an image analysis program the area of each grain according to the magnification conditions were determined.

The grain sizes were computed according to ASTM E112-96, using the formula given below (Eq. 6.3):

$$\text{GRAIN SIZE} = 3.321928 \times \log_{10}(N_A) - 2.954 \tag{6.3}$$

where N_A=1/A and A is the object area (area of each individual grain).

Figure 6.15 gives the microstructure picture of the sheet surface, which is used for the grain size measurement. Note that the grain boundaries are marked during image analysis.

Figure 6.16 gives the distribution of the grain size numbers. The average grain size number is found out to be 10.42. According to ASTM E112-96 standard, the larger the grain size number, the smaller the grains. It is expected that after deformation the grain size will decrease, increasing the grain size number.

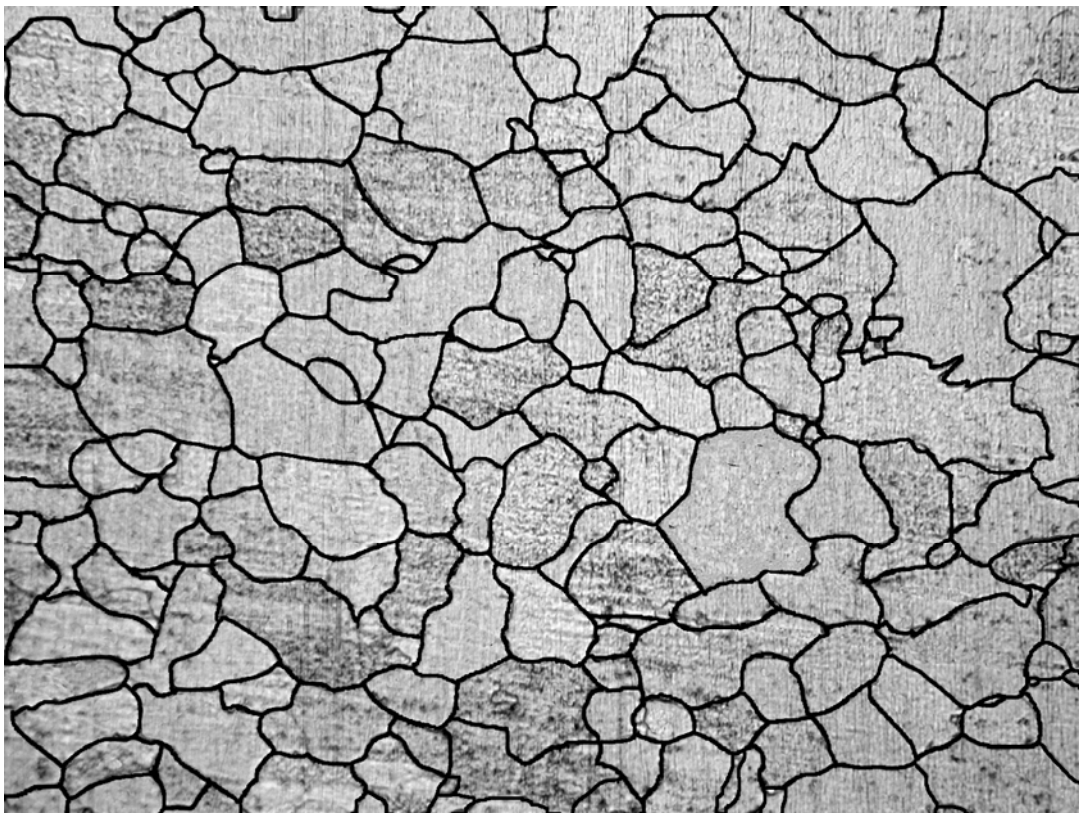

Figure 6.15: Image analysis picture of sheet surface prepared for grain size measurement (825X)

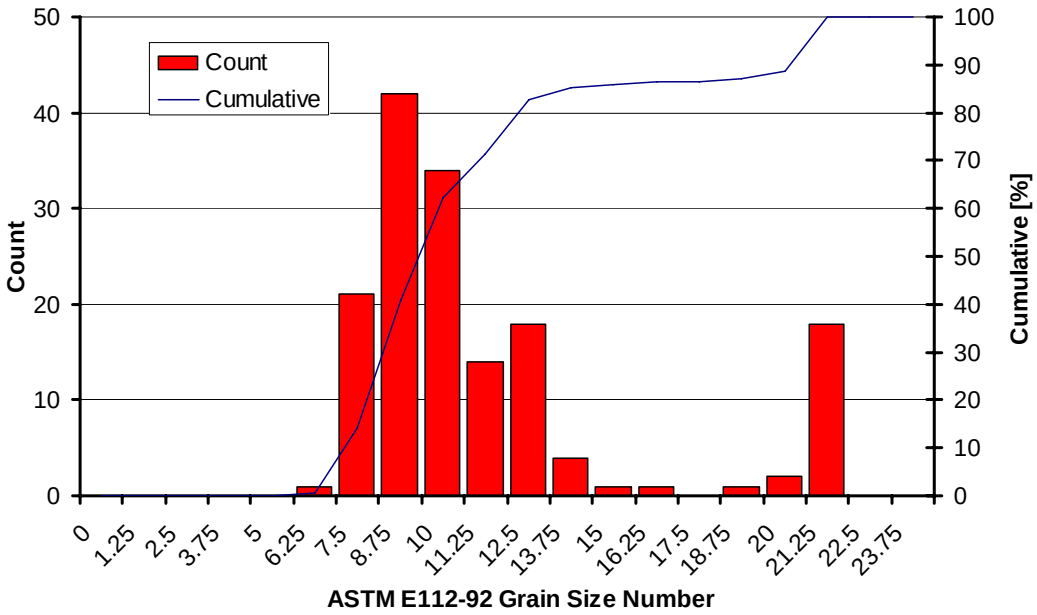

Figure 6.16: Distribution of the grain size numbers for the sheet specimen

6.3.2 Deformed Part

To investigate the effects of the deep drawing operation, several micrographs along a path (as given in Figure 6.17) of the deformed sample were taken.

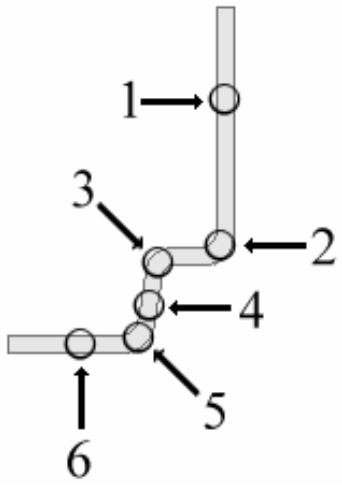

Figure 6.17: Positions of the micrographs of the deformed part

It is known that the grains will align in certain positions, directing the deformation path; the grain alignment shall always be in the thickness direction of the part. This orientation expectance is satisfied as it can be observed from the following pictures (Figures 6.18 to 6.23). The grains follow the deformation path; the rounding of the grains at the corners (Figures 6.19, 6.20 and 6.22) are clearly visible. Where the part is straight, the grains are also straight (Figures 6.18, 6.21 and 6.23). Additionally, the elongations of the grains also depict the deformation. As a final notice, since the samples were small in size, the parts have been deformed uncontrollably during specimen preparation. The parts (having circular shapes) were distorted during holding, prior to cutting. This way, the geometrical details have been deteriorated. Also hot cutting was applied to the parts, which inevitably induced heat effects to the specimens, affecting the microstructure of the parts. For instance, the sharpness of corners in Figures 6.18 and 6.20 (positions 2 and 3) are lost.

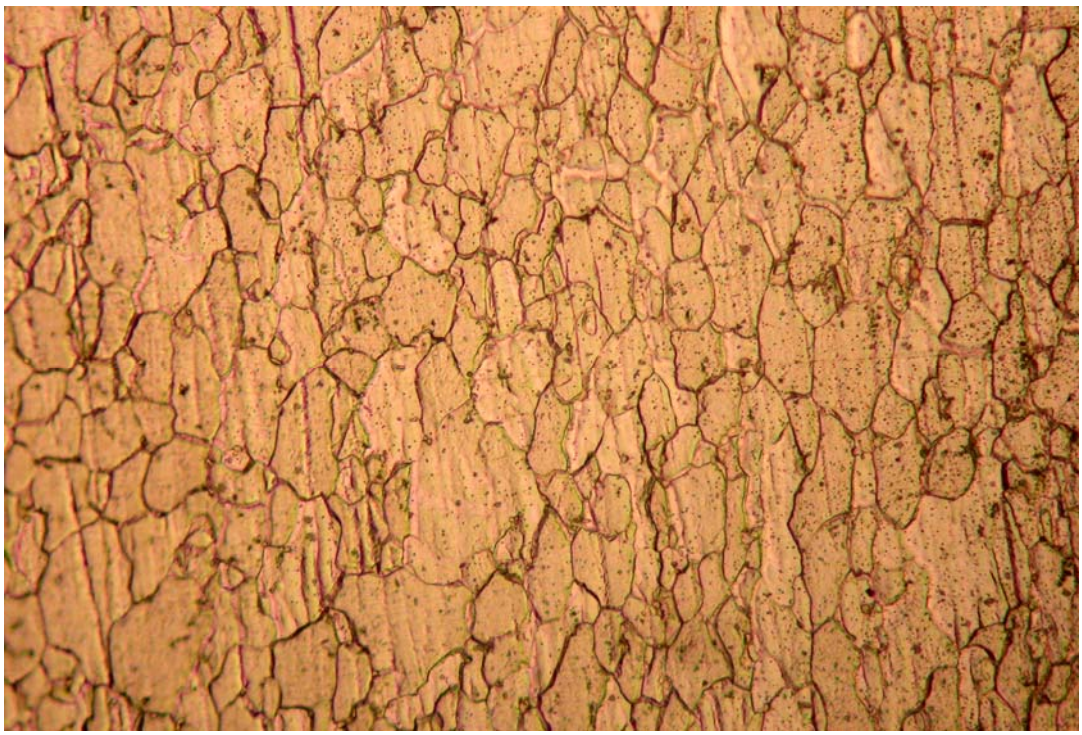

Figure 6.18: Microstructure of the deformed part (position 1) (750X)

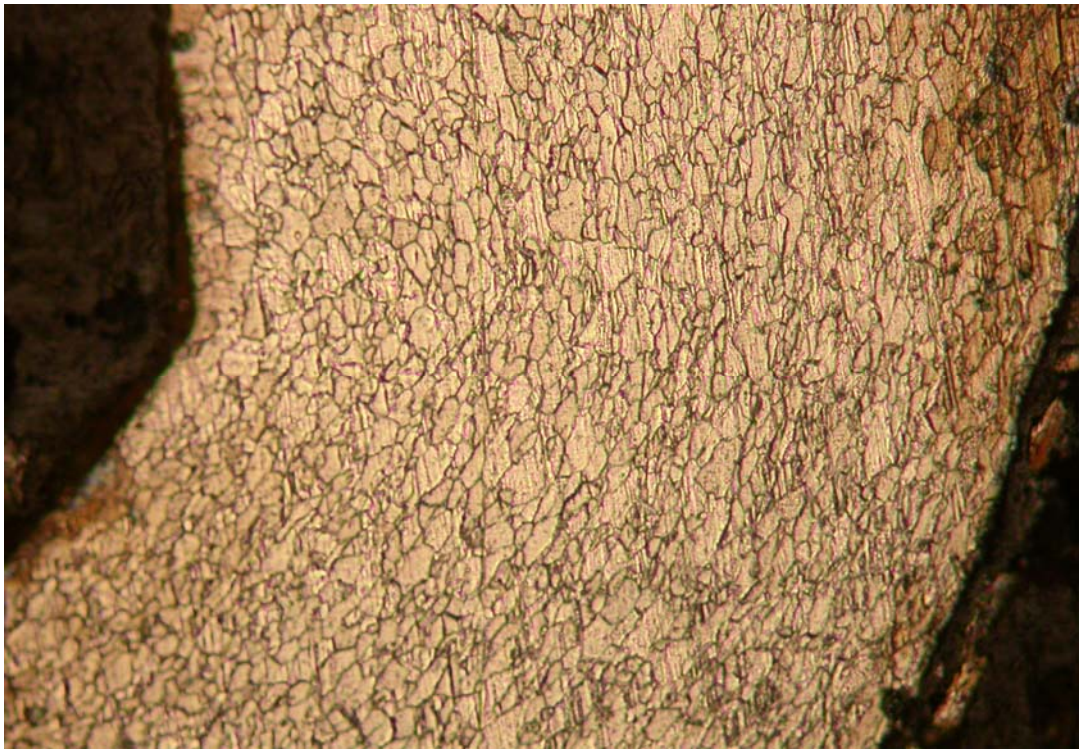

Figure 6.19: Microstructure of the deformed part (position 2) (300X)

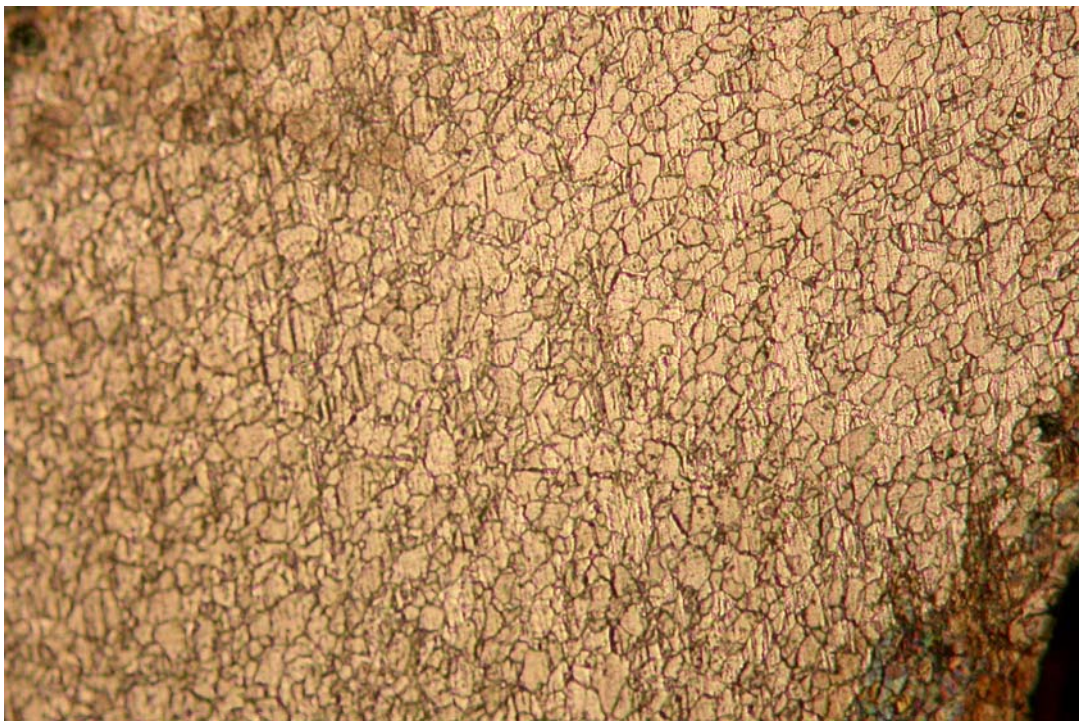

Figure 6.20: Microstructure of the deformed part (position 3) (300X)

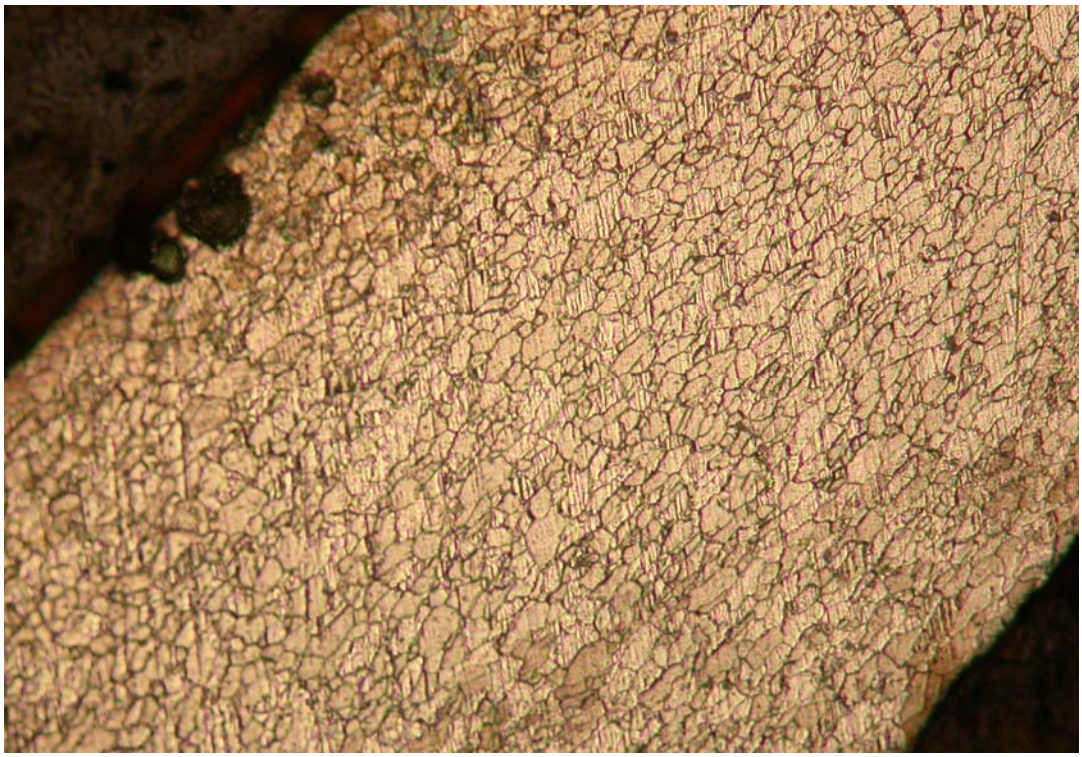

Figure 6.21: Microstructure of the deformed part (position 4) (300X)

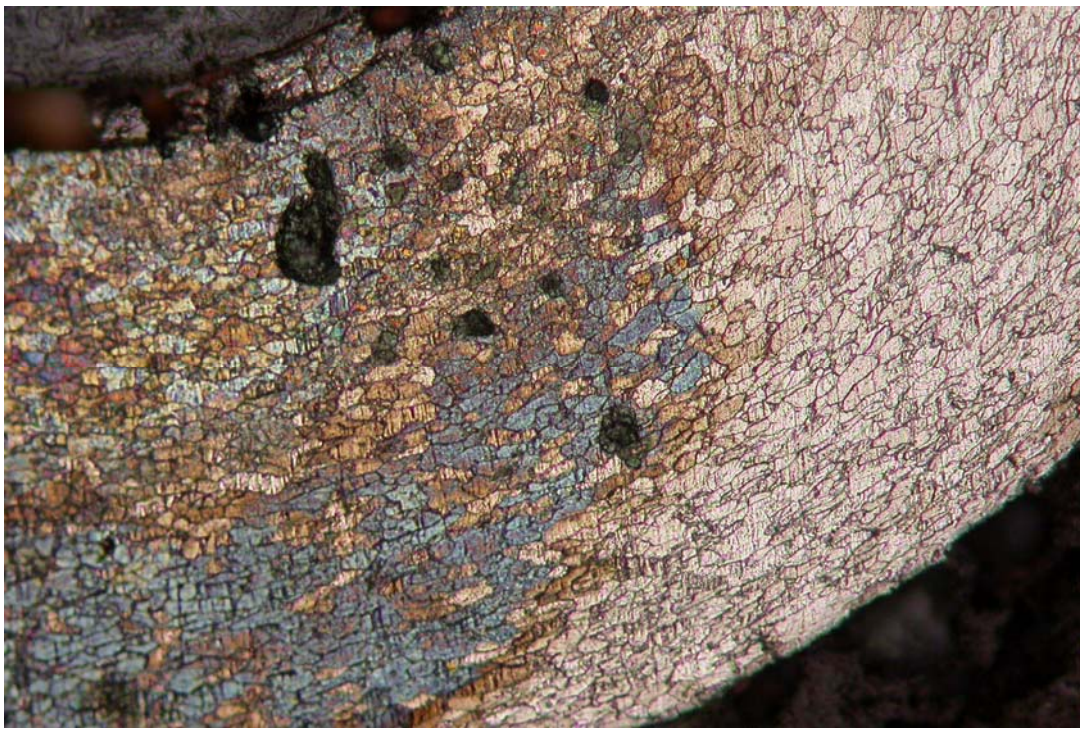

Figure 6.22: Microstructure of the deformed part (position 5) (300X)

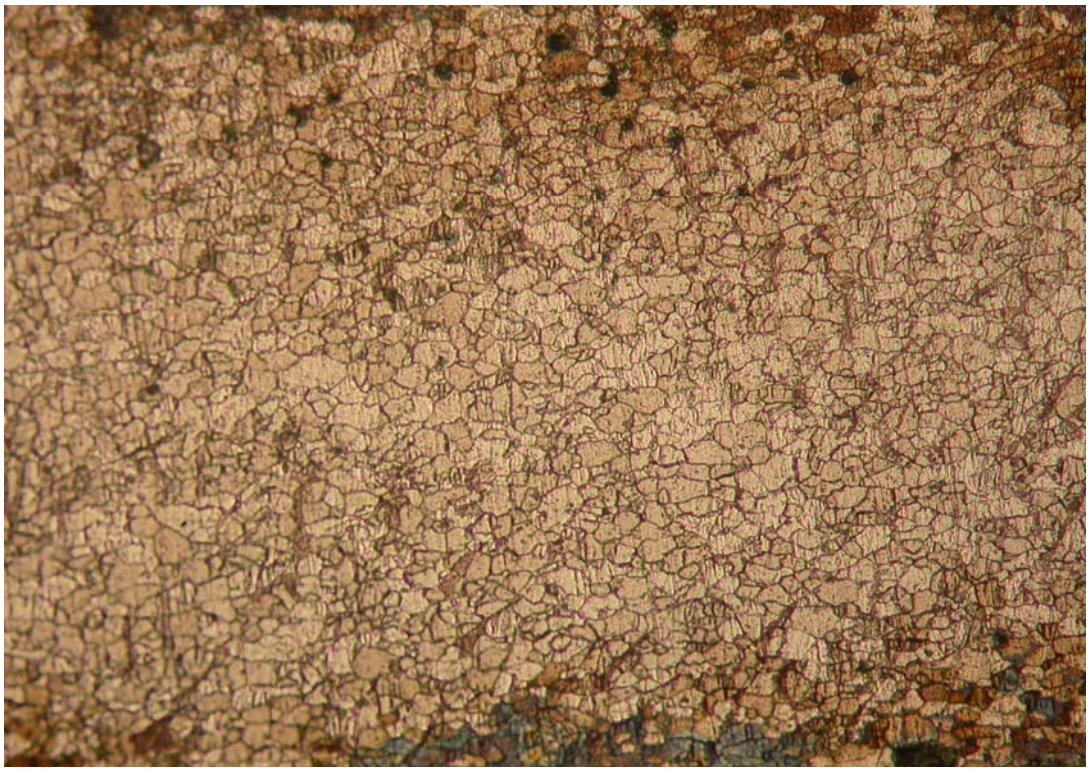

Figure 6.23: Microstructure of the deformed part (position 6) (300X)

As stated before, because of the distortion of the part during part preparation, the geometrical features of the part are somewhat changed. The slightly angled region (position 4 on Figure 6.17) of the part deformed excessively and as it can be observed in Figure 6.21, the inclination has been increased. These deformations during sample preparation have not affected the grain orientations, and they are clearly visible especially in Figures 6.19, 6.20 and 6.22.

The darker regions in Figures 6.20, 6.22 and 6.23 are due to over-etching of the specimen. Sometimes there are pits formed at the side of the sample in the bakelite, causing as a depot for the acid. Excessive acid is filled in these pits, and cannot be fully removed from the pieces; this way at those regions the microstructure is over-etched (or burnt) until the excessive amount of the acid vaporizes in time. This way, the over-etched grains darken.

Table 6.4 gives the results of the Knoop microhardness test measurements from ten different points on the sample. Since more strain hardening will occur at regions that experienced greater deformations, much interest is given on bends on the part. It was found in the numerical simulations that the deformation was the largest at the fillets (Section 6.2.2). This occurrence is also verified by the effective strain distribution at the end of the numerical analysis (Figure 6.24). The largest value of the effective strain is estimated near the corner of the inner ring; corresponding to region 3 on Figure 6.17.

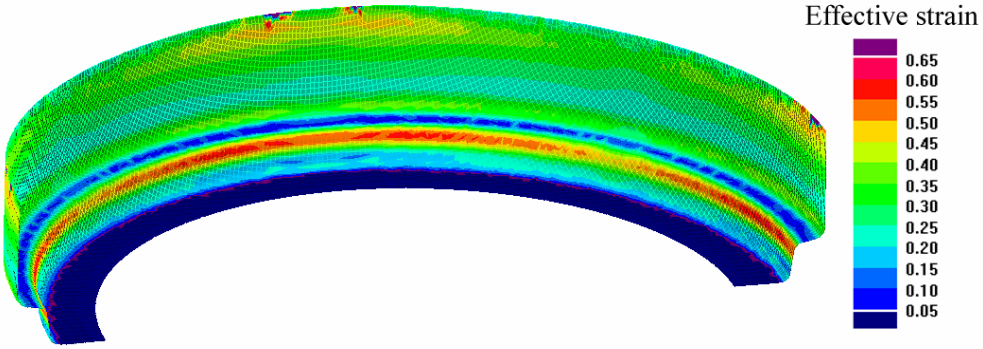

Figure 6.24: Effective strain contour of the part

The same positions were chosen for the microhardness measurements, since these points are at important regions of the part geometry, therefore deformation. The hardness values are given in Figure 6.25.

It is expected that the hardness values will be largest at points 2, 3 and 5, where the part is bent over the punch. Of these, logically the point 3 shall have the highest hardness, since bending and rebending occur near that region. Additionally, the largest amount of thinning (or deformation) is expected at this region according to the numerical simulation (Figure 6.12).

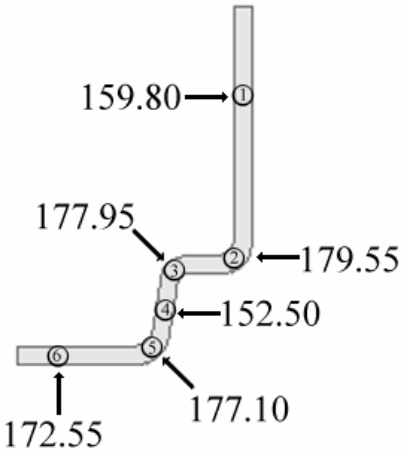

Figure 6.25: Knoop microhardness values of the deformed part along six data points

The results are more or less in agreement with the expectations and previous findings. Data point 2 gave the highest hardness, denoting the severity of the deformation, as it is in points 3 and 5. It is interesting to find out that a comparably high hardness value is obtained at data point 6. The effective strain distribution at Figure 6.24 shows that the region 6 has the slightest deformation. According to the simulation predictions, the smallest value of hardness had to be obtained from data point 6 therefore. The increased value of the hardness at this point may reflect the effect of distortions when the part is held for cutting, or the heat effect of the cutting operation might have induced a hardening effect on the specimen.

Table 6.4: Knoop microhardness test data of the deformed specimen

Data Point	Indentation Depth [μm]	HK
1	211	159.80
2	199.5	179.55
3	200.5	177.95
4	216	152.50
5	200.7	177.10
6	203	172.65

Figure 6.26 demonstrates the processed microstructure picture during the image analysis for the calculation of the final grain size of the deformed specimen:

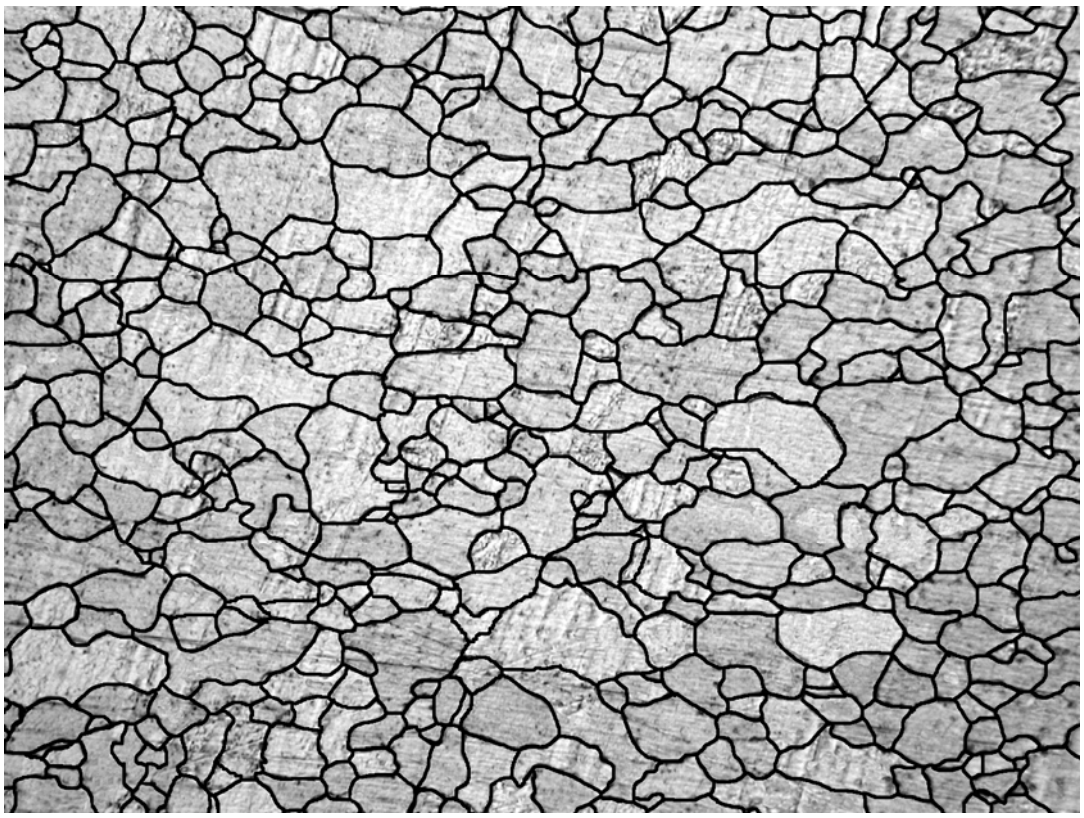

Figure 6.26: Image analysis picture of deformed part prepared for grain size measurement (825X)

The grain size measurement does not show a large variance of the grain size number for the deformed part, compared to the initial sample; the grain size number increased from 10.42 (Figure 6.16) to 11.68 (Figure 6.27). The reason for this may again be the heat effects induced during part preparation. Additionally, for more precise results several grain size measurements have to be conducted, and the average grain size of all these experiments shall be inspected. The results of the grain size measurement of the deformed sample are given in Figure 6.27:

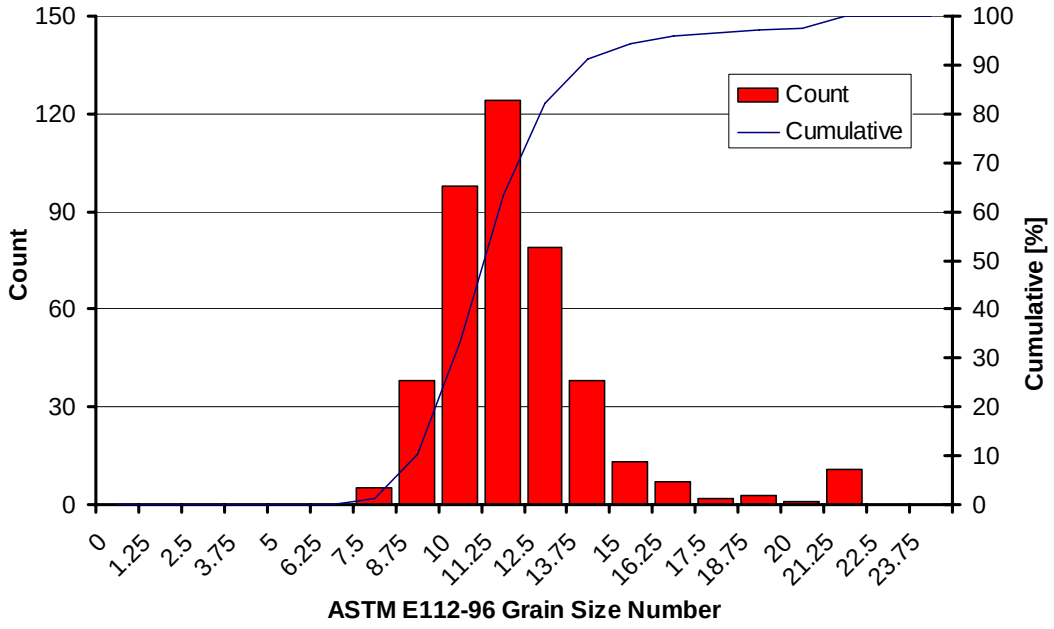

Figure 6.27: Distribution of the grain size numbers for the deformed part

CHAPTER VII

COMPARISON OF ALUMINUM AND STEEL IN A SIMPLE CUP DRAWING SIMULATION

7.1 Overview

In this present chapter, the deep drawing performances of aluminum and steel materials are compared. For this purpose, the axisymmetric dup drawing simulations (proposed by NUMISHEET 2002), for which the tool set-up was given in Figure 5.1, have been conducted. Firstly, results of aluminum and steel simulations utilizing 90 mm and 105 mm blanks are inspected, and then the process windows for the cup drawing of aluminum and steel materials with 90 mm blanks are determined in terms of blank holding pressure and lubrication conditions.

7.2 Direct Comparison

It is known that the utilization of aluminum and steel materials in identical processes (in terms of process geometry and process parameters) usually results in entirely different products. In this section this occurrence was verified. Specific blank holding loads were proposed within NUMISHEET benchmarks for specific blank sizes for both materials, and the effect of varying the blank size upon product properties is inspected within this section. The results for the HBHF aluminum analysis (with a 90 mm blank) were compared with a 90 mm steel blank simulation,

and the results of the LBHF steel simulation were compared with a simulation utilizing a 105 mm aluminum blank.

Steel analyses utilized a 105 mm blank with a blank holder force of 10 kN in the LBHF case and aluminum analyses utilized a 90 mm blank with 50 kN in the HBHF case in Numisheet benchmarks. The corresponding blank holding forces for the 105 mm aluminum and 90 mm steel analyses were calculated by considering the change in the blank holder area (or initial flange area. This way, the blank holding loads are kept constant in terms of pressure. For instance, the actual blank holding pressure for the 90 mm HBHF aluminum analysis is 2.908 MPa. The blank holding loads for 105 mm analysis is also modified that the blank holding pressure of 2.908 MPa is achieved. The calculation of the modified blank holder forces are as follows:

Blank holder areas were calculated using Eq. 5.3 as

$$A_{BH,R} = \pi\left(R^2 - 51.25^2\right)$$

where R is the outer radius of the blank holder area. The inner radius is constant for both blank holder sizes.

Hence, the blank holder sizes are calculated as:

$$A_{BH,90mm} = \pi\left(90^2 - 51.25^2\right) \approx 17195 \text{ mm}^2$$

and

$$A_{BH,105mm} = \pi\left(105^2 - 51.25^2\right) \approx 26384 \text{ mm}^2$$

Here, $A_{BH,90mm}$ denotes the blank holder area for a 90 mm blank, whereas $A_{BH,105mm}$ gives the blank holder area for a 105 mm blank.

The blank holder forces for the modified blank sizes were calculated by converting the initial forces for the actual blank size into the blank holder pressure and finally by multiplying the pressure with the new blank holder area as given in the following equations (Eq. 7.1 and 7.2)

$$F_{Al,105mm,HBHF} = \frac{F_{Al,90mm,HBHF}}{A_{BH,90mm}} \cdot A_{BH,105mm} \approx 76720\text{N} \tag{7.1}$$

$$F_{St,90mm,LBHF} = \frac{F_{St,105mm,LBHF}}{A_{BH,105mm}} \cdot A_{BH,90mm} \approx 6517\text{N} \tag{7.2}$$

where $F_{Al,90mm,HBHF}$ is the standard blank holding force of 50 kN for the aluminum analysis with 90 mm blank size and $F_{St,105mm,LBHF}$ is the standard blank holding force of 10 kN for the steel analysis with the blank size of 105 mm. These were the default blank holding forces utilized in the NUMISHEET 2002 benchmarks. The lubrication conditions (therefore Coulomb friction coefficients) for both materials' simulations are as defined in Numisheet 2002 benchmark. All process and numerical parameters in the comparison study are summarized in Table 7.1 as:

Table 7.1: Simulation parameters for the comparison of material performances

	6111-T4 aluminum	**DDQ mild steel**	**6111-T4 aluminum**	**DDQ mild steel**
Blank holder size [mm]	90		105	
Blank holder force [N]	$F_{Al,90mm,LBHF}$ 10000	$F_{St,90mm,LBHF}$ 6517	$F_{Al,105mm,HBHF}$ 76720	$F_{St,105mm,HBHF}$ 70000
Blank holder pressure [MPa]	0.582	0.379	2.908	2.653
Coulomb friction coefficient	0.0096	0.0426	0.0096	0.0426
Punch speed [mm/s]	500 mm/s			
Punch stroke [mm]	40			
Element size [mm]	3			

Figures 7.1 compares the thickness contours (and the maximum and minimum thicknesses) of aluminum and steel materials for a blank size of 90 mm with the low blank holding conditions, for which the forces are summarized in Table 7.1:

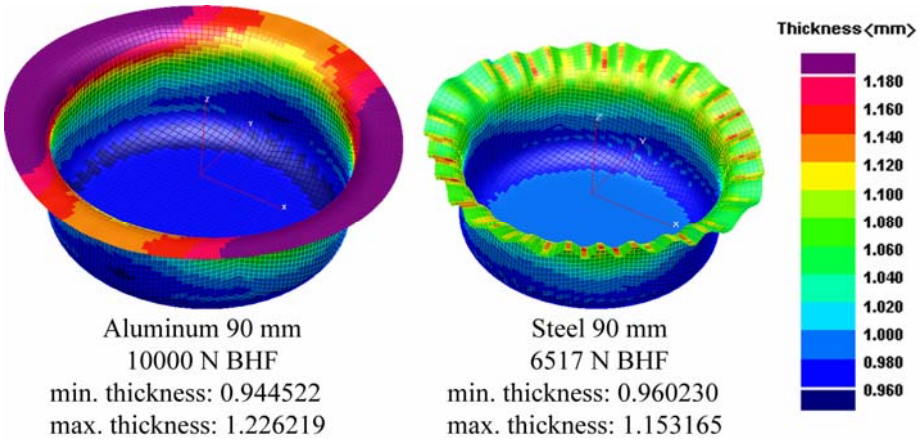

Figure 7.1: Thickness contours for 90 mm blank analyses

Steel material wrinkled severely under the low blank holding force conditions with a 90 mm blank, whereas the aluminum material shows no clear wrinkling (Figure 7.1). For a successful drawing, the minimum blank holding force is estimated by Ramaekers' program as ca. 17200 N. The height profiles of both blanks after drawing are given in Figure 7.2. Aluminum shows slight secondary wrinkling at 90° and 180°. On the other hand, if the maximum and minimum thickness values for both analyses are inspected, it is seen that steel experienced less thinning and less thickening; in other words, the variation of initial thickness (1 mm) is smaller than that of aluminum. Steel analysis gives a maximum thinning of 3.98% whereas aluminum has undergone 5.55% thinning. The thickening values show this different behavior more significantly: aluminum thickens by 22.6% whereas steel has a 15.3% increase in thickness. This occurrence is due to the difference in anisotropic behavior of these two materials. As explained in Chapter 2, the usual normal anisotropy value of 0.6 makes aluminum sheets less formable than steel sheets, since product tolerances are harder to achieve due to larger thinning and thickening of the sheets.

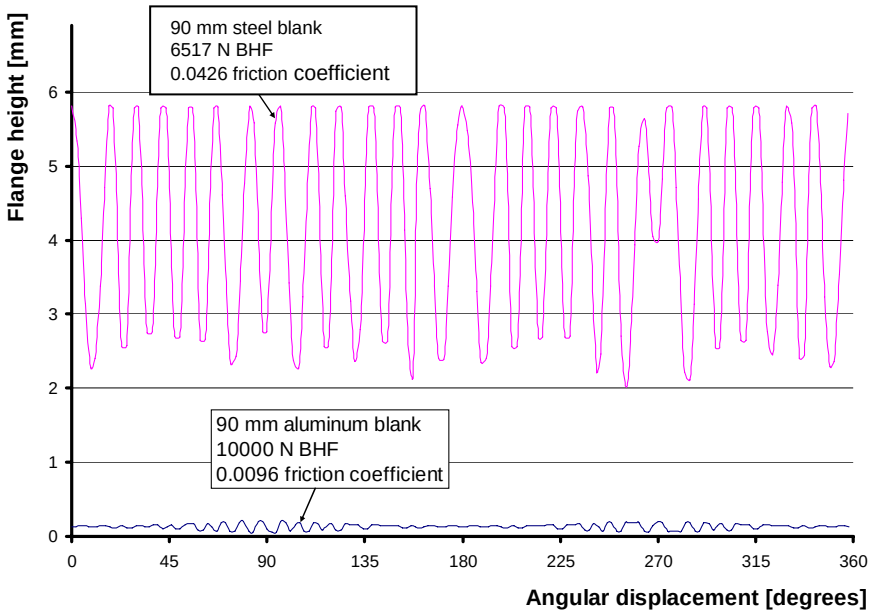

Figure 7.2: Height profiles of 90 mm blank analyses

The punch force – punch displacement curves for both analyses are compared with the analytical punch force – punch displacement curves, estimated by Ramaekers' cup drawing program in Figure 7.3:

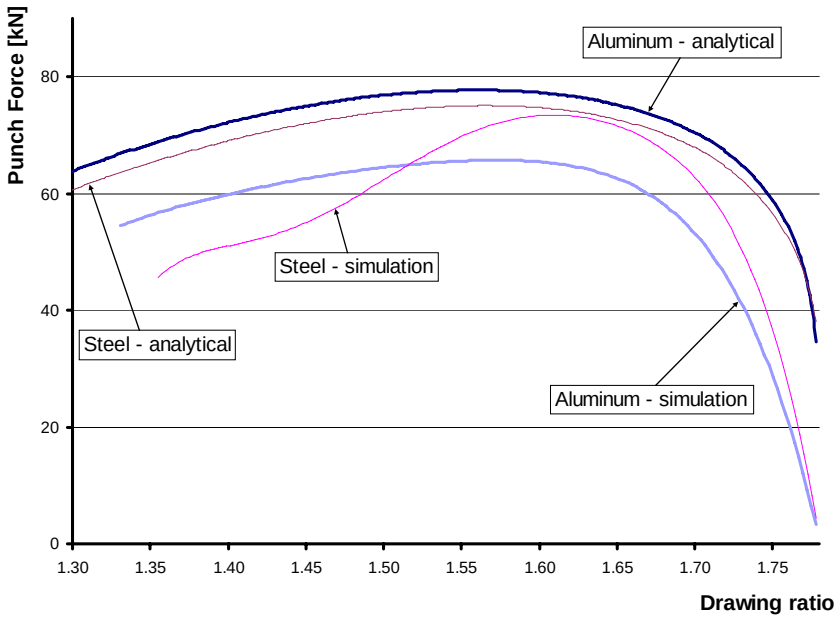

Figure 7.3: Force – displacement curves for 90 mm aluminum and steel blanks

Figure 7.3 shows that the estimated force – displacement curves (from simulations) are below the analytical curves. This is a property of explicit FEA. Forces are normally estimated up to 10% lower than the real values. It is seen that the steel analysis touches the analytical curve near the drawing ratio of 1.65, and then drops swiftly due to wrinkling. Ramaekers' model does not take the effect of wrinkling into consideration at all. Within the program, a minimum blank holding pressure to overcome wrinkling according to the other process parameters is given. This might be the reason for the form of the analytical f-d curve. As expected, the force requirement of the process for aluminum material is found to be much lower than the analytical findings due to the material model utilized. Anyway, knowing that the Hill 48 model for the FEA and Ramaekers' model utilized in the analytical solution are not as accurate for aluminum analyses as they are for steel, these results are acceptable.

Summarizing the results of the first set of analyses with 90 mm blanks, the steel material did not show wrinkling for the standard 105 mm LBHF analysis, whereas it wrinkled when a 90 mm blank analysis although nearly identical blank holding loads (in terms of pressure) are applied for both cases. On the other hand, the 90 mm LBHF aluminum analysis is successful, if the thickness variations are considered acceptable.

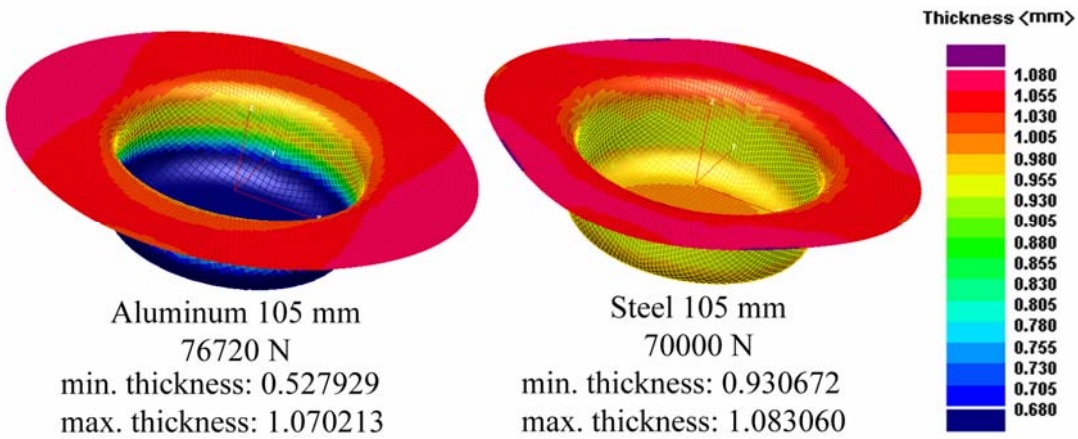

Figure 7.4: Thickness contours for 105 mm blank analyses

When 105 mm blanks are used with the high blank holding condition, aluminum material fails according to the simulation, as seen in Figure 7.4. The bottom of the cup experiences excessive thinning, leading to failure. During the drawing of aluminum the forces restrict the flange region to be drawn into the die cavity, and the punch progression causes stretching in the cup walls. Since there is no material flow from the flange region, the bottom of the cup becomes thinner until fracture. On the other hand, steel analysis is in the safe region, resulting in a successful drawing. Figure 7.5 shows the flange radius profiles for aluminum and steel:

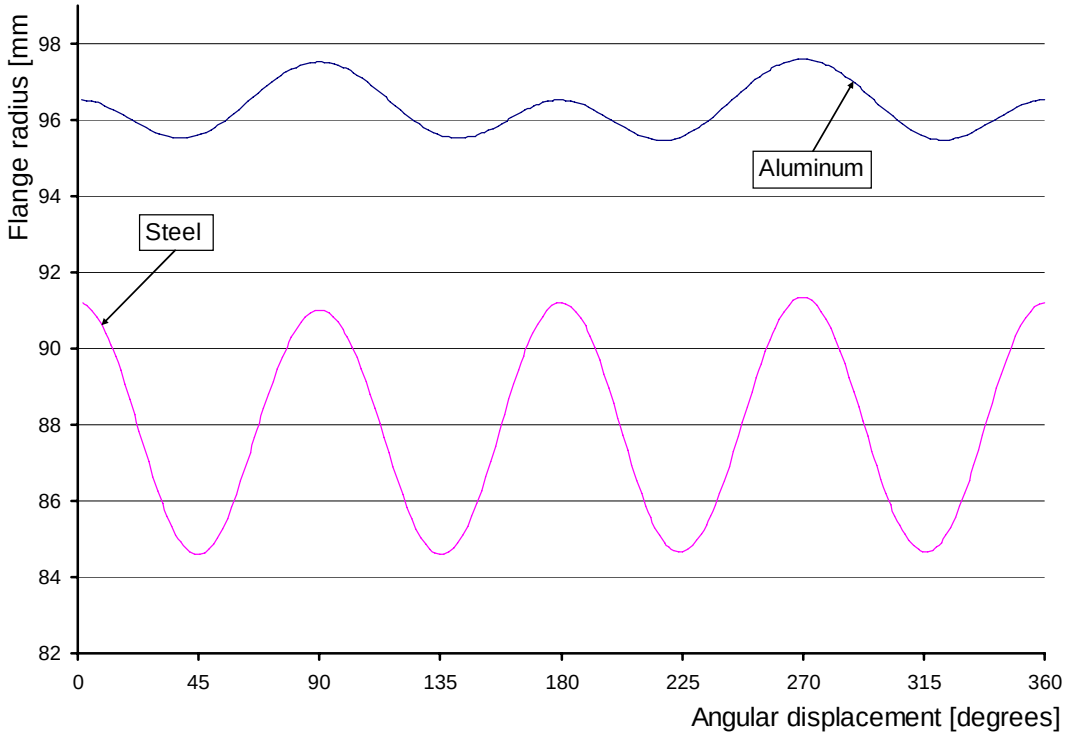

Figure 7.5: Flange radius profiles for 105 mm aluminum and steel analyses

The insufficient drawing of the flange is also visible in Figure 7.5 for aluminum. The flange radius is about 96 mm for the system. The effects of different anisotropic behaviors of steel and aluminum materials are also present in this figure. The variations of flange radii form different waveforms. For both materials the flange radii have minima at 45°, 135°, 225° and 315° whereas the maxima lie at 90°, 180°, 270° and 360°. However, the heights of the peaks vary for aluminum,

whereas the flange radius profile has nearly a sinusoidal waveform in steel. This anisotropic property of steel makes steel flanges more square-like, whereas aluminum flanges exhibit an ellipsoid form usually.

The force requirements of the processes are given in Figure 7.6 and the simulation results are compared to analytical values. It should be noted that the failure in aluminum analysis is also predicted by the analytical solution, since the punch force calculated by the analytical model exceeds the critical force (the failure limit).

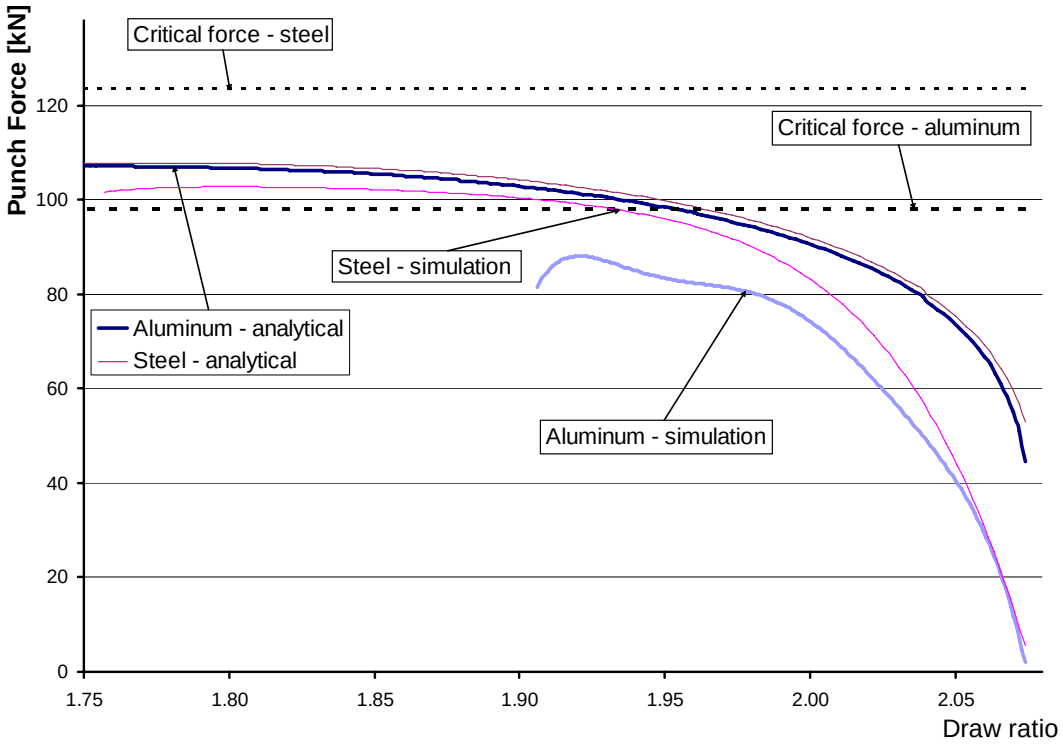

Figure 7.6: Force – displacement curves for 105 mm aluminum and steel blanks

The simulation results give a large drawing ratio for aluminum since the flange radius (which remains large due to insufficient drawing) is used in the calculations (Figure 7.6). However, the punch force estimated by the numerical analysis is well below the critical force calculated by the analytical model. This occurrence is due to the underestimation of the forces by FEM and especially due to the utilized Hill 48

material model. Therefore the punch force inspection would not predict a failure for aluminum simulation. On the other hand, thickness distributions in the simulation results (Figure 7.4) estimate the expected failure of aluminum material according to the analytical model correctly. Additionally, the inspection of the forming limit diagram of aluminum also reveals the failure (Figure 7.7a). The color red denotes the nodes, which have a strain state lying above the forming limit diagram, whereas blue color is for the *safe* nodes. It is observed that the nodes in the bottom of the blank exceed the failure limit. Failure is expected in this region, and the thickness contours of aluminum analysis agree with this expectation. On the other hand, the inspection of steel material's forming limit diagram shows that the steel analysis is successful, since all the strain state of all nodes fall into the safe region (Figure 7.7b). The data for the forming limit diagrams were obtained from Numisheet Benchmarks' material characterization studies.

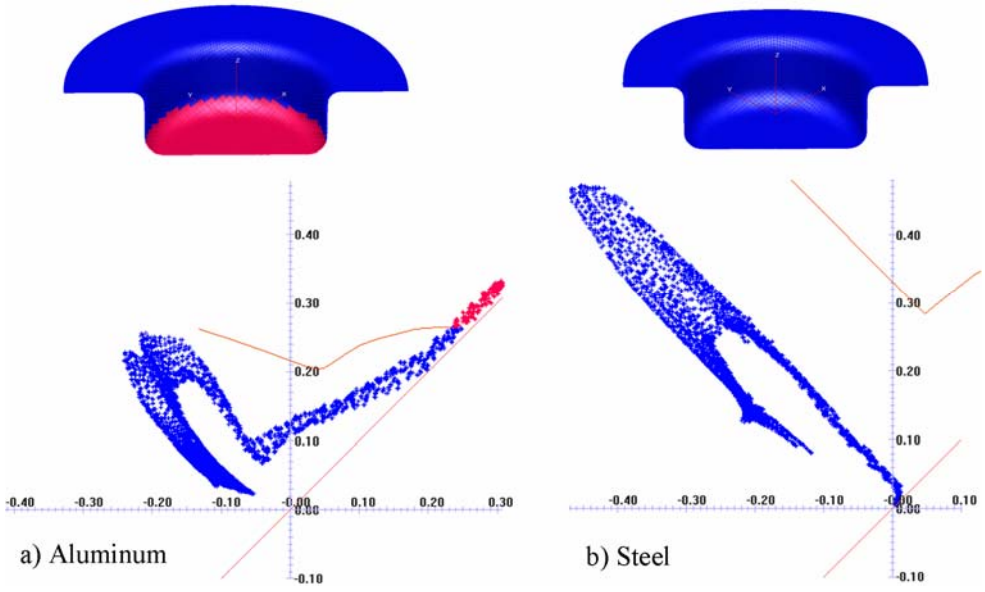

Figure 7.7: Forming limit diagrams of (a) aluminum and (b) steel for the HBHF drawing operation with 105 mm blanks

Summarizing the findings within this section, it is found that 90 mm blanks in low blank holding condition caused steel material to wrinkle, whereas the aluminum

material resulted in a successful product, and 105 mm blanks in high blank holding condition resulted in a failure of the aluminum material and a successful steel material. The overall result of this study is that one *cannot* use aluminum material for a steel production process (without modifying process parameters), or vice versa.

7.3 Inspection of the Process Windows for Steel and Aluminum for the Cup Drawing Operation

The previous section proved that the process parameters for a safe product using aluminum and steel materials are different and must be carefully controlled. In the present section the deep drawability of aluminum and steel will be inspected in an identical process by varying the blank holding force and the friction coefficient throughout the system.

7.3.1 Process Geometry, Process Parameters and Numerical Parameters

The process geometry is given in Figure 5.1, as proposed by Numisheet 2002 benchmarks. 1 mm blanks of 6111-T4 aluminum and DDQ mild steel materials are deep drawn into cups from initially 90 mm sized blanks. The process variables, the blank holding force and the friction coefficient are controlled, whereas the punch speed is kept constant at 500 mm/s. The onsets of wrinkling and failure are compared for aluminum and steel materials by varying the blank holding force and the friction coefficient. Table 7.2 summarizes all process and simulation parameters for the study.

Table 7.2: All process and simulation parameters for the deep drawability comparison study

		6111-T4 aluminum	DDQ mild steel
Material Properties	K [MPa]	538.225	547.763
	n	0.2255	0.2692
	R_0	0.894	2.160
	R_{45}	0.611	1.611
	R_{90}	0.660	2.665
	Δr	0.083	0.401
	r_n	0.694	2.012
	ρ [g/mm³]	2.6	7.8
	ν	0.3395	0.3
	ε_0	0.00256	0.00088
	E [GPa]	70.725	221.368
	σ_Y [MPa]	180.825	193.918
	% Elongation (Total)	27.350	48.069
Process Geometry	Blank thickness	1	
	Blank radius [mm]	90	
	Punch radius [mm]	50	
	Punch stroke [mm]	40	
	Punch speed [mm/s]	500	
	Blank holder size	90 mm outer radius, 51.25 mm inner radius	
	Blank holder area [mm^2]	17195.311	
	Die cavity radius [mm]	51.25	
Numerical Parameters	Punch speed type	Stroke controlled	
	Loading type	As blank holding pressures	
	Blank element size [mm]	3	
	Tools element size [mm]	5	
	Blank mesh topology	Structure A (Figure 5.36)	
	Time step scale factor	0.9 (default)	
	Adaptive meshing	None	
	Mass scaling	None	
	Symmetry conditions	None (Full model)	
	Material Model	Hill 1948 isotropic hardening	
	Anisotropy type	Orthotropic	
	Solver type	Explicit, single precision	
	FEA package	PAM-STAMP 2G v2003	

To determine the process windows for aluminum and steel for the cup drawing operation, a number of analyses are conducted by varying blank holder pressures and friction coefficients. Table 7.3 summarizes the variation of these two parameters:

Table 7.3: Range of the parameters for the deep drawability study

	Minimum	Maximum
Friction Coefficient	0	0.2
Blank holding pressure [MPa]	0	70

The increase interval of friction coefficient is 0.05. Therefore, simulations are conducted by using the Coulomb friction coefficients of 0 (ideal, frictionless condition), 0.05, 0.10, 0.15 and 0.20 (rough surface). The blank holding pressure is increased continuously from 0 MPa to the maximum of 70 MPa for each friction condition until failure by excessive thinning is observed. After failure, no further analyses with larger blank holding loads are conducted, since failure would definitely occur under these conditions. This way, the number of required simulations is minimized.

The simulation results, in other words the deep drawing products according to the simulation are classified as the following:

- Wrinkled: When the height profile across the flange shows a wave-like trend in visual and numerical investigations
- Secondary wrinkled: When the height profile of the flange has a wave-like trend in certain angles due to anisotropy and the presence of rigid tools (Section 5.2.2.2)
- Safe: When the product shows no significant wrinkling or secondary wrinkling, and the thinning of the product is within the allowed limit (determined by the limit of total elongation)
- Failed: When the part shows excessive thinning

The simulation findings are tabulated according to this classification and the process windows are determined. However, to investigate the thickness variations of the *safe* products in detail, maximum and minimum thickness variations of simulation results are also tabulated. This way, a more accurate determination of process windows was made possible. Any user can select the acceptable thickness variation range and choose the suitable process parameters for the cup drawing of 6111-T4 aluminum and DDQ mild steel.

For insufficient blank holding conditions where the blank holder load is low and/or the friction coefficient is low (the lubrication condition is good), wrinkling is expected to be observed, whereas large loads and/or large friction coefficients imposed the ever-increasing risk of failure by excessive thinning. For large friction coefficients, the failure point is achieved earlier (in terms of blank holder pressures) and for small friction coefficients the tendency of wrinkling increases strongly as the pressure is decreased.

On the other hand, the ideal lubrication condition, which has a nil friction coefficient, resulted in unacceptable and invalid simulation results with increasing blank holding pressures. The blanks shifted arbitrarily during the deformation in the frictionless condition, causing the results to be unusable. Figure 7.8 illustrates the shifting of the blank under the frictionless condition (20 MPa blank holding load):

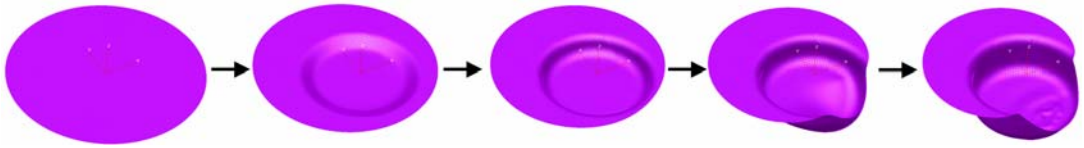

Figure 7.8: Shifting of the blank under frictionless condition

As the blank holding force is increased, the magnitude of these slides increases. This occurrence may be due to numerical errors in the simulation. For instance, due to discretization, the tools and the blank may not be in their actual positions, having

minor shifts in the placements due to round-off errors, or the loading of the punch and/or the blank holder may be not exactly vertical, or so on. These possible numerical errors in the simulated model may form artificial forces on the blank that can move the blank in the XY-plane, and cause the blank to slide away from its actual position just at the moment when the punch *touches* the blank. These artificial forces may also be present in other cases, where the frictional forces are present (when the friction coefficient is non-zero), however the presence of these forces may cause the blank to remain in its neutral position. On the other hand, without the *restricting* effect of the frictional forces, the blank may move arbitrarily at the start of the simulation until the blank position is fixed due to the drawing of the blank into the die by the stroke of the punch. This occurrence is observed for both materials, therefore the simulations under frictionless condition (nil Coulomb friction coefficient) are invalidated; no further comment will be made on the frictionless condition.

7.3.2 Results

Table 7.4 summarizes the outcome of simulation results for aluminum and steel respectively in terms of varying friction coefficients and blank holding pressures, and Table 7.5 gives the process windows according to the analytical calculation. It should be noted that the increments of blank holding loads are not constant.

As expected, aluminum has a significantly poor performance on the simulations of cup drawing (Table 7.4). At 0.20 friction coefficient level, aluminum fails at 4 MPa, whereas steel has a failure limit of 12 MPa. At 0.15 friction coefficient, aluminum shows excessive thinning at 7 MPa, whereas steel has an acceptable performance up to 18 MPa. As the lubrication condition is better and better, the gap between the formability of aluminum and steel increases greatly. At 0.10 level, aluminum shows failure at 9 MPa, whereas steel fails at 35 MPa and at 0.05 friction coefficient, aluminum fails at 18 MPa, whereas steel fails at 70 MPa. At all lubrication levels, steel has an applicable loading range at least three times larger than that of steel.

Table 7.4: Comparison of the process windows of aluminum and steel according to numerical simulations

Aluminum max. 27% elongation		Blank holder pressure [MPa]															
		0	0.5	1	2	3	4	5	6	7	8	9	10	12	14	16	18
Friction coefficient	0.05	WR	WR	WR2	WR2	OK	OK	OK	OK	OK	OK	OK	OK	OK	OK	OK	FAIL
	0.1	WR	WR	WR2	OK	OK	OK	OK	OK	OK	OK	OK	FAIL	FAIL	FAIL	FAIL	FAIL
	0.15	WR	WR	WR2	OK	OK	OK	OK	OK	FAIL	FAIL	FAIL	FAIL	FAIL	FAIL	FAIL	FAIL
	0.2	WR	WR	WR2	OK	OK	FAIL	FAIL	FAIL	FAIL	FAIL	FAIL	FAIL	FAIL	FAIL	FAIL	FAIL

WR	Wrinkled
WR2	Secondary Wrinkled
OK	Safe
FAIL	Excessive thinning

Steel max. 48% elongation		Blank holder pressure [MPa]																							
		0	0.5	1	2	3	4	5	6	7	8	9	10	12	14	16	18	20	30	35	40	45	50	60	70
Friction coefficient	0.05	WR	WR	WR2	OK	OK	OK	OK	OK	OK	OK	OK	OK	OK	OK	OK	OK	OK	OK	OK	OK	OK	OK	OK	FAIL
	0.1	WR	WR2	OK	OK	OK	OK	OK	OK	OK	OK	OK	OK	OK	OK	OK	OK	OK	OK	FAIL	FAIL	FAIL	FAIL	FAIL	FAIL
	0.15	WR	WR2	OK	OK	OK	OK	OK	OK	OK	OK	OK	OK	OK	OK	OK	FAIL	FAIL	FAIL	FAIL	FAIL	FAIL	FAIL	FAIL	FAIL
	0.2	WR	WR2	OK	OK	OK	OK	OK	OK	OK	OK	OK	OK	FAIL	FAIL	FAIL	FAIL	FAIL	FAIL	FAIL	FAIL	FAIL	FAIL	FAIL	FAIL

Table 7.5: Comparison of the process windows of aluminum and steel according to analytical formulation

Aluminum max. 27% elongation		Blank holder pressure [MPa]															
		0	0.5	1	2	3	4	5	6	7	8	9	10	12	14	16	18
Friction coefficient	0.05	WR	WR	WR	OK	OK	OK	OK	OK	OK	OK	OK	OK	FAIL	FAIL	FAIL	FAIL
	0.1	WR	WR	WR	OK	OK	OK	OK	FAIL	FAIL	FAIL	FAIL	FAIL	FAIL	FAIL	FAIL	FAIL
	0.15	WR	WR	WR	OK	OK	FAIL	FAIL	FAIL	FAIL	FAIL	FAIL	FAIL	FAIL	FAIL	FAIL	FAIL
	0.2	WR	WR	WR	OK	FAIL	FAIL	FAIL	FAIL	FAIL	FAIL	FAIL	FAIL	FAIL	FAIL	FAIL	FAIL

WR	Wrinkled
OK	Safe
FAIL	Excessive thinning

Steel max. 48% elongation		Blank holder pressure [MPa]																							
		0	0.5	1	2	3	4	5	6	7	8	9	10	12	14	16	18	20	30	35	40	45	50	60	70
Friction coefficient	0.05	WR	WR	OK	OK	OK	OK	OK	OK	OK	OK	OK	OK	OK	OK	OK	OK	OK	FAIL	FAIL	FAIL	FAIL	FAIL	FAIL	FAIL
	0.1	WR	WR	OK	OK	OK	OK	OK	OK	OK	OK	OK	OK	OK	FAIL	FAIL	FAIL	FAIL	FAIL	FAIL	FAIL	FAIL	FAIL	FAIL	FAIL
	0.15	WR	WR	OK	OK	OK	OK	OK	OK	OK	OK	FAIL	FAIL	FAIL	FAIL	FAIL	FAIL	FAIL	FAIL	FAIL	FAIL	FAIL	FAIL	FAIL	FAIL
	0.2	WR	WR	OK	OK	OK	OK	OK	OK	FAIL	FAIL	FAIL	FAIL	FAIL	FAIL	FAIL	FAIL	FAIL	FAIL	FAIL	FAIL	FAIL	FAIL	FAIL	FAIL

The process windows according to Ramaekers' analytical program (Table 7.5) are much smaller than the simulation findings (Table 7.4). To be able to correlate the results of the simulations and the analytical calculations, the loading ranges in Table 7.5 are given as they are in Table 7.4.

For a friction coefficient value of 0.05, simulations estimate the maximum allowable forming load to be 60 MPa, whereas the analytical formulation predicts failure even at the much lower blank holding load of 30 MPa. This huge difference of the predictions between the two methods is because of the different approaches for determining 'failure' (wrinkling or excessive thinning). In the numerical simulations, failure by wrinkling is detected by inspection of the flange height profiles and the failure by excessive thinning is detected by inspecting the thickness contours of the blanks. Here, the artificial secondary wrinkling occurrences are also present. Secondary wrinkling occurrences are noted (in Table 7.4), but since they do not exist in real processes, products exhibiting secondary wrinkling are also considered within successful simulations. On the other hand, Ramaekers' program calculates a minimum blank holding load, which is material and process geometry dependent (independent of the lubrication condition), and a maximum forming force, or a critical forming force, which considers the thinning at the tip of the drawn cups, dependent again on the process geometry and material properties and independent of the lubrication condition. Exceeding the critical force (the maximum allowable force) will result in failure by bottom tearing according to Ramaekers.

Figure 7.9 and 7.10 give the maximum forming loads for successful simulations and their corresponding analytical findings with respect to varying blank holding pressures and friction coefficients for aluminum and steel respectively. In these figures, the total forming forces obtained from the simulations, which are considered in the *safe* region according to the thinning amount, exceed in many cases the maximum allowable deformation force calculated by the analytical program. Therefore, one can say that the simulation and the analytical findings are in conflict when determining the onset of the bottom tearing failure (Figures 7.9 and

7.10). On the other hand, the wrinkling predictions of the analytical calculation and the simulations are more or less in agreement (Table 7.4 and 7.5).

Hence, it is concluded that it is not suitable to inspect only one property of the results; by only considering the drawing force, one should not determine the onset of failure. At this point, the power of numerical analyses becomes obvious. Although Ramaekers' program is a practical tool for quick evaluation of simple cup drawing operations, having good force predictions for steel materials (due to the semi-empirical nature of the formulation of the program), no specific info about the product properties are obtained from the program. Therefore, the thorough investigation of the simulation results is obligatory, when the performances of aluminum and steel materials are to be determined upon the simple cup drawing operation. In Figures 7.11 and 7.12 the maximum and minimum final thickness values for aluminum and steel simulations are given.

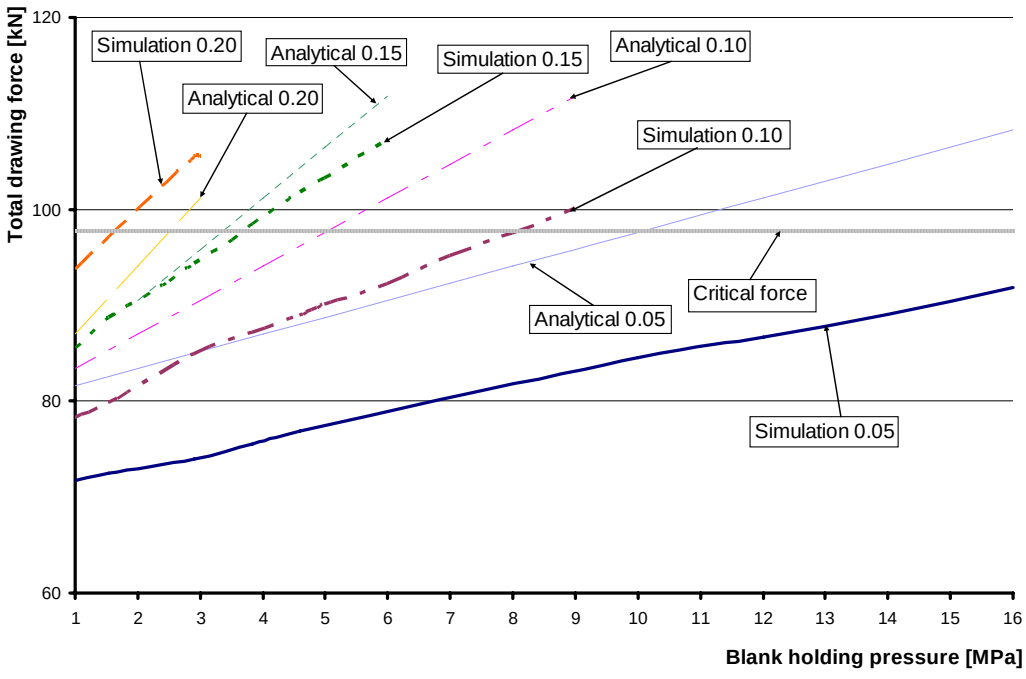

Figure 7.9: Variation of the maximum forming forces for aluminum material in simulations and analytical findings

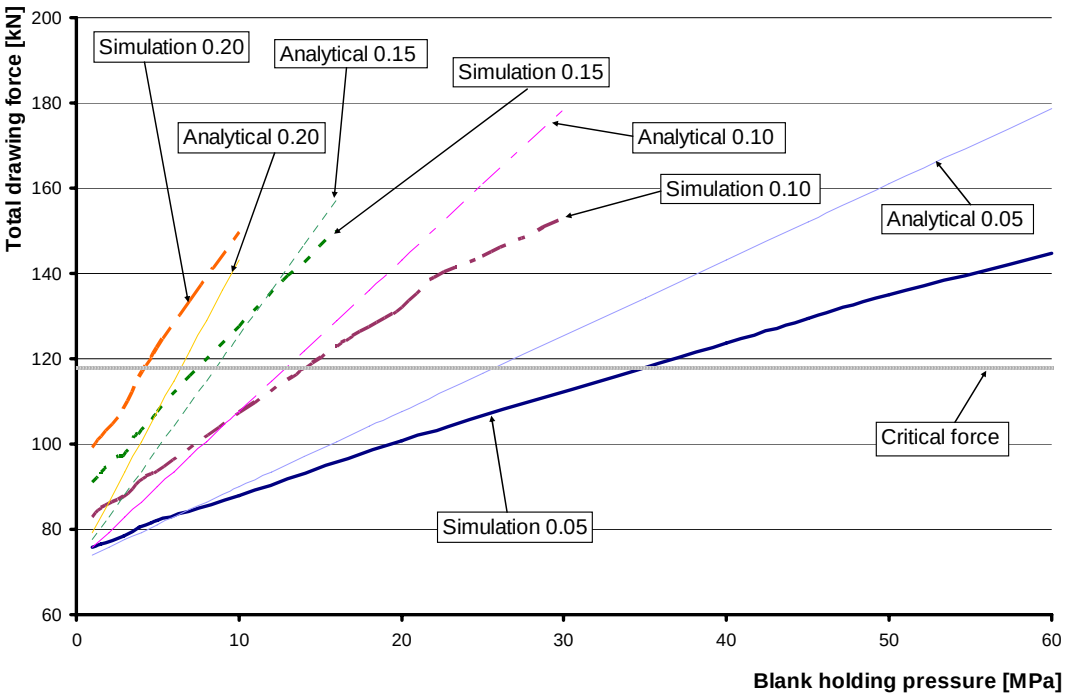

Figure 7.10: Variation of the maximum forming forces for steel material in simulations and analytical findings

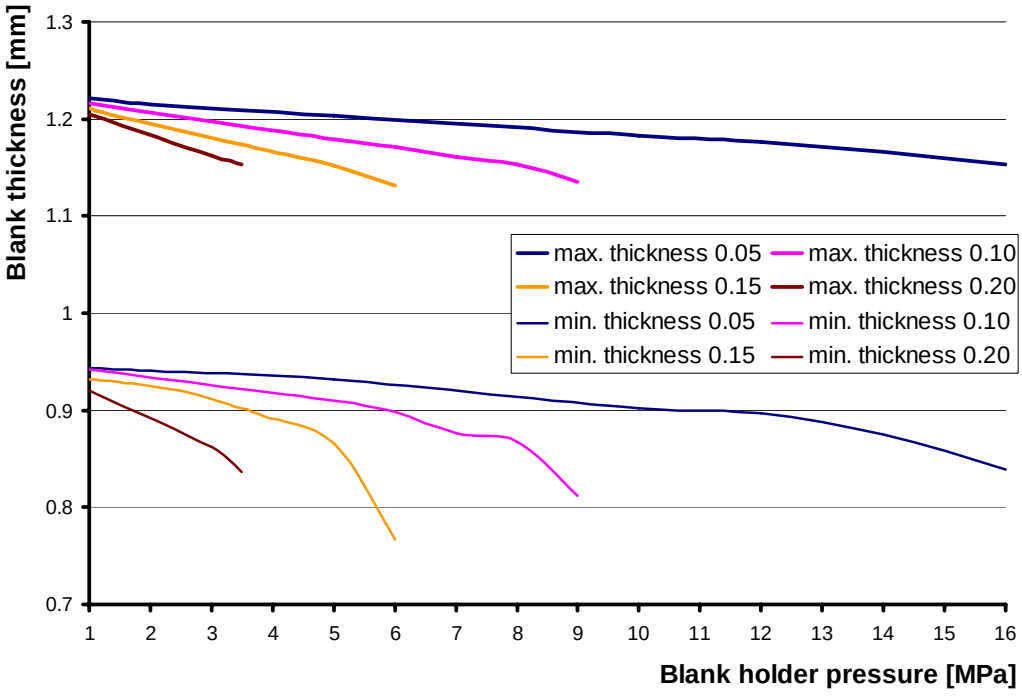

Figure 7.11: Maximum and minimum thickness values of aluminum at the end of the simulations (with respect to blank holding force and friction coefficient)

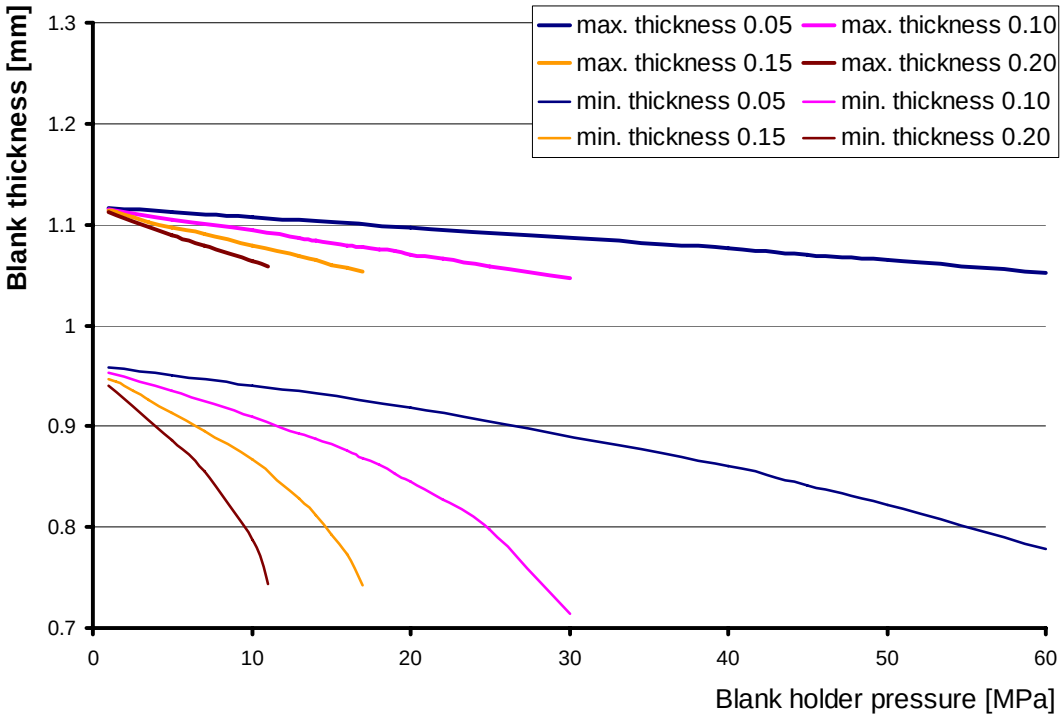

Figure 7.12: Maximum and minimum thickness values of aluminum at the end of the simulations (with respect to blank holding force and friction coefficient)

Comparison of Figures 7.11 and 7.12 reveal that aluminum has a stronger tendency to thicken; the maximum thickness values for all simulations lie near 1.2 mm, whereas steel material thickens up to 1.1 mm at max. On the other hand, if the decrease of the minimum thickness values with increasing blank holder pressures and friction coefficients are investigated, it is observed that aluminum strongly resists drawing and for all loading and lubrication conditions and excessive thinning failures are observed always before steel.

As the anisotropic properties of aluminum denote, the formability of aluminum is significantly lower than steel, and product properties in terms of thickness tolerances are significantly more inferior than steel.

CHAPTER VIII

CONCLUSIONS AND FURTHER STUDIES

In this study, the deep drawability of steel and aluminum sheets were investigated by using the dynamic-explicit FE-code PAM-STAMP 2G. An axisymmetric cup drawing operation was simulated, and the process parameters for aluminum and steel were determined for a successful product. Additionally, the reliability of PAM-STAMP 2G was inspected by comparing simulation results with NUMISHEET 2002 benchmarks, and an experimental verification was also conducted.

It is found that to obtain a valid and useful numerical simulation result, one has to master the mechanics of the numerical analysis method that the program utilizes, as well as the mechanical and metallurgical aspects of the real life situation that is being simulated. The effect of numerical parameters on the output was thoroughly investigated. Although the dynamic-explicit code outputs a simulation result in nearly all cases, it is observed that the simulations may deviate from the physical reality in many cases where the numerical and physical parameters are chosen arbitrarily.

It is also found that the tool size has an effect on the simulation results (by influencing the effectiveness of the loads), and that the mesh structure and quality is

extremely important for meaningful results. It is also proven that the tool mesh and loading conditions are effective in the occurrence and prediction of wrinkling.

Furthermore, the weaknesses of the FEA code were discovered:

- The code has problems in simulating symmetry conditions, therefore symmetry should not be used whenever improved accuracy is needed.
- The application of loads must be conducted carefully in order not to lose precision of results since the magnitudes of the loads depended on tool geometry
- The presence of dynamic effects must be always considered, since they affect results greatly, and it must be beared in mind that their inevitable (due to the mathematical basics of the numerical analysis procedure itself) presence can lead to unrealistic occurrences.
- The simulation model must be as precise and realistic as possible to obtain a useful analysis result, and the user must be qualified enough to interpret the results and discard invalid results due to numerical errors.

Moreover, it has also been proven that when the user has sound knowledge about the mechanics of the FE-code, the dynamic-explicit code PAM-STAMP 2G is successful enough in simulating stamping operations. As it can be seen in chapter 6, although the final part geometry is not successfully predicted, the experimental findings are in agreement with the numerical analysis' results of the ball bearing case simulation, considering the strain hardening occurrences.

In the deep drawability comparison study, it is found that (in terms of failure by tearing, excessive thickness change and wrinkling) aluminum material is less formable than steel due to its anisotropic properties. On the other hand, the process windows for both materials are determined for the cup drawing simulation in terms of lubrication and blank holding forces.

Finally, possible further studies about this subject are recommended.

The utilization of Hill 48 material model leads to inaccurate results for aluminum alloys, since the anisotropic properties of aluminum is not fully compatible with the model. Therefore, the formability of aluminum is overestimated with this model. On the other hand, the utilization of this model is very practical since it requires a small number of basic material parameters, which can be determined, or obtained from the literature easily. More accurate models, having more complex definitions and larger numbers of material parameters (like the Barlat 91 or Hill 90 models) must be utilized for the inspection of the formability of aluminum materials.

In the literature there are insufficient studies about the metallographic aspects of deep drawing. In Chapter 6, the grain distribution of the ball bearing case after production was shortly investigated. One interesting study would be about the grain alignment upon deformations during deep drawing.

Additionally, the springback behaviors of aluminum and steel sheets were not inspected in detail, since the springback algorithm is not precise enough to obtain valid simulation results. The effect of springback in more complex shapes may be investigated, possibly by utilizing different FEA packages.

In general, the deep drawing behavior of aluminum and steel may also be inspected for complex shapes. For an industrial application the determination of the process windows may be useful for the manufacturers.

On the other hand, the effects of these materials upon tool life are another subject that the industry may benefit, if studied.

Finally, the simulations may also be conducted using another (preferably implicit) code and another material model, and the results may also be compared for better verification.

REFERENCES

Banabic, D.; Bunge, H.-J; Pöhlandt, K.; Tekkaya, A. E.: Formability of Metallic Materials, Springer-Verlag: Berlin/Heidelberg/New York/Tokyo, 2000.

Beddoes, J.; Bibby, M. J.: Principles of Metal Manufacturing Processes, Arnold, London, 1999.

Belytschko, T.; Mullen, R.: Explicit Integration of Structural Problems. In: Bergan, P.; et al. (eds): Finite Elements in Nonlinear Mechanics; 1977, 672-720.

Callister, W. D.: Materials Science and Engineering: An Introduction, 4th Edition, John Wiley & Sons, Inc., New York, 1997.

Correia, J. P. M.; Ferron, G.: Wrinkling Predictions in the Deep-drawing Process of Anisotropic Metal Sheets, Journal of Materials Processing Technology, 128 (2002), pp. 178-190.

Desai, S. G.; Date P. P.; Narasimhan K.: (Remarks) Effect of mesh on simulation of cylindrical deep drawing, In: NUMISHEET 2002 Benchmark Test A results, NUMISHEET 2002, Proceedings of the Fifth International Conference and Workshop on Numerical Simulation of 3D Sheet Forming Processes, Jeju Island, Korea, October 21-25, 2002.

Dudzinski, D.; Molinari, A.: Instability of visco-plastic deformation in biaxial loading, Compt. Rend. Acad. Sci. Paris, 307 (1988), 1315-1321.

Engl, B.; Schneider, Ch.: ULSAB-The Ultra Light Steel Auto Body. Proc. of the SheMet298, Enschede/Holland, April 6-8, 1998, pp. 3-11.

El Khaldi, F: New requirements and recent development in sheet metal stamping simulation, 2002.

Gensamer, M.: Strength and Ductility, Trans. ASM. 36 (1946), pp. 30-60.

Goodwin, G. M.: Application of Strain Analysis to Sheet Metal Forming Problems in the Press Shop, Society of Automotive Engineers (1968), No. 680093, 380-387.

Hosford, W. F.; Caddell, R. M.: Metal Forming: Mechanics and Metallurgy, 2nd Edition, PTR Prentice-Hall, Englewood Cliffs, New Jersey, 1993.

Hosford, W.F.; Duncan, J.L.: Sheet Metal Forming: A Review, JOM 51 (11), 1999, pp. 39-44.

Kawka, M.; Olejnik, L.; Rosochowski, A.; Sunaga, H.; Makinouchi, A.: Simulation of Wrinkling in Sheet Metal Forming, Journal of Materials Processing Technology, 109 (2001), 283-289.

Keeler, S. P.: Plastic Instability and Fracture in Sheet Stretched over Rigid Punches, Thesis, Massachusets Institute of Technology, Boston, MA, 1961.

Keeler, S. P.; Brazier, W. G.: Relationship between laboratory material characterization and press-shop formability, Micro Alloying (1975), 21-32.

Lange, K. (Hsrg.): Lehrbuch der Umformtechnik, Band 3: Blechumformung, Springer-Verlag: Berlin, 1985.

Lankford, W. I.; Snyder, S. C.; Bauscher, J. A.: New Criteria for Predicting the Press Performance of Deep-drawing Sheets, Trans. ASM., 42 (1950), pp. 1196-1232.

Leu, D. K.; Wu, J. Y.: A Simplified Approach to Estimate Limiting Drawing Ratio and Maximum Drawing Load in Cup Drawing, Journal of Engineering Materials and Technology, Vol. 126, January 2004, pp. 116-122.

Marciniak, Z.: Stability of plastic shells under tension with kinematic boundary condition, Archiwum Mechaniki Stosorwanej, 17 (1965), 577-592.

Marciniak, Z.; Duncan, J.L.; Hu, S. J.: Mechanics of Sheet Metal Forming, 2nd Edition, Butterworth-Heinemann, Oxford, 2002.

Metal Forming Handbook, Schuler, Springer-Verlag, Berlin Heidelberg, 1998.

N.N.: Aluminium-Zentrale e.V., Düsseldorf, 2001.

NUMISHEET 2002 Benchmark A: Deep Drawing of Cylindrical Cup. NUMISHEET 2002, Proceedings of the Fifth International Conference and Workshop on Numerical Simulation of 3D Sheet Forming Processes, Jeju Island, Korea, October 21-25, 2002.

PAM-STAMP 2G User's Guide, ESI-Software, France, October, 2002.

Quainoo, G. K.; Yannacopoulos, S.: The Effect of Cold Work on the Precipitation Kinetics of AA6111 Aluminum, Journal of Materials Science, 39 (2004), pp. 6495-6502.

Ramaekers, J. A. H.: A Relation between the Limit-Drawing Ratio LDR and the Material Properties Strain-Hardening Exponent n and Anisotropy Factor R, Advanced Technology of Plasticity, Vol. II, Proceedings of the 6th ICTP, Sept. 19-24, 1999, pp. 1997-1404.

Rebelo, N; Nagtegaal, J.C.; Taylor, L.M.: Comparison of implicit and explicit finite element methods in the simulation of forming processes, In: NUMIFORM'92, Balkema, Rotterdam, 1992, pp. 99-108.

Rees, D.W.A.: Factors Influencing the FLD of Automotive Sheet Metal, Journal of Materials Processing Technology, 118 (2001), pp. 1-8.

Roll, K.; Tekkaya, A. E.: Section 13.2: Numerische Verfahren der Prozeßsimulation in der Umformtechnik. Umformtechnik - Handbuch für Industrie und Wissenschaft, Band 4. Springer-Verlag: Berlin/Heidelberg/New York/Tokyo, 1993, 330-435.

Roll, K.: Virtual Metal Forming, METU-Seminar, 2001.

Tekkaya, A. E.: State-of-the-Art of Simulation of Sheet Metal Forming, Journal of Materials Processing Technology, 103 (2000) 1, pp. 15-23.

Tekkaya, A. E.: ME 413 Introduction to Finite Element Analysis, Lecture Notes, Middle East Technical University, Ankara, Turkey, 2002.

Tekkaya, A. E.: ME 453 Metal Forming Technology Lecture Notes, Middle East Technical University, Ankara, Turkey, 2003.

Schweizerhof, K.; Hallquist, J.O.: Explicit integration schemes and contact formulations for thin sheet metal forming, in: FE-Simulation of 3D Sheet Metal Forming Processes in Automotive Industry, Vol. 894, VDI-Berichte, 1991, pp. 405-439.

Weilong, H.; Wang, Z.R.: Anisotropic Characteristics of Material and basic Selecting Rules with Different Sheet Metal Forming Processes, Journal of Materials Processing Technology, 127, 2002, pp. 374-381.

Woodthrope, J.; Pearce, R.: The anomalous behavior of aluminum sheet under balanced biaxial tension, Int. J. Mech. Sci., 12 (1970), 341-347.

Yano, Y.; Akashi, T.: Use of CAD/CAE in the CASE Activities. Proc. of the NUMIFORM 2001, Toyohashi/Japan, June 18-20, 2001, pp. 27-43.

APPENDIX A

RAMAEKERS' CUP DRAWING FORMING FORCE CALCULATION PROGRAM

A.1 Program Input

Punch Radius: $r_p := 50$

Die Radius: $r_{Di} := 51.25$

Die Fillet Radius: $\rho_D := 9.5$

Punch Fillet Radius $\rho_P := 7$

Initial Sheet Thickness: $s_0 := 1$

Initial Sheet Radius: $r_{u0} := 105$

Material Properties: $C := 547.763$

$\varepsilon_0 := 0.08755$

$n := 0.26921$

Anisotropy Factor: $R_{0^\circ} := 2.16$

$R_{45^\circ} := 1.611$

$R_{90^\circ} := 2.665$

Friction Coefficient at the Flange: $\mu_{fl} := 0.0426$

Friction Coefficient at the Die Fillet: $\mu_\rho := 0.12$

Applied Blankholder Pressure: $P_{blh} := 2.564$

A.2 Basic Formulation

Clearance

$$c := r_{Di} - r_p \qquad c = 1.25$$

Mean Radius

$$r_i := \frac{\left(r_p + r_{Di}\right)}{2} \qquad r_i = 50.625$$

Drawing Ratio

$$\beta_0 := \frac{r_{u0}}{r_i} \qquad \beta_0 = 2.074$$

Mean Anisotropy Factor

$$R := \frac{\left(R_{0°} + 2 \cdot R_{45°} + R_{90°}\right)}{4} \qquad R = 2.012$$

Principal Strains

$$i := 0, 0.1 .. \left(r_i\right) \qquad r_u(i) := r_{u0} - i$$

$$s(i) := s_0 \cdot \left(\frac{r_{u0}}{r_u(i)}\right)^{\frac{1}{R+1}}$$

$$\varepsilon_\phi(r, i) := \frac{-\left[\ln\left[\left(\frac{r_{u0}}{r}\right)^2 - \left[\left(\frac{r_u(i)}{r}\right)^2 - 1\right] \cdot \frac{s(i)}{s_0}\right]\right]}{2}$$

$$\varepsilon_z(r, i) := \ln\left(\frac{s(i)}{s_0}\right)$$

$$\varepsilon_r(r, i) := -\left(\varepsilon_\phi(r, i) + \varepsilon_z(r, i)\right)$$

Equivalent Strain

$$\varepsilon_{bar}(r, i) := \sqrt{\left(\frac{R + 1}{2 \cdot R + 1}\right) \cdot \left[\left(\varepsilon_\phi(r, i)\right)^2 + \left(\varepsilon_z(r, i)\right)^2 + R\left(\varepsilon_r(r, i)\right)^2\right]}$$

$$\sigma_f(r, i) := C \cdot \left(\varepsilon_0 + \varepsilon_{bar}(r, i)\right)^n$$

A.3 Flange Deformation Force

$$K_f := 1.06 - 0.015 R$$

$$K_\sigma(i) := \frac{\sigma_f(r_i, i)}{\sigma_f(r_u(i), i)}$$

$$\beta(i) := \frac{r_u(i)}{r_i}$$

$$F_{Dfl}(i) := K_f \cdot \left(\ln\left(\frac{\beta_0}{\beta(i)} \right) + \varepsilon_0 \right)^n \cdot \left(\frac{\beta_0}{\beta(i)} \right)^{\frac{1}{R+1}} \cdot \left[1 - K_\sigma(i) + \left(1 + \frac{K_\sigma(i) - 1}{1 - \frac{1}{\beta(i)}} \right) \cdot \ln(\beta(i)) \right] \left(1 + \frac{s_0}{2 \cdot r_p} \right)$$

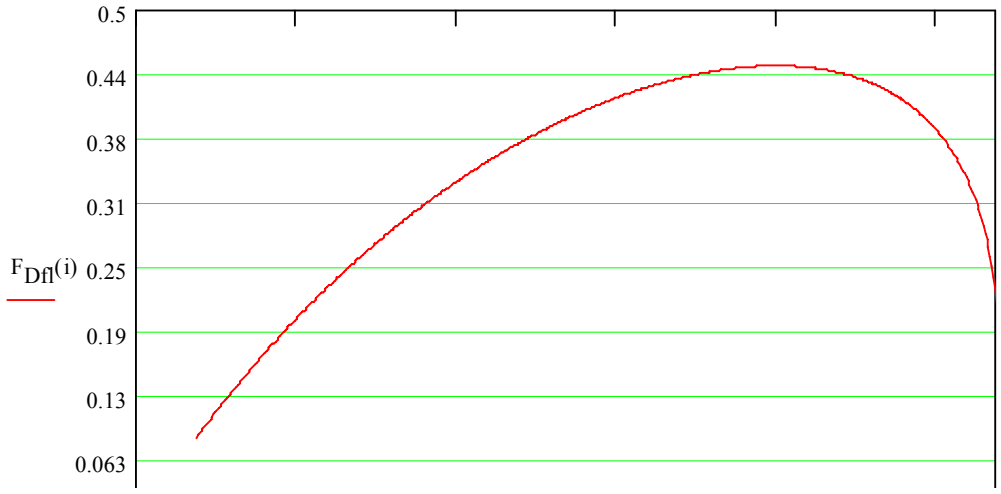

Figure A.1: Flange deformation force

A.4 Bending – Rebending Force

$$F_{D\rho}(i) := 0.8 \cdot \frac{\sigma_f(r_i, i)}{C} \cdot \frac{R + 1}{\sqrt{2 \cdot R + 1}} \cdot \frac{s(i)}{2 \cdot \rho_D + s(i)} \cdot \left(1 + \frac{s_0}{2 \cdot r_p}\right)$$

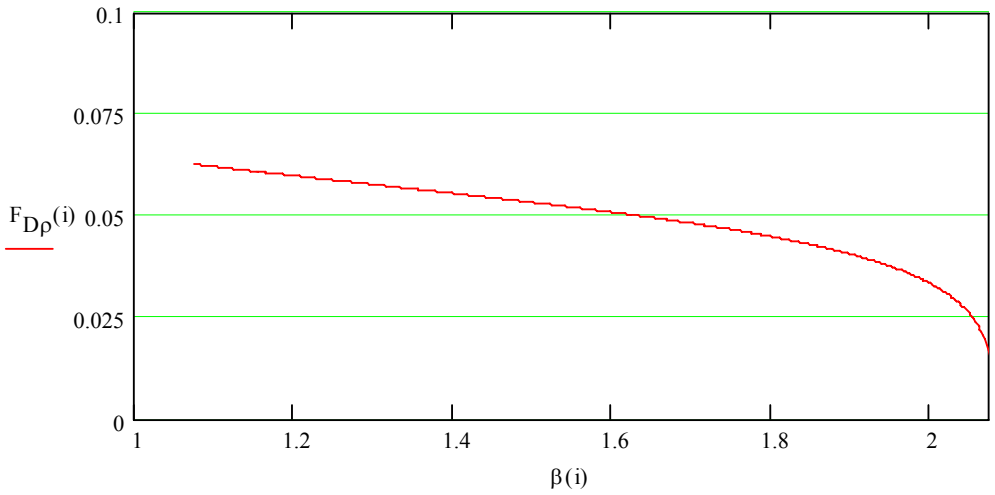

Figure A.2: Bending – rebending force

A.5 Friction Force between Tool and Flange

$$F_{Frfl}(i) := \mu_{fl} \cdot \frac{P_{blh}}{C \cdot r_p \cdot s_0} \cdot \left[(r_{u0})^2 - (r_{Di} + \rho_D)^2 \right]$$

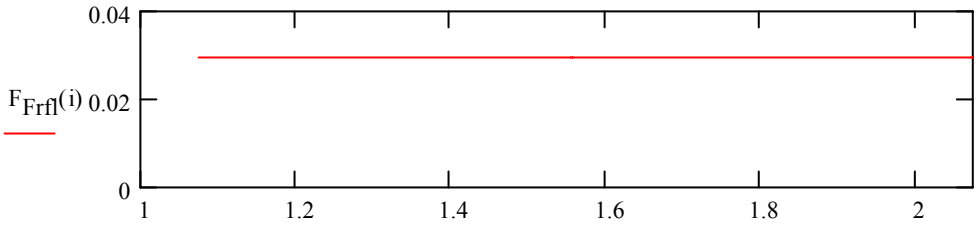

Figure A.3: Friction force between tool and flange

A.6 Friction Force at Die Fillet

$$F_a(i) := F_{Dfl}(i) + F_{Frfl}(i) + \frac{1}{2}\cdot F_{D\rho}(i)$$

$$F_{Fr\rho}(i) := 1.6\cdot\mu_\rho \cdot F_a(i)$$

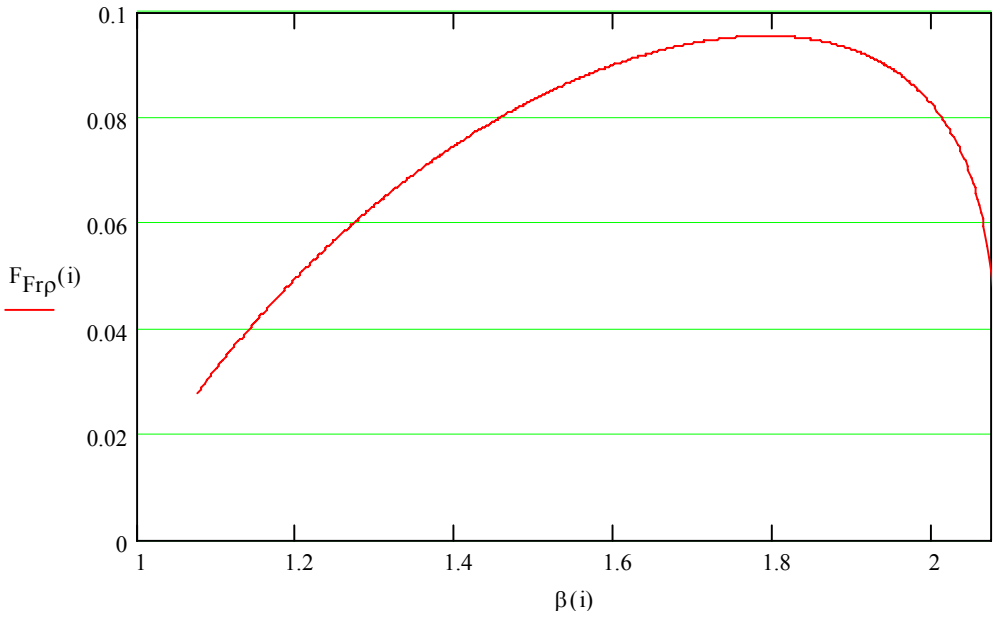

Figure A.4: Friction force at die fillet

A.7 Critical Force

$$F_C := \frac{\left(\frac{R+1}{\sqrt{2\cdot R+1}}\right)^{n+1}\cdot n^n}{\left[\left(\frac{s_0}{\rho_P}\right) + \frac{s_0}{r_p} + e^{n-\frac{\sqrt{2\cdot R+1}}{R+1}\cdot\varepsilon_0}\right]}$$

A.8 Total Forming Force

$$F_D(i) := F_{Fr\rho}(i) + F_{Frfl}(i) + F_{D\rho}(i) + F_{Dfl}(i)$$

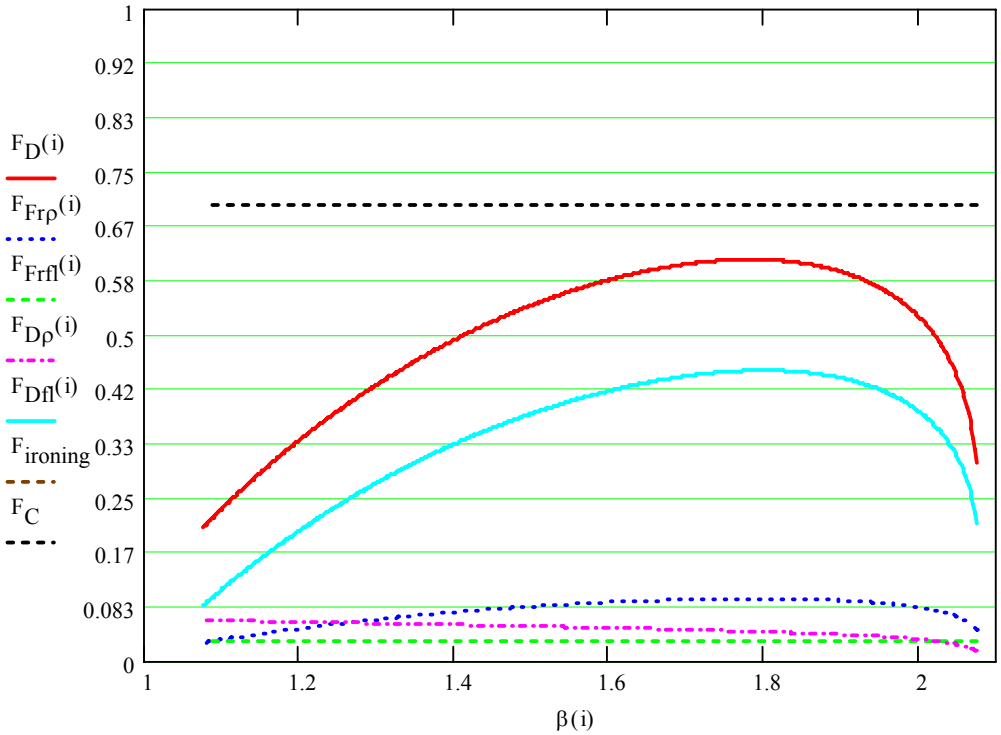

Figure A.5: Total forming force

APPENDIX B

NUMISHEET 2002 BENCHMARK PARTICIPANTS

B.1 Participants who Supplied the Experimental Data

Table B.1: Participant information of AE-01

Experiment:	AE-01
Benchmark participant:	Haruyuki Konishi (Kobe Steel), Robert E Dick(ALCOA)
Address:	5-5 Takatsukadai 1, Nishi-ku, Kobe, 651-2271 JAPAN
Email:	konishi@afrs.kobelco.co.jp, Robert.Dick@alcoa.com
Phone number:	81-78-992-5515
Fax number:	81-78-992-5517

Table B.2: Participant information of AE-03

Experiment:	AE-03
Benchmark participant:	L. Filice
Affiliation:	University of Calabria
Address:	Dep. of Mech. Eng. , 87036 RENDE (CS) - Italy
Email:	l.filice@unical.it
Phone number:	+39 0984 494608
Fax number:	+39 0984 494673

Table B.3: Participant information of AE-04

Experiment:	AE-04
Benchmark participant:	Joachim Danckert
Affiliation:	Department of Production, Aalborg University
Address:	Fibigerstraede 16, DK-9220 Aalborg, Denmark
Email:	i9joach@iprod.auc.dk
Phone number:	45 9635 8959
Fax number:	45 98 15 30 30

Table B.4: Participant information of AE-05

Experiment:	AE-05
Benchmark participant:	P.P. Date, Amit. M. Joshi, V. Anil Kumar. Sammeta
Affiliation:	Indian Institute of Technology, Bombay
Address:	Mech. Eng. Dept. IIT. Bombay, Powai, Mumbai-India
Email:	ppdate@me.iitb.ac.in, amitmechindia@yahoo.com
Phone number:	91 22 576 7511
Fax number:	91 22 572 6875

Table B.5: Participant information of AE-06

Experiment:	AE-06
Benchmark participant:	Jonathan White*, Seung-Geun Lee*, Y.Choi*, J.K.Lee*, R.H. Wagoner**
Affiliation:	The Ohio State University, *Dept. Mech. Eng., **Dept. Mat. Sci. and Eng.
Address:	*209 West 18th Avenue. Columbus Ohio 43210 **2041 College Drive, Columbus Ohio 43210
Email:	choi.43@osu.edu, Lee.71@osu.edu
Phone number:	(614)292-7371
Fax number:	(614)292-7369
Remarks:	All measurements are numerical averaged values of three experiments

Table B.6: Participant information of AE-07

Experiments:	AE-07
Benchmark participant:	E.H. Atzema
Affiliation:	Corus Research, development & Technology
Address:	IJTC-PRA-AUT-STP
Email:	3H36 / 1-18; P.O. Box 10.000; 1970 CA IJmuiden; Netherlands

Phone number:	+31 2514 98524'
Fax number:	+31 2514 70432'
Remarks:	Thickness was obtained from optical surface strain measurements (PHAST tm) on the outside surface of the cup. This means the strains will be over estimated and consequently the thickness underestimated at the punch radius. The other way around at the die radius. Moreover the grid applied may influence the friction. On the aluminum the grid showed no influence on force displacement diagram, on steel a 5% increase in force was seen.

B.2 Participants who Supplied the Simulations

Table B.7: Participant information of AS-01

Simulation:	AS-01
Benchmark participant:	João Pedro DE MAGALHÃES CORREIA, Gérard FERRON
Affiliation:	Laboratoire de Physique et Mécanique des Matériaux
Address:	I.S.G.M.P., Université de Metz, Ile du Saulcy Metz-FRANCE
Email:	pedro@lpmm.sciences.univ-metz.fr
Phone number:	00 333 87 31 53 82
Fax number:	00 333 87 31 53 66
Name of the FEM code:	ABAQUS/Explicit 5.8-15
General aspects of the code:	commercial dynamic explicit finite element code
Basic formulations:	1-for all the simulations, an explicit dynamic finite element analysis has been performed 2-the anisotropic plastic material behavior is modeled with the model proposed by Ferron et al (1994) 3-as regards wrinkling analysis no wrinkling indicator has been used and no defect in the initial mesh has been introduced
Element/Mesh technology:	for the blank: 4-node, reduced integration, doubly curved shell elements (called S4R) with hourglass control, small membrane strains for the tools: 4-node, bilinear quadrilateral, rigid element
Number / type of elements:	blank: 1065 elements S4R die: 360 elements R3D4 blank-holder: 126 elements R3D4 punch: 324 elements R3D4 total number of elements: 1875
Computer used:	HP 9000/785/J5600 2cpus (RAM: 1.5 Gb)
CPU-Time: (average values)	2h50mm (high BHF, with punch speed=2,5 mm/s) 5h10mm (low BHF, H=40 mm and punch speed=1 mm/s)
Remarks:	for the 6111-T4, with a high BHF, necking occurs on the punch shoulder radius at the final stage of the deformation process.

Table B.8: Participant information of AS-02

Simulation:	AS-02
Benchmark participant:	Sharvari G. Desai , P.P.Date , *K.Narasimhan
Address:	Department of Mechanical Engg, and *Department of Metullargy and Material science , IIT powai ,India .
Email:	ppdate@me.iitb.ac.in
Phone number:	91-22-576 7511
Fax number:	91-22-5726875
Name of the FEM code:	OPTRIS ,ESI ,France .
General aspects of the code:	Elasto-plastic shell element
Basic formulations:	Explicit time integration formulation
Element/Mesh technology:	Adaptive meshing
Number and type of elements	4-node and 3-node element
Computer used:	Pentium-4 processor
CPU-Time:	1 hour 30 min
Remarks:	enclosed separately

Table B.9: Participant information of AS-03

Simulation:	AS-03
Benchmark participant:	Raghu Echempati, Ph. D., P.E.
Affiliation:	Mechanical Engineering Dept., Kettering Uni
Address:	1700 W Third Avenue, Flint, MI 48504 (USA)
Email:	rechempa@kettering.edu
Phone number:	810-762-7835
Fax number:	810-762-7860
Name of the FEM code:	Dynaform (version 3.3)/LS-DYNA (version 960)
General aspects of the code:	Explicit Solver, 5 int. points through thickness
Basic formulations:	Quarter Model of the cup
Element/Mesh technology:	Belytschko-Tsay Material 36 in DYNA; Thin Shell elements;
Number and type of elements	# of elements 588 (Quads: 560), shell elements
Computer used:	Sun Blade 1000, 950 MHz, dual processor
CPU-Time:	40 to 50 hours on an average using 2 CPUs
Remarks:	The results obtained at higher punch speeds match closely with the suggested upper bound speed of 50 mm/s, thus reducing the CPU time at 1,000 mm/s punch speed to less than 7 hours.

Table B.10: Participant information of AS-04

Simulation:	AS-04
Benchmark participant:	Tony Chang, Wei Wang
Affiliation:	Rouge Steel Company
Address:	3001 Miller Road, Dearborn, MI 48121
Email:	tchang@rougesteel.com
Phone number:	313 323 1661
Fax number:	313 322 4100
Name of the FEM code:	LS-DYNA3D
General aspects of the code:	Dynamic

Basic formulations:	Explicit
Element/Mesh technology:	Generate geometry and mesh using eta/DYNAFORM based on the information in the benchmark document.
Number and type of elements:	3449 shell elements were in the model with 1092 element initially for the blank. Adaptivity was used in the simulation. The number of elements in the blank at the end of the simulation was 9900 for high BHF case, and it was 9954 for low BHF case.
Computer used:	COMPAQ DEC/Alpha XP1000
CPU-Time:	about 5 hours and 10 minutes for each case.

Table B.11: Participant information of AS-05

Simulation:	AS-05
Benchmark participant:	Jun Park
Address:	Hibbitt, Karlsson & Sorensen, Inc.,1080 Main St. Pawtucket, RI, USA
Email:	park@hks.com
Phone number:	401-727-4208
Fax number:	401-727-4208
Name of the FEM code:	ABAQUS/Explicit
Basic formulations:	explicit time integration
Element/Mesh technology:	shell element with reduced integration
Number and type of elements	6948 and 9278 elements for alu. and steel
Computer used:	Pentium 3, 1GHz
CPU-Time:	Dependent on problems
Remarks:	Results on only a quarter of the circle are presented in this report for both outer profile and height profile in HBHF&LBHF,respectively

Table B.12: Participant information of AS-06

Simulation:	AS-06
Benchmark participant:	Wang Hua, Li Dongsheng,Zhou Xianbin,Jin Chaohai
Affiliation:	Sheet Forming Research Center Beijing University Of Aeronautics & Astronautics
Address:	704, Beijing University of Aeronautics and Astronautics, Beijing, 100083, P.R.China
Email:	LDSHXS@263.net , silente@21cn.com
Phone number:	+86-10-82317701
Fax number:	+86-10-82317774
Name of the FEM code:	PAM-STAMP 2000
Basic formulations:	Dynamic Explicit,Elasto-Plastic Incremental Theory,Updated Lagrangian
Element/Mesh technology:	BT Shell Element
Number and type of elements	Al6114-T4 Blank: 8368 Elements Totally 8104 4-Node Elements with 264 3-Node Elements (local)
	Steel DDQ Blank: 11132 Elements Totally 10804 4-Node Elements with 328 3-Node Elements (local)
Computer used (1):	PC_PentiumII-300 For Al6114-T4 Under 50KN High BHF
CPU-Time:	818 Minutes
Computer used (2):	PC_PentiumIII-866 For Al6114-T4 Under 10KN Low BHF

CPU-Time:	1540 Minutes
Computer used (3):	PC_PentiumIII-550 For Steel-DDQ Under 70KN High BHF
CPU-Time:	570 Minutes
Computer used (4):	PC_PentiumIV-1.7G For Steel-DDQ Under 10KN Low BHF
CPU-Time:	1504 Minutes

Table B.13: Participant information of AS-07

Simulation:	AS-07
Benchmark participant:	Siguang Xu, Jimmy Zhang and Chuan-Tao Wang
Affiliation:	Die Engineering Analysis Department, ,General Motors Corp.
Address:	100 Kirts Blvd, Mail Code: 483-610-501, P.O. Box 5001, Troy, MI
Email:	chuan-tao.wang@gm.com
Phone number:	248-696-5038
Fax number:	248-696-5040
Name of the FEM code:	Ls-Dyna3d Version 960
General aspects of the code:	3D Dynamic explicit, elastic-plastic flow
Basic formulations:	Hill's 48 yield function, planar anisotropic, isotropic hardening
Element/Mesh technology:	B-T shell element
Number / type of elements	23780 (aluminum)/31460(steel) elements for full model
Computer used:	Sun Blade 1000 two CPU machine
CPU-Time:	9hrs 8min(aluminum)/16hrs 48min(steel).
Remarks:	Punch speed is scaled to 1000 mm/s

Table B.14: Participant information of AS-08

Simulation:	AS-08
Benchmark participant:	J. L. Alves, M. C. Oliveira, L. F. Menezes
Affiliation:	Department of Mechanical Engineering, FCTUC, University of Coimbra
Address:	Polo II, Pinhal de Marrocos, 3030 Coimbra, Portugal
Email:	jlalves@dem.uminho.pt
Phone number:	+351 239 790700
Name of the FEM code:	DD3IMP
General aspects of the code:	Fully implicit (single iterative loop to treat non-linear elastoplasticity and contact with friction)
Basic formulations:	Elasto-plastic formulation with isotropic and kinematic hardening, Hill'48 anisotropy and an augmented Lagrangian approach to treat contact with friction (Coulomb's law); tools modeled by Bézier surfaces
Element/Mesh technology:	Isoparametric 3D brick elements with selective reduced integration technique
Number and type of elements	8-node 3D solid FE - DDQ: 3272 FE, 6714 nodes; 6111-T4: 2168 FE, 4476 nodes.
Computer used:	Intel Xeon 1.7GHz 1GB RDRam
CPU-Time:	Earing / Wrinkling simulations: about 33 / 103 hours
Remarks:	Due to the material and part symmetries, only one quarter of the total part was simulated; sheet discretized with 3 FE layers throughout thickness

Table B.15: Participant information of AS-09

Simulation:	AS-09
Benchmark participant:	Chung-Souk Han, Robert H. Wagoner
Affiliation:	The Ohio State University, Dept. Matr.Sci.&Eng.
Address:	2041 College Road, Columbus, OH 43210, USA
Email:	wagoner@mse.eng.ohio-state.edu
Phone number:	1-614-292-2079
Fax number:	1-614-292-6530
Name of the FEM code:	SHEET-3
General aspects of the code:	Static implicit code with N-CFS contact algorithm
Basic formulations:	4 node shallow shell with large membrane strain
Element/Mesh technology:	729 shell elements with 6 degrees of freedom
Computer used:	Pentium II, 450 MHz, 384 MB memory
CPU-Time:	65293 SEC.

Table B.16: Participant information of AS-10

Simulation:	AS-10
Benchmark participant:	Seung-Geun Lee, Yangwook Choi, J.K.Lee
Affiliation:	The Ohio State University
Address:	209 West 18th Avenue. Columbus Ohio 43210 USA
Email:	choi.43@osu.edu, Lee.71@osu.edu
Phone number:	(614)292-7371
Fax number:	(614)292-7369
Name of the FEM code:	ABAQUS v6.21
General aspects of the code:	EXPLICIT
Element/Mesh technology:	Reduced 4 Node Bilinear Shell Element
Computer used:	AMD Athlon 1.0GHz
CPU-Time:	71276sec

Table B.17: Participant information of AS-11

Simulation:	AS-11
Benchmark participant:	E.H. Atzema
Affiliation:	Corus Research, development & Technology
Address:	IJTC-PRA-AUT-STP 3H36 / 1-18; P.O. Box 10.000; 1970 CA IJmuiden; The Netherlands
Phone number:	+31 2514 98524'
Name of the FEM code:	DiekA
General aspects of the code:	Implicit, iterative solver, large strain formulation
Basic formulations:	Vegter yield locus Bergstrom hardening
Element/Mesh technology:	Membrane, DKT, DST elements used. Discrete Shear Triangular elements, 5 i.p. over thickness
Number and type of elements	Steel: 10191 DST + 20382 contact elements / Aluminum: 7682 DST + 15364 contact elements
Computer used:	HP 9000 / 785 (dual 8500 processor)
CPU-Time:	Steel: 1216 min. / Aluminum: 971 min.
Remarks:	Wrinkles are given around averaged profile.

Table B.18: Participant information of AS-12

Simulation:	AS-12
Benchmark participant:	Siguang Xu, Ramesh Joshi, Jimmy Zhang and Chuan-Tao Wang
Affiliation:	Die Engineering Analysis Department, Metal Fabricating Division, General Motors Corp.
Address:	100 Kirts Blvd, Mail Code: 483-610-501, P.O. Box 5001, Troy, MI 48007-5001
Email:	chuan-tao.wang@gm.com
Phone number:	248-696-5038
Name of the FEM code:	Pam-Stamp 2000
General aspects of the code:	3D Dynamic explicit, elastic-plastic, flow Incremental theory
Basic formulations:	Hill's 48 yield function, planar anisotropic, isotropic hardening
Element/Mesh technology:	B-T shell element
Number / type of elements	4105 (aluminum)/5065(steel) elements
Computer used:	Sun Blade 1000 two CPU machine
CPU-Time:	4hrs 5min(aluminum)/5hrs 11min(steel). (2 shared memory processors, double precision)
Remarks:	one quarter of the cup is analyzed. Punch speed is scaled to 1000 mm/s

Table B.19: Participant information of AS-13

Simulation:	AS-13
Benchmark participant:	Maki Nagakura, Masato Takamura, Ohura kenichi
Affiliation:	Integrated V-CAD System Research Program The Institute of Physical and Chemical Research
Address:	2-1, Hirosawa, Wako-shi, Saitama, 351-0198, Japan
Email:	nagakura@astom.co.jp takamura@postman.riken.go.jp
Phone number:	+81(48) 467-9423
Fax number:	+81(48) 467-8705
Name of the FEM code:	ITAS3D
General aspects of the code:	Static-explicit FEM Hill's quadratic yield function and the associative flow rule r-minimum method to control the size of incremental step Point data approach to describe tool geometry
Basic formulations:	Updated Lagrangian rate formulation
Element/Mesh technology:	4-node quadrilateral degenerated shell element
Number / type of elements	Aluminum(M1) High BHF=50N : shell / Number of element=3,210
	Aluminum(M1) Low BHF=10N : solid / Number of element=6,420
	DDQ(M2) High BHF=70N : shell / Number of element=4,296
	DDQ(M2) Low BHF=10N : solid / Number of element=8,592
Computer used:	Pentium4
CPU-Time:	shell : 850min/case, solid : 4050min/case

Table B.20: Participant information of AS-14

Simulation:	AS-14
Benchmark participant:	YongMing Kong, Wan Cheng, DeCai Jia
Affiliation:	Altair Engineering Ltd. (China)
Address:	Suite 305, 53 HuangPu Road, Shanghai 200080, P.R.China
Email:	kym@altair.com.cn, or yongmingkong@yahoo.com
Phone number:	86-21-53930011 ext 204
Fax number:	86-21-53930859
Name of the FEM code:	HyperForm 5.0
General aspects of the code:	Altair HyperForm is a unique finite element based sheet metal forming simulation software solution.
Basic formulations:	Explicit dynamic solver LS-DYNA is adopted
Number / type of elements	4-nodes shell elements are applied, total 20353 elements are used.
Computer used:	PC with one 1.6GHz Processor and 1G RAM
CPU-Time:	56 minutes

Table B.21: Participant information of AS-15

Simulation:	AS-15
Benchmark participant:	T. Meinders
Affiliation:	University of Twente
Address:	P.O.Box 217 7500 AE Enschede
Email:	v.t.meinders@ctw.utwente.nl
Phone number:	0031 53 489 4360
Name of the FEM code:	Dieka
General aspects of the code:	Implicit
Number / type of elements	discrete shear triangles. Initially the simulation is started with 2372 elements, whereafter adaptive mesh refinement is applied
Computer used:	hp8000
CPU-Time:	1.8 hrs
Remarks:	Refinement during simulation is driven by error indicators and wrinkling indicators

Table B.22: Participant information of AS-16

Simulation:	AS-16
Benchmark participant:	Adrian Banks
Affiliation:	Corus Group
Address:	Corus Research, Development & Technology, Po Box 10.000, 1970 CA IJmuiden, The Netherlands.
Email:	adrian.banks@corusgroup.com
Phone number:	+31 (0)251 491735
Name of the FEM code:	Autoform, 3.14
General aspects of the code:	Implicit, adaptive mesh. 5 layers through thickness
Element/Mesh technology:	Autoform automesh
Number and type of elements	6257, triangular
Computer used:	HP 9000 / 785 (dual 8500 processor)
CPU-Time:	High BHF - Aluminum = 253 s ; Low BHF - Aluminum = 245 s ; High BHF - Steel = 263 s ; Low BHF - Steel = 257 s

APPENDIX C

MATERIAL PROPERTIES OF 6111-T4 ALUMINUM AND DDQ MILD STEEL

C.1 Material Properties of 6111-T4 Aluminum Alloy

Alcoa Technical Center provided 6114-T4 aluminum alloy material for Numisheet 2002 benchmark participants and also carried out the material characteristics for the aluminum material.

Table C.1: Chemical composition – 6111-T4 sheet

Element, wt%									
Si	**Fe**	**Cu**	**Mn**	**Mg**	**Cr**	**Ni**	**Zn**	**Ti**	**Be**
0.82	0.28	0.73	0.21	0.65	0.03	0.00	0.02	0.02	0.0000

Table C.2: Equal biaxial tension test data – 6111-T4 sheet

t, mm	**Strain Rate, sec^{-1}**	**Maximum:**		**Hollomon**		**Voce**		
		σ, MPa	**ε**	**n**	**K, MPa**	**A, MPa**	**B, MPa**	**C**
1.0	0.005	456.9	0.519	0.226	547.9	459.8	268.4	6.838
	0.05	448.0	0.521	0.215	535.0	450.4	266.2	7.460

Table C.3: Uniaxial tension test data – 6111-T4 sheet

t, mm	Dir	YS, MPa	UTS, MPa	% Elong.		r	Hollomon		Voce		
				Unif.	Tot.		n	K, MPa	A, MPa	B, MPa	C
1.0	0	194.1	315.7	23.6	27.6	0.894	0.223	550.4	429.8	237.7	8.504
	15	189.6	315.1	23.1	27.7	0.885	0.222	547.9	426.0	233.3	8.749
	30	182.2	312.4	23.7	26.5	0.743	0.224	544.6	424.2	233.6	8.572
	45	177.9	306.7	24.2	27.5	0.611	0.224	534.5	420.1	232.7	8.248
	60	176.5	304.5	24.1	27.8	0.611	0.225	531.5	416.2	230.6	8.322
	75	175.0	304.0	23.8	26.6	0.627	0.227	532.6	414.8	231.7	8.442
	90	173.4	302.5	24.0	26.8	0.660	0.231	533.5	414.9	233.7	8.298
Hollomon Equation: $\sigma = K \varepsilon^{n}$							Voce Equation: $\sigma = A - B \exp(-C \varepsilon)$				

Table C.4: Analyses of engineering stress – strain curve (elastic region) – 6111-T4 sheet

ID	Modulus, GPa	Poisson's Ratio
786052-0	70.5	0.346
786052-45	71.4	0.333
786052-90	69.6	0.346
Average	70.5	0.342

Table C.5: X-ray Laue analyses

~ASTM Grain Size	Degree Recystallization	% Strain
7.0-7.5	Complete	0

Table C.6: X-ray Guinier analyses

$Al_{12}(Fe,Mn)_3Si$	$Al_{12}(Mn,Fe)_3Si$
Large	Medium+

Table C.7: Grain count data – optical microscopy

Grains/mm			Grains/mm^2		Grains/mm^3
X	Y	Z	XZ	YZ	XYZ
38.8	32.6	42.8	1660.6	1395.3	54136.9

Table C.8: Coulomb friction coefficients – aluminum 6111-T4

	Friction Coefficients		
	Test 1	**Test 2**	**Average**
Lubricant (FD-1500)	0.0105	0.0087	0.0096
Without Lubricant	0.1369	0.1327	0.1348

Figure C.1: Longitudinal section at the t/2 location for 6111-T4 sample 786052 in the etched condition (Graff-Sergeant) showing constituent and dispersoid particle distributions (500X)

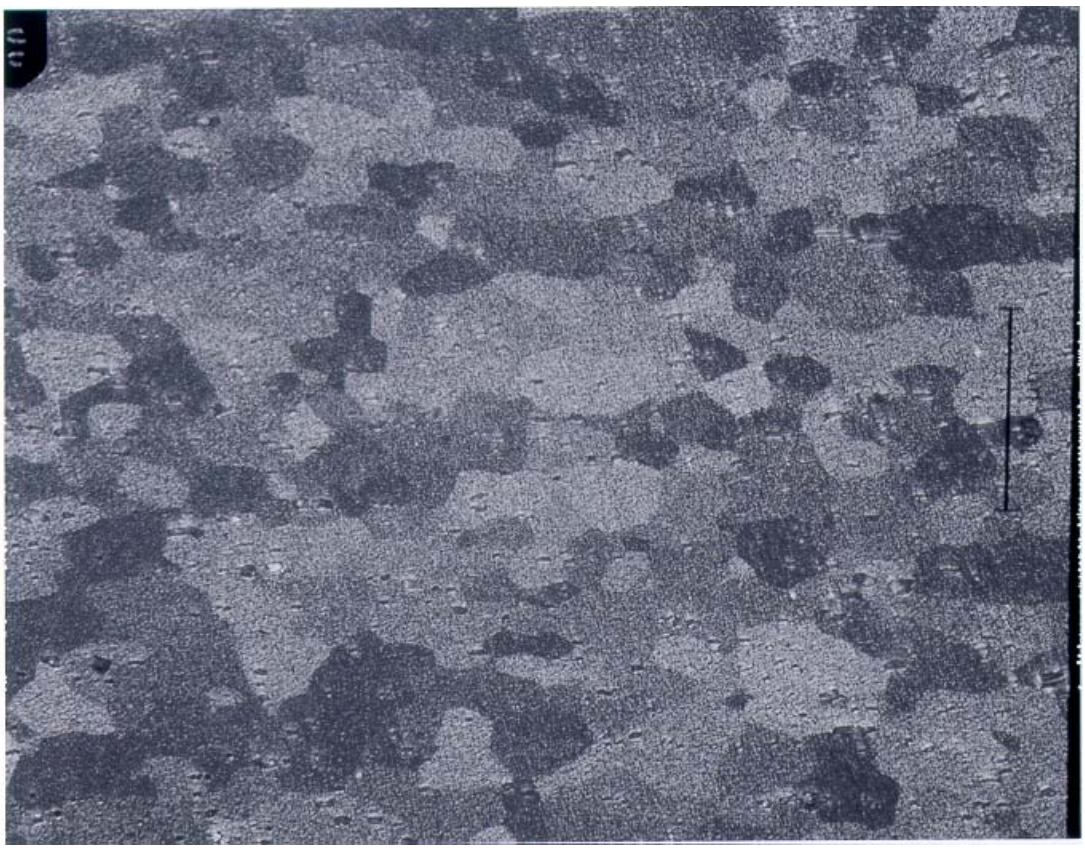

Figure C.2: Longitudinal section at the t/2 location for 6111-T4 sample 786052 in the electro-polished and viewed under polarized light condition (EE/PL) showing grain structure (200X)

C.2 Material Properties of DDQ Mild Steel

POSCO provided mild steel sheet (DDQ grade) for Numisheet 2002 benchmark participants and also carried out the material characteristics for the steel.

Table C.9: Uniaxial tension test data – mild steel (DDQ)

	% Elong. Tot.	TS, MPa	r	Flow Stress [MPa] $\sigma=K(\varepsilon_0+\varepsilon)^n$		
				K [MPa]	ε_0	n
0°	50.732	288.82	2.160	539.87	0.00786	0.27035
45°	47.260	298.18	1.611	558.23	0.00838	0.26644
90°	47.023	284.89	2.665	534.72	0.01040	0.27361

Table C.10: Analyses of Young's modulus values (elastic region) – mild steel (DDQ)

	0°	**45°**	**90°**
Modulus [GPa]	213.14	227.07	218.19
* Average Young's Modulus : 221.37 GPa * Poisson's Ratio : 0.3			

Table C.11: Coulomb friction coefficients – mild steel (DDQ)

	Friction Coefficients			
	Test 1	**Test 2**	**Test 3**	**Average**
Lubricant (FD-1500)	0.0420	0.0419	0.0439	0.0426
Without Lubricant	0.1438	0.1459	0.1479	0.1459